TECHNISCHE UNIVERSITÄT MÜNCHEN
TUM School of Engineering and Design

Modeling and designing lightweight acoustic metamaterials with tailored vibroacoustic properties

Matthias Benedikt Miksch

Vollständiger Abdruck der von der TUM School of Engineering and Design der Technischen Universität München zur Erlangung des akademischen Grades eines

Doktors der Ingenieurwissenschaften

genehmigten Dissertation.

Vorsitz: Prof. Dr.-Ing. Martin Mensinger

Prüfende/-r der Dissertation:

                                   1. Prof. Dr.-Ing. Gerhard Müller

                                   2. Prof. Brian Richard Mace, Ph.D.

Die Dissertation wurde am 05.07.2021 bei der Technischen Universität München eingereicht und durch die TUM School of Engineering and Design am 15.03.2022 angenommen.

Abstract

The presented thesis discusses two concepts which show potentials for future lightweight solutions with improved vibroacoustic properties. The first concept is based on the idea to capture bending waves at predefined locations to reduce structure borne noise. The advantage of this concept is the improvement of the vibroacoustic properties on a broad frequency range while the mass of the overall structure also decreases. Various studies suggest smooth thickness profiles based on the idea of so called "acoustic black holes". This work confirms the benefit of local thickness reduction. Beyond that the presented numerical studies show that an abrupt thickness profile with localized damping measures can outperform smooth profiles with similar damping measures. Comparisons between beams with and without local thickness reductions demonstrate the increased energy dissipation at localized damping treatments and explain the resulting lower amplitudes of the vibration and the reduction of the radiated sound power. The second concept are periodically distributed resonators attached or incorporated in the main structure. So called locally resonant materials show beneficial vibroacoustic properties at specific target frequencies. This work focuses on the design of beam-like resonators and how to adjust their geometry to maximize the performance. The thesis proposes the computation of the spatially decaying characteristics to assess the performance of the resonant material by means of the wave solutions using the Wave Finite Element Method. Based on the spatial decaying characteristics, different configurations of beam-like resonators are evaluated to assess design criteria. The benefit of this approach is that the boundary conditions of the host structure are not necessary, which offers the opportunity to evaluate different resonator configurations at an early stage of development.

Keywords

Acoustic black holes, Acoustic metamaterials, Lightweight solutions, Locally resonant materials, Modeling aspects, Periodic structures, Sound radiation, Vibration control, Vibroacoustic, Wave Finite Element Methods, Wave solutions

Contents

List of Figures

List of Tables

Symbol Directory

Prefixes

$d\square$	Infinitesimal quantity
$\frac{\partial}{\partial x}\square$	Partial derivative
$\nabla\square$	Gradient
$\Delta\square$	Laplace operator
$\delta\square$	Virtual quantity

Supplements

$\underline{\square}$	Complex amplitude
$\square^*$	Complex conjugate
$\square^T$	Transpose
$\hat{\square}$	Fourier transformed quantity
$\dot{\square}$	First derivative with respect to time
$\ddot{\square}$	Second derivative with respect to time

Greek letters

ϵ	-	Strain tensor
η	-	Structural loss factor
θ	rad	Phase
κ	rad/m	Floquet wavenumber
κ_{Re}	rad/m	Phase shift per unit meter
κ_{Im}	rad/m	Decay per unit meter
ν	-	Poisson's ratio

Π	Nm	Work
π	-	Mathematical constant
ρ	$\frac{\text{kg}}{\text{m}^3}$	Density
$\boldsymbol{\sigma}$	$\frac{\text{N}}{\text{m}^2}$	Stress vector
$\boldsymbol{\Phi}$	-	Matrix of right eigenvectors
$\boldsymbol{\Phi}_i$	-	i-th eigenvector
ω	$\frac{\text{rad}}{\text{s}}$	Angular eigenfrequency
Ω	$\frac{\text{rad}}{\text{s}}$	Angular frequency of excitation

Latin letters

A	m^2	Cross sectional area
B	$\frac{\text{N}}{\text{m}}$	Bending stiffness
$\boldsymbol{C}$	$\frac{\text{Ns}}{\text{m}}$	Damping matrix
c	$\frac{\text{Ns}}{\text{m}}$	Damping coefficient
c_g	$\frac{\text{m}}{\text{s}}$	Group velocity
c_p	$\frac{\text{m}}{\text{s}}$	Phase velocity
E	$\frac{\text{N}}{\text{m}^2}$	Young's Modulus
E_{kin}	Nm	Kinetic energy
E_{pot}	Nm	Potential energy
e	-	Euler's number
f	Hz	Frequency
h	m	Thickness of a plate
I	m^4	Area moment of inertia
I_j	$\frac{\text{N}}{\text{sm}}$	Structural intensity in direction j
i	-	Imaginary unit
$\mathfrak{I}$	-	Imaginary part
$\boldsymbol{K}$	$\frac{\text{N}}{\text{m}}$	Stiffness matrix
K	$\frac{\text{N}}{\text{m}^2}$	Bulk modulus
k	$\frac{\text{rad}}{\text{m}}$	Wavenumber
k_{air}	$\frac{\text{rad}}{\text{m}}$	Wavenumber in the air
k_B	$\frac{\text{rad}}{\text{m}}$	Wavenumber of bending wave
k_s	$\frac{\text{N}}{\text{m}}$	Spring stiffness
k_x	$\frac{\text{rad}}{\text{m}}$	Wavenumber in x-direction
k_y	$\frac{\text{rad}}{\text{m}}$	Wavenumber in y-direction
k_z	$\frac{\text{rad}}{\text{m}}$	Wavenumber in z-direction

$\boldsymbol{M}$	kg	Mass matrix
m	kg	Mass
$\bar{n}$	-	Surface normal vector
p	N/m²	Surface load
Q	N	Shear force
R	-	Reflection coefficient
$\mathfrak{R}$	-	Real part
q	N/m	Line load
$\mathbf{S}$	$\frac{\text{N}}{\text{m}^2}$	Dynamic stiffness matrix
t	s	Time variable
u,v,w	m	Displacement in x,y,z
$\mathbf{u}$	m	Vector of displacements
q	$\frac{\text{N}}{\text{m}}$	Line load
W''_{diss}	$\frac{\text{N}}{\text{m}^2}$	Energy dissipation per unit area
x,y,z	m	Spatial coordinates
$\mathbf{x}$	m	Vector of spatial coordinates

Others

$\mathbf{0}$	matrix with zeros
$\mathbf{1}$	identity matrix

Abbreviations

ABH	Acoustic black hole
ALM	Additive layer manufacturing
CLD	Constrained layer damping
DOF	Degree of freedom
FE(M)	Finite Element (Method)
FRF	Frequency response function
RMS	Rout mean squared
SDOF	Single degree of freedom
STI	Structural intensity
TMD	Tuned mass damper
WFE(M)	Wave Finite Element (Method)

1 Introduction

1.1 Motivation

Lightweight structures are commonly used in various parts of planes or other type of vehicles. A high strength is crucial for meeting the requirements for a robust vehicle design. Additionally, low mass increases the cost efficiency and therefore is a driving factor for designing aircraft components. The economic benefit of a lower mass while the stiffness of the structure remains constant implicates poor acoustic properties. This trade-off between reduced mass and reduced acoustic performance is crucial. Recent advances in the development of highly efficient and low-emission propulsion intensify this trade-off. While the energy consumption of open rotors or concepts with larger bypass ratio is lower compared to conventional turbines, it is expected that these propulsions increase air borne noise and structure borne noise [Angrand 2019]. Conventional measures that enhance the vibrational behavior are only effective for higher frequencies and implicate an increase of the mass of the overall structure. Such measures are not suitable as they exhaust the benefit of improved energy consumption. Consequently, there is a need for novel solutions that enables engineers to design lightweight structures with improved vibroacoustic properties.

In aircrafts, there exist several excitation scenarios which occur in a broad frequency range. Besides broadband white noise excitations from the pressure fluctuations of the turbulent boundary layer, there also exist narrow-band excitations. These phenomena result from the blade passing frequency of aircraft propellers, the gear mechanism of helicopters or other narrow-band noise induced by the engines. Consequently, novel lightweight solutions should be able to tackle broadband noise as well as specific excitation frequencies.

In the last decades, the term "metamaterial" appeared in various research fields of physics. Scientists use the term "metamaterial" for a material that has properties which are "beyond" the limits that we observe in nature. In many examples, metamaterials have dynamically modified properties as negative density, negative compressibility, or negative refraction. The main concept for the creation of such unconventional material properties is the arrangement

of repeating sub elements made of conventional material. These sub elements are dimensioned on a scale smaller than the sub wavelength of the media it should interfere with. The macroscopic material behavior of the periodic alignment of such sub elements can be completely different than the material or the individual element it is made of. The idea is to tailor the macroscopic material properties to improve the acoustic performance of the structure. Extending the borders of possible mechanical properties augments the design space for lightweight solutions with enhanced acoustic performance that resolve the trade-off between reduced mass and poor vibroacoustic properties. In general, the design of an acoustic metamaterial has different scales. On the one hand, there is the host structure whose dynamic behavior can be modeled using homogenized mechanical properties. The scale of the host structure is defined as the macro scale. On the other hand, metamaterials introduce local modifications on a much smaller scale, the micro scale. To evaluate the overall behavior the micro scale should be incorporated in the macro scale. Therefore, the models require a detailed description of both scales.

1.2 Discussion about the term "metamaterial"

The recent popularity of the term metamaterial is strongly linked to the advances in additive layer manufacturing (ALM) technology. Due to the increased scale of manufacturing of ALM processes, it is possible to manufacture complex small scale components integrated in a larger scale host structure. This encourages scientists to develop various types of metamaterials. For some of the concepts, one can argue that the fundamental theory is not a new invention. For example tuned mass dampers (TMD) as they are used in building construction ([Pavic et al 2002; Poon et al 2004]) can be interpreted as locally resonant materials. In this work, the author shows that the difference lies in the scale in which the engineers apply the concepts. Instead of applying TMD e.g. to pedestrian bridges where the macro scale is in the range of several meters [Pavic et al 2002], it is now possible to design local resonances that are small enough to be integrated in composite structures such as honeycomb panels [Claeys et al 2016b].

The physics behind metamaterials is not "beyond" the limits that we observe in nature. State of the art mechanics explains all the behavior of the structures. The "unnatural" behavior appears only if the structure is analyzed on the macro scale, which for metamaterials is in the range of a wavelength that is present in the structure. On the macro scale the material seems to behave strange. Investigating the micro structure in detail, the material behavior

of course follows the established laws of Newton's mechanics. Consequently, depending on the point of view the material can be denoted as "metamaterial" or not.

1.3 Research project "Additive Layer Manufacturing for Acoustic metamaterials (ALMA)"

The author issues this thesis in the scope of a cooperation in a joint research project. This project aims to reveal the potentials of additive layer manufacturing (ALM) for the design of acoustic metamaterials with future application in the aircraft industry. ALM offers the possibility to design complex small scale structures incorporated in a large scale macro structure. Due to the enhanced spatial design opportunities of the ALM process compared to conventional manufacturing techniques, it is possible to enlarge the design space of the vibroacoustic properties of such structures. The focus of the project was the design of materials that are able to modify and/or damp acoustic waves in such a way that the structure borne sound is reduced.
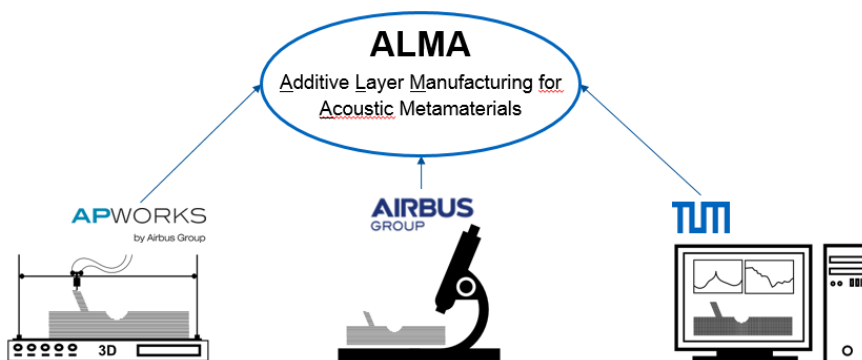
The three partners Airbus, APworks and the Technical University of Munich cooperated to unit their expertise. Airbus defined the applications scenarios for the acoustic metamaterials. APworks focused on improving the manufacturing process to optimize the quality of the ALM designs in terms of minimum printing thickness and accuracy. The Technical University of Munich, more specific the Chair of Structural Mechanics, developed the numerical models and computational procedures to predict the performance of the metamaterials and to define design criteria.

The author of this thesis was responsible for the sub project "Modeling and Simulation", which the chair of structural mechanics conducted in coordination with the project part-

ners. Therefore, this thesis focus on the modeling aspects of different concepts of acoustic metamaterials and the conducted numerical studies.

1.4 Outline of the thesis

This work introduces different concepts for the design of acoustic metamaterials and explains the underlying theory. Furthermore, several numerical studies evaluate the acoustic performance of the different concepts to reveal their potential for novel lightweight structures with improved vibroacoustic properties.

Chapter 2 starts with the introduction of the fundamental theory of structural dynamics. Besides the introduction of the basic equations, this chapter also includes the basic mechanisms for modeling mechanical systems and evaluate the vibroacoustic performance.

Chapter 3 elaborates on different concepts for designing structural components with tailored vibroacoustic properties. Concepts as acoustic black holes, locally resonant materials and how to design wave guides for acoustic waves are addressed. This chapter includes detailed descriptions and derivations of the underlying theory as well as a summary about the current state of the art of the different concepts.

Subsequently, chapter 4 focus on the modeling aspects. The author addresses specific modeling aspects that form the basis for modeling locally resonant materials and periodic structures.

Chapter 5 focuses on numerical studies to demonstrate the working principles of acoustic black holes and locally resonant materials. In this chapter detailed studies on various configurations demonstrate the potential of the concepts and discuss various design parameters to maximize the performance of the metamaterials.

Finally, chapter 6 summarizes the results of the numerical studies and gives an overview on the developed design criteria.

2 Fundamental theory

This chapter covers the fundamental theory for modeling the dynamic behavior of structural components. Section 2.1 introduces the equation of motion for harmonic excitations. Following this, section 2.2 employs the principal of virtual work to the equation of motion. Based on the principle of virtual work, section 2.3 explains how one can generate a discretized model using finite elements. Section 2.4 introduces the different wave types that define the motion of the structure. Finally, section 2.5 demonstrates mechanisms for the evaluation of the radiated sound.

2.1 Equation of motion for harmonic excitations

The general equation of motion for elasto-dynamics is given by

$$\rho \ddot{\mathbf{u}} - \mathbf{L}^T \boldsymbol{\sigma} - \mathbf{b} = 0 \ . \tag{2.1}$$

$\mathbf{u}$ denotes the deformation of the structure in the three spatial directions. ρ is the density of the material. $\boldsymbol{\sigma}$ describes the stress tensor and $\mathbf{b}$ the body force. $\mathbf{L}$ is a differential operator in the spatial domain. Damping can be included in the stress tensor or as an additional term. In general, $\boldsymbol{\sigma}$ is a second order tensor, but it is also possible to write it as a vector [Zienkiewicz et al 2005]

$$\boldsymbol{\sigma} = \begin{bmatrix} \sigma_{xx} & \sigma_{yy} & \sigma_{zz} & \sigma_{xy} & \sigma_{yz} & \sigma_{zx} \end{bmatrix}^T \ . \tag{2.2}$$

Arranging the stresses in a vector, the differential operator in x, y and z reads

$$\mathbf{L} = \begin{bmatrix} \frac{\partial}{\partial x} & 0 & 0 \\ 0 & \frac{\partial}{\partial y} & 0 \\ 0 & 0 & \frac{\partial}{\partial z} \\ \frac{\partial}{\partial y} & \frac{\partial}{\partial x} & 0 \\ 0 & \frac{\partial}{\partial z} & \frac{\partial}{\partial y} \\ \frac{\partial}{\partial z} & 0 & \frac{\partial}{\partial x} \end{bmatrix} . \tag{2.3}$$

In structural dynamics, one solves the equation of motion for a harmonic excitation of the form [Müller 2019b]

$$\mathbf{f}(\mathbf{x},t) = \underline{\mathbf{f}}_+(\mathbf{x})e^{i\Omega t} + \underline{\mathbf{f}}_-(\mathbf{x})e^{-i\Omega t} . \tag{2.4}$$

The under bar $\underline{\square}$ marks a complex amplitude. $\underline{\mathbf{f}}_-$ is the complex conjugate of $\underline{\mathbf{f}}_+$. The complex conjugate is marked with a superscript $\square^*$ (thus $\underline{\mathbf{f}}_- = \underline{\mathbf{f}}_+^*$). In general, the solution of the displacements $\mathbf{u}$ consists of a homogenous part $\mathbf{u}_h$ which describes the free vibration and the particular part $\mathbf{u}_p$ which describes the steady state solution

$$\mathbf{u} = \mathbf{u}_h + \mathbf{u}_p . \tag{2.5}$$

The homogenous solution usually decays after a short amount of time. Therefore, it is often neglected in structural dynamics. For practical applications in vibroacoustics, this is a valid assumption as long as there are no large deformations that might result in material failure or plastic deformations while the homogenous solution decays. The steady state solution oscillates with the same frequency as the excitation frequency. Therefore, for the particular solution, the following approach is applied [Petersen 1996]

$$\underline{\mathbf{u}}_p = \underline{\mathbf{u}}_{p+}e^{i\Omega t} + \underline{\mathbf{u}}_{p-}e^{-i\Omega t} . \tag{2.6}$$

The terms related to $e^{i\Omega t}$ and $e^{-i\Omega t}$ can be considered separately and due to the fact that $\underline{\mathbf{u}}_{p-} = \underline{\mathbf{u}}_{p+}^*$, it is sufficient to solve for $\underline{\mathbf{u}}_+$. Therefore, the steady-state solution simplifies

to

$$\mathbf{u} = \underline{\mathbf{u}}\mathrm{e}^{i\Omega t} \, ,$$
$$\dot{\mathbf{u}} = i\Omega\underline{\mathbf{u}}\mathrm{e}^{i\Omega t} \, ,$$
$$\ddot{\mathbf{u}} = -\Omega^2\underline{\mathbf{u}}\mathrm{e}^{i\Omega t} \, . \tag{2.7}$$

Inserting (2.7) in the equation of motion results in

$$-\Omega^2\rho\underline{\mathbf{u}} - \mathbf{L}^T\underline{\boldsymbol{\sigma}} - \underline{\mathbf{b}} = 0 \, . \tag{2.8}$$

2.2 Principle of virtual work

In the following, the equation of motion (2.8) is formulated in a weak sense. The presented procedure follows the derivation of Zienkiewicz and Taylor [2005] and Hughes [2002]. The governing equation (here the equation of motion) is multiplied with an arbitrary function $\delta\underline{\mathbf{u}}$ and than integrated over the domain of interest

$$\delta\Pi = \int_V \delta\underline{\mathbf{u}}^T \left(-\rho\Omega^2\underline{\mathbf{u}} - \mathbf{L}^T\underline{\boldsymbol{\sigma}} - \underline{\mathbf{b}}\right) dV = 0 \, . \tag{2.9}$$

From the mathematical point of view, $\delta\mathbf{u}$ is a test function. The expression in the brackets which is the equation of motion (2.8) should vanish. The integral describes a residuum. By choosing a specific test function, the residuum of the equation of motion (2.8) is weighted. If a solution $\underline{\mathbf{u}}$ of (2.8) is inserted the integral of the arbitrarily weighted residual vanishes. From the mechanical point of view, δu is felt as a virtual displacement that generates an amount of virtual work $\delta\Pi$. First, the second term in (2.9) is integrated by parts

$$\int_V \delta\underline{\mathbf{u}}^T\mathbf{L}^T\underline{\boldsymbol{\sigma}} \, dV = -\int_V (\mathbf{L}\delta\underline{\mathbf{u}})^T\underline{\boldsymbol{\sigma}} \, dV + \int_S \delta\underline{\mathbf{u}}^T\mathbf{L}^T\underline{\boldsymbol{\sigma}} \cdot \mathbf{n} \, dS \, . \tag{2.10}$$

The external forces $\underline{\mathbf{t}}$ balance the stresses ($\underline{\mathbf{t}} = \mathbf{L}^T\underline{\boldsymbol{\sigma}} \cdot \mathbf{n}$) at the boundary S. Thus, the first integral describes the internal virtual work and the second term is related to the work done by the forces $\mathbf{t}$ acting on the boundary of the domain.

In the last step, one inserts the constitutive equation $\underline{\boldsymbol{\sigma}} = \mathbf{C}\underline{\boldsymbol{\epsilon}}$ describing Hooke's law for the linear case. In general, $\mathbf{C}$ is the forth order elasticity tensor. Due to the vector notation of the

stresses introduced in (2.2), $\mathbf{C}$ is written as a second order matrix [Link 1984]. Furthermore, the kinematic relation is $\underline{\boldsymbol{\epsilon}} = \mathbf{L}\underline{\mathbf{u}}$ [Klausner 1991]. Summarizing, the virtual work reads

$$
\begin{aligned}
\delta\Pi = & -\int_V \delta\underline{\mathbf{u}}^T \rho\Omega^2 \underline{\mathbf{u}}\, dV \\
& +\int_V (\mathbf{L}\delta\underline{\mathbf{u}})^T \mathbf{C}\mathbf{L}\underline{\mathbf{u}}\, dV \\
& -\int_S \delta\underline{\mathbf{u}}^T \underline{\mathbf{t}}\, dS \\
& -\int_V \delta\underline{\mathbf{u}}^T \underline{\mathbf{b}}\, dV \\
& = 0\,.
\end{aligned}
\tag{2.11}
$$

2.3 Finite element discretization

The weak formulation of the equation of motion (2.11) is the basis for finding an approximated solution for the equation of motion using the finite element method. Applying the Galerkin method which is based on the work of Ritz [1909] and Galerkin [1915], one approximates the domain V with n non-overlapping domains V_e such that

$$
V \approx \cup_i^n V_{e,i} \quad \text{with} \quad V_{e,i} \cap V_{e,j} = \emptyset \quad \text{for} \quad i \neq j\,, \tag{2.12}
$$
$$
S \approx \cup_i^n S_{e,i} \quad \text{with} \quad S_{e,i} \cap S_{e,j} = \emptyset \quad \text{for} \quad i \neq j\,. \tag{2.13}
$$

In addition, the displacements $\underline{\mathbf{u}}$ and the virtual displacements $\delta\underline{\mathbf{u}}$ are discretized using a discrete set of nodal values $\underline{u}_i$ and $\delta\underline{u}_i$ that are multiplied with different shape functions N_i. A fundamental property of the basis is that they only have local support. This means that the basis function N_i of node i is zero at all the other nodes. Figure 2.1 illustrates the finite element discretization for a one dimensional domain.

For each element, we map the shape functions and coordinates to local element coordinates $\boldsymbol{\xi}$. The advantage of the global to local mapping is that the element shape functions in local
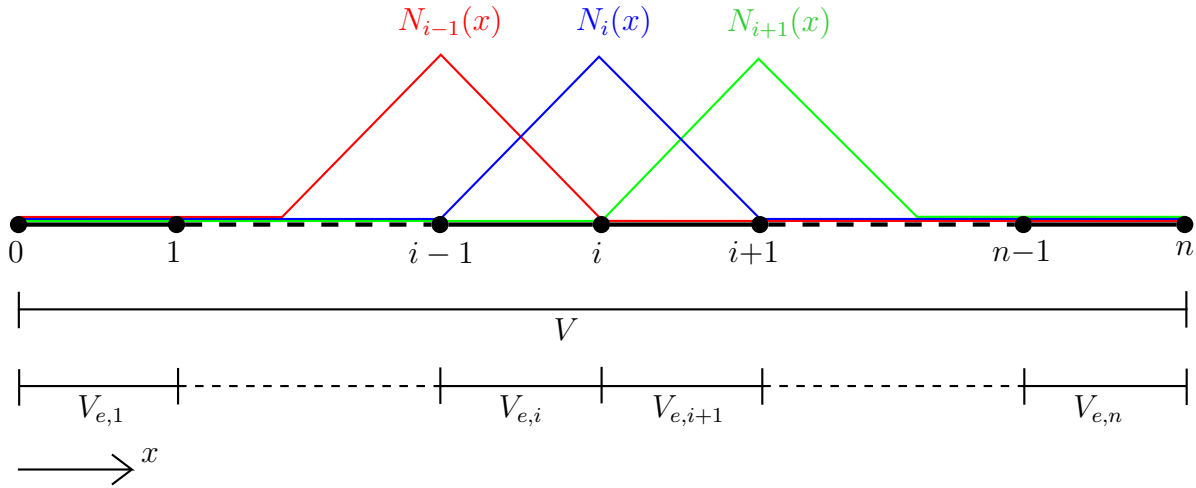
Figure 2.1: Finite element discretization of a one dimensional domain with shape functions that only have local support.
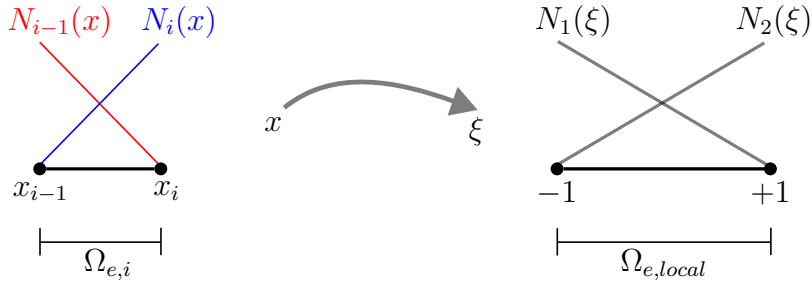
Figure 2.2: Global to local mapping of the shape functions and the coordinates for a one dimensional element.

coordinates are identical for each element

$$\mathbf{u}_e \approx \begin{bmatrix} N_1(\boldsymbol{\xi}) & 0 & 0 \\ 0 & N_1(\boldsymbol{\xi}) & 0 \\ 0 & 0 & N_1(\boldsymbol{\xi}) \\ \vdots & \vdots & \vdots \\ N_r(\boldsymbol{\xi}) & 0 & 0 \\ 0 & N_r(\boldsymbol{\xi}) & 0 \\ 0 & 0 & N_r(\boldsymbol{\xi}) \end{bmatrix} \begin{bmatrix} \underline{u}_{x,1} \\ \underline{u}_{y,1} \\ \underline{u}_{z,1} \\ \vdots \\ \underline{u}_{x,r} \\ \underline{u}_{y,r} \\ \underline{u}_{z,r} \end{bmatrix} = \mathbf{N}(\boldsymbol{\xi})\tilde{\mathbf{u}}_e \ . \tag{2.14}$$

r are the number of nodes per element and $\tilde{\mathbf{u}}_e$ contains the nodal deformations. This discretization leads to an approximation of the virtual work, where the integration is performed

for each element e in local coordinates $\boldsymbol{\xi}$

$$
\begin{aligned}
\delta\Pi \approx \sum_e \delta\tilde{\underline{\mathbf{u}}}_e^T \Big[&\int_{V_{e,local}} \mathbf{N}(\boldsymbol{\xi})^T \rho \mathbf{N}(\boldsymbol{\xi})|\mathbf{J}_e|\, dV_{e,local}(-\Omega^2\tilde{\mathbf{u}}_e) \\
&\int_{V_{e,local}} (\mathbf{L}\mathbf{N}(\boldsymbol{\xi}))^T \mathbf{C}\mathbf{L}\mathbf{N}(\boldsymbol{\xi})|\mathbf{J}_e|\, dV_{e,local}\tilde{\mathbf{u}}_e \\
&-\int_{S_{e,local}} \mathbf{N}(\boldsymbol{\xi})^T \tilde{\underline{\mathbf{t}}}|\mathbf{J}_e|\, dS_{e,local} \\
&-\int_{V_{e,local}} \mathbf{N}(\boldsymbol{\xi})^T \tilde{\underline{\mathbf{b}}}|\mathbf{J}_e|\, dV_{e,local}\Big] \\
&= 0 \; .
\end{aligned} \tag{2.15}
$$

$\mathbf{J}_e$ is the Jacobian that describes the mapping. Using the isoparametric approach, the same shape functions that approximate the deformation also approximate the geometry

$$
\mathbf{x}(\boldsymbol{\xi}) = \mathbf{N}(\boldsymbol{\xi})\mathbf{x}_i \; . \tag{2.16}
$$

$\mathbf{x}_i$ are the nodal locations. This results in the following expression for the Jacobian

$$
\mathbf{J}_e = \frac{\partial \mathbf{x}}{\partial \boldsymbol{\xi}} = \frac{\mathbf{N}(\boldsymbol{\xi})}{\partial \boldsymbol{\xi}}\mathbf{x}_{e,i} \; . \tag{2.17}
$$

$\mathbf{x}_{e,i}$ are the nodal coordinates of element e. Finally, for the integration over the element coordinates $\boldsymbol{\xi}$, one applies the Gaussian quadrature [Gauß 1815; Jacobi 1826]. The evaluation yields the element mass matrix $\mathbf{M}_e$ and stiffness matrix $\mathbf{K}_e$ as well as the element load vector $\underline{\mathbf{f}}_e$

$$
\mathbf{M}_e = \int_{V_{e,local}} \mathbf{N}(\boldsymbol{\xi})^T \rho \mathbf{N}(\boldsymbol{\xi})|\mathbf{J}_e|\, dV_{e,local} \; , \tag{2.18}
$$

$$
\mathbf{K}_e = \int_{V_{e,local}} (\mathbf{L}\mathbf{N}(\boldsymbol{\xi}))^T \mathbf{C}\mathbf{L}\mathbf{N}(\boldsymbol{\xi})|\mathbf{J}_e|\, dV_{e,local} \; , \tag{2.19}
$$

$$
\underline{\mathbf{f}}_e = \int_{S_{e,local}} \mathbf{N}(\boldsymbol{\xi})^T \tilde{\underline{\mathbf{t}}}|\mathbf{J}_e|\, dS_{e,local} + \int_{V_{e,local}} \mathbf{N}(\boldsymbol{\xi})^T \tilde{\underline{\mathbf{b}}}|\mathbf{J}_e|\, dV_{e,local} \; . \tag{2.20}
$$

As several nodes contribute to multiple elements, the summation over the elements (see (2.15)) corresponds to an assembling of the contribution of each element in the global matrices ($\mathbf{M}$ and $\mathbf{K}$) and the global load vector $\underline{\mathbf{f}}$. As the virtual work of the discretized virtual displacement should vanish, the finite element discretization yields

$$
\left(\mathbf{K} - \Omega^2\mathbf{M}\right)\tilde{\underline{\mathbf{u}}} = \underline{\mathbf{f}} \; . \tag{2.21}
$$

This equation is the discretized equation of motion for a harmonic excitation. The matrix $(\mathbf{K} - \Omega^2\mathbf{M})$ is called dynamic stiffness matrix.

2.4 Acoustic waves

In a linear case, the motion of a structure can be described as a superposition of various waves. A wave is a disturbance that propagates through a media. Depending on the deformation pattern, one can distinguish different wave types which have different characteristics. One of the basic properties of a wave is the propagation speed c_p

$$c_p = \lambda f = \frac{\Omega}{k} \ . \tag{2.22}$$

λ is the wavelength and f the frequency of oscillation in Hertz (1/s). Ω describes the angular frequency (2π/s). Correspondingly to the oscillations per second, there exists the spatial wavenumber k that describes the number of oscillations per meter

$$k = \frac{2\pi}{\lambda} \ . \tag{2.23}$$

2.4.1 Longitudinal waves

For longitudinal waves, the particle motion of the structures aligns with the direction of propagation of the waves (see figure 2.3a). Longitudinal waves are also called compressional waves or P-waves. The propagation speed of longitudinal waves is

$$c_L = \sqrt{D_L/\rho} \ . \tag{2.24}$$

D_L is the longitudinal stiffness and ρ the density of the material. Pure longitudinal waves do only occur in infinitely extended structures.

2.4.2 Quasi-longitudinal waves

In general, structural components are spatially limited and therefore, instead of longitudinal waves quasi-longitudinal waves occur. Besides compression or elongation in the direction of propagation, the structure experiences extension and compression in vertical direction,

respectively (see figure 2.3b). Depending on the geometry, the longitudinal stiffness varies. Therefore, the propagation speed of quasi-longitudinal waves in beams and plates is different [Cremer and Heckl 1967]

$$c_{L,beam} = \sqrt{E/\rho} \, , \tag{2.25}$$

$$c_{L,plate} = \sqrt{\frac{E}{\rho(1 - \nu^2)}} \, . \tag{2.26}$$

E is the Young's modulus and ν the Poisson's ratio of the material.

(a) Longitudinal wave

(b) Quasi-longitudinal wave
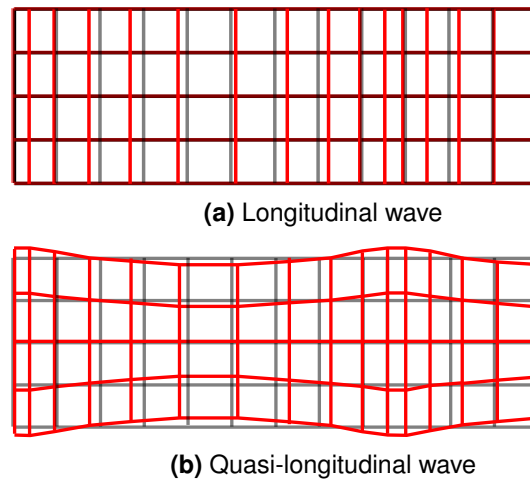
Figure 2.3: Difference of the deformation pattern of longitudinal waves and quasi longitudinal waves.

2.4.3 Shear waves

For shear waves, the particles of the structure oscillate perpendicular to the propagation direction of the wave (see figure 2.4). Shear waves propagate due to the resistance against shear deformation. Thus, such waves do not appear in ideal fluids [Möser and Kropp 2010]. The wave speed depends on the shear modulus G

$$c_T = \sqrt{G/\rho} \, . \tag{2.27}$$

G is related to the Young's modulus [Cremer and Heckl 1967]

$$G = \frac{E}{2(1 + \nu)} \, . \tag{2.28}$$
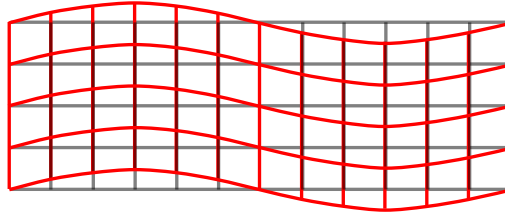
Figure 2.4: Deformation pattern of a shear wave.

2.4.4 Bending waves

For bending waves, the particles in the structure move parallel and perpendicular to the direction of propagation (see figure 2.5). Bending waves occur in thin structures where the assumptions of the Euler-Bernoulli theory are fulfilled:

- The length of the beam is much larger then the cross section

- Cross sections that are perpendicular to the neutral axis of the beam remain perpendicular after deformation of the beam

- The cross section of the beam remains plane after deformation

If the assumptions are fulfilled, the rotational inertia and the shear deformation can be neglected. Consequently, the force equilibrium in vertical direction yields the differential equation of the Euler-Bernoulli beam [Cremer and Heckl 1967]

$$EI\frac{\partial^4 w}{\partial x^4} + \rho A\frac{\partial^2 w}{\partial t^2} = 0 \ . \tag{2.29}$$

E is the Young's modulus, A is the cross section of the beam and I the area moment of inertia.

The differential equation (2.29) describes a dispersive wave motion. The reason is the different orders of derivation with respect to time and space [Cremer and Heckl 1967]. Inserting a wave of the form

$$w = \underline{w}\sin\left(\Omega t - kx + \theta\right) \ , \tag{2.30}$$

one observes that any wave with arbitrary amplitude $\underline{w}$ and phase θ that satisfies

$$EIk^4 = \rho A\Omega^2 \tag{2.31}$$

is a solution of the differential equation. Knowing that the wave speed is the ratio of the angular frequency and the angular wavenumber, the propagation speed of bending waves is

$$c_{B,beam} = \left(\frac{EI}{\rho A} \Omega^2 \right)^{1/4} .$$

(2.32)

For plates, the propagation speeds is given by

$$c_{B,plate} = \left(\frac{Eh^2}{12\rho(1 - \nu^2)} \Omega^2 \right)^{1/4} .$$

(2.33)
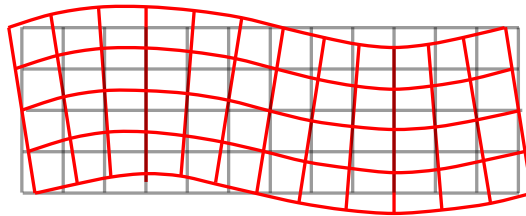
Figure 2.5: Deformation pattern of a bending wave.

In thin walled structures, bending waves dominate the motion of the structure. For reducing structure borne noise, it is crucial to control the motion of bending waves as they typically are easily excited and are linked with a radiation of noise into the surrounding fluid.

2.5 Sound radiation using the Rayleigh integral

The following section presents the fundamental theory for the computation of the radiated sound of a vibrating structure. The structure is finite and radiates in an infinite baffle. The fundamental theory presented here are based on the published work of Cremer and Heckl [1967], Fahy and Gardonio [2007] and Hambric et al [2016].

The radiated power from a structure into the adjacent fluid depends on the velocity distribution of the structure. In general, only the vertical displacements significantly contribute to the sound power radiated into the far-field. Therefore, one only considers the velocity v_z perpendicular to the surface. Knowing the surface velocity v_z of the structure and the pressure p in the air the radiated sound power can be computed. Transforming the surface

velocity into the Fourier domain, it is possible to consider the sound radiation of each wave component separately [Cremer and Heckl 1967]

$$\underline{v}(x,y,z = 0) \quad \overset{\mathcal{F}}{\circ\!\!-\!\!\bullet} \quad \hat{\underline{v}}(k_x,k_y) \ . \tag{2.34}$$

The pressure and the surface velocity determine the sound intensity I_p [Müller and Möser 2013]

$$I_p = \frac{1}{2}\Re\{\hat{\underline{p}}\hat{\underline{v}}_z^*\}. \tag{2.35}$$

$\hat{\underline{p}}$ is the Fourier transform of the pressure and $\hat{\underline{v}}_z^*$ denotes the complex conjugate velocity spectra. Integrating the sound intensity over the radiating surface yields the radiated power

$$P = \int_A I_p dA \ . \tag{2.36}$$

2.5.1 Wavenumber approach

The pressure in the air results from the surface velocity and the impedance of the air [Cremer and Heckl 1967]

$$\hat{\underline{p}}(k_x,k_y,z = 0) = \hat{Z}_{air}(k_x,k_y)\hat{\underline{v}}(k_x,k_y) \tag{2.37}$$

$$= \rho_{air}c_{air}\frac{k_{air}}{\sqrt{k_{air}^2 - (k_x^2 + k_y^2)}}\hat{\underline{v}}(k_x,k_y) \ . \tag{2.38}$$

The pressure depends on the wavenumber in the structure ($k = \sqrt{k_x^2 + k_y^2}$). For $k < k_{air}$, the pressure is real and sound waves radiate in the air. In contrast, for $k > k_{air}$ the pressure is imaginary. The pressure in the near field decays exponentially with increasing distance from the radiating plate (see figure 2.6).
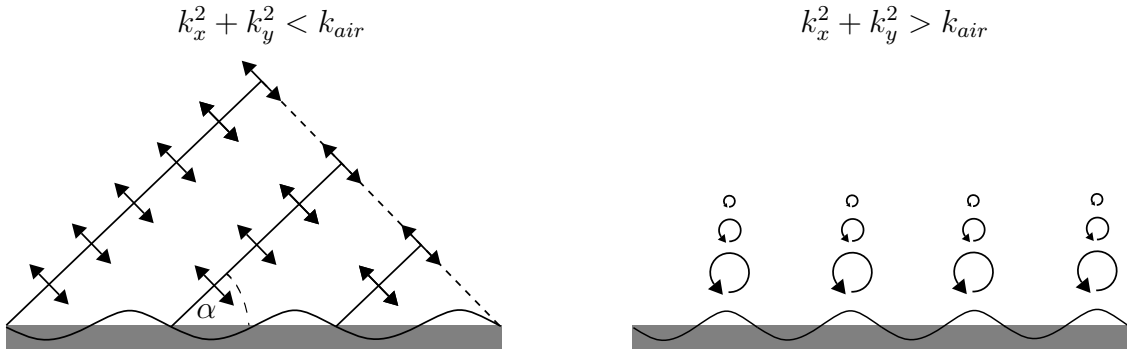
Figure 2.6: Pressure field in front of a vibrating structure.

An integration of the sound intensity gives the radiated sound power

$$P = \frac{\rho_{air} c_{air}}{2} \frac{1}{(2\pi)^2} \int_{-\infty}^{\infty} \int_{-\infty}^{\infty} \Re \left\{ \frac{k_{air}}{\sqrt{k_{air}^2 - (k_x^2 + k_y^2)}} \right\} \|\hat{\underline{v}}(k_x, k_y)\|^2 dk_x dk_y. \tag{2.39}$$

Only the real part of the product of the surface velocity and the pressure of the air contributes to the radiated sound power. The angle α depends on the relation of the wavenumber in the structure and the wavenumber in the air

$$\alpha(k_x, k_y) = \tan^{-1} \left(\frac{k_{air}}{\sqrt{k_{air}^2 - (k_x^2 + k_y^2)}} \right) . \tag{2.40}$$

For the limit case $k = k_{air}$, the angle of radiation α is 90° and the impedance of the air is infinite. For a vibrating structure $(\hat{v}(k_x^2 + k_y^2 = k_{air}^2) \neq 0)$, this would result in a infinite radiated sound power.
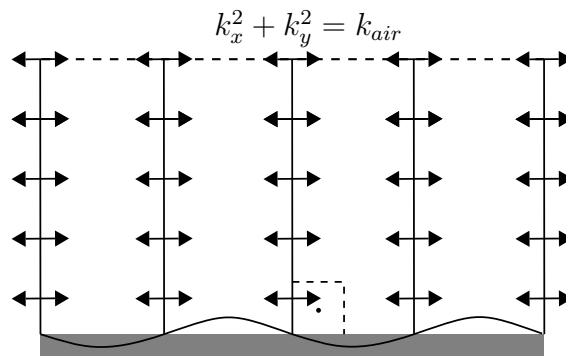
Figure 2.7: Pressure field for a angle of radiation of 90°.

Obviously, the limit case is not realistic. The reason is that in this approach, the interaction of the structure and the air is not bidirectional. The velocity in the structure is computed

neglecting the impedance of the air. This is only valid as long as the impedance of the air is small compared to the impedance of the structure. For the limit case $k = k_{air}$, the impedance of the air can not be neglected.

The following paragraph demonstrates how the influence of the impedance of the air can be included. Depending on the ratio of the impedances, there is a relative velocity $\hat{\underline{v}}_{rel}$ between the velocity of the structure and the air

$$\hat{\underline{v}}_{rel} = \hat{\underline{v}}_{unidirectional}(k) \frac{Z_{air}(k)}{Z_{air}(k) + Z_{structure}(k)} \ . \tag{2.41}$$

For $Z_{air} << Z_{structure}$ the relative velocity is zero and for $Z_{air} >> Z_{structure}$ the relative velocity equals the velocity of the structure. The resulting velocity that includes the impedance of the air is respectively

$$\hat{\underline{v}}_{bidirecctional} = \hat{\underline{v}}_{unidirectional} - \hat{\underline{v}}_{rel} \ . \tag{2.42}$$

For bending waves in thin structures the impedance is given by

$$Z_{structure} = \frac{B}{i\Omega} \left(k^4 - \Omega^2 \rho h \right) \ , \tag{2.43}$$

where B is the bending stiffness and h is the thickness. For most cases, the impedance of the structure is larger compared to the impedance of the air. Therefore, the impedance of the air is typically neglected for the computation of the motion of the structure.

2.5.2 Discrete solution of the Rayleigh integral

An alternative approach considers the structure as a combination of elementary radiators (see figure 2.8). The presented approach is taken from Mollo and J. [1989] and Vitiello et al [1989].

One discretizes the structure in small elements, whose size is significantly smaller than the acoustic wavelength of the surrounding air [Fahy and Gardonio 2007]. The radiated power is computed considering each radiator as a monopole

$$P = \underline{\mathbf{v}}_e^{*T} \mathbf{R} \underline{\mathbf{v}}_e. \tag{2.44}$$
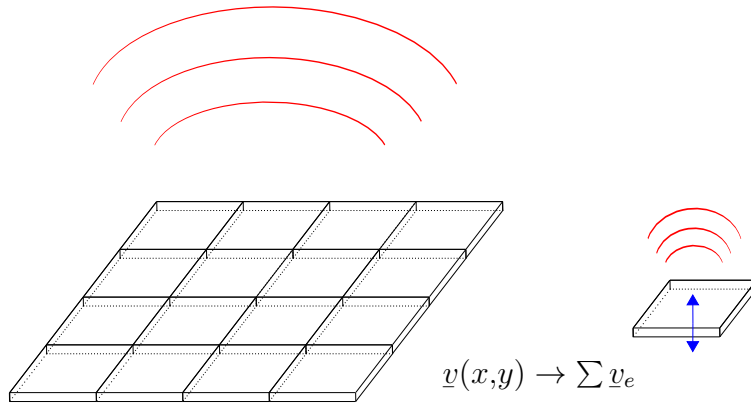
Figure 2.8: Sound radiation of the overall structure is estimated by a sum of elementary radiators that behave as monopoles.

$\underline{\mathbf{v}}_e$ is the vector of velocities of the radiators. The matrix $\mathbf{R}$ describes the interaction between the monopoles. It contains the impedance of the air and weighting functions that depends on the distance between the different elements

$$\mathbf{R} = \frac{\omega^2 \rho_{air} A_e^2}{4\pi c_{air}} \begin{bmatrix} 1 & \frac{\sin(k_{air} D_{12})}{k_{air} D_{12}} & \cdots \\ \frac{\sin(k_{air} D_{21})}{k_{air} D_{21}} & 1 & \\ \vdots & & \ddots \end{bmatrix} . \tag{2.45}$$

A_e is the surface area of an elementary radiator. D_{ij} is the distance between radiator i and j

$$D_{ij} = \|x_i - x_j\| . \tag{2.46}$$

Depending on the distance, each individual radiator affects all other radiators. Summing up all the contributions yields the radiated sound power.

3 Different concepts for the design of acoustic metamaterials

This chapter introduces conceptual ideas that offer potentials for the design of materials that demonstrate beneficial vibroacoustic properties. The author presents three different concepts including the fundamental theory as well as a literature review presenting the state of the art of the concepts. Section 3.1 explains the idea of acoustic black holes for bending waves. Section 3.2 elaborates on locally resonant materials and their potential to reduce structure borne noise for specific frequency ranges. Finally, section 3.3 elaborates on the design of wave guides that create desired acoustic fields using spatially varying material properties.

3.1 Acoustic black holes (ABH)

An acoustic black holes is a local thickness reduction that modulates the wave propagation of bending waves in thin walled structures. The main idea is to reduce the propagation speed. A decrease of the thickness of the structure results in a decrease of the propagation speed of bending waves.
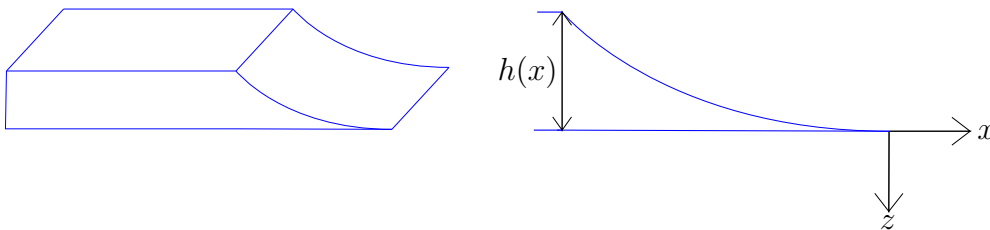
Figure 3.1: Characteristic thickness profile of an ABH.

k_B is the wavenumber of the bending wave. This wavenumber depends on the thickness variation $h(x)$

$$k_B(x) = \left(\frac{12\rho(1-\nu^2)\Omega^2}{Eh^2(x)} \right)^{\frac{1}{4}} . \tag{3.1}$$

Using (3.1), the phase velocity c_p and the group velocity c_g of bending waves are

$$c_p(x) = \frac{\Omega}{k_B} = \left(\frac{Eh^2(x)\Omega^2}{12\rho(1-\nu^2)} \right)^{\frac{1}{4}} , \tag{3.2}$$

$$c_g(x) = \frac{\partial \Omega}{\partial k_B} = \left(\frac{64Eh^2(x)\Omega^2}{3\rho(1-\nu^2)} \right)^{\frac{1}{4}} . \tag{3.3}$$

The phase velocity c_p is the speed at which the part of the wave with a fixed phase and frequency will propagate through space. In contrast, the group velocity c_g describes the speed at which the envelope of a wave packages travels through space [Cremer and Heckl 1967]. From (3.2) and (3.3), it is obviously that with vanishing thickness h the phase and group velocities vanish, too.

The thickness profile that creates an ABH effect needs a sufficiently smooth form. Otherwise, the thickness profile generates a reflection of the bending wave. This deteriorates the ABH effect. According to Mironov [1988], the ABH effect occurs for thickness profiles that fulfill the smoothness condition

$$\frac{dk_B}{dx} \frac{1}{k_B} \ll k_B . \tag{3.4}$$

This condition is fulfilled using a thickness profile of the form

$$h(x) = \epsilon x^\beta \text{ with } \beta > 2 \text{ and } \epsilon \ll (3\rho\Omega^2/E)^{1/2} . \tag{3.5}$$

Mironov [1988] shows that theoretically, it is possible to capture bending waves using such a local thickness reduction. The reason is that with decreasing thickness the bending stiffness reduces and the bending wave speed decreases while, due to the conservation of energy, the amplitude of the bending wave increases. To the authors knowledge, Krylov [2001] established herefore the term "acoustic black holes". This term is based on the theoretical limit case of a smoothly vanishing thickness of the structure. In that case, the bending wave speed decreases to zero and the wave basically stops propagating without any reflection. The wave is "trapped" inside the ABH. In practice, this limit case is unfeasible since a perfectly vanishing thickness profile can not be manufactured. Furthermore, a vanishing wave speed would implicate a infinite wave amplitude which would result in material failure. Therefore, it is not possible that the bending wave "disappears" at the ABH.

3.1.1 **State of the art**

Mironov [1988] introduced the basic idea of an ABH. Although, the term "acoustic black holes" might be misleading, it has been used for smooth profile reductions with and without attached damping layers [Krylov 2001; Krylov and Tilman 2004; O'Boy et al 2010; Conlon and Fahnline 2015; Huang et al 2018]. Smooth thickness profiles combined with damping material show high potentials for reducing structure borne noise. Based on a simple numerical model, Krylov [2001]; Krylov and Tilman [2004]; Krylov [2004] illustrate that a small amount of local damping material at the ABH can dissipate a large amount of vibrational energy. The amount of energy that "escapes" the ABH is determined using a reflection coefficient [Krylov 2001]. This reflection coefficient is frequency dependent: for lower frequency the reflection coefficient is relatively large and it decreases with increasing frequency [Krylov 2004].
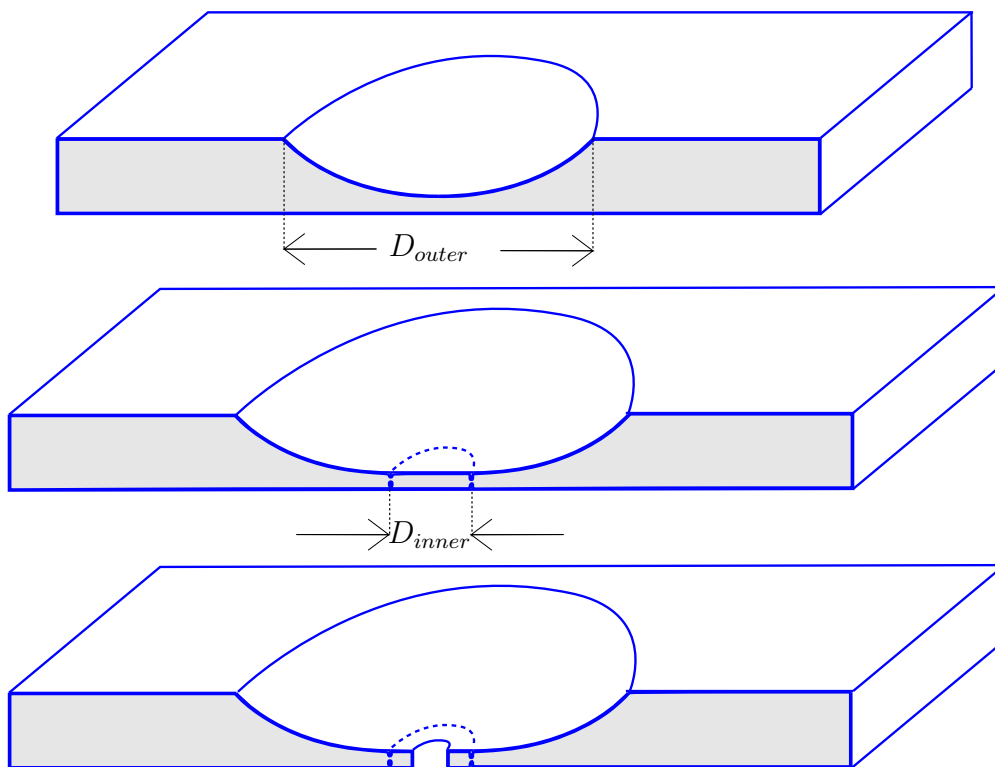
Figure 3.2: Geometric features of an ABH.

According to various studies, there are several geometrical features of an ABH profile that influence the ABH effect [Krylov and Tilman 2004; Conlon and Fahnline 2015; Tang et al 2016; Krylov 2019]. Depending on the outer diameter of the ABH, there exists a cut-on frequency at which the ABH acts as broadband absorber. Conlon and Fahnline [2015] compute this frequency with $f = c_B/D_{outer}$, where D_{outer} is the outer diameter and c_B the

wave speed of the bending waves outside of the ABH. Zhao et al [2015]; Tang et al [2016]; Mironov and Gladilin [2016]; Miksch [2017] confirm the correlation of the outer diameter and the cut-on frequency. A lower cut-on frequency requires a larger ABH profile. Jeon [2016] demonstrates the ABH effect for a one dimensional coiled ABH. This results in a more compact ABH design. At frequencies below the cut-on frequency, the absorption characteristic of the ABH depends on the local mode inside of the ABH [Conlon and Fahnline 2015]. Krylov [2019] investigates the role of the localized modes at the ABH feature and the impact on the reflection of bending waves.
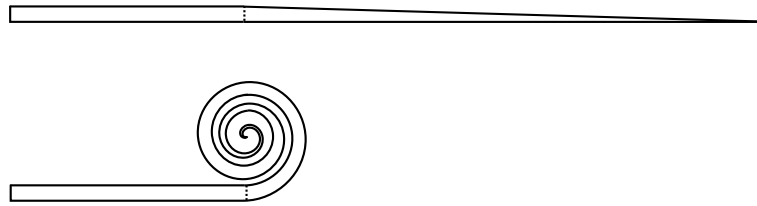
Figure 3.3: Conventional ABH (top), coiled ABH (bottom).

Krylov and Winward [2007] publish a first experimental verification of the ABH effect. Measurements of the deflection at the point of excitation for a plate with a one dimensional ABH show a reduced deflection in the resonance peaks. O'Boy et al [2010] investigate plates with embedded two dimensional ABH. At low frequencies, the admittance increases using ABH features. Whereas for higher frequencies, an ABH reduces the admittance compared to a uniform plate with similar damping mechanism. Besides studies on single ABH, also investigations on plates with multiple ABH are conducted. Conlon and Fahnline [2015] show that using multiple ABH features does not necessarily increase the vibration reduction in plate-like structures. However, for an optimal ABH configuration the input-output response of an ABH plate with damping treatment can reach the characteristic phase accumulation of an infinite plate [Conlon and Feurtado 2018].

Feurtado and Conlon [2016]; Prill et al [2016] argue that the robustness of the ABH effect with respect to deviation from the idealized ABH profile from Mironov [1988] results from the additional damping layer. Therefore, small defects that might occur during the manufacturing of the ABH profile, deteriorate the performance but do not ruin the operating principle of the ABH [Bowyer and Krylov 2016]. Additionally, numerical studies reveal potentials for noise reduction using linear, quadratic, or cubic power law profiles with circular or elliptical circumferences [Prill et al 2016]. Huang et al [2016] confirm that the general focalization of the energy of bending waves even works for power law profiles $h(x) = x^\beta$ with exponent $\beta < 2$.

Conlon et al [2015] cover the numerical evaluation of the sound radiation of plates with embedded ABH and show that an ABH reduces the radiated sound power of a thin plate. Prill et al [2016] demonstrate that applying ABH (with damping layers) to the underfloor of a car decreases the sound level inside the car. There are two reasons for the reduced radiated sound power [Feurtado and Conlon 2016]. First, the reduction of the vibration amplitudes due to the increased dissipation of energy. Second, the radiation efficiency is reduced, because the ABH transforms some of the supersonic bending waves into subsonic bending waves. Besides the amount of radiated sound, ABH also show potentials for sound insulation as it increases the sound transmission loss of plate-like structures [Feurtado and Conlon 2017].

Besides the modulation of wave amplitude and wave speed, a two dimensional ABH also influences the propagation direction. Krylov [2007] covers this topic and shows that the propagation direction of a bending waves bends towards the middle of the acoustic black hole. Huang et al [2018] show that linked to the change of the wave speed the refraction index for bending waves gradually decreases in an ABH. Besides the dissipation of energy at the ABH, it is also possible to harvest the energy [Zhao et al 2014]. Zhao et al [2015] verify this concepts by experimental evaluations and show that the harvested energy increases for frequencies above the cut-on frequency. For a device that harvests energy using an ABH combined with a electric-mechanical transducer, there exist a patent by Unruh et al [2016].

3.1.2 Fundamentals of the ABH effect for bending waves

The following section summarizes the fundamental theory of the ABH effect for bending waves. Mironov and Gladilin [2016] derive the differential equation for bending waves in beams of varying thickness. Figure 3.4 shows a beam with initial thickness h_0 and initial width d_0.
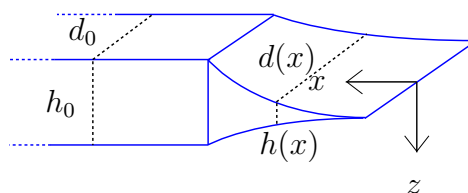
Figure 3.4: Beam with reduced cross section at the end.

The cross section at the end of the beam decreases. Therefore, the cross section A and the

area moment of inertia I varies with x

$$A(x) = h(x) \cdot d(x) \ , \tag{3.6}$$

$$I(x) = \frac{h^3(x) \cdot d(x)}{12} \ . \tag{3.7}$$

$h(x)$ and $d(x)$ describe the thickness and width of the beam, respectively. Due to the spatially varying cross section the differential equation based on Euler-Bernoulli theory is

$$\frac{\partial^2}{\partial x^2} \left(EI(x) \frac{\partial^2 w}{\partial x^2} \right) + \rho A(x) \frac{\partial^2 w}{\partial t^2} = q \ . \tag{3.8}$$

E is the Young's modulus and ρ the density of the material. q denotes the external loading. Mironov and Gladilin [2016] introduce the following cross section

$$h(x) = h_0 (x/x_0)^2 \ , \tag{3.9}$$

$$d(x) = d_0 (x/x_0)^\alpha \ . \tag{3.10}$$

Usually, α equals to zero. For a cross section described by the above defined height and width, the solution of the harmonic equation for the beam has the following form [Mironov and Gladilin 2016]

$$\underline{w}(x) = x^\gamma \ . \tag{3.11}$$

A.1 shows the detailed derivation of the homogenous solution of the harmonic equation for the beam with varying cross section (3.8). There exist four solution for γ

$$\gamma_{1,2,3,4} = -\frac{\alpha + 3}{2} \pm \left[\frac{1}{2} \left(\left(\frac{\alpha + 3}{2} \right)^2 + \left(\frac{\alpha + 5}{2} \right)^2 \right) \right. \tag{3.12}$$

$$\left. \pm \sqrt{\frac{1}{4} \left(\left(\left(\frac{\alpha + 3}{2} \right)^2 + \left(\frac{\alpha + 5}{2} \right)^2 \right)^2 - \left(\frac{\alpha + 5}{2} \right)^2 \left(\frac{\alpha + 3}{2} \right)^2 \frac{12 \rho \Omega^2}{E} \left(\frac{x_0^2}{h_0} \right)^2 \right)} \right]^{\frac{1}{2}} \ . \tag{3.13}$$

In the case that all solutions γ are real, no oscillation appears. Therefore, the ABH effect is only observable for

$$\left(\left(\frac{\alpha + 3}{2} \right)^2 - \left(\frac{\alpha + 5}{2} \right)^2 \right)^2 < \left(\frac{\alpha + 5}{2} \right)^2 \left(\frac{\alpha + 3}{2} \right)^2 \frac{12 \rho \Omega^2}{E} \left(\frac{x_0^2}{h_0} \right)^2 \ . \tag{3.14}$$

Resolving the square of the left-hand side and dividing both sides by $\left(\frac{\alpha+5}{2}\right)^2 \left(\frac{\alpha+3}{2}\right)^2$ yields

$$\left(\frac{\alpha+3}{\alpha+5}\right)^2 - 2 + \left(\frac{\alpha+5}{\alpha+3}\right)^2 < \frac{12\rho\Omega^2}{E}\left(\frac{x_0^2}{h_0}\right)^2 . \tag{3.15}$$

This results in a lower limit for the frequency Ω, which is necessary to ensure the ABH effect

$$\sqrt{\frac{E}{12\rho}\left(\frac{h_0}{x_0^2}\right)^2\left(\left(\frac{\alpha+3}{\alpha+5}\right)^2 - 2 + \left(\frac{\alpha+5}{\alpha+3}\right)^2\right)} < \Omega . \tag{3.16}$$

For lower frequencies the waves do not propagate in the ABH, because all solutions of γ are purely real.

The ABH effect occurs also in plate-like structures, as shown in figure 3.5.
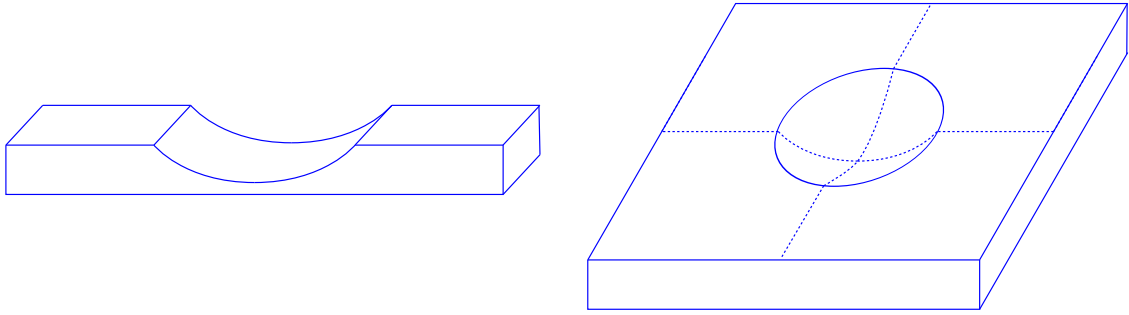
Figure 3.5: Different ABH in plate-like structures.

The differential equation for plates in bending, neglecting shear deformations and rotational inertia, results from the force equilibrium in the vertical direction [Timoshenko and Woinowsky-Krieger 1959]

$$\frac{\partial^2}{\partial x^2}M_{xx} + \frac{\partial^2}{\partial x \partial y}M_{xy} - \frac{\partial^2}{\partial y \partial x}M_{yx} + \frac{\partial^2}{\partial y^2}M_{yy} - \rho h \frac{\partial^2 w}{\partial t^2} + q = 0 . \tag{3.17}$$

ρ is the density of the plate and h the thickness. The plate is loaded with the external force q. Due to the bending deformation in two dimensions there exists four bending moments. Bending around the y-axis yields a stress distribution σ_{xx} and σ_{yx}. The respective bending moments are named M_{xx} and M_{yx}. Accordingly, bending around the x-axis generates the

bending moments M_{yy} and M_{xy}, respectively.

$$M_{xx} = -B \left(\frac{\partial^2 w}{\partial x^2} + \nu \frac{\partial^2 w}{\partial y^2} \right) \tag{3.18}$$

$$M_{yx} = -M_{xy} = -B \left(1 - \nu \right) \frac{\partial^2 w}{\partial x \partial y} \tag{3.19}$$

$$M_{yy} = -B \left(\frac{\partial^2 w}{\partial y^2} + \nu \frac{\partial^2 w}{\partial x^2} \right) \tag{3.20}$$

B is the bending stiffness of the plate and ν denotes the Poisson's ratio.

$$B = \frac{Eh^3}{12(1-\nu^2)} \ . \tag{3.21}$$

For the plate with constant thickness h the differential equation is given by [Timoshenko and Woinowsky-Krieger 1959]

$$-B \left(\frac{\partial^4 w}{\partial x^4} + 2 \frac{\partial^4 w}{\partial x^2 \partial y^2} + \frac{\partial^4 w}{\partial y^4} \right) - \rho h \frac{\partial^2 w}{\partial t^2} + q = 0 \ . \tag{3.22}$$

For a plate with spatially varying thickness $h(x,y)$ the bending stiffness also depends on the spatial location

$$B(x,y) = \frac{Eh^3(x,y)}{12(1-\nu^2)} \ . \tag{3.23}$$

E denotes the Young's modulus of the material. Accordingly, the differential equation for the plate with varying thickness contains additional terms that contain the derivatives of the bending stiffness

$$\frac{\partial^2}{\partial x^2} \left(-B(x,y) \left(\frac{\partial^2 w}{\partial x^2} + \nu \frac{\partial^2 w}{\partial y^2} \right) \right) + 2 \frac{\partial^2}{\partial x \partial y} \left(-B(x,y) \left(1 - \nu \right) \frac{\partial^2 w}{\partial x \partial y} \right)$$
$$+ \frac{\partial^2}{\partial y^2} \left(-B(x,y) \left(\frac{\partial^2 w}{\partial y^2} + \nu \frac{\partial^2 w}{\partial x^2} \right) \right) - \rho h \frac{\partial^2 w}{\partial t^2} + q = 0 \ . \tag{3.24}$$

For thickness profiles $h(x,y)$ that follow a parabolic profile as described in (3.5), it is not possible to find an analytically solution. However, Krylov [1990] describes the derivation for an approximated solution based on an approximation that reduces the wave propagation of

bending waves to a differential equation with a single variable [Krylov 1989]. To demonstrate the effect of parabolic profiles, the propagation time t_{ABH} of a wave traveling through the thickness reduction $h(s) = \epsilon s^{\beta}$ is computed. Therefore, one integrates the inverse of the group velocity (3.3) along the direction of the thickness reduction

$$t_{ABH} = \int_{s_0}^{s_1} \frac{ds}{c_g} = \int_{s_0}^{s_1} \left(\frac{3\rho(1-\nu^2)}{64E\epsilon^2\Omega^2} \right)^{\frac{1}{4}} s^{-\beta/2} ds = \left(\frac{3\rho(1-\nu^2)}{64E\epsilon^2\Omega^2} \right)^{\frac{1}{4}} \frac{2}{2-\beta} \left(s_1^{1-\beta/2} - s_0^{1-\beta/2} \right).$$

$$(3.25)$$
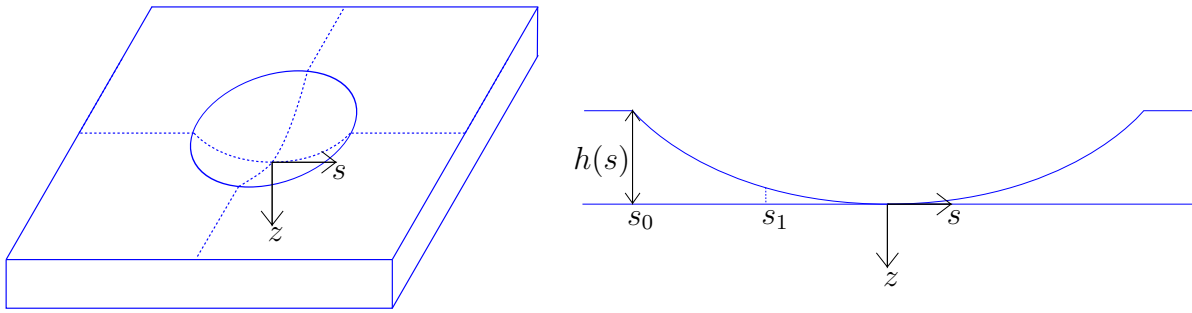
Figure 3.6: Computation of the propagation time along the direction s for a profile of the form $h(s) = \epsilon s^{\beta}$.

For $\beta > 2$ and $s_1 \to 0$ the propagation time in the ABH is infinite Zhao et al [2014]. Due to the fact that the profile reduction occurs on a finite interval, the wave propagating in the ABH can not "escape" because it never reaches the center of the ABH.

3.1.3 Application of ABH in practice

In practice, it is not feasible to manufacture ideally vanishing thickness profiles. Furthermore, a vanishing thickness would generate infinite amplitudes of the oscillation which cause material failure. As a consequence, the waves entering the ABH are able to "escape" the ABH. Therefore, the naming "acoustic black holes" might be misleading. Nevertheless, the large amplitudes and the focalization of the vibrational energy in the vicinity of the thickness reduction show potentials for vibration reduction for lightweight structures.

Figure 3.7 shows a one dimensional ABH with local damping layers. In the case of a simply attached layer, the offset from the neutral axis predominates the dissipation in the damping layer. The shear deformation is negligible and the loss factor of such a damping treatment
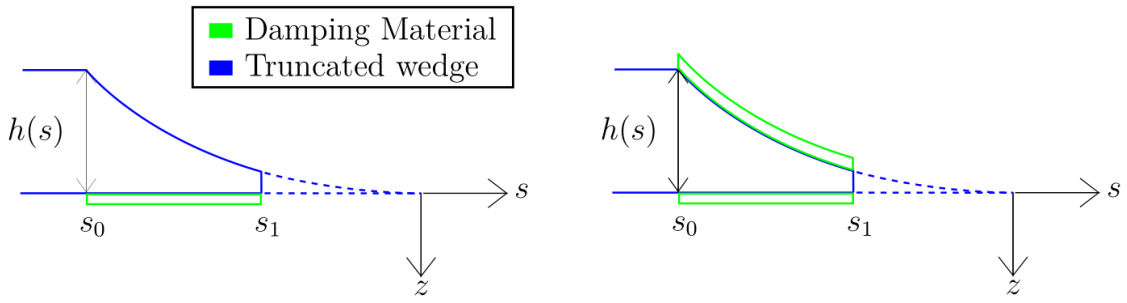
Figure 3.7: Truncated thickness profile with attached damping layers.

is driven by an extension of the damping layer [Cremer and Heckl 1967]

$$\xi = \beta d_{mid} \ . \tag{3.26}$$

δ denotes the thickness of the damping layer. The distance d_{mid} is the distance from the neutral axis of the beam with attached damping layer. It can be approximated with [Cremer and Heckl 1967]

$$d_{mid} \approx \delta/2 + h_1/2 \ , \tag{3.27}$$

where h_1 is the thickness of the structure.
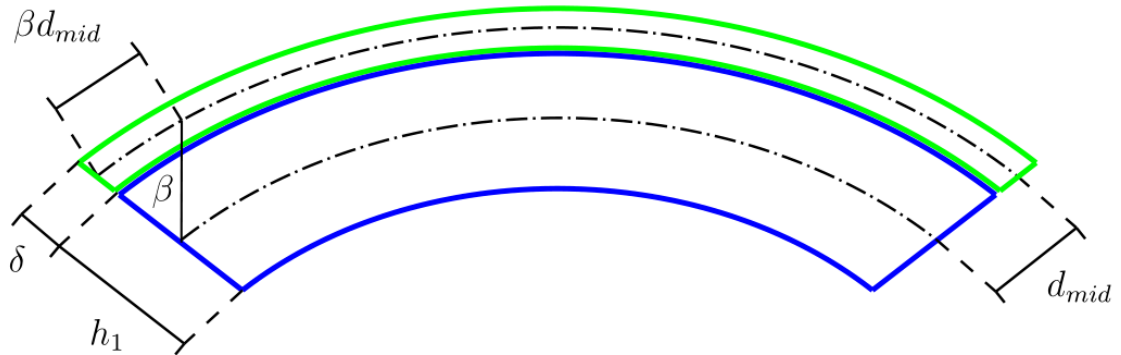
Figure 3.8: Deformation of a simple damping layer attached to a host structure which is subjected to pure bending.

The approximation of the elongation of the damping layer (3.26) is valid under the assumption that the thickness of the damping layer is small compared to the thickness of the structure. Based on the elongation of the damping layer, the dissipated energy per unit area

at the damping layer is

$$W_{diss} = \pi \eta_2 E_2 \delta \left| \frac{\partial \xi}{\partial x} \right|^2 . \tag{3.28}$$

E_2 and η_2 are the Young's modulus and the loss factor of the damping layer. The corresponding stored potential energy is approximated by

$$W_{pot} = \pi B \left| \frac{\partial \beta}{\partial x} \right|^2 . \tag{3.29}$$

The bending stiffness B contains the stiffness contributions of the structure and the damping layer. The ratio of the dissipated and stored energy yields the additional loss factor due to the attached damping layer.

$$\eta_{add} = \frac{W_{diss}}{W_{pot}} = \eta_2 \frac{E_2 \delta d_{mid}^2}{B} . \tag{3.30}$$

It is possible to approximate the bending stiffness of the compound structure [Cremer and Heckl 1967]

$$B \approx \frac{E_1 h_1^3}{12} . \tag{3.31}$$

E_1 is the Young's modulus of the material of the plate. Summarizing, the additional loss factor simplifies to [Krylov 2004]

$$\eta_{add} = 3 \frac{\delta}{h_1} \frac{E_2}{E_1} \eta_2 . \tag{3.32}$$

For thick damping layers, the above mentioned approximation is not accurate. Ross et al [1960] explain how damping layers affects the overall damping of viscoelastic laminae. Assuming that $\frac{\delta}{h_1} \frac{E_2}{E_1} \ll 1$ [Oberst 1952] the additional loss factor can be approximated

$$\eta_{add} = \frac{\eta_2 \frac{E_2}{E_1} \frac{\delta}{h_1} \left(3 + 6 \frac{\delta}{h_1} + 4 \left(\frac{\delta}{h_1} \right)^2 \right)}{1 + \frac{E_2}{E_1} \frac{\delta}{h_1} \left(3 + 6 \left(\frac{\delta}{h_1} \right)^2 + 4 \left(\frac{\delta}{h_1} \right)^2 \right)} . \tag{3.33}$$

For spatially varying thickness profile $h(s)$ with an attached damping layer the additional loss factor modifies the imaginary part of the wavenumber [Krylov 2004]. The spatially varying imaginary part of the wavenumber for a thin damping layer ($\frac{\delta}{h_1} \ll 1$) is

$$\text{Im}\{k(s)\} = \left(\frac{12\Omega^2}{c_p^2 h^2(s)} \right)^{\frac{1}{4}} \left(\frac{\eta_1}{4} + \frac{3}{2} \frac{\delta}{h(s)} \frac{E_2}{E_1} \eta_2 \right) \ . \tag{3.34}$$

η_1 is the loss factor of the plate material. To measure the efficiency of an ABH, Mironov [1988] introduces a reflection coefficient R that determines the amount of energy that "escapes" the ABH feature

$$R = \exp \left(-2 \int_{s_0}^{s_1} \text{Im}\{k(s)\} ds \right) \ . \tag{3.35}$$

As previously mentioned, several studies show that the reflection coefficient of a truncated thickness profile with locally attached damping layers in the vicinity of the ABH can strongly decrease the amount of energy that escapes the ABH [Krylov 2001; Conlon and Fahnline 2015; Tang et al 2016]. Assuming an ABH profile of the form $h(s) = \epsilon s^2$ results in the following reflection coefficient [Krylov 2004]

$$R = \exp\left(-2\mu_1 - 2\mu_2 \right) , \tag{3.36}$$

with

$$\mu_1 = \frac{12^{1/4} \eta_1}{4} \left(\frac{\Omega}{\epsilon \, c_p} \right)^{1/2} \ln\left(\frac{s_0}{s_1} \right) , \tag{3.37}$$

$$\mu_2 = \frac{3 \cdot 12^{1/4} \eta_2 \delta}{8} \left(\frac{\Omega}{\epsilon^3 \, c_p} \right)^{1/2} \frac{E_2}{E_1} \left(\frac{1}{s_1^2} - \frac{1}{s_0^2} \right) \ \text{(for single-sided damping layer)} , \tag{3.38}$$

$$\mu_2 = \frac{3 \cdot 12^{1/4} \eta_2 \delta}{4} \left(\frac{\Omega}{\epsilon^3 \, c_p} \right)^{1/2} \frac{E_2}{E_1} \left(\frac{1}{s_1^2} - \frac{1}{s_0^2} \right) \ \text{(for the double-sided damping layer).}$$

$$\tag{3.39}$$

For thick damping layers, there is no closed form expression for the reflection coefficient R.

In this case, the integral in (3.35) has to be solved numerically

$$R = \exp\left(-\int_{s_0}^{s_1} \frac{12^{1/4}}{2} \left(\frac{\Omega}{c_p\, h(x)}\right)^{1/2}\right.$$

$$\left. \cdot \frac{\left(1 + \frac{\rho_2}{\rho_1}\frac{\delta}{h(x)}\right)^{1/4} \left(\eta_1 + \eta_2 \frac{E_2}{E_1}\frac{\delta}{h(x)}\left(3 + 6\frac{\delta}{h(x)} + 4\left(\frac{\delta}{h(x)}\right)^2\right)\right)}{\left(1 + \frac{E_2}{E_1}\frac{\delta}{h(x)}\left(3 + 6\frac{\delta}{h(x)} + 4\left(\frac{\delta}{h(x)}\right)^2\right)\right)^{5/4}} dx\right) . \tag{3.40}$$

In general, constrained layer damping (CLD) is recommended as state of the art damping treatment for thin walled structures where bending waves dominate the vibrations. The reason is the activation of shear stress and strains that increase the dissipation compared to single layer damping. For constrained layers, shear deformation in the damping layer predominates the dissipation of energy

$$W_{diss} = \pi \eta_2 G_2 \delta \left|\gamma\right|^2 . \tag{3.41}$$

G_2 and η_2 are the shear modulus and the loss factor of the damping layer. The shear γ occurs due to differences in the extension at the top of the base structure and the bottom of the cover layer. Due to the cover sheet, the shear angle γ is related the elongation in the cover layer

$$\gamma\delta = d_{cov}\beta - \xi \tag{3.42}$$
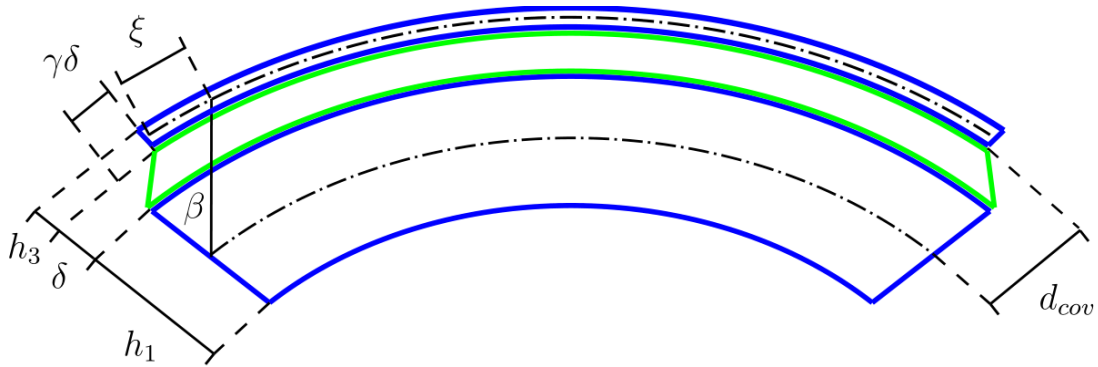
Figure 3.9: Deformation of a constrained damping layer attached to a host structure which is subjected to pure bending.

Assuming that the cover layer dominantly deforms in extension, the shear forces of the

damping layer balances the normal forces of the cover layer [Cremer and Heckl 1967]

$$E_3 h_3 \frac{\partial^2 \xi}{\partial x^2} + G_2 \gamma = 0 \ . \tag{3.43}$$

E_3 is the Young's modulus and h_3 is the thickness of the cover layer. According to Cremer and Heckl [1967], the maximal loss factor for the CLD is

$$\eta_{max} = \eta_2 \frac{E_3 h_3 d_{mid}^2}{B} \frac{1}{2 \left(1 + \sqrt{1 + \eta_2^2}\right)} \ , \tag{3.44}$$

The loss factor of CLD does not depend on the Young's modulus or the shear modulus of the attached damping layer and therefore, it is possible to use damping materials with larger loss factors which are usually very soft. Consequently, the maximum loss factor of a CLD is tremendously larger than the maximum loss factor of a simple damping layer.

3.2 Locally resonant material

The basic idea of locally resonant material is that locally resonant modes that oscillate out of phase reduce the vibration of the main structure. In this case, the vibration of the main structure is reduced because vibrational energy is transferred to the relative motion between the local resonator and the main structure. The working principle of a resonating sub structures is well established in several applications, e.g. the Taipei 101 tower [Poon et al 2004] or the Millennial Bridge in London [Pavic et al 2002]. In this context, the local resonator is termed "tuned mass damper (TMD)". To the author's knowledge, the term "locally resonant material" appeared after Liu et al [2000] demonstrated the formation of frequency ranges where the propagation of waves are suppressed.

3.2.1 State of the art

Ormondroyd and Den Hartog [1928] introduce the basic idea of a single local resonance that reduce the vibration of the main structure. They formulate an optimization problem of a single TMD that minimize the maximal amplitude of the system. [Hartog 1956] summarizes the optimal parameters for the tuning and the damping of the TMD for an undamped main structure. The optimal tuning frequency of the TMD is based on the work of Hahnkamm [1933] and the optimal damping of the TMD is from Brock [1945]. Inglis [1951] and Bishop and Welbourn [1952] derive optimal parameters for a damped host structure. For an overview of optimal TMD parameters for different optimization objectives, the author refers to Asami et al [2002].

Besides single resonators, there also exist several studies on host structures modified by multiple resonators [Igusa and Xu 1993; Rade and Steffen 2000; Gündel 2008; Mohtat and Dehghan-Niri 2011]. Igusa and Xu [1993] use an impedance model to find optimal parameters for multiple resonators attached to the host structure. They show that multiple resonators with slightly varying resonance frequencies around the target frequency yield a broadband vibration reduction of the host structure. Claeys et al [2016a] verify this effect for two different sets of resonators with similar resonance frequencies. Rade and Steffen [2000] determine the frequency response function (FRF) of the overall structure by coupling the FRF of the host structure and the FRF of the resonators. The advantage of this methodology is that the FRF from measurements, numerical simulations or analytical expressions can be combined. Gündel [2008] describes three different methods to include the resonators into the model of the host structure: First, applying the resonators as additional degrees of

freedoms. Second, adding them as a frequency dependent dynamic inertia term into the frequency dependent dynamic stiffness matrix of the host structure. Or third, modeling the resonators as external attenuation forces. A more detailed explanation of the different methods follows in section 4.1.3. Mohtat and Dehghan-Niri [2011] develop a methodology to include uncertainties of the host structure into the design process of the resonators.

For periodic structures, the Wave Finite Element method (WFEM) computes the waves that propagate through the structure. Claeys et al [2011, 2013]; Xiao et al [2012, 2013] apply the WFEM to demonstrate the band gap formation resulting from a periodic alignment of resonators. The investigation of infinite repetitions of identical unit cells shows that there exists a frequency range around the target frequency of the resonator, where no free wave propagation is possible. This frequency range is called resonance stop band. Periodically attached resonators can generate stop bands in beams and plates [Claeys et al 2011, 2013]. Miranda and Dos Santos [2016] compare different computational models for the band gap formation of locally resonant beam structures. In general, the stop band size increases with increasing mass of the resonators [Claeys et al 2013]. Likewise, the vibration reduction at resonance increases with increasing mass [Claeys et al 2016a]. In addition, Claeys et al [2013] show that damped resonators increase the frequency range of vibration reduction, while also decreasing the peak vibration reduction at the target frequency of the resonators. For an effective vibration reduction of the host structure, a resonator spacing smaller than half of the wavelength of the wave that the resonator interferes with is beneficial [Claeys et al 2013].

Besides a vibration reduction, distributed resonators also affect the radiation efficiency of planar structures [Nateghi et al 2019]. For resonators tuned below the coincidence frequency, there appears a frequency range slightly above the resonance band gap where the radiation efficiency increases [Claeys et al 2014b]. For resonators tuned above the coincidence frequency of the host structure, such an increased radiation efficiency is not observed. Besides the sound radiation, resonant materials show potential for increasing the sound transmission loss at the target frequency of the resonators [Claeys et al 2016b; Egashira et al 2016; Van Belle et al 2019].

Xiao et al [2012, 2013] investigate the combination of the resonance effect and the interference effect due to the spacing of the resonators. According to Xiao et al [2013]; Sharma and Sun [2016], it is not possible to combine the resonance band gap and the interference band gap to form one large band gap. Using a numerical model of a Timoshenko beam, Sharma and Sun [2016] demonstrate that there exists a pass band between the resonance and the interference band gaps. The size of this pass band depends on the resonator spacing [Xiao et al 2013].

For the realization of locally resonant materials, there exist different design proposals. Claeys et al [2016a]; Egashira et al [2016] include beam-like resonators into the cells of a honeycomb panel. In contrast, Spadoni et al [2009b] and Ruzzene [2015] introduce a periodic chiral lattice structure that generates local resonances in the low frequency range. Liu et al [2000] present a three dimensional lattice structure that generates a stop band. The lattice structure consists of a sphere made of lead which is covered in silicone. Chen and Wang [2014] introduce a three dimensional crystal made of ceramic and glass polymer. Such resonant lattice structures are also called phononic crystals [Deymier 2013].

3.2.2 Fundamentals of locally resonant materials

This section explains the underlying theory of locally resonant materials. The first part demonstrates the principle of local resonances for vibration suppression. The second part elaborates on the occurrence of band gaps for periodic resonant materials.

Effect of local resonances

A simple two degree of freedom oscillator explains the working principle of a local resonance. Figure 3.10 shows a discrete model of a two-DOF-oscillator.
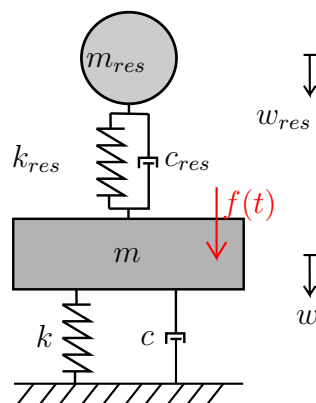
Figure 3.10: Simple model for a locally resonant material: the two-DOF-oscillator.

m, k_s, and c are the mass, stiffness, and damping constants of the main structure. A discrete resonator connected to the main structure introduces a local resonance. The subscript "res" denotes the parameters of the resonator. Accordingly, w is the displacements of the main structure and w_{res} the displacements of the resonator. $\dot{\square}$ and $\ddot{\square}$ mark the respective velocities and accelerations. The external force $f(t)$ excites the main structure. Without the resonator

mass m_{res}, the main structure experiences large deflection for excitation frequencies close to the resonance frequency of the main structure. A resonator tuned to the resonance frequency of the main structure absorbs the vibration of the main structure at the target frequency. The two-DOF-oscillator has two vibrational modes. In the first resonance mode, the masses move in phase. For the second resonance, the two masses oscillates out of phase (see figure 3.11).
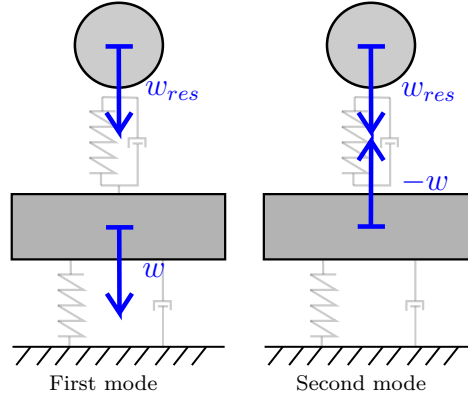
Figure 3.11: Vibrational modes of the two-DOF-oscillator.

The following paragraph derives the differential equation for the two-DOF-oscillator. Figure 3.12 shows the internal and external forces acting on the main structure and the resonator. Balancing the forces acting on the masses m and m_{res} yields the differential equation of the two-DOF-oscillator

$$f(t) - m\ddot{w} - c\dot{w} - k_s w + c_{res}(\dot{w}_{res} - \dot{w}) + k_{res}(w_{res} - w) = 0 \ , \tag{3.45}$$

$$-m_{res}\ddot{w}_{res} - c_{res}(\dot{w}_{res} - \dot{w}) - k_{res}(w_{res} - w) = 0 \ . \tag{3.46}$$
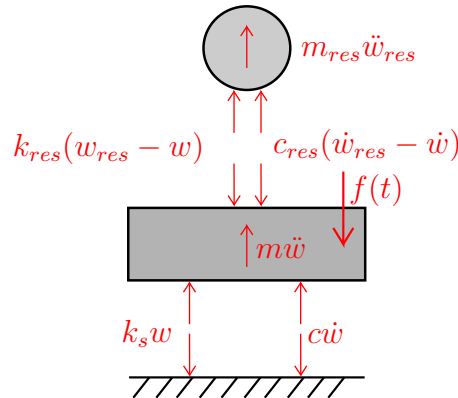
Figure 3.12: Visualization of the forces acting on the structure and the resonator.

The tuned mass damper absorbs the vibration of the main structure by a relative displacements. Therefore, it is beneficial to introduce the relative displacement $w_{rel} = w_{res} - w$

$$f(t) - m\ddot{w} - c\dot{w} - k_s w + c_{res}\dot{w}_{rel} + k_{res}w_{rel} = 0 \ , \tag{3.47}$$

$$-m_{res}(\ddot{w}_{rel} + \ddot{w}) - c_{res}\dot{w}_{rel} - k_{res}w_{rel} = 0 \ . \tag{3.48}$$

Consider the steady state solution for a harmonic excitation $f(t) = \underline{f}e^{i\Omega t}$, the displacements have the form

$$w = \underline{w}e^{i\Omega t} \ , \tag{3.49}$$

$$w_{rel} = \underline{w}_{rel}e^{i\Omega t} \ . \tag{3.50}$$

$\underline{f}$ and $\underline{w}$ describe complex amplitudes and Ω is the excitation frequency. A characteristic quantity to evaluate the dynamic behavior of the system is the amplification function V. It is the absolute value of the particular solution normalized with the static displacements $w_{stat} = \frac{|\underline{f}|}{k_s}$

$$V = \frac{|\underline{w}|}{w_{stat}} \ . \tag{3.51}$$

The author attaches a detailed derivation of the amplification functions V and V_{rel} in the appendix (A.2)

$$V = \frac{|\underline{w}|}{w_{stat}} = \sqrt{\frac{e^2 + f^2}{g^2 + h^2}} \ , \tag{3.52}$$

$$V_{rel} = \frac{|\underline{w}_{rel}|}{w_{stat}} = \sqrt{\frac{\alpha^4}{g^2 + h^2}} \ , \tag{3.53}$$

with

$$e = \beta^2 - \alpha^2 \ , \tag{3.54}$$

$$f = 2\alpha\beta D_{res} \ , \tag{3.55}$$

$$g = \alpha^4 - \alpha^2(1 + \beta^2 + \mu\beta^2 + 4\beta DD_{res}) + \beta^2 \ , \tag{3.56}$$

$$h = \alpha[2D(\beta^2 - \alpha^2) + 2\beta D_{res}(1 - \alpha^2 - \mu\alpha^2)] \ . \tag{3.57}$$

The amplification function describe the amplification of the displacements based on the dimensionless parameters α, β, μ, D and D_{res}:

- $\alpha = \frac{\Omega}{\omega}$ describes the ratio between the excitation frequency and the eigenfrequency of the main structure

- $\beta = \frac{\omega_{res}}{\omega}$ describes the ratio between the eigenfrequency of the resonator and the eigenfrequency of the main structure

- $\mu = \frac{m_{res}}{m}$ describes the ratio between the mass of the resonator and the mass of the main structure

- $D = \frac{c}{c_{crit}}$ describes the amount of critical damping that is applied to the main structure

- $D_{res} = \frac{c_{res}}{c_{res,crit}}$ describes the amount of critical damping that is applied to the resonator
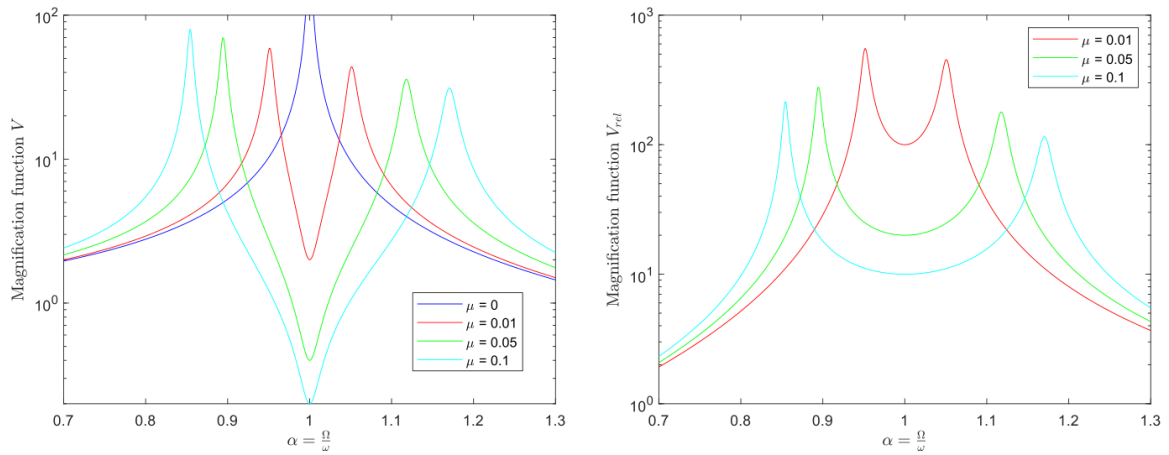
Figure 3.13: Influence of the mass of the resonator on the amplification functions; damping ratio of the main structure $D = 0$, damping ratio of the resonator $D_{res} = 0.01$ and frequency tuning of the resonator $\beta = 1$.

Figure 3.13 shows the amplification functions of the main system and the relative motion for three different mass ratios μ. The main structure is undamped and the damping ratio of the resonator is fixed to 0.01. The eigenfrequency of the resonator is the same as the eigenfrequency of the main structure ($\beta = 1$). From figure 3.13, it is obvious that the resonator strongly reduces the vibration of the main mass in the vicinity of the target frequency. A larger resonator mass m_{res} results in a smaller deflections of the main structure at the resonance frequency. Furthermore, the frequency range of vibration reduction increases with increasing mass. The resonator introduces an additional resonance into the system. The new system has two resonances that split up around the original resonance.

The amplification function of the relative motion V_{rel} implicates that a lower resonator mass yields higher relative motion. For practical application, the relative motion is important to consider, because it defines the installation space that is needed. For a detailed discussion

about the influences of the different parameters (β and D_{res}) of the two-DOF-oscillators, the author refers to the appendix A.3.

Bandgap formation of locally resonant materials

This section investigates the impact of multiple local resonators and how they can create band gaps where no free wave propagation occurs. A one dimensional chain of discrete masses demonstrates the band gap formation of a locally resonant material.
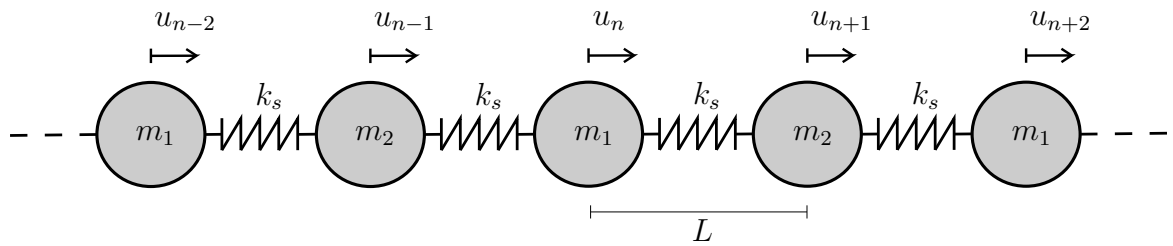
Figure 3.14: Simple model of a resonant crystal consisting of a periodic repetition of two concentrated masses that are linked via discrete springs.

Figure 3.14 shows a one dimensional infinite lattice that consists of a periodically alignment of two different masses m_1 and m_2. Discrete springs with spring stiffness k_s link the masses. The length L defines the distance between the masses.
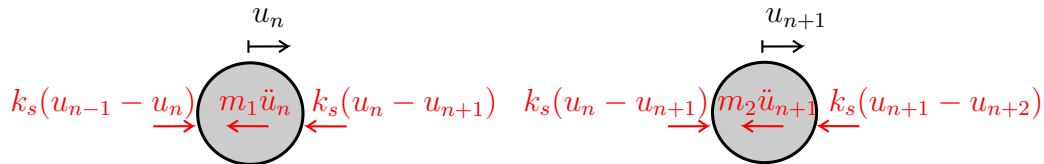
Figure 3.15: Visualization of the forces acting in a unit cell of the diatomic crystal.

The equilibrium of the forces yields the equation of motion for the one dimensional lattice

$$m_1 \ddot{u}_n = k_s(u_{n-1} - u_n) - k_s(u_n - u_{n+1}) = k_s(u_{n-1} - 2u_n + u_{n+1}) \,, \tag{3.58}$$

$$m_2 \ddot{u}_{n+1} = k_s(u_n - u_{n+1}) - k_s(u_{n+1} - u_{n+2}) = k_s(u_n - 2u_{n+1} + u_{n+2}) \,. \tag{3.59}$$

Thus, the steady state solution of a time harmonic free oscillation has the form

$$u = \underline{u} e^{i\Omega t} \,. \tag{3.60}$$

Inserting that into the force equilibrium yields

$$-\Omega^2 m_1 \underline{u}_n = k_s(\underline{u}_{n-1} - 2\underline{u}_n + \underline{u}_{n+1}) \,,$$
$$-\Omega^2 m_2 \underline{u}_{n+1} = k_s(\underline{u}_n - 2\underline{u}_{n+1} + \underline{u}_{n+2}) \,.$$

(3.61)

The Bloch's theorem, which for one dimension corresponds to the Floquet Theorem, links the displacements of the masses m_1 and m_2 of two neighboring unit cells [Bloch 1929; Floquet 1883]

$$\underline{u}_{n-1} = \underline{u}_{ref,m_2} \mathrm{e}^{-i\kappa 2aL} \,,$$
$$\underline{u}_n = \underline{u}_{ref,m_1} \mathrm{e}^{-i\kappa 2aL} \,,$$
$$\underline{u}_{n+1} = \underline{u}_{ref,m_2} \mathrm{e}^{-i\kappa(2a+2)L} \,,$$
$$\underline{u}_{n+2} = \underline{u}_{ref,m_1} \mathrm{e}^{-i\kappa(2a+2)L} \,.$$

(3.62)

κ is a the phase change per unit meter which in general can be complex $\kappa = \kappa_{Re} + i\kappa_{Im}$. $\underline{u}_{ref,m_1}$ and $\underline{u}_{ref,m_2}$ are the solutions in the reference cell. a is an arbitrary integer that defines any of the masses m_1 and m_2 as reference mass. L is the distance between the masses. First, it is assumed that the wavenumber is purely real $\kappa = \kappa_{Re}$. Inserting (3.62) into the equation of motion of the unit cell (3.61) yields

$$-\Omega^2 m_1 \underline{u}_{ref,m_1} \mathrm{e}^{-i\kappa_{Re} 2aL}$$
$$= k_s \left(\underline{u}_{ref,m_2} \mathrm{e}^{-i\kappa_{Re} 2aL} - 2\underline{u}_{ref,m_1} \mathrm{e}^{-i\kappa_{Re} 2aL} + \underline{u}_{ref,m_2} \mathrm{e}^{-i\kappa_{Re}(2a+2)L} \right) \,,$$

(3.63)

$$-\Omega^2 m_2 \underline{u}_{ref,m_2} \mathrm{e}^{-i\kappa_{Re}(2a+2)L}$$
$$= k_s \left(\underline{u}_{ref,m_1} \mathrm{e}^{-i\kappa_{Re} 2aL} - 2\underline{u}_{ref,m_2} \mathrm{e}^{-i\kappa_{Re}(2a+2)L} + \underline{u}_{ref,m_1} \mathrm{e}^{-i\kappa_{Re}(2a+2)L} \right) \,.$$

(3.64)

Further simplifications result in

$$(2k_s - \Omega^2 m_1)\underline{u}_{ref,m_1} \mathrm{e}^{-i\kappa_{Re} 2aL} - k_s \left(1 + \mathrm{e}^{-i\kappa_{Re} 2L} \right) \underline{u}_{ref,m_2} \mathrm{e}^{-i\kappa_{Re} 2aL} = 0 \,,$$

(3.65)

$$(2k_s - \Omega^2 m_2)\underline{u}_{ref,m_2} \mathrm{e}^{-i\kappa_{Re}(2a+2)L} - k_s \left(\mathrm{e}^{i\kappa_{Re} 2L} + 1 \right) \underline{u}_{ref,m_1} \mathrm{e}^{-i\kappa_{Re}(2a+2)L} = 0 \,.$$

(3.66)

The exponential terms depending on a cancel out and (3.65) and (3.66) simplifies to

$$\begin{bmatrix} 2k_s - \Omega^2 m_1 & -k_s \left(1 + \mathrm{e}^{-i\kappa_{Re} 2L} \right) \\ -k_s \left(\mathrm{e}^{i\kappa_{Re} 2L} + 1 \right) & 2k_s - \Omega^2 m_2 \end{bmatrix} \begin{bmatrix} \underline{u}_{ref,m_1} \\ \underline{u}_{ref,m_2} \end{bmatrix} = \begin{bmatrix} 0 \\ 0 \end{bmatrix} \,.$$

(3.67)

Looking for a non-trivial solution with $\underline{u}_{ref,m_1} \neq 0$ and $\underline{u}_{ref,m_2} \neq 0$, the determinant needs to vanish

$$
\begin{vmatrix}
2k_s - \Omega^2 m_1 & -k_s \left(1 + e^{-i\kappa_{Re}2L}\right) \\
-k_s \left(e^{i\kappa_{Re}2L} + 1\right) & 2k_s - \Omega^2 m_2
\end{vmatrix} = 0 \ . \tag{3.68}
$$

Introducing the cosine as a combination of exponential terms $(2cos(x) = e^{ix} + e^{-ix})$ defines the eigenvalue problem with $\lambda = \Omega^2$

$$
\lambda^2 - 2k_s \left(\frac{1}{m_1} + \frac{1}{m_2}\right) \lambda + \frac{2k_s^2}{m_1 m_2} \left(1 - \cos(2\kappa_{Re}L)\right) = 0 \ . \tag{3.69}
$$

Consequently, there exist two solutions for λ

$$
\lambda_{1,2} = k_s \left(\frac{1}{m_1} + \frac{1}{m_2}\right) \pm \sqrt{k_s^2 \left(\frac{1}{m_1} + \frac{1}{m_2}\right)^2 - \frac{2k_s^2}{m_1 m_2} \left(1 - \cos(2\kappa_{Re}L)\right)} \ . \tag{3.70}
$$

For the circular frequency Ω, there exist four solutions

$$
\Omega_1(\kappa_{Re}) = \sqrt{\lambda_1} \ , \tag{3.71}
$$

$$
\Omega_2(\kappa_{Re}) = -\sqrt{\lambda_1} \ , \tag{3.72}
$$

$$
\Omega_3(\kappa_{Re}) = \sqrt{\lambda_2} \ , \tag{3.73}
$$

$$
\Omega_4(\kappa_{Re}) = -\sqrt{\lambda_2} \ . \tag{3.74}
$$

These solutions show for which combination of frequency and phase a wave can propagate through the lattice.

Figure 3.16 shows the four solutions of Ω. The negative frequencies ($\Omega_2(\kappa)$ and $\Omega_4(\kappa)$) do not yield any new information about the band formation. To identify the frequency range where wave can propagate, it is sufficient to compute the phase change along a single unit cell (dashed rectangle). There are three frequencies that mark the starting and ending of
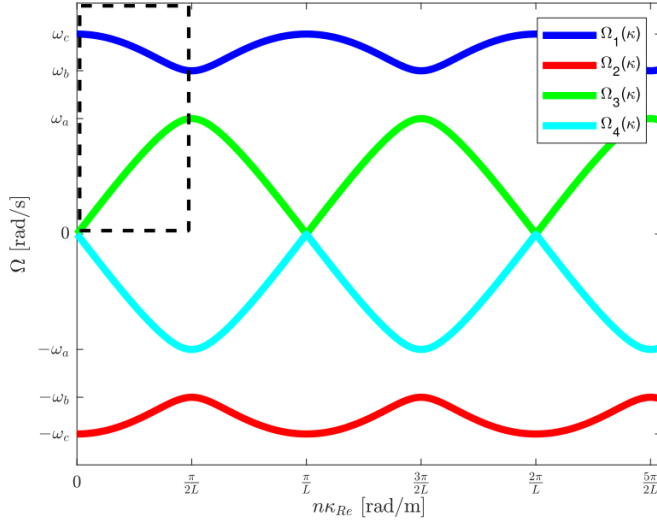
Figure 3.16: Dispersion of the phase per unit length for the diatomic crystal, the phase κ_{Re} is multiplied with an integer n.
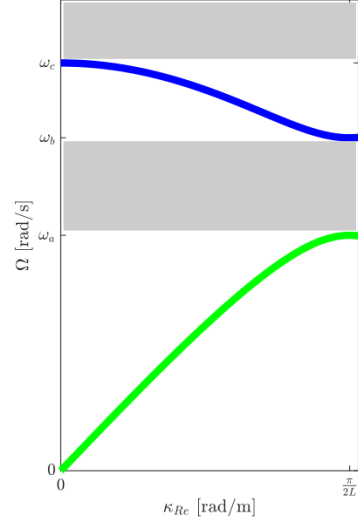
Figure 3.17: Dispersion relation along a single unit cell.

the ranges where no wave propagation is possible.

$$\omega_a = \Omega_3(\pi/2L) = \sqrt{\frac{2k_s}{m_2}} \quad \text{for } m_2 > m_1 \,, \tag{3.75}$$

$$\omega_b = \Omega_1(\pi/2L) = \sqrt{\frac{2k_s}{m_1}} \quad \text{for } m_2 > m_1 \,, \tag{3.76}$$

$$\omega_c = \Omega_1(0) = \sqrt{2k_s \left(\frac{1}{m_1} + \frac{1}{m_2} \right)} \,. \tag{3.77}$$

Only for pairs of real κ and real frequency Ω the wave motion describes an harmonic oscillation [Doyle 1997]. For the first band gap which appears from $\omega_a < \Omega < \omega_b$ such a pair is not found. This gap is formed by the local resonance. A mono-atomic crystal ($m_1 = m_2$) has no frequency gap between ω_a and ω_b. For frequencies above ω_c, the model does not reveal pairs of real κ and real Ω. The reason is that the model of the diatomic crystal maps the higher oscillating solutions onto the respective lower order motion that have the same phase (see figure 3.18). The model is not able to distinguish the different waves.

Applying a imaginary phase ($\kappa_{Im} \neq 0$), it is possible to find a solution for the frequency range where no free waves propagate. Setting $\kappa_{Re} = 0$ in (3.62) yields the following approach
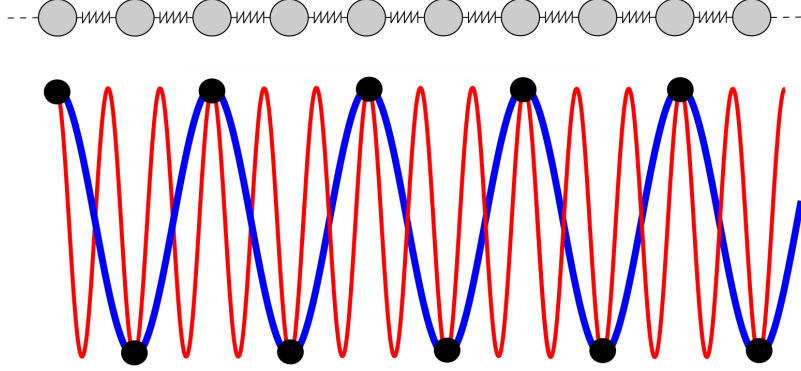
Figure 3.18: Two wave motion with different wavelength but identical phase.

for the motion of the crystal

$$
\begin{aligned}
\underline{u}_{n-1} &= \underline{u}_{ref,m_2}\mathrm{e}^{+\kappa_{Im}2aL} \ , \\
\underline{u}_{n} &= \underline{u}_{ref,m_1}\mathrm{e}^{+\kappa_{Im}2aL} \ , \\
\underline{u}_{n+1} &= \underline{u}_{ref,m_2}\mathrm{e}^{+\kappa_{Im}(2a+2)L} \ , \\
\underline{u}_{n+2} &= \underline{u}_{ref,m_1}\mathrm{e}^{+\kappa_{Im}(2a+2)L} \ .
\end{aligned}
\tag{3.78}
$$

This yields the following equation of motion

$$
-\Omega^2 m_1 \underline{u}_{ref,m_1}\mathrm{e}^{+\kappa_{Im}2aL} = k_s\left(\underline{u}_{ref,m_2} - 2\underline{u}_{ref,m_1} + \underline{u}_{ref,m_2}\mathrm{e}^{\kappa_{Im}2L}\right)\mathrm{e}^{+\kappa_{Im}2aL} \ ,
\tag{3.79}
$$

$$
-\Omega^2 m_2 \underline{u}_{ref,m_2}\mathrm{e}^{+\kappa_{Im}(2a+2)L} = k_s\left(\underline{u}_{ref,m_1}\mathrm{e}^{-\kappa_{Im}2L} - 2\underline{u}_{ref,m_2} + \underline{u}_{ref,m_1}\right)\mathrm{e}^{+\kappa_{Im}(2a+2)L} \ .
\tag{3.80}
$$

The equation of motion simplifies to

$$
\begin{bmatrix}
2k_s - \Omega^2 m_1 & -k_s\left(1 + \mathrm{e}^{\kappa_{Im}2L}\right) \\
-k_s\left(\mathrm{e}^{-\kappa_{Im}2L} + 1\right) & 2k_s - \Omega^2 m_2
\end{bmatrix}
\begin{bmatrix}
\underline{u}_{ref,m_1} \\
\underline{u}_{ref,m_2}
\end{bmatrix}
=
\begin{bmatrix}
0 \\
0
\end{bmatrix} \ .
\tag{3.81}
$$

As previously, for a non-trivial solution, the determinant vanishes. Using the relation $2\cosh(x) = e^x + e^{-x}$, the determinant results in

$$
\bar{\lambda}^2 - 2k_s\left(\frac{1}{m_1} + \frac{1}{m_2}\right)\bar{\lambda} + \frac{2k_s^2}{m_1 m_2}\left(1 - \cosh(2\kappa L)\right) = 0 \ .
\tag{3.82}
$$
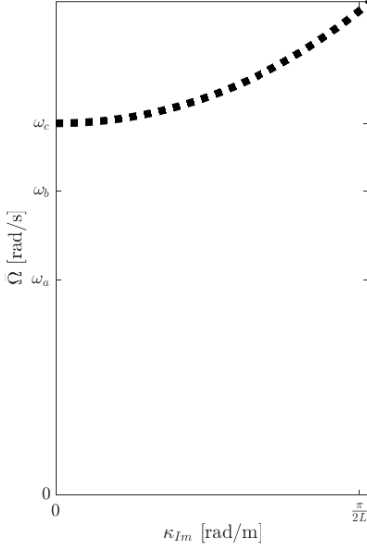
Figure 3.19: Dispersion relation of the imaginary phase per unit length with $\kappa_{Re} = 0$.
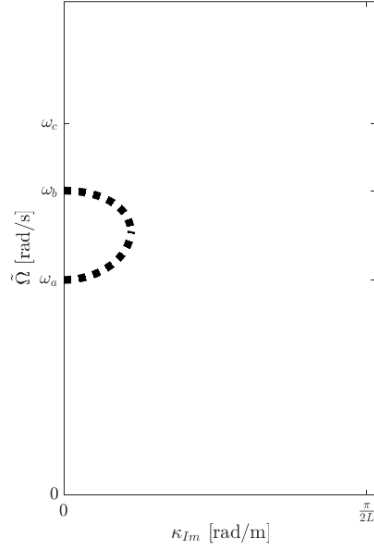
Figure 3.20: Dispersion relation of the imaginary phase per unit length with $\kappa_{Re} = \frac{\pi}{2L}$.

The solution for the evanescent waves in the frequency range above ω_c are

$$\bar{\lambda}_{1,2} = k_s \left(\frac{1}{m_1} + \frac{1}{m_2} \right) \pm \sqrt{k_s^2 \left(\frac{1}{m_1} + \frac{1}{m_2} \right)^2 - \frac{2k_s^2}{m_1 m_2} \left(1 - \cosh(2\kappa L) \right)} \,. \tag{3.83}$$

Calculating the corresponding four solutions for $\bar{\omega}$ yields one solution that is physically relevant (Ω real and positive)

$$\bar{\Omega}_1 = \sqrt{\bar{\lambda}_1} \,. \tag{3.84}$$

Figure 3.19 shows the non negativ solution $\bar{\Omega}$ of the evanescent waves for $\kappa_{Re} = 0$. One can observe that we have found a solution for the frequency range $\omega_c < \Omega$. This solution is not physical and occurs due to modeling of the diatomic crystal (see figure 3.18). To find a solution for the frequency range $\omega_a < \Omega < \omega_b$, one defines κ_{Re} as $\frac{\pi}{2L}$. Thus, the approach for

the motion of the crystal is

$$
\begin{aligned}
\underline{u}_{n-1} &= \underline{u}_{ref,m_2} \mathrm{e}^{-i\pi a} \mathrm{e}^{+\kappa_{Im} 2aL} \ , \\
\underline{u}_{n} &= \underline{u}_{ref,m_1} \mathrm{e}^{-i\pi a} \mathrm{e}^{+\kappa_{Im} 2aL} \ , \\
\underline{u}_{n+1} &= \underline{u}_{ref,m_2} \mathrm{e}^{-i\pi(a+1)} \mathrm{e}^{+\kappa_{Im}(2a+2)L} \ , \\
\underline{u}_{n+2} &= \underline{u}_{ref,m_1} \mathrm{e}^{-i\pi(a+1)} \mathrm{e}^{+\kappa_{Im}(2a+2)L} \ .
\end{aligned}
\tag{3.85}
$$

In that case the equation of motion of the diatomic crystal is

$$
-\Omega^2 m_1 \underline{u}_{ref,m_1} \mathrm{e}^{-i\pi a} \mathrm{e}^{+\kappa_{Im} 2aL} \ ,
$$

$$
= k_s \left(\underline{u}_{ref,m_2} - 2\underline{u}_{ref,m_1} + \underline{u}_{ref,m_2} \mathrm{e}^{-i\pi} \mathrm{e}^{\kappa_{Im} 2L} \right) \mathrm{e}^{-i\pi a} \mathrm{e}^{+\kappa_{Im} 2aL} \ ,
\tag{3.86}
$$

$$
-\Omega^2 m_2 \underline{u}_{ref,m_2} \mathrm{e}^{-i\pi(a+1)} \mathrm{e}^{+\kappa_{Im}(2a+2)L} \ ,
$$

$$
= k_s \left(\underline{u}_{ref,m_1} \mathrm{e}^{i\pi} \mathrm{e}^{-\kappa_{Im} 2L} - 2\underline{u}_{ref,m_2} + \underline{u}_{ref,m_1} \right) \mathrm{e}^{-i\pi(a+1)} \mathrm{e}^{+\kappa_{Im}(2a+2)L} \ .
\tag{3.87}
$$

The exponential terms depending on a cancel out and the exponential term $\mathrm{e}^{\pm i\pi}$ equals -1

$$
-\Omega^2 m_1 \underline{u}_{ref,m_1} = k_s \left(\underline{u}_{ref,m_2} - 2\underline{u}_{ref,m_1} - \underline{u}_{ref,m_2} \mathrm{e}^{-\kappa_{Im} 2L} \right) \ ,
\tag{3.88}
$$

$$
-\Omega^2 m_2 \underline{u}_{ref,m_2} = k_s \left(-\underline{u}_{ref,m_1} \mathrm{e}^{\kappa_{Im} 2L} - 2\underline{u}_{ref,m_2} + \underline{u}_{ref,m_1} \right) \ .
\tag{3.89}
$$

As previously, the determinant should vanish

$$
\begin{bmatrix}
2k_s - \Omega^2 m_1 & -k_s \left(1 - \mathrm{e}^{-\kappa_{Im} 2L} \right) \\
-k_s \left(-\mathrm{e}^{\kappa_{Im} 2L} + 1 \right) & 2k_s - \Omega^2 m_2
\end{bmatrix}
\begin{bmatrix}
\underline{u}_{ref,m_1} \\
\underline{u}_{ref,m_2}
\end{bmatrix}
=
\begin{bmatrix}
0 \\
0
\end{bmatrix} \ .
\tag{3.90}
$$

Searching for a vanishing determinant yields the corresponding quadratic equation

$$
\tilde{\lambda}^2 - 2k_s \left(\frac{1}{m_1} + \frac{1}{m_2} \right) \tilde{\lambda} + \frac{2k_s^2}{m_1 m_2} \left(1 + \cosh(2\kappa L) \right) = 0 \ .
\tag{3.91}
$$

Finally, there is another set of solutions for the frequency range $\omega_a < \Omega < \omega_b$

$$
\tilde{\lambda}_{1,2} = k_s \left(\frac{1}{m_1} + \frac{1}{m_2} \right) \pm \sqrt{ k_s^2 \left(\frac{1}{m_1} + \frac{1}{m_2} \right)^2 - \frac{2k_s^2}{m_1 m_2} \left(1 + \cosh(2\kappa L) \right) } \ .
\tag{3.92}
$$

Figure 3.20 shows the physical relevant solution $\tilde{\Omega}$ for $\kappa_{Re} = \frac{\pi}{2L}$. One can observe that the solution $\tilde{\Omega}$ is defined for the frequency range $\omega_a < \Omega < \omega_b$.

Combining the solutions of the propagating and the evanescent waves, the dispersion can be plotted in a three dimensional plot.
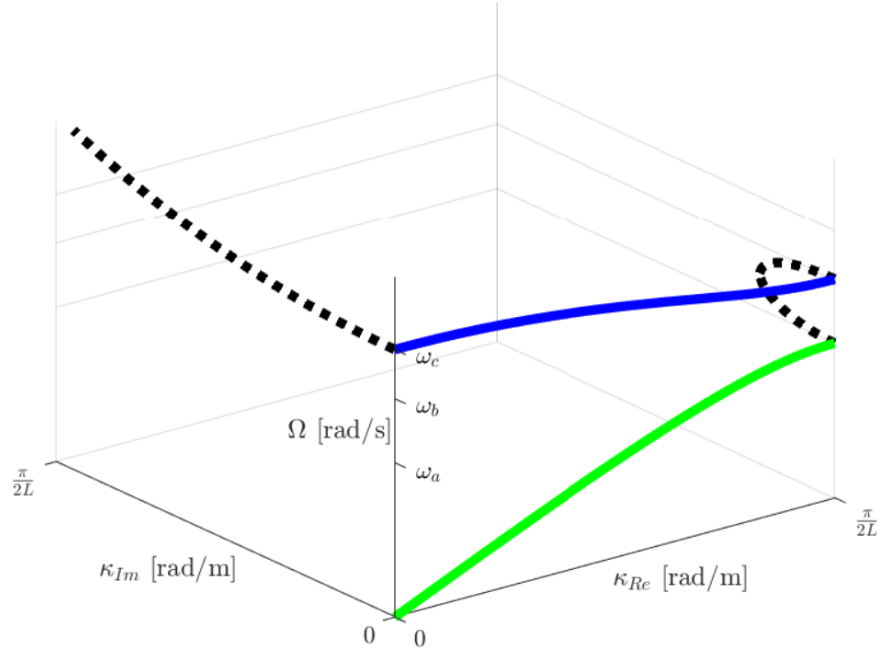
Figure 3.21: Dispersion relation of the unit cell of the diatomic crystal including the evanescent waves.

The horizontal plane show the real and imaginary part of the phase κ and the vertical axis shows the circular frequency Ω. For $\Omega < \omega_a$ the masses m_1 and m_2 oscillate in phase. This frequency branch is named acoustical branch. In contrast, the frequency range $\omega_b < \Omega < \omega_c$ is called optical branch as the masses moves out of phase [Deymier 2013]. The frequency gap $\omega_a < \Omega < \omega_b$ occurs due to the local resonance. The motion of the local resonance compensates the vibrational energy and no free waves can propagate through the diatomic crystal as the phase is imaginary.

3.3 Wave guides for acoustic waves

In general, the motion in structural components is a superposition of different waves that propagate in the structure. The examples in the previous chapter only consider one dimensional wave propagation, where refraction of acoustic waves does not exist. In two dimensions, refraction of waves becomes relevant as the transmitted waves change their direction of propagation in the case of a change in the transmitting medium.
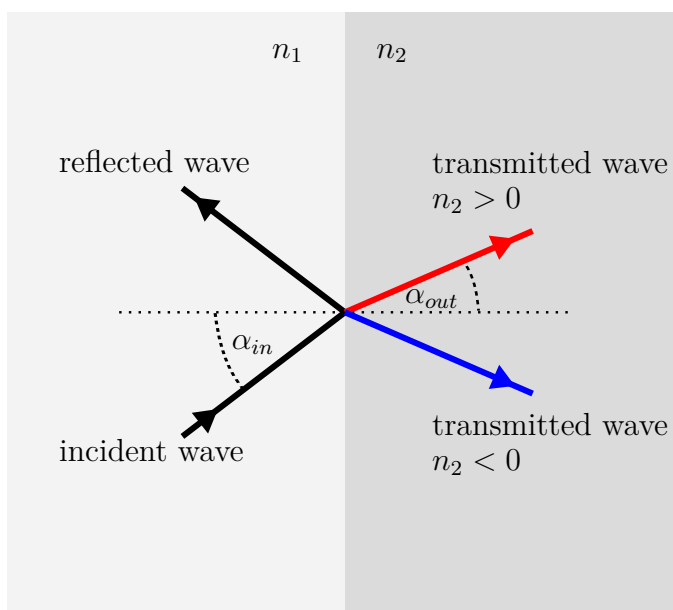
Figure 3.22: Impact of the refraction index n on transmitted waves.

According to Snell's Law, the angle of the refracted wave depends on the refraction index n_i

$$n_1 \sin(\alpha_{in}) = n_2 \sin(\alpha_{out}). \tag{3.93}$$

In general, the refraction index is positive. This limits the possible directions of the transmitted waves. In electromagnetism, Veselago [1968] shows that a material with negative dielectric constant and negative magnetic permeability has a negative refraction index for electromagnetic waves. That means the material refracts waves with an negative angle of refraction α_{out} (see figure 3.22). This unconventional behavior offers the possibility to guide waves in arbitrary directions. Pendry et al [1999] introduce a specific design of a material with negative refraction index and Shelby et al [2001] prove the existence of such a material by experiments.

The basic concept of wave guides for acoustic waves is similar to the wave guides for electro-magnetic waves. Due to analogy of the fundamentals of acoustic waves and electromagnetic waves, the material parameters influence the refraction of acoustic waves similar to the refraction of electromagnetic waves. A negative density and negative stiffness generates a negative refraction index for acoustic waves [Li and Chan 2004]. In general, it is only possible to generate such negative effective material properties in a limited frequency range. Locally resonant materials show such material behavior in the vicinity of the local resonance. Thus, there is a link between the design of wave guides and locally resonant materials.

3.3.1 State of the art

A major application of wave guides for acoustic waves is the prevention of the interference of the waves with specific objects. Such material behavior is called "acoustic cloaking". Several authors demonstrate acoustic cloaking. Cummer and Schurig [2007] show that it is possible to generate a two dimensional circular acoustic cloaking for compressional waves using a coordinate transformation. Based on this work, Huanyang and Chan [2009] demonstrate a three dimensional transformation for acoustic cloaking. Zhang [2010] experimentally verifies the two dimensional cloaking in water for frequencies from 52 to 64 kHz. Popa et al [2011] derive a two dimensional transformation that hides an object located in front of an rigid wall (ground cloaking). Experiments show an almost ideal reflection for two bell-shaped incident waves with center frequency of 1.5 and 3 kHz. Zigoneanu et al [2014] extend this concept to three dimensions. Numerical and experimental measurements reveal omnidirectional ground cloaking.

Farhat et al [2009] numerically demonstrate a circular acoustic cloak for bending waves in thin plates. Their design consists of multiple layers of different materials. Stenger et al [2012] manufacture this design and show the cloaking effect for bending waves between 200 and 400 Hz. The cloaking device is made of a combination of polyvinyl chloride (PVC) and polydimethylsiloxane (PDMS). Ruzzene and Scarpa [2003] present a two dimensional lattice structure that suppresses the propagation of bending waves in specific direction. The lattice structure consists of hour glass shaped cells arranged similar to the hexagonal cells of a honeycomb lattice. The hour class shaped cells cause a negative Poisson's ratio. The inner angles of the cells adjust the angle in which bending waves can propagate.

Besides acoustic cloaking, there also exist other examples of wave guides. Cummer et al [2008] derive a transformation that shifts a wave beam. Wei et al [2014] experimentally verify the beam shifting phenomena in air at around 2.8 to 4.6 kHz. The shifter consists of

a parallel alignment of acrylic glass. Assouar et al [2012] present a wave guide that directs bending waves in a thin plate along a specific path. The design is based on a dense periodic grid of local resonators. By removing some of the resonators, it is possible to guide the bending waves along the path of missing pillows for frequencies around 1.75 kHz. Sun and Wu [2006] demonstrate wave guiding in air at frequencies from 90 to 143 kHz and 154 to 199 kHz using rigid pillows.

Other authors use piezoelectric crystals to block bending waves in thin walled structures [Airoldi and Ruzzene 2011; Casadei et al 2009; Spadoni et al 2009a]. Airoldi and Ruzzene [2011] use periodic piezoelectric patches connected to a shunt circuit to dissipate vibrational energy. This results in tunable stop bands at frequencies of 5 kHz and 11 kHz for a cantilever beam. Casadei et al [2009]; Spadoni et al [2009a] present similar results using a two dimensional grid of periodic piezoelectric patches on an aluminum plate. Measurements demonstrates the appearance of a stop band from 1.6 kHz to 1.9 kHz [Casadei et al 2009].

There are many designs for wave guides in fluids. Most of the wave guides in solid materials only tackle one type of wave. The reason is the dependency of the shear and the bulk modulus in conventional materials. It is very difficult to find a transformation that simultaneously guides waves based on bulk and shear deformation. In many fluids, there only exist one wave type because the rotational part of the strain does not cause stresses due to the zero shear resistance. To generate similar effects in solids, pentamode material might be a solution. Milton and Cherkaev [1995] present a lattice structure that behaves as an isotropic fluid. According to Milton and Cherkaev [1995], it is possible to generate any elasticity tensor using pentamode metamaterial. A realization of such a material consists of a lattice structure of double cones [Kadic et al 2012]. Bückmann et al [2014] apply the design of Kadic et al [2012] to demonstrate the cloaking effect for structure borne noise. Spadoni et al [2014] provide a different design that also exhibit pentamode mechanical behavior. Their design consists of fluid filled cells assembled in a crystalline foam.

3.3.2 Fundamentals of wave guides

For designing metamaterials that guide acoustic waves in a prescribed manner the main idea is that a spatially varying distribution of the material properties influences the wave field of the acoustic waves. The desired acoustic wave field requires a transformation. This transformation is necessary to find the required spatial material properties. In many cases, the required material properties oppose the natural limits of positive material density and material stiffness. There exists no conventional material which has negative material properties.

Negative effective material properties of metamaterials appear due to a macroscopic point of observation while the variation of geometry and material happens on the micro scale.

Effective material parameters

The following section explains the concept of effective material parameters. Effective material parameters are derived on a macro scale where local wave scattering effects are smeared. Based on the two-DOF-oscillator, one can derive an effective negative mass.
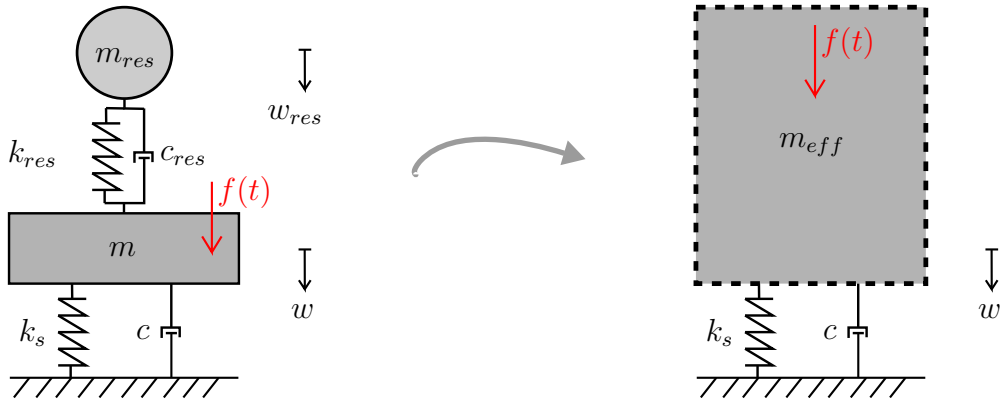
Figure 3.23: Transition from micro scale to macro scale for the two-DOF-oscillator.

Figure 3.23 shows to different observation scales of the two-DOF-oscillator. The micro scale (left) describes the model in detail. The model on the right describes the larger macro scale. The right model ignores the wave propagation between the local resonance and the main structure. The effective mass m_{eff} of the model incorporates the effects of the local resonance. The equation of motion of the model in the macro scale is

$$(k_s + i\Omega c - \Omega m_{eff})\,\underline{w}\mathrm{e}^{i\Omega t} = \underline{f}\mathrm{e}^{i\Omega t}\ . \tag{3.94}$$

Section A.2 derives the solution for $\underline{w}$ depending on the dimensionless parameters α, β, μ, D and D_{res}

$$\underline{w} = \frac{\underline{f}}{m}\frac{e + if}{g + ih}\ , \tag{3.95}$$

with

$$e = \beta^2 - \alpha^2 \, , \tag{3.96}$$

$$f = 2\alpha\beta D_{res} \, , \tag{3.97}$$

$$g = \alpha^4 - \alpha^2(1 + \beta^2 + \mu\beta^2 + 4\beta DD_{res}) + \beta^2 \, , \tag{3.98}$$

$$h = \alpha[2D(\beta^2 - \alpha^2) + 2\beta D_{res}(1 - \alpha^2 - \mu\alpha^2)] \, . \tag{3.99}$$

α, β, μ, D and D_{res} are the dimensionless parameters introduced in section 3.2.2. Assuming that the main structure is undamped ($c = 0$), the effective mass m_{eff} is

$$m_{eff} = \frac{f - k_s \underline{w}}{-\Omega^2 \underline{w}} \, . \tag{3.100}$$

Inserting the solution for $\underline{w}$ (3.95) yields

$$m_{eff} = \frac{1 - \frac{k_s}{m}\frac{e+if}{g+ih}}{-\Omega^2 \frac{1}{m}\frac{e+if}{g+ih}} \, , \tag{3.101}$$

which simplifies to

$$m_{eff} = -\frac{m}{\Omega^2}\frac{g + ih}{e + if} + \frac{m}{\alpha^2} \, . \tag{3.102}$$

Figure 3.24, shows the real part of the normalized effective mass for different mass ratios $\mu = m_{res}/m$. If there is no resonator ($\mu = 0$), the effective mass is greater than zero for all frequencies. Introducing a resonator, there is a frequency range where the effective mass is negative. The frequency range of negative effective mass depends on the target frequency of the resonator.

Similar to negative density, it is possible to generate a negative effective elastic modulus. Section 3.2.2 introduced the diatomic crystal. In the following, one considers a finite diatomic crystal, as shown in figure 3.25, from the macroscopic perspective.

The displacement u_{n+2} is fixed ($u_{n+2} = 0$). Thus, the solution of the displacements u_n and u_{n+1} for the steady state solution of a harmonic forced vibration is

$$\begin{bmatrix} -\Omega^2 + \omega_1^2 & -\omega_1^2 \\ -\omega_2^2 & -\Omega^2 + 2\omega_2^2 \end{bmatrix} \begin{bmatrix} \underline{u}_n \\ \underline{u}_{n+1} \end{bmatrix} = \begin{bmatrix} \frac{f}{m_1} \\ 0 \end{bmatrix} \, , \tag{3.103}$$
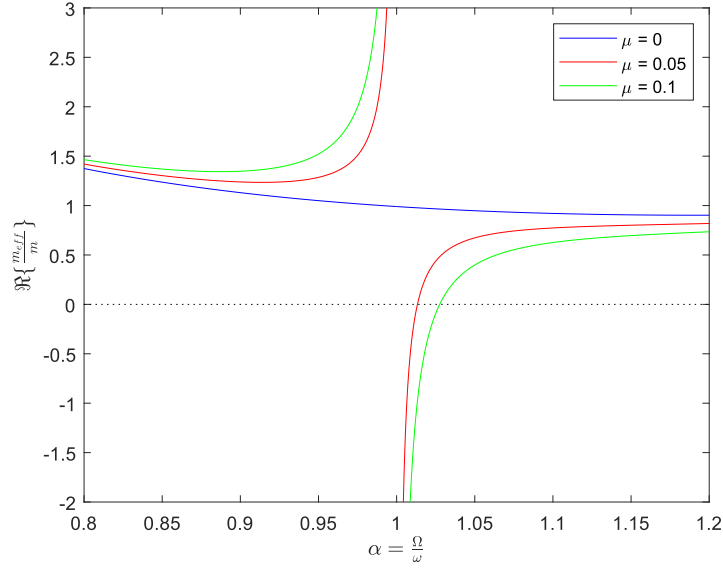
Figure 3.24: Real part of the normalized effective mass of the two-DOF-oscillator modeled with a single degree of freedom.
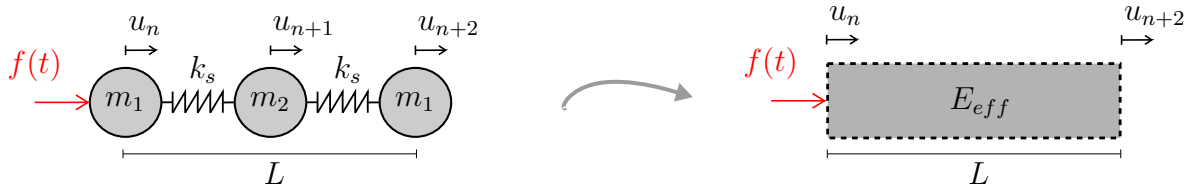
Figure 3.25: Transition from micro scale to macro scale for a finite diatomic crystal.

with $\omega_1 = \sqrt{k_s/m_1}$ and $\omega_2 = \sqrt{k_s/m_2}$. The second line of (3.103) yields the relation between the displacements $\underline{u}_n$ and $\underline{u}_{n+1}$

$$\underline{u}_{n+1} = \underline{u}_n \frac{\omega_2^2}{-\Omega^2 + 2\omega_2^2} \; . \tag{3.104}$$

Inserting this expression in the first line of (3.103) gives

$$\underline{u}_n = \frac{\underline{f}}{m_1} \frac{2\omega_2^2 - \Omega^2}{\Omega^4 - \Omega^2(\omega_1^2 + 2\omega_2^2) - \omega_1^2\omega_2^2} \; . \tag{3.105}$$

Applying Hooke's law to the macroscopic model shown in figure 3.25, it is possible to determine the effective Young's modulus E_{eff} based on the stress σ and the strain ϵ

$$E_{eff} = \frac{\sigma}{\epsilon} = \frac{\underline{f}}{A} \frac{L}{\underline{u}_n} = \frac{Lm_1}{A} \frac{\Omega^4 - \Omega^2(\omega_1^2 + 2\omega_2^2) - \omega_1^2\omega_2^2}{2\omega_2^2 - \Omega^2} \; . \tag{3.106}$$

A is the cross section of the macroscopic bounding box. L is the length of a unit cell. The frequency of the local resonance is $\omega_{res} = \sqrt{\frac{2k_s}{m_2}}$.
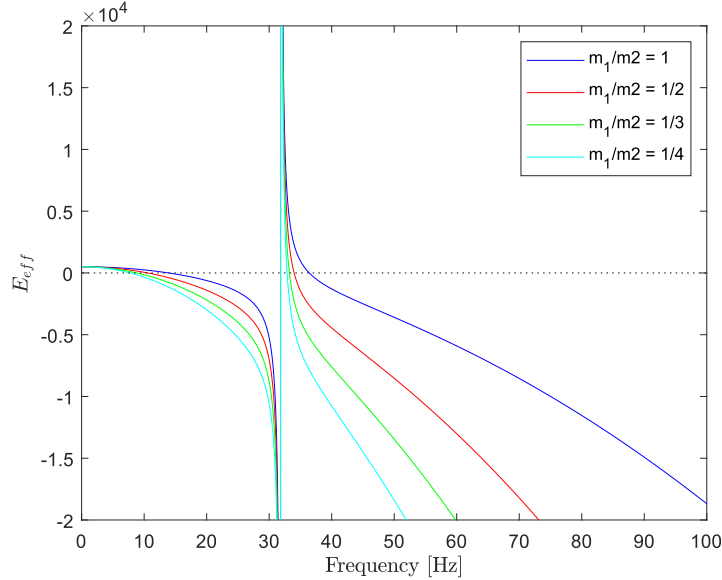
Figure 3.26: Real part of the normalized effective Young's modulus of the diatomic crystal modeled as single degree of freedom.

Figure 3.26 shows the normalized effective Young's modulus for the macroscopic model of the diatomic crystal for different ratios of m_1/m_2. There are two frequency ranges where the effective stiffness is negative. A negative stiffness occurs slightly before the local resonance. The second frequency range of negative effective stiffness appears due to the limits of the model. At higher frequencies, the mass m_1 more and more blocks the excitation.

Transformation of acoustic wave fields

Spatially designed material properties offer the possibility to design acoustic wave fields. The following paragraph introduces the transformation of an acoustic wave field using the wave equation for compressional waves. In this case, the wave equation for the acoustic pressure p summarizes the conservation of mass and momentum for time harmonic wave propagation. The equation describes the wave propagation in an Cartesian coordinate system [Craster and Guenneau 2013]

$$\nabla \rho^{-1} \nabla \underline{p} + \frac{\Omega^2}{K} \underline{p} = 0 \ . \tag{3.107}$$

∇ is the gradient in the Cartesian coordinate system. K is the bulk modulus and ρ is the density of the media. Applying a general transformation of the coordinates from x_i to $\bar{x}_i$, one defines the transformation matrix $\mathbf{T}$ as [Arens et al 2012]

$$\mathbf{T} = \begin{bmatrix} \frac{\partial \bar{x}}{\partial x} & \frac{\partial \bar{x}}{\partial y} & \frac{\partial \bar{x}}{\partial z} \\ \frac{\partial \bar{y}}{\partial x} & \frac{\partial \bar{y}}{\partial y} & \frac{\partial \bar{y}}{\partial z} \\ \frac{\partial \bar{z}}{\partial x} & \frac{\partial \bar{z}}{\partial y} & \frac{\partial \bar{z}}{\partial z} \end{bmatrix} \tag{3.108}$$
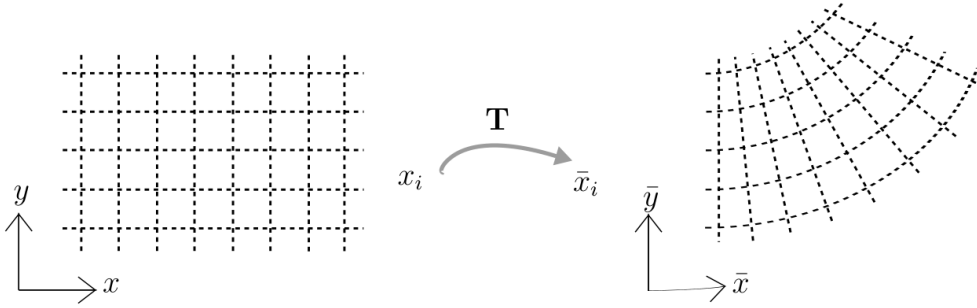
Figure 3.27: Example of a coordinate transformation.

Using the transformation $\mathbf{T}$, the pressure p can be expressed in the transformed domain

$$\underline{p} = \underline{\bar{p}}/\det(\mathbf{T}) . \tag{3.109}$$

Furthermore, the gradient in the Cartesian coordinates system can be expressed in terms of the gradient in the transformed coordinate system $\bar{x}_i$. This yields the following expressions for the respective terms in (3.107)

$$\nabla \rho^{-1} = \bar{\nabla}\mathbf{T}\rho^{-1} \tag{3.110}$$

$$\nabla \underline{p} = \mathbf{T}^T \nabla_{\bar{x}} \, \underline{\bar{p}}/\det(\mathbf{T}) . \tag{3.111}$$

Inserting the transformations (3.109), (3.110) and (3.111) into the wave equation (3.107) results in the following equation

$$\nabla_{\bar{x}} \frac{\mathbf{T}\rho^{-1}\mathbf{T}^T}{\det(\mathbf{T})} \nabla_{\bar{x}}\underline{\bar{p}} + \frac{\Omega^2}{K\det(\mathbf{T})}\underline{\bar{p}} = 0 . \tag{3.112}$$

Comparing (3.112) to (3.107), it is clear that the transformation does not change the general form of the wave equation. Instead of considering the transformation $\mathbf{T}$ as a coordinate

transformation, one can consider it as a transformation of the material parameters ρ and K

$$\bar{\rho} = \left(\frac{\mathbf{T}\rho^{-1}\mathbf{T}^{T}}{\det(\mathbf{T})} \right)^{-1} \;, \tag{3.113}$$

$$\bar{K} = K \det(\mathbf{T}) \;. \tag{3.114}$$

Applying the transformation $\mathbf{T}$ to the density ρ and the bulk modulus K, the resulting material tensors $\bar{\rho}$ and $\bar{K}$ contain the modified properties that are necessary to guide the wave along the modified direction $\bar{x}_i$ (see figure 3.28).
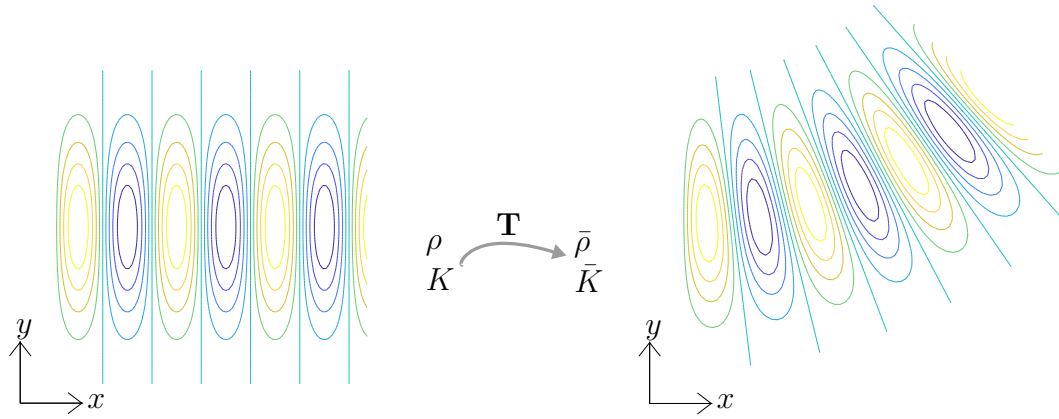
Figure 3.28: Influence of the transformation of the material properties on the acoustic field.

Solving the wave equation in the original coordinate system x_i using the transformed material properties generates the desired acoustic field

$$\nabla \bar{\rho}^{-1} \nabla \underline{p} + \frac{\Omega^2}{\bar{K}} \underline{p} = 0 \;. \tag{3.115}$$

There are various transformations for different types of wave guides (e.g. acoustic cloaking or lensing). The motion in solids is generally a superposition of multiple wave types. Neglecting body forces, the equation of motion is

$$\nabla \cdot \left(\mathbf{C}\nabla\mathbf{u} \right) = \rho\ddot{\mathbf{u}} \;. \tag{3.116}$$

$\mathbf{C}$ is the elasticity tensor, which is a fourth order tensor describing the relation between stresses σ and strains ϵ ($\boldsymbol{\sigma} = \mathbf{C} : \boldsymbol{\epsilon}$). Due to the symmetry of stresses and strains and the

derivation of the elasticity tensor based on the strain energy density U ($C_{ijkl} = \frac{\partial^2 U}{\partial \epsilon_{ij}\epsilon_{kl}} = \frac{\partial^2 U}{\partial \epsilon_{kl}\epsilon_{ij}}$), the following symmetries hold for $\mathbf{C}$

$$
\begin{aligned}
C_{ijkl} &= C_{jikl} \ , \\
C_{ijkl} &= C_{ijlk} \ , \\
C_{ijkl} &= C_{klij} \ .
\end{aligned}
\tag{3.117}
$$

For isotropic material the elasticity tensor can be expressed with the Lamé paramters

$$
C_{ijkl} = \lambda \delta_{ij}\delta_{kl} + \mu \left(\delta_{ik}\delta_{jl} + \delta_{il}\delta_{jk} \right) \ .
\tag{3.118}
$$

δ_{ij} is the Kronecker delta. Inserting the (3.118) into (3.116) results in

$$
\left(\lambda + 2\mu \right) \nabla \left(\nabla \cdot \mathbf{u} \right) - \mu \nabla \times \nabla \times \mathbf{u} = \rho \frac{\partial^2 \mathbf{u}}{\partial t^2}
\tag{3.119}
$$

Applying the Helmholtz decomposition, the displacement $\underline{\mathbf{u}}$ can be decomposed in a solenoidal and a rotation free part [Arfken and Weber 1995]

$$
\mathbf{u} = \underbrace{\nabla \psi}_{\nabla \times (\nabla \psi) = 0} + \underbrace{\nabla \times \boldsymbol{v}}_{\nabla \cdot (\nabla \times \boldsymbol{v}) = 0} \ .
\tag{3.120}
$$

ψ is a scalar potential and $\boldsymbol{v}$ a vector potential. Inserting this into (3.119) yields

$$
\left(\lambda + 2\mu \right) \nabla \left(\nabla \cdot \left(\nabla \psi \right) \right) - \mu \nabla \times \nabla \times \left(\nabla \times \boldsymbol{v} \right) = \rho \frac{\partial^2}{\partial t^2} (\nabla \psi) + \rho \frac{\partial^2}{\partial t^2} (\nabla \times \boldsymbol{v})
\tag{3.121}
$$

Using the relation $\nabla \times \nabla \times \square = \nabla\nabla \cdot \square - \Delta\square$ [Arens et al 2012] results in the following expression

$$
\frac{\lambda + 2\mu}{\rho} \nabla \left(\Delta \psi \right) - \frac{\mu}{\rho} \nabla\nabla \cdot \left(\nabla \times \boldsymbol{v} \right) + \frac{\mu}{\rho} \Delta (\nabla \times \boldsymbol{v}) = \frac{\partial^2}{\partial t^2} (\nabla \psi) + \frac{\partial^2}{\partial t^2} (\nabla \times \boldsymbol{v})
\tag{3.122}
$$

Applying $\nabla \cdot \nabla \times \square = 0$ and further simplifications yield

$$
\nabla \left(\frac{\partial^2}{\partial t^2} \psi - \frac{\lambda + 2\mu}{\rho} \Delta \psi \right) + \nabla \times \left(\frac{\partial^2}{\partial t^2} \boldsymbol{v} - \frac{\mu}{\rho} \Delta \boldsymbol{v} \right) = 0 \ .
\tag{3.123}
$$

This equation is fullfilled if each of the expression in the brackets is fulfilled.

$$\frac{\partial^2}{\partial t^2}\psi - \frac{\lambda + 2\mu}{\rho}\Delta\psi = 0 \tag{3.124}$$

$$\frac{\partial^2}{\partial t^2}\boldsymbol{v} - \frac{\mu}{\rho}\Delta\boldsymbol{v} = 0 \ . \tag{3.125}$$

The terms in front of the Laplace operator Δ are the square of the wave speed of the compressional waves (3.124) and the shear waves (3.125). Consequently, there is one wave equation for the compressional waves and three wave equations for the shear waves.

Deriving a transformation that guides different wave types in the same manner is not possible because the different waves have different propagation characteristics. Applying the coordinate transformation to the equation of motion demonstrates the issue that arises. The following derivations are extracted from Craster and Guenneau [2013] and refers to the original publications from Willis [1981], Milton et al [2006] and Norris and Shuvalov [2011]. As previously, the coordinate transformation $T_{ij} = \frac{\partial \bar{x}_i}{\partial x_j}$ yields

$$\underline{\mathbf{u}}(\mathbf{x}) = \mathbf{T}^{-1}\underline{\bar{\mathbf{u}}}(\bar{\mathbf{x}}) \ ,$$
$$\nabla = \nabla_{\bar{x}}\mathbf{T} \ , \tag{3.126}$$
$$\nabla\underline{\mathbf{u}} = \nabla(\mathbf{T}^{-1}\underline{\bar{\mathbf{u}}}) = \mathbf{T}^T \ \nabla_{\bar{x}}\underline{\bar{\mathbf{u}}}(\bar{\mathbf{x}}) \ \mathbf{T} + \nabla\mathbf{T}^{-1} \ \underline{\bar{\mathbf{u}}}(\bar{\mathbf{x}}) \ .$$

Assuming that the material properties depend on the spatial location, the equation of motion reads

$$\nabla \cdot \left(\mathbf{C}(\mathbf{x})\nabla\mathbf{u}\right) = \rho(\mathbf{x})\ddot{\mathbf{u}} \ . \tag{3.127}$$

Applying the transformations (3.126), there appear additional terms in the transformed equation of motion

$$\nabla_{\bar{x}} \cdot \left(\bar{\mathbf{C}}(\bar{\mathbf{x}})\nabla_{\bar{x}}\underline{\bar{\mathbf{u}}} + \mathbf{A}(\bar{\mathbf{x}})\underline{\bar{\mathbf{u}}}\right) + \mathbf{B}(\bar{\mathbf{x}})\nabla_{\bar{x}}\underline{\bar{\mathbf{u}}} = -\Omega^2\bar{\rho}(\bar{\mathbf{x}})\underline{\bar{\mathbf{u}}} \ . \tag{3.128}$$

The tensors $\mathbf{A}$ and $\mathbf{B}$ depend on the transformation $\mathbf{T}$, its spatial derivatives, and the elasticity tensor $\mathbf{C}$. Therefore, the equation of motion (3.116) is not invariant with respect to an arbitrary coordinate transformation. An arbitrary transformation matrix $\mathbf{T}$ does not necessarily conserve the form of the original equation. Further restriction emerge, if the

transformed elasticity tensor $\bar{\mathbf{C}}$ needs to satisfy the same symmetries as the original elasticity tensor $\mathbf{C}$.

4 Modeling aspects

In this chapter, the author addresses specific modeling aspects that form the basis for modeling locally resonant materials and periodic structures. The first section covers the modeling of local resonances. Besides different models of beam-like resonators, it also explains the modeling of beam-like resonators as discrete resonators and how the dynamic behavior is integrated in the host structure. The second section introduces the Wave Finite Element Method (WFEM) for modeling periodic structures. After the introduction of various formulations of the WFEM, it follows a comparison of the different methods.

4.1 Modeling of resonators

In practical applications, beam-like resonators are widely used [Claeys et al 2016b; Egashira et al 2016; Van Belle et al 2019]. The general design of such a resonator consists of a beam segment connected to an end mass. The following sections focus on the modeling of such beam-like resonators.

4.1.1 Models of beam-like resonators

There exist different models that derive the dependency between the geometry and the dynamic behavior of the resonator. The following paragraph describes four different models. The resonator consists of a beam-like structure that is connected to the host structure.
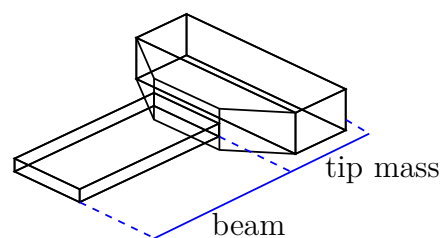
Figure 4.1: Example geometry of a beam-like resonator.

The target frequency of the local resonance determines the eigenfrequency of the beam-like resonator. In general, the host structure behaves much stiffer than the resonator. Therefore, one derives the eigenfrequency of the resonator assuming it is clamped at one side.

3D FE-Model: Using three dimensional finite elements, it is possible to achieve an accurate representation of the geometry.
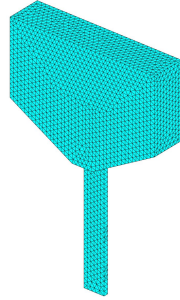
Figure 4.2: Three dimensional finite element model of a resonator.

Depending on the element formulation, such a representation also considers multidimensional deformation patterns. However, the modeling and computational effort is higher compared to other methods. There exist simplified models for such beam-like structures. Nevertheless, such simplification can result in strong deviations.

Beam with concentrated mass: A very simple model for a beam-like resonator consists of an Euler-Bernoulli beam with a concentrated end mass. For the first eigenfrequency, there exist approximated solutions in literature. These approximation neglect the rotational inertia of the end mass and approximate the inertia of the beam [Blevins 2016]

$$f_1 = \frac{1}{2\pi}\sqrt{\frac{3EI}{L^3(m_{tip} + 0.24\rho AL)}} \quad . \quad (4.1)$$
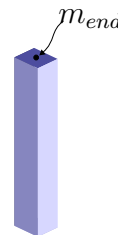
E and ρ denote the Young's modulus and the density of the material. The variables A and I name the cross sectional area and the respective second moment of area. The weight of the concentrated mass is m_{tip}.

Beam with concentrated mass and additional rotational inertia   Including the mass moment of inertia of the tip mass I_{tip} results in a more accurate representation. The first resonance frequency is

$$f_1 = \frac{\lambda_1^2}{2\pi L^2}\sqrt{\frac{EI}{\rho A}} \ . \qquad (4.2)$$
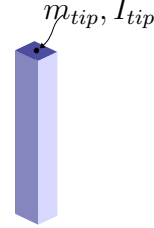
The corresponding λ_1 results from the smallest solution of the equation [Erturk and Inman 2011]

$$1 + \cos\lambda\cosh\lambda + \lambda\frac{m_{tip}}{m_{beam}}(\cos\lambda\sinh\lambda - \sin\lambda\cosh\lambda)$$

$$-\lambda^3\frac{I_{tip}}{m_{beam}L^2}(\cosh\lambda\sin\lambda + \sinh\lambda\cos\lambda) + \lambda^4\frac{m_{tip}I_{tip}}{m_{beam}^2L^2}(1 - \cos\lambda\cosh\lambda) = 0 \ . \qquad (4.3)$$

Coupled beam finite elements: One could also model the tip mass using several coupled beam elements.
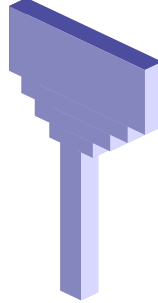
Figure 4.3: Coupled Euler-Bernoulli beams with different cross sections.

The motion of the beam is approximated using Hermite polynomials [Zienkiewicz and Taylor 2005]

$$\underline{w}(\xi) = \underline{w}_1\frac{1}{4}(2 - 3\xi + \xi^3) + \underline{w}_2\frac{1}{4}(2 + 3\xi - \xi^3) \ . \qquad (4.4)$$

ξ is the element coordinate. Based on the polynomials, the element stiffness and mass matrix

can be generated

$$\boldsymbol{K}_{ele} = \frac{EI}{L_{ele}^3} \begin{bmatrix} 12 & 6L_{ele} & -12 & 6L_{ele} \\ 6L_{ele} & 4L_{ele}^2 & -6L_{ele} & 2L_{ele}^2 \\ -12 & -6L_{ele} & 12 & -6L_{ele} \\ 6L_{ele} & 2L_{ele}^2 & -6L_{ele} & 4L_{ele}^2 \end{bmatrix}, \tag{4.5}$$

$$\boldsymbol{M}_{ele} = \frac{\rho A_{ele} L_{ele}}{420} \begin{bmatrix} 156 & 22L_{ele} & 54 & -13L_{ele} \\ 22L_{ele} & 4L_{ele}^2 & 13L_{ele} & -3L_{ele}^2 \\ 54 & 13L_{ele} & 156 & -22L_{ele} \\ -13L_{ele} & -3L_{ele}^2 & -22L_{ele} & 4L_{ele}^2 \end{bmatrix}. \tag{4.6}$$

The coupling of several beam elements with different cross sections results in a more accurate representation of the mass distribution along the beam axis and allows the deformation of the end mass. Nevertheless, it makes several assumptions about the deformation as it only considers pure bending deformation in a single direction and neglects shear and torsional modes as well as rotational inertia. In general, the beam elements should be significantly slender, which means that the length should be larger than the width and the height. However, for the derivation of the first eigenfrequency. The coupled beam model with beam elements shorter than the respective dimensions of the cross section also generates accurate results. The reason is that the bending wavelength that occurs at the first eigenfrequency is larger compared to the dimension of the cross sections. This ensures that the motion in of the beam is dominated by bending.

Coupled spectral elements: Similar to coupling multiple finite beam elements, it is also possible to couple spectral beam elements. The element formulation of spectral beam elements is based on the analytic solution of the Euler-Bernoulli beam theory [Kausel 2017]

$$\underline{w}(\xi) = C_1 \cos(k\xi) + C_2 \sin(k\xi) + C_3 \cosh(k\xi) + C_4 \sinh(k\xi) \quad \text{with} \quad k^4 = \Omega^2 \frac{\rho A_{ele}}{EI_{ele}} \tag{4.7}$$

ξ is the element coordinate. Deriving the shear and bending moment, it is possible to couple the different beams segments [Stanton and Mann 2010]. The computation of the first eigenfrequency is more complex than using finite elements, because the eigenvalue problem should be solved analytically. Using coupled spectral beam elements to represent the

geometry accurately results in higher computational effort than using coupled finite beam elements.

Table 4.1 shows the first eigenfrequencies for different beam-like resonators using different models. Appendix A.4 lists the geometry parameters of the different designs.

Design	3D FE-model	1st eigenfrequency		
		Beam with end mass	Beam with end mass and rotational inertia	Coupled beams
1	59.6 Hz	85.0 Hz	70.5 Hz	59.5 Hz
2	72.6 Hz	72.7 Hz	110.0 Hz	85.3 Hz
3	95.8 Hz	160.0 Hz	109.3 Hz	95.6 Hz
4	98.0 Hz	160.0 Hz	112.7 Hz	97.9 Hz
5	99.2 Hz	160.0 Hz	114.2 Hz	98.9 Hz
6	141.8 Hz	263.4 Hz	154.9 Hz	141.3 Hz
7	169.5 Hz	295.7 Hz	193.3 Hz	169.1 Hz
8	183.4 Hz	331.9 Hz	206.4 Hz	182.9 Hz
9	190.7 Hz	351.6 Hz	213.0 Hz	190.2 Hz
10	217.2 Hz	394.7 Hz	245.7 Hz	216.5 Hz
11	251.3 Hz	443.0 Hz	290.9 Hz	250.5 Hz
12	271.6 Hz	497.3 Hz	310.6 Hz	270.9 Hz
13	318.9 Hz	526.8 Hz	376.4 Hz	318.4 Hz
14	449.1 Hz	770.0 Hz	472.3 Hz	446.5 Hz
15	1412.8 Hz	1540.0 Hz	1515.9 Hz	1340.0 Hz

Table 4.1: Comparison of the first eigenfrequency.

Comparing the results of the different models, one can see that the coupled beam model and the three dimensional FE-model show similar results. The relative deviation is less than 1 %, except for design 15. That means that the first mode of the presented designs is obviously a pure bending mode and the modeling with Euler-Bernoulli beams with relatively short beam length is able to capture the deformation.

In contrast, the model with the concentrated end mass is not able to estimate the first eigenfrequency with an acceptable accuracy for the here presented designs. Including the rotational inertia of the tip mass improves the accuracy. However, the deviations to the other models are still relatively high. There are two reasons for the strong deviation: Depending on the design of the tip mass, suppressing the deformation of the tip mass can result in an overestimation of the stiffness of the beam-like resonator. Furthermore, the center of mass of the tip mass is not located at the end of the beam. Consequently, the inertia term of the concentrated tip mass m_{tip} does not only depend on the displacement at

the end of the beam segment but also on the rotation and the lever arm to the center of mass.

$$\ddot{w}m_{tip} = \left(\ddot{w}_{beam}(x = L) + \ddot{\phi}_{beam}(x = L)l_c \right) m_{tip} \qquad (4.8)$$
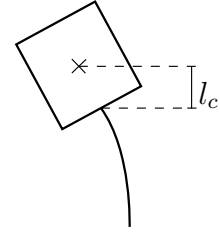
As shown in table 4.1, using the mass moment of inertia around the center of gravity of the tip mass results in significant deviations. Therefore, correct estimation of the eigenfrequency requires the computation of the mass moment of inertia applying Steiner's theorem.

4.1.2 Modeling beam-like resonators as discrete oscillators

In general, it is efficient to model a resonator as a discrete oscillators with a single degree of freedom. The reason is that in many applications the resonator is tuned to a desired target frequency. The following derivation shows how a beam-like resonator is linked to a discrete oscillator. Therefore, the author shows the effect of a single mode of the beam-like resonator on the host structure. Due to simplicity, the host structure is a simple discrete mass-spring system.
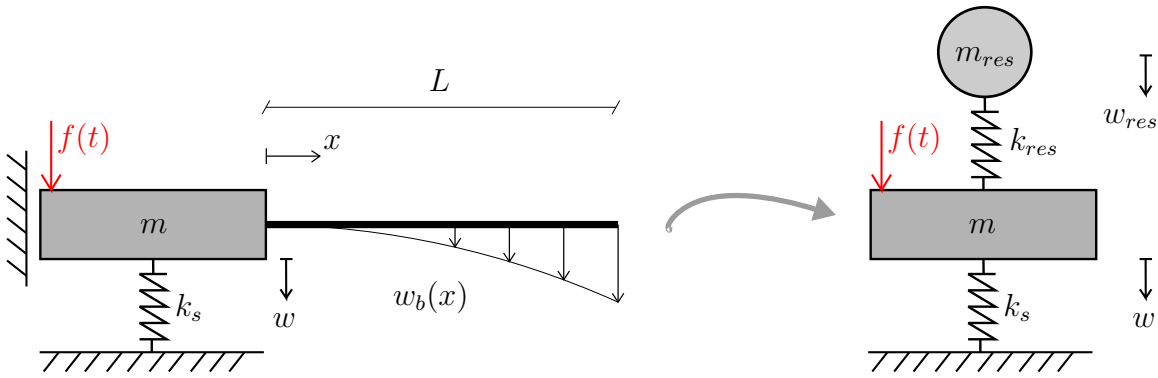
Figure 4.4: Translation of the beam-like resonator to a discrete mass-spring system.

The general equation for the Euler-Bernoulli beam describes the relative motion w_b of the beam

$$\frac{\partial^4}{\partial x^4} w_b - \frac{\Omega^2 \rho A}{EI} w_b = 0 \ . \qquad (4.9)$$

The solution of the equation is a superposition of sine, cosine, hyperbolic sine, and hyperbolic

cosine [Petersen 1996]

$$\underline{w}_b(x) = C_1 \cosh \frac{\lambda}{L}x + C_2 \sinh \frac{\lambda}{L}x + C_3 \cos \frac{\lambda}{L}x + C_4 \sin \frac{\lambda}{L}x \ . \tag{4.10}$$

The parameter λ depends on the material, the geometry of the beam and the frequency of excitation

$$\lambda = L \left(\frac{\Omega^2 \rho A}{EI} \right)^{1/4} \ . \tag{4.11}$$

The boundary conditions at $x = 0$ and $x = L$ determine the constants C_i. The relative motion of the beam is described by the superposition of the modes of the clamped beam, w_b reads

$$\underline{w}_b(x) = \sum_{j=1}^{\infty} \underline{w}_{0,j} \left(\sin \frac{\lambda_j}{L}x - \sinh \frac{\lambda_j}{L}x + Y_j \left(\cosh \frac{\lambda_j}{L}x - \cos \frac{\lambda_j}{L}x \right) \right) \ , \tag{4.12}$$

where the factor Y_j is determined using

$$Y_j = \frac{\sinh \lambda_j + \sin \lambda_j}{\cosh \lambda_j + \cos \lambda_j} \ . \tag{4.13}$$

There exists infinite mode shapes in which the beam oscillates. The corresponding eigenvalues λ_j for these shapes are given by

$$\cosh(\lambda_j) \cos(\lambda_j) + 1 = 0 \ . \tag{4.14}$$

Table 4.2 lists the solutions.

j	λ_j
1	1.87510407
2	4.69409113
3	7.85475744
4	10.99554073
5	14.13716839
j>5	$\approx$(j-1/2)π

Table 4.2: Solutions for λ that satisfy (4.14); extracted from [Blevins 2016].

Inserting the different solutions for λ_j in (4.11) yields the corresponding eigenfrequencies ω_j. The following derivation focuses on the solution of one single mode λ_j

$$\underline{w}_b(x) = \underline{w}_{j,0} \underbrace{\left(\sin\frac{\lambda_j}{L}x - \sinh\frac{\lambda_j}{L}x + Y_j \left(\cosh\frac{\lambda_j}{L}x - \cos\frac{\lambda_j}{L}x \right) \right)}_{\Phi_j} . \tag{4.15}$$

The generalized quantities for an Euler-Bernoulli beam excited by the base excitation w_{base} are [Müller 2019b]

$$m_j = \rho A \int_0^L \Phi_j^2 dx , \tag{4.16}$$

$$k_j = EI \int_0^L \Phi_j''^2 dx = EI\frac{\lambda_j^4}{L^4} \int_0^L \tilde{\Phi}_j^2 dx , \tag{4.17}$$

$$\text{with} \quad \tilde{\Phi}_j = -\sin\frac{\lambda_j}{L}x - \sinh\frac{\lambda_j}{L}x + Y_j \left(\cosh\frac{\lambda_j}{L}x + \cos\frac{\lambda_j}{L}x \right) \tag{4.18}$$

$$p_j = \int_0^L p(x)\Phi_j dx = \Omega^2 \rho A \int_0^L \Phi_j dx\, w_{base} . \tag{4.19}$$

This reveals the equation of motion for the relative motion of the beam excited by the movement $w = w_{base}$ of the mass m

$$\left(-\Omega \rho A \int_0^L \Phi_j^2 dx + EI\frac{\lambda_j^4}{L^4} \int_0^L \tilde{\Phi}_j^2 dx \right) \underline{w}_{j,0} - \Omega^2 \rho A \int_0^L \Phi_j dx\, \underline{w} = 0 . \tag{4.20}$$

A division by $\rho A \int_0^L \Phi_j^2(x)dx$ yields

$$\left(-\Omega + \frac{EI}{\rho A}\frac{\lambda_j^4}{L^4} \underbrace{\frac{\int_0^L \tilde{\Phi}_j^2 dx}{\int_0^L \Phi_j^2 dx}}_{=1} \right) \underline{w}_{j,0} - \Omega^2 \underbrace{\frac{\int_0^L \Phi_j dx}{\int_0^L \Phi_j^2 dx}}_{\gamma_j} \underline{w} = 0 . \tag{4.21}$$

The values γ_j are independent of the length of the beam L and decrease with increasing j

Inserting the link between λ_j and the first eigenfrequency of the beam $\omega_{j,beam}^2 = \frac{\lambda_j^4}{L^4}\frac{EI}{\rho A}$ results in

$$\left(-\Omega + \omega_{j,beam}^2 \right) \underline{w}_{j,0} - \Omega^2 \gamma_j\, \underline{w} = 0 . \tag{4.22}$$

j	γ_j
1	0.57479073
2	0.44194953
3	0.25422799
4	0.18190413
5	0.14147049
6	0.11574906
7	0.09794150
⋮	⋮

Table 4.3: Values of γ_j for the different modes.

In the following, one divides by the square of the eigenfrequency of the main structure ω^2 and introduces the dimensionless frequency ratios $\alpha = \frac{\Omega}{\omega}$ and $\beta_j = \frac{\omega_{j,beam}}{\omega}$

$$\left(\beta_j^2 - \alpha^2\right) \underline{w}_{j,0} - \alpha^2 \gamma_j \, \underline{w} = 0 \ . \tag{4.23}$$

Now the derivation of the motion w of the mass m follows.
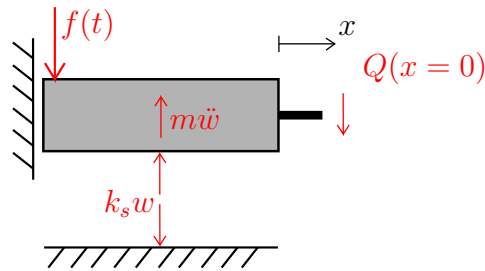
Figure 4.5: Visualization of the forces acting on the structure and the resonator.

The force equilibrium from figure 4.5 yields

$$\left(-\Omega^2 m + k_s\right) \underline{w} - \underline{Q}(x = 0) = \underline{f} \ . \tag{4.24}$$

The shear force in the beam is related to the third derivative of the displacement with respect to the spatial coordinate and the bending stiffness $Q(x) = -EI\frac{\partial^3}{\partial x^3}w_b$. The relative motion of the beam w_b is defined by (4.12). Thus, the shear force at the connecting point with the

beam is

$$
\begin{aligned}
\underline{Q}(x=0) &= \sum_{k=1}^{\infty} -EI\underline{w}_{k,0}\frac{\lambda_k^3}{L^3}\left[-\cos\frac{\lambda_k}{L}x - \cosh\frac{\lambda_k}{L}x + Y_k\left(\sinh\frac{\lambda_k}{L}x - \sin\frac{\lambda_k}{L}x\right)\right]_{x=0} \\
&= \frac{2EI}{L^3}\sum_{k=1}^{\infty}\lambda_k^3\underline{w}_{k,0} \; .
\end{aligned}
\tag{4.25}
$$

Inserting the link between λ and the eigenfrequency of the beam (4.11), the shear force at the connecting point results in

$$
\underline{Q}(x=0) = \frac{2EI}{L^3}\sum_{k=1}^{\infty}\lambda_k^3\underline{w}_{k,0} = 2\rho AL\sum_{k=1}^{\infty}\frac{\omega_{k,beam}^2\underline{w}_{k,0}}{\lambda_k} \; .
\tag{4.26}
$$

Inserting (4.26) in (4.24) and dividing it by the mass of the host structure m results in

$$
\left(-\Omega^2 + \frac{k_s}{m}\right)\underline{w} - 2\frac{\rho AL}{m}\sum_{k=1}^{\infty}\frac{\omega_{k,beam}^2\underline{w}_{k,0}}{\lambda_k} = \frac{\underline{f}}{m}
\tag{4.27}
$$

As previously, the division by the square of the eigenfrequency of the main structure ω^2 offers the possibility to introduce the dimensionless frequency ratios $\alpha = \frac{\Omega}{\omega}$ and $\beta_k = \frac{\omega_{k,beam}}{\omega}$

$$
\left(1 - \alpha^2\right)\underline{w} - 2\frac{\rho AL}{m}\sum_{k=1}^{\infty}\frac{\beta_k^2\underline{w}_{k,0}}{\lambda_k} = \frac{\underline{f}}{k_s} \; .
\tag{4.28}
$$

Consequently, the following two equations describe the motion of the host structure and the beam-like resonator

$$
\left(1 - \alpha^2\right)\underline{w} - 2\frac{\rho AL}{m}\sum_{k=1}^{\infty}\frac{\beta_k^2\underline{w}_{k,0}}{\lambda_k} = \frac{\underline{f}}{k} \; ,
\tag{4.29}
$$

$$
\left(\beta_j^2 - \alpha^2\right)\underline{w}_{j,0} - \alpha^2\gamma_j\,\underline{w} = 0 \; .
\tag{4.30}
$$

Reformulating (4.30) yields

$$
\underline{w}_{j,0} = \frac{\alpha^2\gamma_j}{\beta_j^2 - \alpha^2}\underline{w} \; .
\tag{4.31}
$$

Inserting (4.31) in (4.29) results in

$$\left(1 - \alpha^2\right)\underline{w} - 2\frac{\rho A L}{m} \sum_{k=1}^{\infty} \frac{\beta_k^2}{\lambda_k} \frac{\alpha^2 \gamma_k}{\beta_k^2 - \alpha^2} \underline{w} = \frac{\underline{f}}{k_s} \; . \tag{4.32}$$

Finally, one solves for the displacement of the host structure $\underline{w}$

$$\underline{w} = \frac{\underline{f}}{k_s} \frac{1}{\left(1 - \alpha^2\right) - 2\frac{\rho A L}{m} \sum_{k=1}^{\infty} \frac{\beta_k^2}{\lambda_k} \frac{\alpha^2 \gamma_k}{\beta_k^2 - \alpha^2}} \; . \tag{4.33}$$

Plugging in (4.33) in (4.31) solves for the unknown beam deflection $\underline{w}_{j,0}$

$$\underline{w}_{j,0} = \frac{\underline{f}}{k_s} \frac{\alpha^2 \gamma_j}{\beta_j^2 - \alpha^2} \frac{1}{\left(1 - \alpha^2\right) - 2\frac{\rho A L}{m} \sum_{k=1}^{\infty} \frac{\beta_k^2}{\lambda_k} \frac{\alpha^2 \gamma_k}{\beta_k^2 - \alpha^2}} \; . \tag{4.34}$$

Similarly to the derivations in section 3.2.2, one can establish the amplification functions for the host structure and the relative motion of the beam. Therefore, the absolute value of the displacement is normalized by the static deflection $w_{stat} = \frac{|f|}{k_s}$

$$V = \frac{|\underline{w}|}{w_{stat}} = \sqrt{\frac{1}{\left(\left(1 - \alpha^2\right) - 2\frac{\rho A L}{m} \sum_{k=1}^{\infty} \frac{\beta_k^2}{\lambda_k} \frac{\alpha^2 \gamma_k}{\beta_k^2 - \alpha^2}\right)^2}} \; , \tag{4.35}$$

$$V_{j,0} = \frac{|\underline{w}_{j,0}|}{w_{stat}} = \sqrt{\frac{\alpha^4 \gamma_j^2}{\left(\left(1 - \alpha^2\right) - 2\frac{\rho A L}{m} \sum_{k=1}^{\infty} \frac{\beta_k^2}{\lambda_k} \frac{\alpha^2 \gamma_k}{\beta_k^2 - \alpha^2}\right)^2}} \; . \tag{4.36}$$

Figure 4.6 shows the amplification functions of the main structure for different summation terms. The first eigenfrequency of the beam is tuned to the resonance frequency of the host structure ($\beta_1 = 1$). The summation is carried out including the first five terms. One can see that including the terms for $k \neq 1$ does not strongly affect the amplification function in the frequency range around β_1. Therefore, the summation term can be simplified The effect of the summation ($\frac{\alpha^2}{1 - \alpha^2/\beta_k^2}$) depends on the tuning ratio of the resonator β_k and the excitation frequency ratio α. The term tends to infinity when the excitation frequency matches the resonance frequencies of the beam. Thus, the effect of a single mode k is limited to a specific frequency (see figure 4.7).
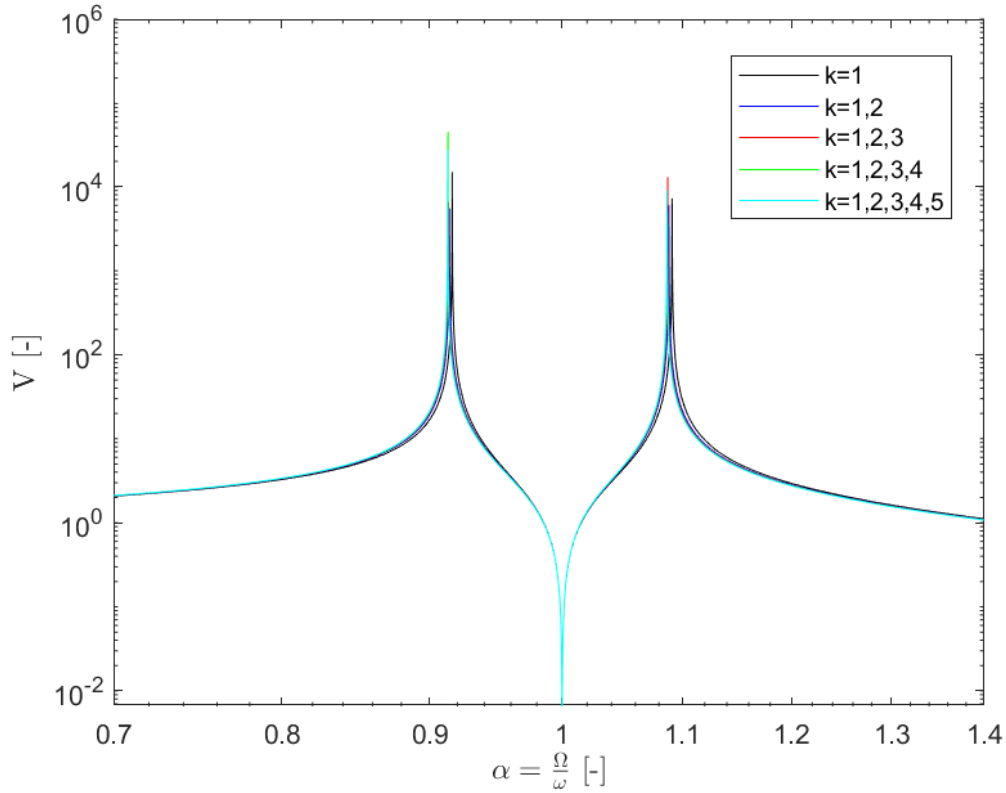
Figure 4.6: Influence of the different modes.

Around a resonance frequency of the beam ($\alpha \approx \beta_j$), a single term dominates the summation. Therefore, it is possible to simplify the summation in that frequency range

$$\sum_{k=1}^{\infty} \frac{\gamma_k}{\lambda_k} \frac{\beta_k^2 \alpha^2}{\beta_k^2 - \alpha^2} \approx \frac{\gamma_j}{\lambda_j} \frac{\beta_j^2 \alpha^2}{\beta_j^2 - \alpha^2} \; . \tag{4.37}$$

This simplification is possible because in beam structures the modes are well separated. Using this it is possible to approximate the displacement for frequencies around the target frequency of the resonator

$$\underline{w} \approx \frac{f}{k_s} \frac{1}{(1 - \alpha^2) - 2\frac{\rho A L}{m} \frac{\beta_j^2}{\lambda_j} \frac{\alpha^2 \gamma_j}{\beta_j^2 - \alpha^2}} = \frac{f}{k_s} \frac{\beta_j^2 - \alpha^2}{(1 - \alpha^2)\left(\beta_j^2 - \alpha^2\right) - 2\frac{\rho A L}{m} \frac{\gamma_j}{\lambda_j} \beta_j^2 \alpha^2} \; , \tag{4.38}$$

$$\underline{w}_{j,0} \approx \frac{f}{k_s} \frac{\alpha^2 \gamma_j}{\beta_j^2 - \alpha^2} \frac{1}{(1 - \alpha^2) - 2\frac{\rho A L}{m} \frac{\gamma_j}{\lambda_j} \beta_j^2 \alpha^2} = \frac{f}{k_s} \frac{\alpha^2 \gamma_j}{(1 - \alpha^2)\left(\beta_j^2 - \alpha^2\right) - 2\frac{\rho A L}{m} \frac{\gamma_j}{\lambda_j} \beta_j^2 \alpha^2} \; . \tag{4.39}$$
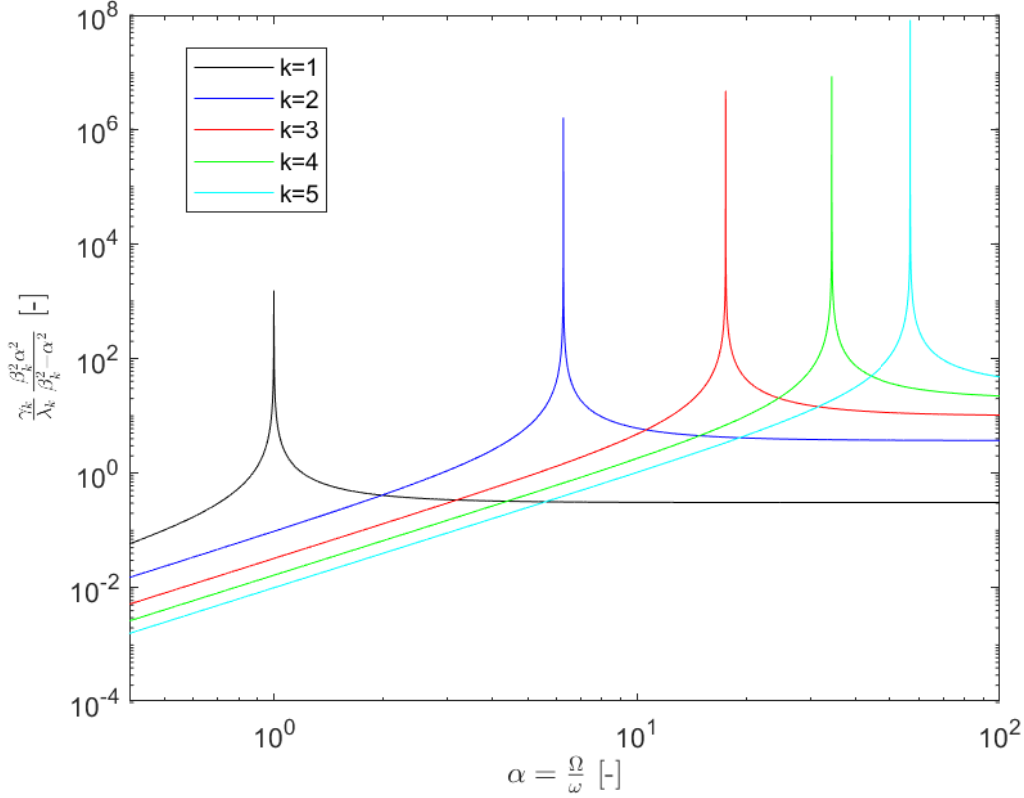
Figure 4.7: Influence of the first five terms of equation (4.37).

The corresponding amplification functions are

$$V \approx \sqrt{\frac{\left(\beta_j^2 - \alpha^2\right)^2}{\left(\left(1 - \alpha^2\right)\left(\beta_j^2 - \alpha^2\right) - 2\frac{\rho AL}{m}\frac{\gamma_j}{\lambda_j}\beta_j^2\alpha^2\right)^2}} \ , \tag{4.40}$$

$$V_{j,0} \approx \sqrt{\frac{\alpha^4\gamma_j^2}{\left(\left(1 - \alpha^2\right)\left(\beta_j^2 - \alpha^2\right) - 2\frac{\rho AL}{m}\frac{\gamma_j}{\lambda_j}\beta_j^2\alpha^2\right)^2}} \ . \tag{4.41}$$

The solution is analogous to the solution of the undamped two-DOF-oscillator in (3.52) and (3.53)

$$V = \sqrt{\frac{\left(\beta_{SDOF}^2 - \alpha^2\right)^2}{\left(\left(1 - \alpha^2\right)\left(\beta_{SDOF}^2 - \alpha^2\right) - \mu\beta_{SDOF}^2\alpha^2\right)^2}} \ , \tag{4.42}$$

$$V_{rel} = \sqrt{\frac{\alpha^4}{\left(\left(1 - \alpha^2\right)\left(\beta_{SDOF}^2 - \alpha^2\right) - \mu_{SDOF}\beta_{SDOF}^2\alpha^2\right)^2}} \ , \tag{4.43}$$

and reveals the link between the beam-like resonator and the discrete mass-spring resonator.

First, the mass ratio and the frequency tuning of the discrete resonator needs to be adjusted to generate the same amplification function for the main structure

$$\mu_{SDOF} = 2\frac{\gamma_j}{\lambda_j}\frac{\rho AL}{m} = \frac{2}{\lambda_j}\frac{\int_0^L \Phi_j dx}{\int_0^L \Phi_j^2 dx}\frac{\rho AL}{m} \ , \tag{4.44}$$

$$\beta_{SDOF} = \beta_j \ . \tag{4.45}$$

Second, γ_j additionally scales the amplification function of the relative motion

$$V_{j,0} = \gamma_j V_{rel} = \frac{\int_0^L \Phi_j dx}{\int_0^L \Phi_j^2 dx}V_{rel} \ . \tag{4.46}$$

The term in front of the mass ratio $\frac{2}{\lambda_j}\frac{\int_0^L \Phi_j dx}{\int_0^L \tilde{\Phi}_j^2 dx}$ scales the over all mass of the resonator according to the mode in which the beam-like resonator vibrates. Summing up all the contribution of all modes yields the equivalent mass of the resonator.

$$\sum_{j=1}^{\infty} \frac{2}{\lambda_j}\frac{\int_0^L \Phi_j dx}{\int_0^L \tilde{\Phi}_j^2(x)dx} = 1$$
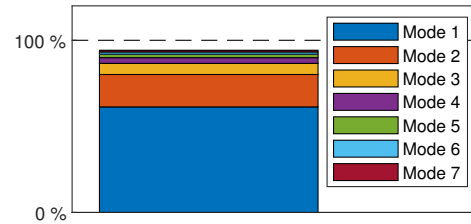
The contribution of higher modes decreases with increasing mode number. Therefore, the first mode of the resonator has the largest influence on the dynamics of the host structure.

In many cases, beam-like resonators consist of a beam with a tip mass m_{tip}. The first mode shape of such resonators are similar to the first mode shape of a beam without tip mass, whereas the eigenfrequencies differ consciously.
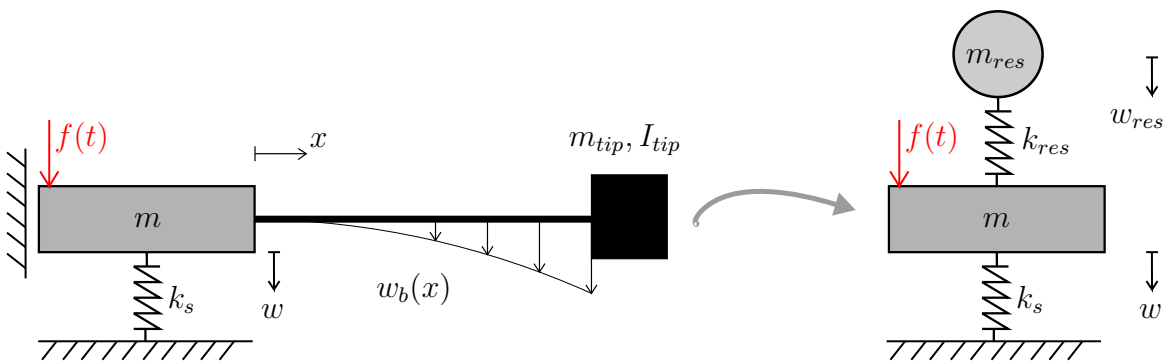
Figure 4.8: Translation of the beam-like resonator with tip mass to a discrete mass-spring system.

According to Erturk and Inman [2011], the mode shapes of a cantilever beam with tip mass are

$$\Phi_r = \cos\frac{\lambda_r}{L}x - \cosh\frac{\lambda_r}{L}x + Y_r\left(\sin\frac{\lambda_r}{L}x - \sinh\frac{\lambda_r}{L}x\right) \ , \tag{4.47}$$

with

$$Y_r = \frac{\sin\lambda_r - \sinh\lambda_r + \lambda_r\frac{m_{tip}}{m_{beam}}(\cos\lambda_r - \cosh\lambda_r)}{\cos\lambda_r + \cosh\lambda_r - \lambda_r\frac{m_{tip}}{m_{beam}}(\sin\lambda_r - \sinh\lambda_r)} \ . \tag{4.48}$$

The corresponding λ_r results from the solution of the equation

$$1 + \cos\lambda\cosh\lambda + \lambda\frac{m_{tip}}{m_{beam}}(\cos\lambda\sinh\lambda - \sin\lambda\cosh\lambda)$$

$$-\lambda^3\frac{I_{tip}}{m_{beam}L^2}(\cosh\lambda\sin\lambda + \sinh\lambda\cos\lambda) + \lambda^4\frac{m_{tip}I_{tip}}{m_{beam}^2L^2}(1 - \cos\lambda\cosh\lambda) = 0 \ , \tag{4.49}$$

where I_{tip} is the mass moment of inertia of the tip mass at $x = L$. As mentioned in section 4.1.1, I_{tip} should be computed using Steiner's theorem to accurately capture the eigenfrequencies. Figure 4.9 shows the influence of the tip mass and the mass moment of inertia on the mode shapes of the beam.
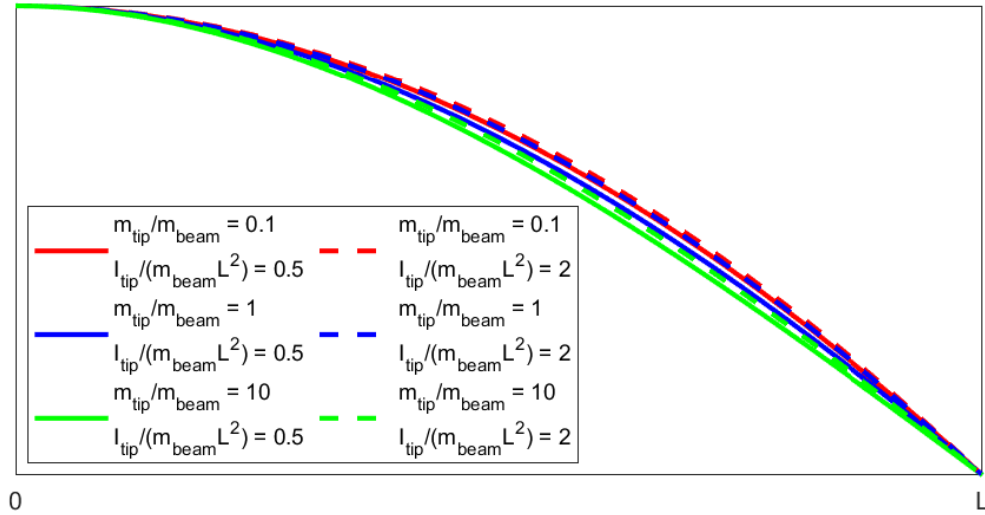
Figure 4.9: Influence of the tip mass and the mass moment of inertia on the mode shapes for a clamped beam with additional tip mass.

The derivation of the motion of the beam resonator with tip mass follows the same scope as the beam resonator without tip mass. Appendix A.5 illustrates a detailed derivation. The

motion of the main structure $\underline{w}$ and the beam mode $\underline{w}_{r,0}$ are

$$\underline{w} \approx \frac{\underline{f}}{k_s} \frac{\beta_r^2 \xi_{3,r} - \alpha^2 (1 + \zeta \xi_{1,r} + \tau \xi_{2,r})}{(1 - \alpha^2)(\beta_r^2 \xi_{3,r} - \alpha^2(1 + \zeta \xi_{1,r} + \tau \xi_{2,r})) - 2\frac{\mu}{1+\zeta}\frac{Y_r}{\lambda_r}\beta_r^2 \alpha^2 (\xi_{4,r} + \zeta \xi_{5,r})} \, ,$$

$$\underline{w}_{r,0} \approx \frac{\underline{f}}{k_s} \frac{\alpha^2 (\xi_{4,r} + \zeta \xi_{5,r})}{(1 - \alpha^2)(\beta_r^2 \xi_{3,r} - \alpha^2(1 + \zeta \xi_{1,r} + \tau \xi_{2,r})) - 2\frac{\mu}{1+\zeta}\frac{Y_r}{\lambda_r}\beta_r^2 \alpha^2 (\xi_{4,r} + \zeta \xi_{5,r})} \, . \tag{4.50}$$

The respective amplification functions are

$$V \approx \sqrt{\frac{(\beta_r^2 \xi_3 - \alpha^2(1 + \zeta \xi_{1,r} + \tau \xi_{2,r}))^2}{\left((1 - \alpha^2)(\beta_r^2 \xi_{3,r} - \alpha^2(1 + \zeta \xi_{1,r} + \tau \xi_{2,r})) - \frac{2Y_r}{\lambda_r}\frac{\mu}{1+\zeta}\beta_r^2 \alpha^2 (\xi_{4,r} + \zeta \xi_{5,r})\right)^2}} \, ,$$

$$V_{r,0} \approx \sqrt{\frac{\alpha^4 (\xi_{4,r} + \zeta \xi_{5,r})^2}{\left((1 - \alpha^2)(\beta_r^2 \xi_{3,r} - \alpha^2(1 + \zeta \xi_{1,r} + \tau \xi_{2,r})) - \frac{2Y_r}{\lambda_r}\frac{\mu}{1+\zeta}\beta^2 \alpha^2 (\xi_{4,r} + \zeta \xi_{5,r})\right)^2}} \, . \tag{4.51}$$

The parameters $\zeta = \frac{m_{tip}}{\rho A L}$ describes the mass ratio between tip mass and mass of the beam. Respectively, the ratio $\tau = \frac{I_{tip}}{m_{beam}L^2}$ describes the relation between the mass moments of inertia of the tip mass and the beam. The parameters ξ_i contain information about the shapes of the deformation. These parameters are dimensionless and are independent of the geometry of the beam-like resonator. They only depend on the mode shape Φ_r

$$\xi_{1,r} = L \frac{\Phi_r^2|_{x=L}}{\int_0^L \Phi_r^2(x)dx} \, , \tag{4.52}$$

$$\xi_{2,r} = L\lambda_r^2 \frac{\Phi_r'^2|_{x=L}}{\int_0^L \Phi_r^2(x)dx} \, , \tag{4.53}$$

$$\xi_{3,r} = \frac{\int_0^L \tilde{\Phi}_r^2 dx}{\int_0^L \Phi_r^2(x)dx} \, , \tag{4.54}$$

$$\xi_{4,r} = \frac{\int_0^L \Phi_r dx}{\int_0^L \Phi_r^2(x)dx} \, , \tag{4.55}$$

$$\xi_{5,r} = L \frac{\Phi_r|_{x=L}}{\int_0^L \Phi_r^2(x)dx} \, . \tag{4.56}$$

Figure 4.10 illustrates the amplification functions for different ratios $\zeta = \frac{m_{tip}}{m_{beam}}$ and $\tau = \frac{I_{tip}}{m_{beam}L^2}$. The overall additional mass is constant ($\mu = \frac{m_{tip}+m_{beam}}{m} = 0.05$).

Increasing the tip mass ratio ζ increases the frequency range in which the magnification function is reduced, whereas an increased ratio of mass moment of inertia τ reduces the frequency range in which the magnification function is reduced. For the evaluation of the
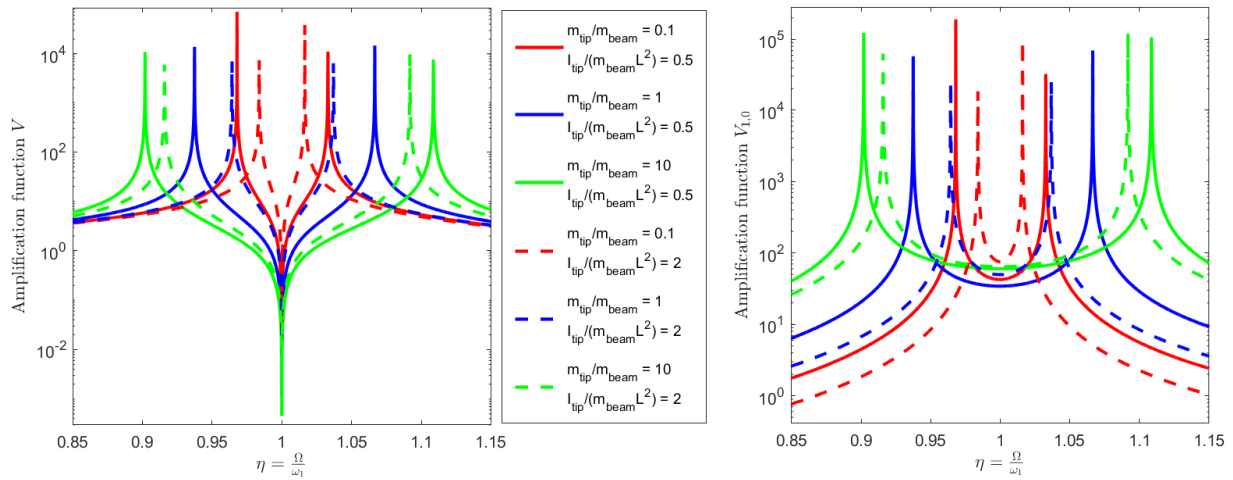
Figure 4.10: Influence of the mass ratio ζ and mass moment of inertia ratio τ on amplification functions for a fixed additional mass $\mu = 0.05$.

maximal reduction of the amplification function at the resonance frequency of the host structure, one determines the minimum value of the amplification functions (see figure 4.11). The close up shows that a larger tip mass and a lower mass moment of inertia of the tip mass is beneficial for a maximum reduction of the amplification function in the vicinity of the resonance frequency of the host structure.
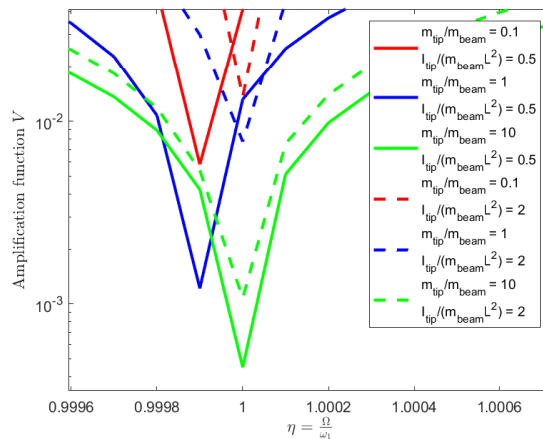
Figure 4.11: Influence of the mass ratio ζ and mass moment of inertia ratio τ on the minimum value of the amplification functions for a fixed mass ratio $\mu = 0.05$.

To relate the amplification functions of a mode r of the beam resonator to the solutions of a discrete SDOF system additional reformulations are required . Therefore, one multiplies

the nominator and denominator of the motion (4.50) with $\frac{1}{1+\zeta\xi_{1,r}+\tau\xi_{2,r}}$. This yields

$$
\begin{aligned}
\underline{w} &\approx \frac{f}{k_s} \frac{\frac{\beta_r^2\xi_{3,r}}{1+\zeta\xi_{1,r}+\tau\xi_{2,r}} - \alpha^2}{(1-\alpha^2)\left(\beta_r^2 \frac{\xi_{3,r}}{1+\zeta\xi_{1,r}+\tau\xi_{2,r}} - \alpha^2\right) - 2\frac{\mu}{1+\zeta}\frac{Y_r}{\lambda_r}\beta_r^2 \frac{1}{1+\zeta\xi_{1,r}+\tau\xi_{2,r}}\alpha^2\left(\xi_{4,r}+\zeta\xi_{5,r}\right)} , \\
\underline{w}_{r,0} &\approx \frac{f}{k_s} \frac{\alpha^2 \frac{\xi_{4,r}+\zeta\xi_{5,r}}{1+\zeta\xi_{1}+\tau\xi_{2,r}}}{(1-\alpha^2)\left(\beta_r^2 \frac{\xi_{3,r}}{1+\zeta\xi_{1,r}+\tau\xi_{2,r}} - \alpha^2\right) - 2\frac{\mu}{1+\zeta}\frac{Y_r}{\lambda_r}\beta_r^2 \frac{1}{1+\zeta\xi_{1,r}+\tau\xi_{2,r}}\alpha^2\left(\xi_{4,r}+\zeta\xi_{5,r}\right)} .
\end{aligned}
\tag{4.57}
$$

The resulting amplification functions are

$$
\begin{aligned}
V &\approx \sqrt{\frac{\left(\beta_r^2 \frac{\xi_{3,r}}{1+\zeta\xi_{1,r}+\tau\xi_{2,r}} - \alpha^2\right)^2}{\left((1-\alpha^2)\left(\beta_r^2 \frac{\xi_{3,r}}{1+\zeta\xi_{1,r}+\tau\xi_{2,r}} - \alpha^2\right) - \frac{2Y_r}{\lambda_r}\frac{\mu}{1+\zeta}\beta_r^2 \frac{1}{1+\zeta\xi_{1,r}+\tau\xi_{2,r}}\alpha^2\left(\xi_{4,r}+\zeta\xi_{5,r}\right)\right)^2}} , \\
V_{r,0} &\approx \sqrt{\frac{\alpha^4 \frac{(\xi_{4,r}+\zeta\xi_{5,r})^2}{(1+\zeta\xi_{1,r}+\tau\xi_{2,r})^2}}{\left((1-\alpha^2)\left(\beta_r^2 \frac{\xi_{3,r}}{1+\zeta\xi_{1,r}+\tau\xi_{2,r}} - \alpha^2\right) - \frac{2Y_r}{\lambda_r}\frac{\mu}{1+\zeta}\beta_r^2 \frac{1}{1+\zeta\xi_{1,r}+\tau\xi_{2,r}}\alpha^2\left(\xi_{4,r}+\zeta\xi_{5,r}\right)\right)^2}} .
\end{aligned}
\tag{4.58}
$$

Comparing these solutions to the solution of the SDOF-resonator from (4.42) and (4.43), the parameters for the discrete mass-spring resonator are

$$
\mu_{SDOF} = \frac{2Y_r}{\lambda_r}\frac{\mu}{1+\zeta}\frac{\xi_4+\zeta\xi_5}{\xi_3} ,
\tag{4.59}
$$

$$
\beta_{SDOF} = \beta\sqrt{\frac{\xi_3}{1+\zeta\xi_1+\tau\xi_2}} .
\tag{4.60}
$$

In addition, the amplification function for the relative motion of the beam needs a scaling

$$
V_{j,0} = \frac{\xi_4+\zeta\xi_5}{1+\zeta\xi_1+\tau\xi_2}V_{rel,SDOF} .
\tag{4.61}
$$

Summarizing, the dynamic behavior of a single mode of a beam-like resonator can be incorporated in the host structure using a SDOF system with parameters adjusted to the properties of the beam-like resonator.

4.1.3 Integrating the resonators into the host structure

This section describes different methods to incorporate the dynamic behavior of a discrete resonator into a discretized model of the host structure.
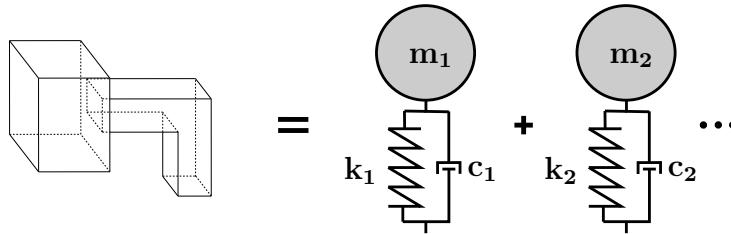
Figure 4.12: Integrate beam-like resonators as discrete mass-spring systems.

Gündel [2008] proposes three different options:

1. discrete oscillator as additional degree of freedom (DOF)

2. discrete oscillator as dynamic inertia

3. discrete oscillator as external attenuation force

Discrete oscillator as additional degree of freedom: Modeling the oscillator as an additional degree of freedom (DOF) is straightforward. The corresponding contribution of the mass m, spring stiffness k_s and damping coefficient c of the resonator extend the dynamic stiffness matrix $\mathbf{S}$

$$\mathbf{S}_{mod} = \begin{pmatrix} S_{1,1} & S_{1,2} & S_{1,3} & \dots & S_{1,n} & 0 \\ S_{2,1} & S_{2,2} + k_s + i\Omega c & S_{2,3} & \dots & S_{2,n} & -k_s - i\Omega c \\ S_{2,1} & S_{2,2} & S_{2,3} & \dots & S_{2,n} & 0 \\ \vdots & \vdots & \vdots & \ddots & \vdots & \vdots \\ S_{n,1} & S_{n,2} & S_{n,3} & \dots & S_{n,n} & 0 \\ 0 & -k_s - i\Omega c & 0 & \dots & 0 & +k_s + i\Omega c - \Omega^2 m \end{pmatrix} . \tag{4.62}$$

Discrete oscillator as dynamic inertia: A second possibility is the implementation of the oscillator as a dynamic inertia that modifies the inertia of the host structure. In that case,

the diagonal entry of the system matrix $\mathbf{S}$ of the coupling DOF changes

$$\mathbf{S}_{mod} = \begin{pmatrix} S_{1,1} & s_{1,2} & S_{1,3} & \dots & S_{1,n} \\ S_{2,1} & s_{2,2}-\Omega^2 m_q(\omega) & S_{2,3} & \dots & S_{2,n} \\ S_{2,1} & s_{2,2} & S_{2,3} & \dots & S_{2,n} \\ \vdots & \vdots & \vdots & \ddots & \vdots \\ s_{n,1} & s_{n,2} & S_{n,3} & \dots & S_{n,n} \end{pmatrix} . \tag{4.63}$$

The dynamic mass m_q is frequency dependent and depends on the ratio of the displacement of the resonator $\underline{u}_{res}$ and the displacement of the host structure at the coupling DOF $\underline{u}_2$

$$m_q(\Omega) = m\frac{\underline{u}_{res}}{\underline{u}_2} . \tag{4.64}$$

The parameters of the discrete oscillator determine the displacement ratio

$$\frac{\underline{u}_{res}}{\underline{u}_2} = \frac{k_s + i\Omega c}{k_s + i\Omega c - \Omega^2 m} . \tag{4.65}$$

Discrete oscillator as external attenuation force: Using this approach, the external force vector $\mathbf{f}$ contains the influence of the resonator

$$\underline{\mathbf{f}}_{mod} = \underline{\mathbf{f}} + \underline{\mathbf{f}}_{res}(\Omega) = \begin{bmatrix} \underline{f}_1 \\ \underline{f}_2 \\ \underline{f}_3 \\ \vdots \\ \underline{f}_n \end{bmatrix} + \begin{bmatrix} 0 \\ \underline{f}_{res}(\Omega) \\ 0 \\ \vdots \\ 0 \end{bmatrix} . \tag{4.66}$$

The external attenuation force of an oscillator is equal to the dynamic inertia term multiplied with the displacements at the coupling DOF.

$$\underline{f}_{res} = \Omega^2 m_q(\Omega)\underline{u}_{mod,2} \tag{4.67}$$

The computation of the attenuation force requires the displacement at the coupling DOF. Assuming that the overall structure behaves linearly, the displacements of the total structure $\underline{\mathbf{u}}_{mod}$ (including the oscillator) can be computed based on the displacements of the host structure without the oscillators $\underline{\mathbf{u}}$

$$\underline{\mathbf{u}}_{mod} = \underline{\mathbf{u}} + \mathbf{S}^{-1}\underline{\mathbf{f}}_{res}(\Omega) = \underline{\mathbf{u}} + \mathbf{P}\underline{f}_{res}(\Omega) . \tag{4.68}$$

Sorting the DOF by those who are coupled to an oscillator (index C) and those who are uncoupled (index F) yields

$$
\begin{bmatrix} \underline{\mathbf{u}}_{mod,F} \\ \underline{\mathbf{u}}_{mod,C} \end{bmatrix} = \begin{bmatrix} \underline{\mathbf{u}}_F \\ \underline{\mathbf{u}}_C \end{bmatrix} + \begin{bmatrix} \mathbf{P}_{FF} & \mathbf{P}_{FC} \\ \mathbf{P}_{CF} & \mathbf{P}_{CC} \end{bmatrix} \cdot \begin{bmatrix} \mathbf{0} \\ \underline{\mathbf{f}}_{res}(\Omega) \end{bmatrix} \tag{4.69}
$$

$$
= \begin{bmatrix} \underline{\mathbf{u}}_F \\ \underline{\mathbf{u}}_C \end{bmatrix} + \begin{bmatrix} \mathbf{P}_{FC} \cdot \underline{\mathbf{f}}_{res}(\Omega) \\ \mathbf{P}_{CC} \cdot \underline{\mathbf{f}}_{res}(\Omega) \end{bmatrix} . \tag{4.70}
$$

The second line of this equation defines the displacements at the coupling DOF

$$
\underline{\mathbf{u}}_{mod,C} = \underline{\mathbf{u}}_C + \mathbf{P}_{CC}\underline{\mathbf{f}}_{res}(\Omega) . \tag{4.71}
$$

Using (4.67), the displacements at the coupling DOF $\mathbf{u}_{mod,C}$ is

$$
\underline{\mathbf{u}}_{mod,C} = \left[1 - \mathbf{P}_{CC}\, \Omega^2 m_q \right]^{-1} \underline{\mathbf{u}}_C . \tag{4.72}
$$

For multiple oscillators, (4.72) reads

$$
\underline{\mathbf{u}}_{mod,C} = \left[\mathbf{I} - \mathbf{P}_{CC}\, \Omega^2 \begin{pmatrix} m_{q,1} & & \mathbf{0} \\ & \ddots & \\ \mathbf{0} & & m_{q,N} \end{pmatrix} \right]^{-1} \underline{\mathbf{u}}_C . \tag{4.73}
$$

Inserting the displacements $\underline{\mathbf{u}}_{mod,C}$ in (4.67) yields the attenuation force $\underline{\mathbf{f}}_{res}(\Omega)$. Furthermore, the displacements $\mathbf{u}_{mod,F}$ result from the first line of (4.70).

The different approaches have different advantages and disadvantages. In general, modeling the oscillators as additional DOF increases the system size. The advantage of this approach is that an eigenvalue problem based on the system matrices yields the correct system characteristics as eigenfrequencies and mode shapes. Thus, analysis methods that require the system matrices (mass and stiffness) to be in the correct modal vector space only work with this method. Examples of such methods are reduction methods based on modal truncation. Applying the dynamic inertia of the oscillators directly into the system matrix does not increase the system size but the mass and stiffness contributions of the system matrix $\mathbf{S}$ are no longer separable. In addition, the dynamic inertia can affect the condition of the system matrix which can generate problems for solving the matrix equation. In many cases, the displacements of the host structure without the resonators are necessary to assess the impact of the resonators. Applying the approach of external attenuation forces, the system response of a modified structure can be computed very fast from the solution of the unmodified sys-

tem. Therefore, this approach is very efficient for the evaluation of different configurations of resonators or for the optimization of the parameters of the resonators.

4.2 Modeling periodic structures using the WFEM

The Wave Finite Element Method (WFEM) is a useful method to compute wave propagation in repetitive structures. The benefit of this method is that it is based on the finite element formulation of a small unit that is repeated several times to form the over all structure. In many cases acoustic metamaterials consists of periodic repetitions of small unit cells.

Mead [1973]; Orris and Petyt [1974]; Mead [1996] formulate the basic theory of the Wave Finite Element Method (WFEM). There are two different approaches to formulate an eigenvalue problem that describes the wave propagation in periodic structures [Mead 1973]. First, the inverse approach assumes a purely real phase constant to solve for the frequencies of free wave propagation. The inverse approach is commonly used to demonstrate the formation of band gaps [Claeys et al 2011, 2014a, 2016b, 2017; Melo et al 2016]. Second, the direct approach formulates the eigenvalue problem for every frequency, which yields complex phase constants. Therefore, the direct approach computes all wave solutions and also determines the decaying wave solutions. Using the direct approach, it is possible to compute the forced response of periodic structures. This requires all wave solutions including the decaying wave solutions. There are various formulations of the direct approach. Zhong and Williams [1995] formulate an alternative eigenvalue problem exploiting the symplectic property. This formulation overcomes issues with ill-conditioned formulations. Mace et al [2005] formulate a transfer matrix approach using finite elements for one dimensional wave propagation and Mace and Manconi [2008] extend this to two dimensional wave propagation. Zhou [2014] develops a condensed WFEM which reduces the modal space and therefore reduces the computational effort.

The following section derives the different approaches and formulations. The starting point is a discretized model of the unit cell. The unit cell is the smallest unit that represents the overall structure by repeating it several times in different directions. Due to the periodicity of the structure, it is sufficient to consider the unit cell to compute the harmonic wave propagation in the overall structure. Based on the Floquet theorem [Floquet 1883], the solution of the state variables in a periodic structure is periodic itself and only varies by an exponential term with respect to the length of the unit cell

$$u(x + L) = u(x)\, e^{-i\kappa L} = u(x)\, \mu\, . \tag{4.74}$$

κ is the Floquet wavenumber and L is the length of the unit cell. [Bloch 1929] derives a similar relation for the motion of electrons in three dimensional lattices. According to the derivation of [Floquet 1883] and [Bloch 1929], (4.74) is sometimes called Floquet theorem for one dimensional periodicity and Bloch theorem for higher dimensional periodicity. (4.74) relates the state vectors of two neighboring unit cells (see figure 4.13)

$$\mathbf{q}_R = \mu \mathbf{q}_L \ , \tag{4.75}$$

$$\mathbf{f}_R = -\mu \mathbf{f}_L \ . \tag{4.76}$$
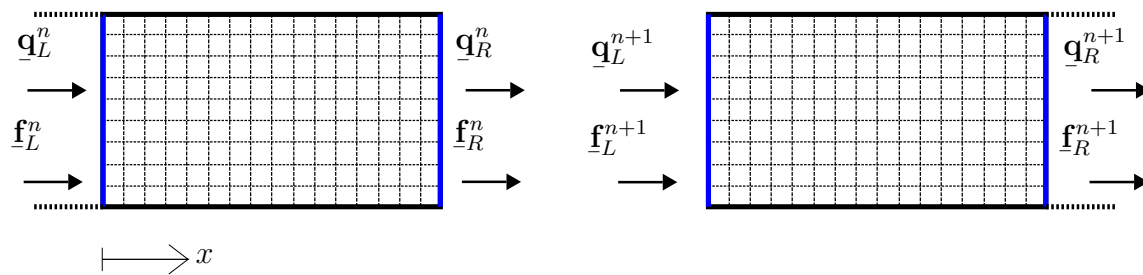
Figure 4.13: Relation of the state variables between the boundaries of a unit cell of a one dimensional periodic structure.

The indices L and R denote the left and right boundary of the unit cell, respectively. The negative algebraic sign results from the force equilibrium between two neighboring unit cells: $\mathbf{f}_R^n = -\mathbf{f}_L^{n+1}$.

$|\mu|$	κ_{Im}	κ_{Re}	propagation direction	wave type
1	0	$\neq 0$	positive/negative	undamped
< 1	< 0	$\neq 0$	positive	damped
< 1	< 0	0	positive	evanescent
> 1	> 0	$\neq 0$	negative	damped
> 1	> 0	0	negative	evanescent
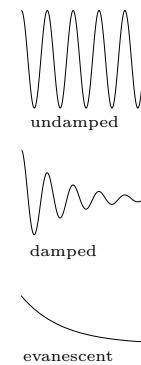
Figure 4.14: Relation between Floquet wavenumber and the different waves and their propagation direction.

The Floquet wavenumber κ of the respective wave solution determines the wave type. Figure 4.14 lists the different wave types. As previously mentioned, there are two different approaches to formulate an eigenvalue problem that describes the wave propagation: an inverse approach and a direct approach.

4.2.1 Inverse approach

Using the inverse approach, an eigenvalue problem for a specific value of $\mu = \mathrm{e}^{-i\kappa L}$ is defined. Thereby, the imaginary part of the Floquet wavenumber κ_{Im} is commonly set to zero. The time harmonic equation of motion of the unit cell is

$$
\left(\begin{bmatrix} \mathbf{K}_{LL} & \mathbf{K}_{LR} & \mathbf{K}_{LI} \\ \mathbf{K}_{RL} & \mathbf{K}_{RR} & \mathbf{K}_{RI} \\ \mathbf{K}_{IL} & \mathbf{K}_{IR} & \mathbf{K}_{II} \end{bmatrix} - \Omega^2 \begin{bmatrix} \mathbf{M}_{LL} & \mathbf{M}_{LR} & \mathbf{M}_{LI} \\ \mathbf{M}_{RL} & \mathbf{M}_{RR} & \mathbf{M}_{RI} \\ \mathbf{M}_{IL} & \mathbf{M}_{IR} & \mathbf{M}_{II} \end{bmatrix} \right) \begin{bmatrix} \underline{\mathbf{q}}_L \\ \underline{\mathbf{q}}_R \\ \underline{\mathbf{q}}_I \end{bmatrix} = \begin{bmatrix} \underline{\mathbf{f}}_L \\ \underline{\mathbf{f}}_R \\ \underline{\mathbf{f}}_I \end{bmatrix} \ . \tag{4.77}
$$

The indices L, R and I denote the left, right and interior DOF. $\mathbf{K}$ and $\mathbf{M}$ describe the stiffness and mass matrix. A reduction matrix $\mathbf{R}$ enforces the relation between the right displacements $\underline{\mathbf{q}}_R$ and the left displacements $\underline{\mathbf{q}}_L$ from (4.75)

$$
\mathbf{q} = \begin{bmatrix} \underline{\mathbf{q}}_L \\ \underline{\mathbf{q}}_I \\ \underline{\mathbf{q}}_R \end{bmatrix} = \begin{bmatrix} \mathbf{1} & \mathbf{0} \\ \mathbf{0} & \mathbf{1} \\ \mathbf{1}\mathrm{e}^{-i\kappa L} & \mathbf{0} \end{bmatrix} \begin{bmatrix} \underline{\mathbf{q}}_L \\ \underline{\mathbf{q}}_I \end{bmatrix} = \mathbf{R}\underline{\mathbf{q}}^{red} \ . \tag{4.78}
$$

Inserting (4.78) and multiplying both sides of (4.77) with $\mathbf{R}^{*T}$ yields an eigenvalue problem

$$
\left(\mathbf{K}^{\mathbf{red}} - \Omega^2 \mathbf{M}^{\mathbf{red}} \right) \begin{bmatrix} \underline{\mathbf{q}}_L \\ \underline{\mathbf{q}}_I \end{bmatrix} = \mathbf{0} \tag{4.79}
$$

with

$$
\begin{aligned}
\mathbf{K}^{\mathbf{red}} &= \mathbf{R}^{*\mathbf{T}}\mathbf{K}\mathbf{R} \ , \\
\mathbf{M}^{\mathbf{red}} &= \mathbf{R}^{*\mathbf{T}}\mathbf{M}\mathbf{R} \ .
\end{aligned} \tag{4.80}
$$

The reduced force vector vanishes due to the Floquet theorem (4.76) and due to the assumption that there is no external loading on the interior DOF

$$
\underline{\mathbf{f}}^{red} = \underbrace{\begin{bmatrix} \mathbf{1} & \mathbf{0} & \mathbf{1}\mathrm{e}^{i\kappa L} \\ \mathbf{0} & \mathbf{1} & \mathbf{0} \end{bmatrix}}_{\mathbf{R}^*} \begin{bmatrix} \underline{\mathbf{f}}_L \\ \underline{\mathbf{f}}_I \\ \underline{\mathbf{f}}_R \end{bmatrix} = \begin{bmatrix} \mathbf{0} \\ \mathbf{0} \end{bmatrix} \ . \tag{4.81}
$$

For purely real κ, the reduced matrices $\mathbf{K^{red}}$ and $\mathbf{M^{red}}$ are hermitian and the eigenvalues Ω^2 are real [Langley 1993].

Extension for two-dimensional and three dimensional periodic structures

Mead [1973] introduces the approach for two dimensional periodicity. The provided reduction matrices generate the correct phase surfaces but the power flow at the corners is incorrect. Langley [1993] correctes the periodicity conditions for the corners. Figure 4.15 visualizes the periodicity condition for a two dimensional unit cell. Equations (4.82) to (4.86) describe the relation between the displacements. The relations of the forces are similar except for the switched algebraic sign (compare to (4.76)).
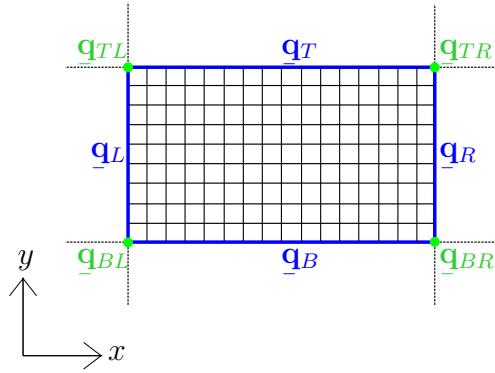
$$\underline{\mathbf{q}}_R = \mu_x \underline{\mathbf{q}}_L \tag{4.82}$$

$$\underline{\mathbf{q}}_T = \mu_y \underline{\mathbf{q}}_B \tag{4.83}$$

$$\underline{\mathbf{q}}_{BR} = \mu_x \underline{\mathbf{q}}_{BL} \tag{4.84}$$

$$\underline{\mathbf{q}}_{TL} = \mu_y \underline{\mathbf{q}}_{BL} \tag{4.85}$$

$$\underline{\mathbf{q}}_{TR} = (\mu_x \mu_y) \underline{\mathbf{q}}_{BL} \tag{4.86}$$

Figure 4.15: Relation of the state variables between the boundaries of a unit cell of a two dimensional periodic structure.

This results in the following reduction matrix $\mathbf{R}$ for the eigenvalue problem (4.79)

$$\underline{\mathbf{q}} = \begin{bmatrix} \underline{\mathbf{q}}_L \\ \underline{\mathbf{q}}_R \\ \underline{\mathbf{q}}_B \\ \underline{\mathbf{q}}_T \\ \underline{\mathbf{q}}_I \\ \underline{\mathbf{q}}_{BL} \\ \underline{\mathbf{q}}_{TL} \\ \underline{\mathbf{q}}_{BR} \\ \underline{\mathbf{q}}_{TR} \end{bmatrix} = \begin{bmatrix} 1 & 0 & 0 & 0 \\ 1\mu_x & 0 & 0 & 0 \\ 0 & 1 & 0 & 0 \\ 0 & 1\mu_y & 0 & 0 \\ 0 & 0 & 1 & 0 \\ 0 & 0 & 0 & 1 \\ 0 & 0 & 0 & 1\mu_y \\ 0 & 0 & 0 & 1\mu_x \\ 0 & 0 & 0 & 1\mu_x\mu_y \end{bmatrix} \begin{bmatrix} \underline{\mathbf{q}}_L \\ \underline{\mathbf{q}}_B \\ \underline{\mathbf{q}}_I \\ \underline{\mathbf{q}}_{BL} \end{bmatrix} = \mathbf{R}\underline{\mathbf{q}}^{red}. \tag{4.87}$$

Accordingly, one defines the reduction matrix for three dimensions.
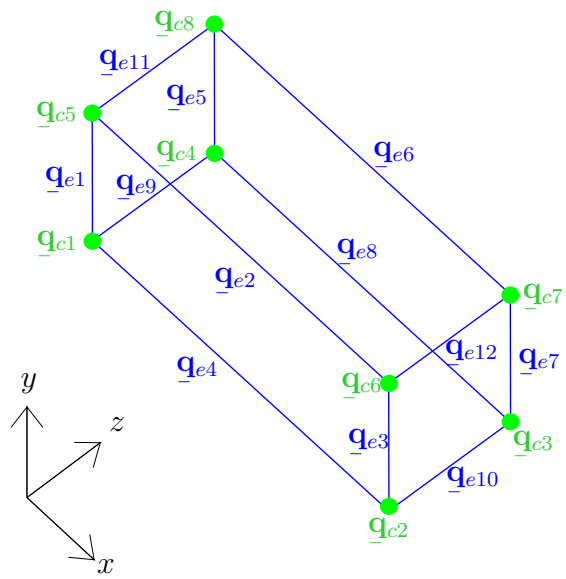
Figure 4.16: Boundaries of a three dimensional unit cell.

$$
\underline{\mathbf{q}} =
\begin{bmatrix}
\underline{\mathbf{q}}_{K1} \\
\underline{\mathbf{q}}_{K2} \\
\underline{\mathbf{q}}_{K3} \\
\underline{\mathbf{q}}_{K4} \\
\underline{\mathbf{q}}_{K5} \\
\underline{\mathbf{q}}_{K6} \\
\underline{\mathbf{q}}_{K7} \\
\underline{\mathbf{q}}_{K8} \\
\underline{\mathbf{q}}_{E1} \\
\underline{\mathbf{q}}_{E2} \\
\underline{\mathbf{q}}_{E3} \\
\underline{\mathbf{q}}_{E4} \\
\underline{\mathbf{q}}_{E5} \\
\underline{\mathbf{q}}_{E6} \\
\underline{\mathbf{q}}_{E7} \\
\underline{\mathbf{q}}_{E8} \\
\underline{\mathbf{q}}_{E9} \\
\underline{\mathbf{q}}_{E10} \\
\underline{\mathbf{q}}_{E11} \\
\underline{\mathbf{q}}_{E12} \\
\underline{\mathbf{q}}_{F1} \\
\underline{\mathbf{q}}_{F2} \\
\underline{\mathbf{q}}_{F3} \\
\underline{\mathbf{q}}_{F4} \\
\underline{\mathbf{q}}_{F5} \\
\underline{\mathbf{q}}_{F6} \\
\underline{\mathbf{q}}_{I}
\end{bmatrix}
=
\begin{bmatrix}
1 & 0 & 0 & 0 & 0 & 0 & 0 & 0 \\
1\mu_x & 0 & 0 & 0 & 0 & 0 & 0 & 0 \\
1\mu_x\mu_z & 0 & 0 & 0 & 0 & 0 & 0 & 0 \\
1\mu_z & 0 & 0 & 0 & 0 & 0 & 0 & 0 \\
1\mu_y & 0 & 0 & 0 & 0 & 0 & 0 & 0 \\
1\mu_x\mu_y & 0 & 0 & 0 & 0 & 0 & 0 & 0 \\
1\mu_x\mu_y\mu_z & 0 & 0 & 0 & 0 & 0 & 0 & 0 \\
1\mu_y\mu_z & 0 & 0 & 0 & 0 & 0 & 0 & 0 \\
0 & 1 & 0 & 0 & 0 & 0 & 0 & 0 \\
0 & 0 & 1\mu_y & 0 & 0 & 0 & 0 & 0 \\
0 & 1\mu_x & 0 & 0 & 0 & 0 & 0 & 0 \\
0 & 0 & 1 & 0 & 0 & 0 & 0 & 0 \\
0 & 1\mu_z & 0 & 0 & 0 & 0 & 0 & 0 \\
0 & 0 & 1\mu_y\mu_z & 0 & 0 & 0 & 0 & 0 \\
0 & 1\mu_x\mu_z & 0 & 0 & 0 & 0 & 0 & 0 \\
0 & 0 & 1\mu_z & 0 & 0 & 0 & 0 & 0 \\
0 & 0 & 0 & 1 & 0 & 0 & 0 & 0 \\
0 & 0 & 0 & 1\mu_x & 0 & 0 & 0 & 0 \\
0 & 0 & 0 & 1\mu_y & 0 & 0 & 0 & 0 \\
0 & 0 & 0 & 1\mu_x\mu_y & 0 & 0 & 0 & 0 \\
0 & 0 & 0 & 0 & 1 & 0 & 0 & 0 \\
0 & 0 & 0 & 0 & 0 & 1\mu_x & 0 & 0 \\
0 & 0 & 0 & 0 & 1\mu_y & 0 & 0 & 0 \\
0 & 0 & 0 & 0 & 0 & 1 & 0 & 0 \\
0 & 0 & 0 & 0 & 0 & 0 & 1 & 0 \\
0 & 0 & 0 & 0 & 0 & 0 & 1\mu_z & 0 \\
0 & 0 & 0 & 0 & 0 & 0 & 0 & 1
\end{bmatrix}
\begin{bmatrix}
\underline{\mathbf{q}}_{K1} \\
\underline{\mathbf{q}}_{E1} \\
\underline{\mathbf{q}}_{E4} \\
\underline{\mathbf{q}}_{E9} \\
\underline{\mathbf{q}}_{F1} \\
\underline{\mathbf{q}}_{F4} \\
\underline{\mathbf{q}}_{F5} \\
\underline{\mathbf{q}}_{I}
\end{bmatrix}
= \mathbf{R}\underline{\mathbf{q}}_{red}
$$

$$(4.88)$$

4.2.2 Direct approach

The direct approach formulates the eigenvalue problem in terms of the wave solutions for each frequency of interest. Similarly to the inverse approach, the starting point is the sorted

dynamic stiffness $\mathbf{S} = \mathbf{K} - \Omega^2 \mathbf{M}$ according to the left, interior and right DOF.

$$\mathbf{S} = \begin{bmatrix} \mathbf{S}_{LL} & \mathbf{S}_{LR} & \mathbf{S}_{LI} \\ \mathbf{S}_{RL} & \mathbf{S}_{RR} & \mathbf{S}_{RI} \\ \mathbf{S}_{IL} & \mathbf{S}_{IR} & \mathbf{S}_{II} \end{bmatrix} . \tag{4.89}$$

Thus the harmonic equation of motion is

$$\begin{bmatrix} \mathbf{S}_{LL} & \mathbf{S}_{LR} & \mathbf{S}_{LI} \\ \mathbf{S}_{RL} & \mathbf{S}_{RR} & \mathbf{S}_{RI} \\ \mathbf{S}_{IL} & \mathbf{S}_{IR} & \mathbf{S}_{II} \end{bmatrix} \begin{bmatrix} \mathbf{q}_L \\ \mathbf{q}_R \\ \mathbf{q}_I \end{bmatrix} = \begin{bmatrix} \mathbf{f}_L \\ \mathbf{f}_R \\ \mathbf{0} \end{bmatrix} . \tag{4.90}$$

Next, one condenses the interior degrees of freedom

$$\mathbf{q}_I = -\mathbf{S}_{II}^{-1}(\mathbf{S}_{IL}\mathbf{q}_L + \mathbf{S}_{IR}\mathbf{q}_R) . \tag{4.91}$$

This yields a reduced equation of motion

$$\begin{bmatrix} \tilde{\mathbf{S}}_{LL} & \tilde{\mathbf{S}}_{LR} \\ \tilde{\mathbf{S}}_{RL} & \tilde{\mathbf{S}}_{RR} \end{bmatrix} \begin{bmatrix} \mathbf{q}_L \\ \mathbf{q}_R \end{bmatrix} = \begin{bmatrix} \mathbf{f}_L \\ \mathbf{f}_R \end{bmatrix} , \tag{4.92}$$

with

$$\tilde{\mathbf{S}}_{LL} = \mathbf{S}_{LL} - \mathbf{S}_{LI}\mathbf{S}_{II}^{-1}\mathbf{S}_{IL} , \tag{4.93}$$

$$\tilde{\mathbf{S}}_{RL} = \mathbf{S}_{RL} - \mathbf{S}_{RI}\mathbf{S}_{II}^{-1}\mathbf{S}_{IL} , \tag{4.94}$$

$$\tilde{\mathbf{S}}_{LR} = \mathbf{S}_{LR} - \mathbf{S}_{LI}\mathbf{S}_{II}^{-1}\mathbf{S}_{IR} , \tag{4.95}$$

$$\tilde{\mathbf{S}}_{RR} = \mathbf{S}_{RR} - \mathbf{S}_{RI}\mathbf{S}_{II}^{-1}\mathbf{S}_{IR} . \tag{4.96}$$

Due to the symmetry of $\mathbf{S}$, the condensed $\tilde{\mathbf{S}}$ is symmetric as well. Rearranging the condensed equation of motion (4.92) reveals a relation between the displacements and the forces of two neighboring cells in terms of a transfermatrix $\mathbf{T}$ [Mace et al 2005]

$$\begin{bmatrix} \mathbf{q}_L \\ \mathbf{f}_L \end{bmatrix}_{n+1} = \mathbf{T}(\Omega) \begin{bmatrix} \mathbf{q}_L \\ \mathbf{f}_L \end{bmatrix}_n = \begin{bmatrix} -\tilde{\mathbf{S}}_{LR}^{-1}\tilde{\mathbf{S}}_{LL} & \tilde{\mathbf{S}}_{LR}^{-1} \\ -\tilde{\mathbf{S}}_{RL} + \tilde{\mathbf{S}}_{RR}\tilde{\mathbf{S}}_{LR}^{-1}\tilde{\mathbf{S}}_{LL} & -\tilde{\mathbf{S}}_{RR}\tilde{\mathbf{S}}_{LR}^{-1} \end{bmatrix} \begin{bmatrix} \mathbf{q}_L \\ \mathbf{f}_L \end{bmatrix}_n . \tag{4.97}$$

The previous equation ensures the continuity of the displacements and the force equilibrium between two neighboring cells

$$\underline{\mathbf{q}}_R^n = \underline{\mathbf{q}}_L^{n+1} \ , \tag{4.98}$$

$$\underline{\mathbf{f}}_R^n = -\underline{\mathbf{f}}_L^{n+1} \ . \tag{4.99}$$

The Floquet theorem (4.75) and (4.76) yields the same relation as described by the transfermatrix $\mathbf{T}$

$$\begin{bmatrix} \mathbf{q}_L \\ \underline{\mathbf{f}}_L \end{bmatrix}_{n+1} = \boldsymbol{\mu} \begin{bmatrix} \mathbf{q}_L \\ \underline{\mathbf{f}}_L \end{bmatrix}_n \qquad \Leftrightarrow \qquad \begin{bmatrix} \mathbf{q}_L \\ \underline{\mathbf{f}}_L \end{bmatrix}_{n+1} = \mathbf{T}(\Omega) \begin{bmatrix} \mathbf{q}_L \\ \underline{\mathbf{f}}_L \end{bmatrix}_n \ . \tag{4.100}$$

Consequently, the wave solutions result from the eigenvalue problem

$$\boldsymbol{\mu} \begin{bmatrix} \mathbf{q}_L \\ \underline{\mathbf{f}}_L \end{bmatrix}_n = \mathbf{T}(\Omega) \begin{bmatrix} \mathbf{q}_L \\ \underline{\mathbf{f}}_L \end{bmatrix}_n \ . \tag{4.101}$$

This eigenvalue problem reveals complex valued pairs of eigenvalues $(\mu, 1/\mu)$ [Mace et al 2005]. These pairs correspond to waves propagating in opposite directions. Using the Floquet theorem (4.74), the eigenvalue μ defines the complex wavenumber

$$\mu = \mathrm{e}^{-i\kappa L} = \mathrm{e}^{-i(\kappa_{Re} + i\kappa_{Im})L} \ . \tag{4.102}$$

Using (4.102), the reciprocal of μ is

$$\frac{1}{\mu} = \mathrm{e}^{i(\kappa_{Re} + i\kappa_{Im})L} \ . \tag{4.103}$$

Consequently, the pairs $(\mu, 1/\mu)$ describe wave pairs with same absolute value of the phase $(\kappa_{Re}L)$ and decay $(\kappa_{Im}L)$ but opposite sign.

4.2.3 Alternative formulations for the direct approach

The computational effort for the direct approach can be very high, because each frequency of interest requires a matrix inversion and solving an eigenvalue problem. Furthermore, the combination of deformations and forces in the eigenvalue problem results in small and very large entries in the eigenvectors. This might decrease the accuracy as the condition number of the transfer matrix $\mathbf{T}$ increases. Therefore, there are different reformulations of the

eigenvalue problem (4.101) that improve the condition and/or decrease the computational effort.

Duhamel's LR method

Duhamel et al [2005] rearrange the eigenvalue problem to eliminate the force relation. The force relation is eliminated using (4.92). Thus, the first line of (4.101) yields

$$\mu \tilde{\mathbf{S}}_{RL} \mathbf{q}_L = \tilde{\mathbf{S}}_{RL} \mathbf{q}_R \ . \tag{4.104}$$

Similarly, the second line of (4.101) can be rearranged

$$\mu \tilde{\mathbf{S}}_{LR} \mathbf{q}_R = -\tilde{\mathbf{S}}_{RL} \mathbf{q}_L - \tilde{\mathbf{S}}_{LL} \mathbf{q}_R - \tilde{\mathbf{S}}_{RR} \mathbf{q}_R \ . \tag{4.105}$$

Combining (4.104) and (4.104) yields the generalized eigenvalue problem

$$\mathbf{L} \begin{bmatrix} \mathbf{q}_L \\ \mathbf{q}_R \end{bmatrix} = \mu \mathbf{R} \begin{bmatrix} \mathbf{q}_L \\ \mathbf{q}_R \end{bmatrix} \ , \tag{4.106}$$

with $\mathbf{L}$ and $\mathbf{R}$ having the form

$$\mathbf{L} = \begin{bmatrix} \mathbf{0} & \tilde{\mathbf{S}}_{RL} \\ -\tilde{\mathbf{S}}_{RL} & -\tilde{\mathbf{S}}_{LL} - \tilde{\mathbf{S}}_{RR} \end{bmatrix} \ , \tag{4.107}$$

$$\mathbf{R} = \begin{bmatrix} \tilde{\mathbf{S}}_{RL} & \mathbf{0} \\ \mathbf{0} & \tilde{\mathbf{S}}_{LR} \end{bmatrix} \ . \tag{4.108}$$

Knowing the displacements at the boundaries, the reduced equation of motion (4.92) determines the interface forces.

Zhong's method

The symplectic feature of the transfer matrix $\mathbf{T}$ offers the opportunity to define the eigenvalues as $\lambda = \mu + 1/\mu$ [Zhong and Williams 1995]. Therefore, the following relations are

valid

$$\underline{\mathbf{q}}_R = \mu \underline{\mathbf{q}}_L \ , \tag{4.109}$$

$$\underline{\mathbf{f}}_R = -\mu \underline{\mathbf{f}}_L \ , \tag{4.110}$$

and

$$\underline{\mathbf{q}}_L = \frac{1}{\mu} \underline{\mathbf{q}}_R \ , \tag{4.111}$$

$$\underline{\mathbf{f}}_L = -\frac{1}{\mu} \underline{\mathbf{f}}_R \ . \tag{4.112}$$

Eliminating the force relation using (4.92) and multiplying (4.109) with $\tilde{\mathbf{S}}_{RL}$ and (4.111) with $-\tilde{\mathbf{S}}_{LR}$ yields four equations

$$\tilde{\mathbf{S}}_{RL} \underline{\mathbf{q}}_R = \mu \tilde{\mathbf{S}}_{RL} \underline{\mathbf{q}}_L \ , \tag{4.113}$$

$$\tilde{\mathbf{S}}_{RL} \underline{\mathbf{q}}_L + \tilde{\mathbf{S}}_{RR} \underline{\mathbf{q}}_R = -\mu \left(\tilde{\mathbf{S}}_{LL} \underline{\mathbf{q}}_L + \tilde{\mathbf{S}}_{LR} \underline{\mathbf{q}}_R \right) \ , \tag{4.114}$$

$$-\tilde{\mathbf{S}}_{LR} \underline{\mathbf{q}}_L = -\frac{1}{\mu} - \tilde{\mathbf{S}}_{LR} \underline{\mathbf{q}}_R \ , \tag{4.115}$$

$$-\tilde{\mathbf{S}}_{LL} \underline{\mathbf{q}}_L - \tilde{\mathbf{S}}_{LR} \underline{\mathbf{q}}_R = \frac{1}{\mu} \left(\tilde{\mathbf{S}}_{RL} \underline{\mathbf{q}}_L + \tilde{\mathbf{S}}_{RR} \underline{\mathbf{q}}_R \right) \ . \tag{4.116}$$

Summing up (4.113) and (4.116) and rearranging the terms results in

$$-\left(\tilde{\mathbf{S}}_{LL} + \tilde{\mathbf{S}}_{RR} \right) \underline{\mathbf{q}}_L + \left(\tilde{\mathbf{S}}_{RL} - \tilde{\mathbf{S}}_{LR} \right) \underline{\mathbf{q}}_R = \mu \tilde{\mathbf{S}}_{RL} \underline{\mathbf{q}}_L + \frac{1}{\mu} \tilde{\mathbf{S}}_{RL} \underline{\mathbf{q}}_L \ . \tag{4.117}$$

Similarly, (4.114) and (4.115) are summed up and reordered

$$\left(\tilde{\mathbf{S}}_{RL} - \tilde{\mathbf{S}}_{LR} \right) \underline{\mathbf{q}}_L + \left(\tilde{\mathbf{S}}_{LL} + \tilde{\mathbf{S}}_{RR} \right) \underline{\mathbf{q}}_R = -\mu \tilde{\mathbf{S}}_{LR} \underline{\mathbf{q}}_R - \frac{1}{\mu} \tilde{\mathbf{S}}_{LR} \underline{\mathbf{q}}_R \ . \tag{4.118}$$

This allows the formulation of an eigenvalue problem with an improved condition

$$\begin{bmatrix} \tilde{\mathbf{S}}_{RL} - \tilde{\mathbf{S}}_{LR} & \tilde{\mathbf{S}}_{LL} + \tilde{\mathbf{S}}_{RR} \\ -(\tilde{\mathbf{S}}_{LL} + \tilde{\mathbf{S}}_{RR}) & \tilde{\mathbf{S}}_{RL} - \tilde{\mathbf{S}}_{LR} \end{bmatrix} \begin{bmatrix} \underline{\mathbf{q}}_L \\ \underline{\mathbf{q}}_R \end{bmatrix} = \lambda \begin{bmatrix} \mathbf{0} & -\tilde{\mathbf{S}}_{LR} \\ \tilde{\mathbf{S}}_{RL} & \mathbf{0} \end{bmatrix} \begin{bmatrix} \underline{\mathbf{q}}_L \\ \underline{\mathbf{q}}_R \end{bmatrix} \ . \tag{4.119}$$

The resulting double eigenvalue $\lambda_k = (\mu_k + 1/\mu_k)$ define the original eigenvalue μ_k [Zhong

and Williams 1995; Silva 2015]

$$\mu_k = \frac{1}{2}\left(\lambda_k \pm \sqrt{\lambda_k^2 - 4}\right) \ . \tag{4.120}$$

Condensed WFEM

Zhou [2014] proposes the condensed WFEM which reduces the computational effort by mapping the internal DOF on a reduced basis using component mode synthesis (CMS). The mapping reduces the computational costs of the inversion of the matrix $\mathbf{S}_{II}$. In addition, a rearrangement of the eigenvalue problem similar to the previous methods improve the condition.

The mapping of the internal DOF demands a transformation $\boldsymbol{\Theta}$

$$\begin{bmatrix} \mathbf{q}_L \\ \mathbf{q}_R \\ \mathbf{q}_I \end{bmatrix} = \boldsymbol{\Theta} \begin{bmatrix} \mathbf{q}_L \\ \mathbf{q}_R \\ \mathbf{q}_H \end{bmatrix} \ . \tag{4.121}$$

The transformation does not affect the boundaries of the cell

$$\boldsymbol{\Theta} = \begin{bmatrix} \mathbf{1} & \mathbf{0} & \mathbf{0} \\ \mathbf{0} & \mathbf{1} & \mathbf{0} \\ \boldsymbol{\Psi}_L & \boldsymbol{\Psi}_R & \boldsymbol{\Psi}_H \end{bmatrix} \ . \tag{4.122}$$

$\boldsymbol{\Psi}_L$ and $\boldsymbol{\Psi}_R$ are the static boundary modes derived from the stiffness matrix $\mathbf{K}$

$$\boldsymbol{\Psi}_L = -\mathbf{K}_{II}^{-1}\mathbf{K}_{IL} \ , \tag{4.123}$$

$$\boldsymbol{\Psi}_R = -\mathbf{K}_{II}^{-1}\mathbf{K}_{IR} \ . \tag{4.124}$$

The following eigenvalue problem determines the internal modes $\boldsymbol{\Psi}_H$

$$\left[\mathbf{K}_{II} - \Omega^2\mathbf{M}_{II}\right]\boldsymbol{\Psi}_I = \mathbf{0} \ . \tag{4.125}$$

The basis $\boldsymbol{\Psi}_H$ consists of a reduced set of n_H eigenvectors of the basis $\boldsymbol{\Psi}_I$

$$\boldsymbol{\Psi}_H = \begin{bmatrix} \boldsymbol{\Psi}_{H,1} & \boldsymbol{\Psi}_{H,2} \cdots \boldsymbol{\Psi}_{H,n_H} \end{bmatrix} . \tag{4.126}$$

where the eigenvectors corresponds to the n_H lowest eigenvalues. A convergence criteria assesses the number of eigenvectors n_H. According to Zhou [2014], the solution already

converges for small n_H and it is sufficient to choose n_H such that

$$f_{n_H} = \frac{\sqrt{\omega_{n_H}^2}}{2\pi} \geq 3 f_{max} , \tag{4.127}$$

where f_{max} is the largest frequency for which the wave solutions are calculated. In the following, the matrix $\boldsymbol{\Theta}$ transforms the system matrix $\mathbf{S}$

$$\begin{bmatrix} \mathbf{S}_{LL}^* & \mathbf{S}_{LR}^* & \mathbf{S}_{LH}^* \\ \mathbf{S}_{RL}^* & \mathbf{S}_{RR}^* & \mathbf{S}_{RH}^* \\ \mathbf{S}_{HL}^* & \mathbf{S}_{HR}^* & \mathbf{S}_{HH}^* \end{bmatrix} = \boldsymbol{\Theta}^T \begin{bmatrix} \mathbf{S}_{LL} & \mathbf{S}_{LR} & \mathbf{S}_{LI} \\ \mathbf{S}_{RL} & \mathbf{S}_{RR} & \mathbf{S}_{RI} \\ \mathbf{S}_{IL} & \mathbf{S}_{IR} & \mathbf{S}_{II} \end{bmatrix} \boldsymbol{\Theta} . \tag{4.128}$$

This results in a reduced effort for the matrix inversion for the condensation of the internal degrees of freedoms (compare to (4.91)). The reason is the projection of the internal degrees of freedom on a the reduced basis $\boldsymbol{\Psi}_H$. The reduced equation of motion is

$$\begin{bmatrix} \tilde{\mathbf{S}}_{LL}^* & \tilde{\mathbf{S}}_{LR}^* \\ \tilde{\mathbf{S}}_{RL}^* & \tilde{\mathbf{S}}_{RR}^* \end{bmatrix} \begin{bmatrix} \mathbf{q}_L \\ \mathbf{q}_R \end{bmatrix} = \begin{bmatrix} \mathbf{f}_L \\ \mathbf{f}_R \end{bmatrix} , \tag{4.129}$$

with

$$\tilde{\mathbf{S}}_{LL}^* = \mathbf{S}_{LL}^* - \mathbf{S}_{LH}^* \mathbf{S}_{HH}^{*-1} \mathbf{S}_{HL}^* , \tag{4.130}$$

$$\tilde{\mathbf{S}}_{RL}^* = \mathbf{S}_{RL}^* - \mathbf{S}_{RH}^* \mathbf{S}_{HH}^{*-1} \mathbf{S}_{HL}^* , \tag{4.131}$$

$$\tilde{\mathbf{S}}_{LR}^* = \mathbf{S}_{LR}^* - \mathbf{S}_{LH}^* \mathbf{S}_{HH}^{*-1} \mathbf{S}_{HR}^* , \tag{4.132}$$

$$\tilde{\mathbf{S}}_{RR}^* = \mathbf{S}_{RR}^* - \mathbf{S}_{RH}^* \mathbf{S}_{HH}^{*-1} \mathbf{S}_{HR}^* . \tag{4.133}$$

The eigenvalue problem is than formulated

$$\mathbf{N}^* \begin{bmatrix} \mathbf{q}_L \\ \mathbf{q}_R \end{bmatrix} = \mu \mathbf{L}^* \begin{bmatrix} \mathbf{q}_L \\ \mathbf{q}_R \end{bmatrix} , \tag{4.134}$$

with

$$\mathbf{N}^* = \begin{bmatrix} \mathbf{0} & \mathbf{1} \\ \tilde{\mathbf{S}}_{RL}^* & \tilde{\mathbf{S}}_{RR}^* \end{bmatrix} , \tag{4.135}$$

$$\mathbf{L}^* = \begin{bmatrix} \mathbf{1} & \mathbf{0} \\ -\tilde{\mathbf{S}}_{LL}^* & -\tilde{\mathbf{S}}_{LR}^* \end{bmatrix} . \tag{4.136}$$

4.2.4 Comparison of the different methods of the WFEM

The following section compares the different methods in terms of accuracy and computation time. The accuracy of the methods results from the computation of a simple beam geometry for which an analytical expression is known. Subsequently, the comparison of the computation time is conducted on a more complex geometry. For both comparison, the author solves the different eigenvalue problems using MATLAB®'s eigensolver.

Accuracy of the different methods

A comparison of the solutions of the different approaches to the analytic relation of the Euler-Bernoulli beam theory assesses the accuracy of the different methods. The dispersion relation of an Euler-Bernoulli beam is given by

$$f = \frac{1}{2\pi}\sqrt{\frac{\rho A}{EI}}\kappa_{Re}^2 \; . \tag{4.137}$$

For this comparison, the numerical model of the unit cell consists of ten equally sized Euler-Bernoulli elements based on the element formulation of ANSYS®'s element BEAM3. The total length of the unit cell is 10 cm. The cross section A is 1 cm^2. I denotes the second moment of area. The beam consists of titanium ($E = 104\,\text{GPa}$, $\rho = 4430\,\text{kg\,m}^{-3}$). Table 4.4 lists the relative error of the wavenumber κ_{Re}. The different methods are labeled with the following abbreviations:

- Inverse - Inverse formulation of the WFEM

- TW - Transfer matrix formulation (direct)

- LR - Duhamel's LR method (direct)

- CW - Condensed WFEM (direct)

- ZW - Zhong's method (direct)

For this simple example the accuracy of the dispersion relation (4.137) is similar for the different methods. For a more detailed comparison, the following investigation compares the accuracy of the pairs of eigenvalues and eigenvectors. For the exact eigenvectors and eigenvalues the following expression vanishes

$$\mathbf{A}_{left}\mathbf{\Phi} - \mathbf{A}_{right}\mathbf{\Phi}\boldsymbol{\mu} = \mathbf{0} \tag{4.138}$$

Frequency	Inverse	TW	LR	CW	ZW
200 Hz	187.14	187.14	187.14	187.14	187.14
400 Hz	374.26	374.26	374.26	374.25	374.26
600 Hz	561.36	561.36	561.36	561.33	561.36
800 Hz	748.44	748.44	748.44	748.39	748.44
1000 Hz	935.49	935.49	935.49	935.42	935.49

Table 4.4: Comparison of the relative error of the wavenumber in 10^{-6} radians per meter for different frequencies.

$\boldsymbol{\Phi}$ is the matrix of right eigenvectors and $\boldsymbol{\mu}$ is the diagonal matrix of the respective eigenvalues. $\mathbf{A}_{left}$ and $\mathbf{A}_{right}$ are the matrices that define the eigenvalue problem

$$\det\left(\mathbf{A}_{left} - \mu\mathbf{A}_{right}\right) = 0 \; . \tag{4.139}$$

To assess the error of an approximated solution, the maximum metric $\|\Box\|_{max} = \max_{\forall i, \forall j} |\Box_{ij}|$ is applied

$$error = \|\mathbf{A}_{left}\boldsymbol{\Phi} - \mathbf{A}_{right}\boldsymbol{\Phi}\boldsymbol{\mu}\|_{max} \; . \tag{4.140}$$
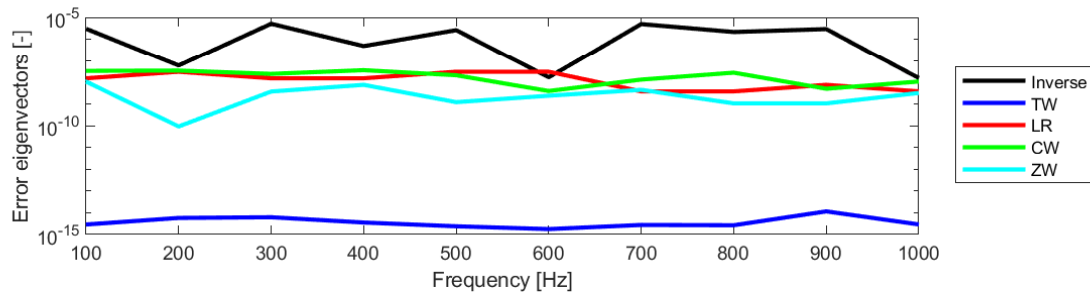
Figure 4.17: Comparison of the accuracy of the eigenvectors for different frequencies.

Figure 4.17 shows the norm (4.140) for the different methods. For most of the frequencies, the largest error occurs for the Inverse approach. The transfer matrix formulation yields the most accurate eigenvectors. However, it is difficult to compare the results of the transfer matrix formulation to the other solutions because the algorithm of MATLAB®'s eigensolver changes. The reason is that the formulation of the transfer matrix yields a symmetric matrix and therefore MATLAB®'s eigensolver uses the Cholesky factorization [Benoît 1924], whereas for the other formulations the matrices are not symmetric and the eigensolver applies the generalized Schur decomposition [Schur 1909]. The accuracy of the LR method and the Condensed WFEM is similar, whereas Zhong's method yields slightly better results.

Besides the accuracy of the eigenvectors, the condition numbers of the eigenvalue problem is

also relevant for evaluating the solution of the problem. Solving an ill-conditioned eigenvalue problem is numerically demanding and can yield to inaccurate results [Waki et al 2009]. Figure 4.18 shows the condition number of the matrices that are involved in the eigenvalue problem. The plus signs indicate the left matrices and the circles mark the right matrices of the respective eigenvalue problem. The transfer matrix formulation yields the largest condition number and it increases with increasing frequency. The condition numbers of the Condensed WFEM are slightly lower and also increase with increasing frequency, but with a smaller slope. The condition number of both matrices involved in the eigenvalue problem are similar. For 200 Hz, the left matrix of the inverse eigenvalue problem has similar condition numbers as the CW and the TW formulation, but it decreases with increasing frequency. In contrast, the condition number of the right matrix is almost constant and well below the condition number of the left matrix. Zhong's method generates the lowest condition numbers for both of the matrices involved in the eigenvalue problem. Finally, Duhamel's method introduces a slightly higher condition number than Zhong's method.
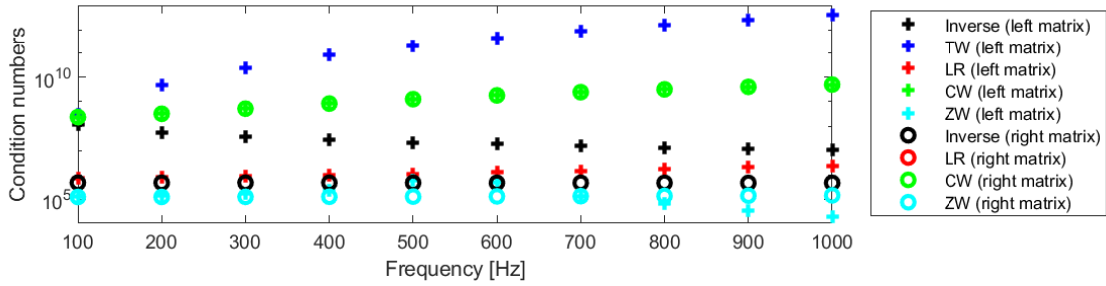
Figure 4.18: Comparison of the conditions of the eigenvalue problem for different frequencies.

In addition to the previously mentioned errors, discretization errors can occur. Due to the common discretization requirements using finite elements, there exists a minimum number of elements per wavelength to accurately describe the motion of the structure. According to Silva [2015], the element size should be at least one tenth of the wavelength in the structure and it is also possible to determine the required size of the element based on the phase diagram

$$\frac{L}{4n} > l_{ele} \,. \tag{4.141}$$

L is the length of the unit cell, l_{ele} the element size and n the number of crosses by π or zero in the phase diagram.

Besides the upper limit from (4.141), the WFEM also requires a lower limit. The reason is that using element size in the range of the machine accuracy results in errors in the wave
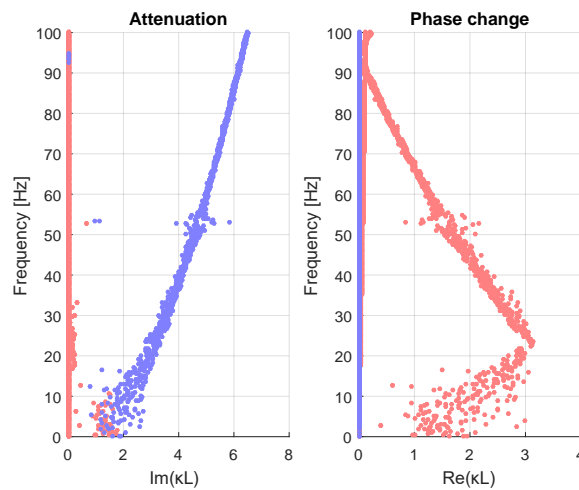
Figure 4.19: Wave solutions of a one dimensional model of an Euler-Bernoulli beam (ANSYS®'s element formulation BEAM3) with numerical errors due to a very small element size with respect to the wavelength; from [Perez Ramirez 2017].

solutions [Mace et al 2005]. Figure 4.19 shows the wave solutions of a unit cell with numerical errors due to an element size in the range of the machine accuracy. The small size of the element deteriorates the phase and decay characteristics at lower frequencies. The reason is the small change of the phase at low frequencies for wave traveling trough the unit cell. The phase change is comparable to the machine accuracy. Consequently, at lower frequencies the truncation error in the numerical computations disperse the phase.

Computation time

The following section presents the comparison of the computation time of the different methods using a more complex geometry. This comparison is conducted for a geometry with different numbers of degrees of freedom (DOF). Table 4.5 lists the number of internal and boundary DOF.

models	DOF	internal DOF	boundary DOF
2×2 cells	3270	3090	180
2×4 cells	6450	6270	180
2×6 cells	9630	9450	180

Table 4.5: Number of degrees of freedoms (DOF) of the different models.

The models consists of an arrangement of honeycomb cells with integrated resonant sub-structures. The three models with 2×2, 2×4 and 2×6 cells have a fixed number of boundary DOF while the number of internal DOF increase. The boundary DOF lie on the red edges marked in the model shown in figure 4.20.
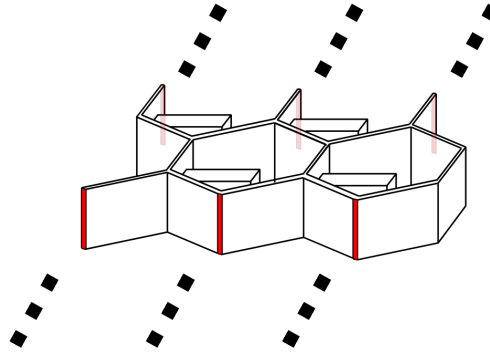
Figure 4.20: Model of a honeycomb structure with integrated resonant substructures (2×2 cells) that forms a infinite periodic structure; the red colored edges mark the boundaries which are linked by the Bloch theorem.

The computation of the waves that travel through the periodic structure requires several intermediate tasks. First, the model setup requires sorted system matrices according to the interior and boundary DOF of the unit cell. Second, each phase step requires the computation of an eigenvalue problem.
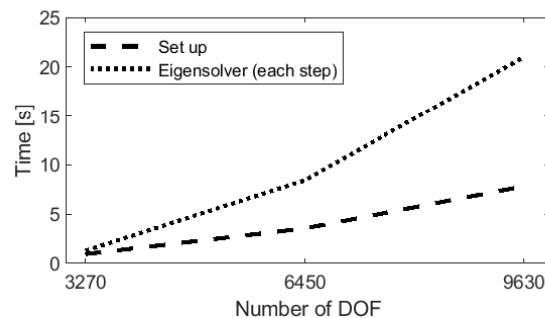
Figure 4.21: Computation time using the inverse approach of the WFEM applied to the different models.

Figure 4.21 shows the computation times for the different models using the inverse approach. The computational costs for setting up the model are smaller than solving the eigenvalue problem and are not of great relevance for the overall cost as it only arises once. The computation of the eigenvalue problem requires the greatest computational effort. These costs arise for each step (phase step) and therefore have a strong impact on the overall computation time. The computation time exponentially increases with increasing number of DOF.

In contrast to the inverse approach, the direct approach needs additional tasks before and after solving the eigenvalue problem. The computation time of these tasks depend on the number of interior and boundary DOF. Besides setting up the model, the direct approach condensates the interior DOF to generate the matrices for the eigenvalue problem (in each frequency step). Figure 4.22 compares the computation time of the different tasks for the models with varying internal DOF.

Figure 4.22: Computation time using the direct approach of the WFEM applied to different models with increasing number of internal degrees of freedoms (DOF); number of boundary DOF are the same for the models.

The transfer matrix formulation, Duhamel's LR method, and Zhong's method require a similar amount of time for setting up the model. As the computation is relatively small and it only arises once, it can be neglected. The costs for setting up the model for the Condensed WFEM increases strongly with increasing number of interior DOF. The reason is the computation of the static boundary and the internal modes. These computations require a matrix inversion and solving an eigenvalue problem. Due to the mapping of the interior DOF on a reduced space the evaluation of the matrices for the eigenvalue problem is significantly reduced. In comparison to the other methods, the Condensed WFEM reduce the time to find the matrices for the eigenvalue problem up to 80%. Zhong's method needs slightly more time than the transfer matrix formulation and Duhamel's LR method because it needs more matrix operations. The cost for solving the eigenvalue problem is similarly small and does not depend on the number of internal DOF. Due to the form of the formulation of the transfer matrix formulation, the eigenvalue problem is solved most rapidly. Due to the symmetric transfer matrix, MATLAB®'s eigensolver uses the Cholesky factorization [Benoît 1924], whereas for the other formulations the matrices are not symmetric and the eigensolver applies the generalized Schur decomposition [Schur 1909].
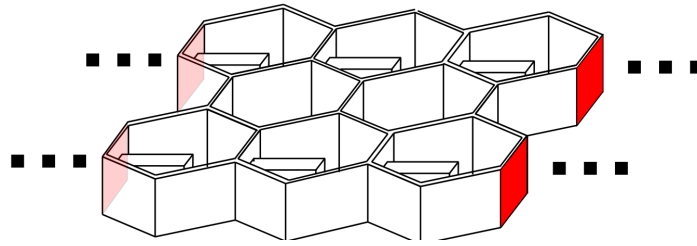
Figure 4.23: Model of a honeycomb structure with integrated resonant substructures (2×3 cells) that forms a infinite periodic structure; the red colored faces mark the boundaries which are linked by the Bloch theorem.

The next section investigates another set of unit cells where the amount of internal DOF are (almost) constant and the number of boundary DOF vary. The models consists of six honeycomb cells with integrated resonator.

models	DOF	internal DOF	boundary DOF
1×6 cells	5790	5370	420
2×3 cells	6450	5610	840
3×2 cells	6810	5550	1260

Table 4.6: Number of degrees of freedoms (DOF) of the different models with increasing numbers of boundary DOF.

Figure 4.23 shows an exemplary model. The 1×6 cells model has two boundary faces, the 2×3 cells model has four boundary faces and the 3×2 cells model has six boundary faces. As mentioned in section 4.2.3, the transfer matrix formulation might generate ill-conditioned eigenvalue problems.
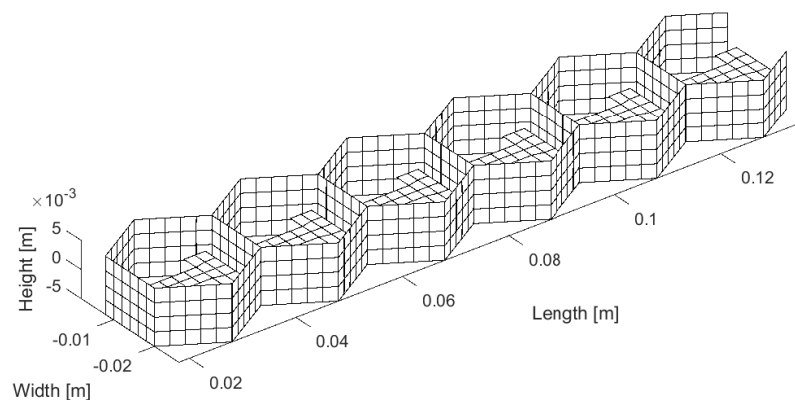
Figure 4.24: Finite element mesh of the unit cell model with 1x6 cells.
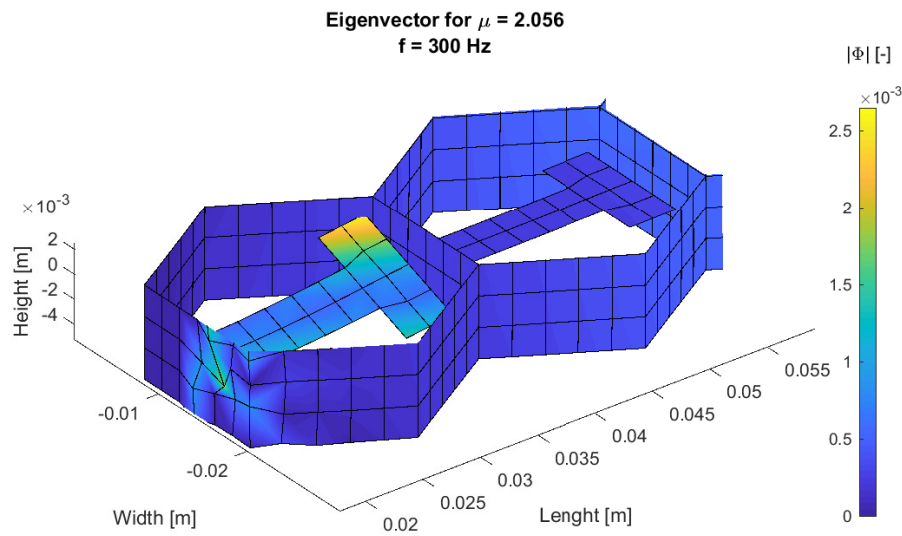
Figure 4.25: Exemplary visualization of an eigenvector that describes the wave motion in the unit cell of a rapidly decreasing evanescent wave.

Figure 4.24 shows the finite element mesh for the 1×6 cells model. The eigenvalue formulation (4.101) yields $2n$ eigenvalues where n is the number of DOF at the left and right boundary of the cell. The 1×6 cells model has 420 boundary DOF, which results in 420 wave solutions for each frequency. For a fixed frequency, there exist only a limit amount of propagating waves. The rest of the wave solutions represent evanescent waves that rapidly decay.

Figure 4.25 shows the eigenvector for such a rapidly decreasing evanescent wave. These wave solution are required when the wave motion is prescribed at the boundaries. Therefore, the number of evanescent waves is linked to the number of boundary DOF. Increasing the number of boundary DOF also increases the number of evanescent wave solutions. Multiple strongly decreasing wave solutions result in multiple almost identical eigenvalues. The respective matrix of eigenvectors can be poorly conditioned [Golub et al 1996]. For the transfer matrix formulation (TW), the ill-conditioning of the eigenvectors leads to numerical problems that makes the eigenvalue problem not solvable for the presented models in table 4.6. Therefore, the following comparison excludes the TW formulation.

In figure 4.26, one observes that the time for setting up the model and the time for the computation of the matrices for the eigenvalue problem do not strongly depend on the number of boundary DOF. As previously, the Condensed WFEM needs most time for setting up the model, however it strongly reduces the time to find the matrices for the eigenvalue problem formulation. Zhong's method needs slightly more time than Duhamel's LR method
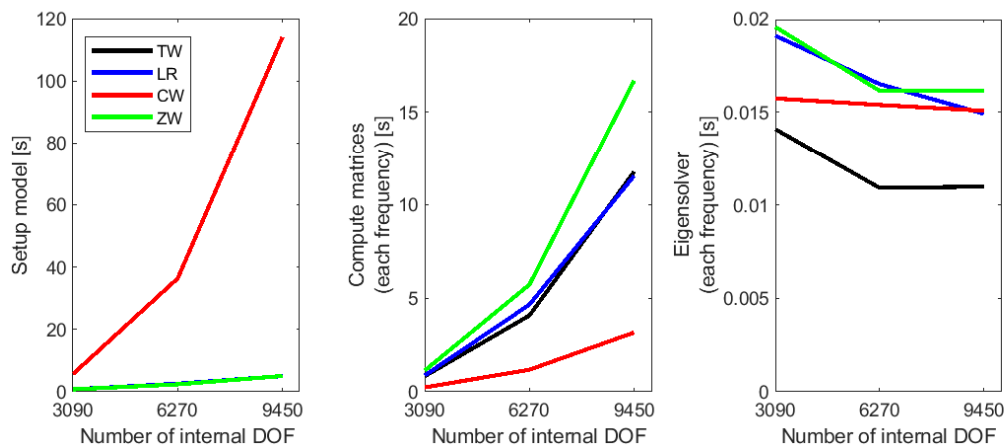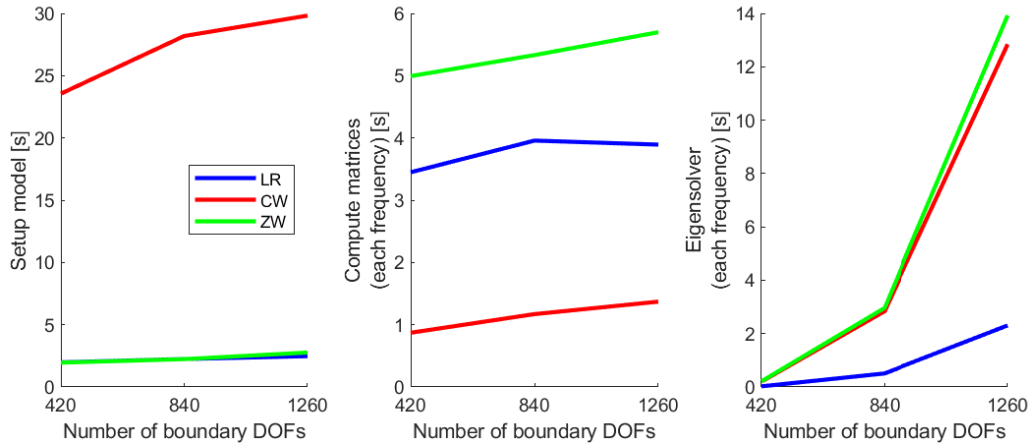
Figure 4.26: Computation time using the direct approach of the WFEM applied to different models with increasing number of boundary degrees of freedoms (DOF); number of internal DOF are almost equal for the models.

because it requires more matrix operations. The cost for solving the eigenvalue problem increases exponentially with the number of boundary DOF. The computation time for the eigenvalue problem of Duhamel's method is the smallest.

Regarding the total computation time, the Condensed WFEM is the best direct formulation if a lot of frequency steps are evaluated. The reason is the low cost for the evaluation of each frequency. Therefore, the additional costs for the model set up are usually well invested as the benefit of the time reduction comes into effect each step. In terms of computation time, the transfer matrix formulation and Duhamel's LR method are better than Zhong's method. For very small models the transfer matrix formulation yields fast and accurate results. However, the transfer matrix formulation shows problems solving the eigenvalue problem when the unit cell model has large number of boundary DOFs. In terms of the conditioning, Zhong's method yields most beneficial conditioning of the eigenvalue problem. Nevertheless, the Condensed WFEM and the Duhamel's approach can also accurately solve larger models.

4.2.5 Computation of the frequency response function (FRF) based on the wave solutions

Using a direct formulation to solve for the wave solutions, it is possible to compute the FRF. Each of the $2r$ eigenvalues μ_i computed with one of the previous mentioned direct formulations has a corresponding right eigenvector $\mathbf{\Phi}_i$. Each eigenvector relates the wave

amplitudes to the displacements $\underline{\mathbf{q}}$ and the forces $\underline{\mathbf{f}}$ at the boundary of the unit cell

$$\mathbf{\Phi}_i = \begin{bmatrix} \mathbf{\Phi}_q \\ \mathbf{\Phi}_f \end{bmatrix}_i . \tag{4.142}$$

For the computation of the forced response of a structure consisting of an alignment of several unit cells, it is crucial to distinguish the positive and negative going waves. Mace et al [2005] distinguish the propagation direction of the waves checking the absolute value of the eigenvalues. Waves related to eigenvalues with $\|\mu_i\| < 1$ propagate in the positive direction and waves with $\|\mu_i\| > 1$ propagate in the negative direction. For eigenvalues with $\|\mu_i\| = 1$, the sign of the power flow determines the propagation direction. For waves traveling in the positive direction the power flow is positive. The power flow of each wave is the real part of the dot product of the force contribution and the velocity contribution of the eigenvector

$$P = \mathrm{Re}\{(\mathbf{\Phi}_f)^T (i\Omega \mathbf{\Phi}_q)^*\} . \tag{4.143}$$

For symmetric unit cells, the positive and negative going waves are symmetric as well. That means that the eigenvalues and -vectors of forward traveling waves also define the backward traveling waves

$$\mu_i^- = 1/\mu_i^+ , \tag{4.144}$$
$$\mathbf{\Phi}_q^- = \mathbf{W}\mathbf{\Phi}_q^+ , \tag{4.145}$$
$$\mathbf{\Phi}_f^- = -\mathbf{W}\mathbf{\Phi}_f^+ . \tag{4.146}$$

The minus sign for the force eigenvectors $\mathbf{\Phi}_f$ results from the force relation (4.76). $\mathbf{W}$ is a $r \times r$ matrix with

$$\mathbf{W} = \begin{bmatrix} 1 & 0 & \dots & \dots & \dots & 0 \\ 0 & \ddots & \ddots & \ddots & \ddots & \vdots \\ \vdots & \ddots & 1 & \ddots & \ddots & \vdots \\ \vdots & \ddots & \ddots & -1 & \ddots & \vdots \\ \vdots & \ddots & \ddots & \ddots & \ddots & 0 \\ 0 & \dots & \dots & \dots & 0 & -1 \end{bmatrix} . \tag{4.147}$$

Due to round off errors that occur during the numerical computation of the wave modes, Mencik [2014] recommends to enforce the relation (4.144)-(4.146) analytically to avoid numerical dispersion. The following relations proof the symmetry of the wave shapes (eigenvectors)

$$\tilde{\mathbf{S}}_{RR} = \mathbf{W}^T \tilde{\mathbf{S}}_{LL} \mathbf{W} \, , \tag{4.148}$$

$$\tilde{\mathbf{S}}_{RL} = \mathbf{W}^T \tilde{\mathbf{S}}_{LR} \mathbf{W} \, . \tag{4.149}$$

These relations are also valid for non-symmetric finite element meshes, as long as the mesh describing the unit cell is fine enough to accurately describe the wave shapes at the interfaces [Mencik 2014].

The eigenvalues and the eigenvectors, representing the wave solutions of a unit cell, relate the displacements and forces at the boundary of each unit cell to the wave amplitudes $\mathbf{Q}$

$$\begin{bmatrix} \mathbf{q}_L \\ -\mathbf{f}_L \end{bmatrix}_n = \begin{bmatrix} \mathbf{q}_R \\ \mathbf{f}_R \end{bmatrix}_n = \begin{bmatrix} \mathbf{\Phi}_q^+ & \mathbf{\Phi}_q^- \\ \mathbf{\Phi}_f^+ & \mathbf{\Phi}_f^- \end{bmatrix} \begin{bmatrix} \mathbf{Q}^+ \\ \mathbf{Q}^- \end{bmatrix}_n \, . \tag{4.150}$$

$\mathbf{Q}$ are complex amplitudes that scales the eigenvectors related to the displacements and the forces. Knowing all wave solutions that can propagate in the structure, it is possible to compute the FRF of a periodic structure that consists of n unit cells in the wave domain.
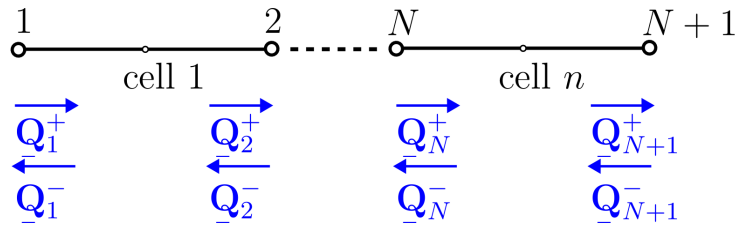
Figure 4.27: Wave amplitudes of positive and negative going waves of a periodic structure consisting of n unit cells.

According to the Bloch theorem, the eigenvalues describes the relation between the wave amplitudes inside the periodic structures

$$\begin{bmatrix} \mathbf{Q}^+ \\ \mathbf{Q}^- \end{bmatrix}_{N+1} = \begin{bmatrix} \boldsymbol{\mu}^+ & \mathbf{0} \\ \mathbf{0} & \boldsymbol{\mu}^- \end{bmatrix} \begin{bmatrix} \mathbf{Q}^+ \\ \mathbf{Q}^- \end{bmatrix}_N \, . \tag{4.151}$$

Using this equation, the wave amplitudes of the positive going waves at the right end of the

structure determine the wave amplitudes at the left end of the structure

$$\mathbf{Q}_{N+1}^{+} = [\boldsymbol{\mu}^{+}]^{N} \mathbf{Q}_{1}^{+} . \tag{4.152}$$

A similar expression holds for the negative going wave amplitudes

$$\mathbf{Q}_{1}^{-} = [\boldsymbol{\mu}^{+}]^{N} \mathbf{Q}_{N+1}^{-} . \tag{4.153}$$

Consequently, the wave amplitudes traveling from the left and right end into the structure describe the motion of the structure [Mencik 2014].
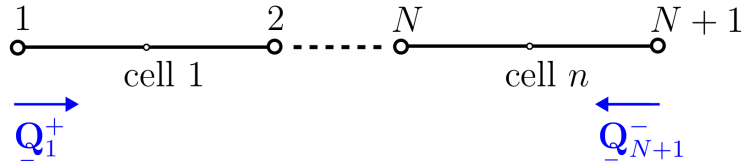
Figure 4.28: Wave amplitudes of waves that travel into the structure.

In a further step, it is possible to fulfill different boundary conditions at the boundaries of the structure. Equations (4.150), (4.152) and (4.153) formulate the boundary condition for the left end of the structure

$$\begin{bmatrix} \mathbf{q}_{1} \\ -\mathbf{f}_{1} \end{bmatrix} = \begin{bmatrix} \boldsymbol{\Phi}_{q}^{+} & \boldsymbol{\Phi}_{q}^{-}[\boldsymbol{\mu}^{+}]^{N} \\ \boldsymbol{\Phi}_{f}^{+} & \boldsymbol{\Phi}_{f}^{-}[\boldsymbol{\mu}^{+}]^{N} \end{bmatrix} \begin{bmatrix} \mathbf{Q}_{1}^{+} \\ \mathbf{Q}_{N+1}^{-} \end{bmatrix} . \tag{4.154}$$

The minus sign in front of the applied force $\mathbf{f}_{1}$ comes from the fact that it is the left boundary force of the first unit cell. Accordingly, the boundary conditions for the right end are

$$\begin{bmatrix} \mathbf{q}_{N+1} \\ \mathbf{f}_{N+1} \end{bmatrix} = \begin{bmatrix} \boldsymbol{\Phi}_{q}^{+}[\boldsymbol{\mu}^{+}]^{N} & \boldsymbol{\Phi}_{q}^{-} \\ \boldsymbol{\Phi}_{f}^{+}[\boldsymbol{\mu}^{+}]^{N} & \boldsymbol{\Phi}_{f}^{-} \end{bmatrix} \begin{bmatrix} \mathbf{Q}_{1}^{+} \\ \mathbf{Q}_{N+1}^{-} \end{bmatrix} . \tag{4.155}$$

At each DOF, there is either a prescribed displacement or a prescribed force. As a consequence, at the left and right end of the structure there are r equations. Thus, solving the $2r$ equations yields the unknown wave amplitudes $\mathbf{Q}_{1}^{+}$ and $\mathbf{Q}_{N+1}^{-}$. Applying a force $\mathbf{f}_{0}$ to the left side of the structures and a displacement $\mathbf{q}_{0}$ to the right end of the structure, the system of equations to solve is

$$\begin{bmatrix} \boldsymbol{\Phi}_{q}^{+}[\boldsymbol{\mu}^{+}]^{N} & \boldsymbol{\Phi}_{q}^{-} \\ \boldsymbol{\Phi}_{f}^{+} & \boldsymbol{\Phi}_{f}^{-}[\boldsymbol{\mu}^{+}]^{N} \end{bmatrix} \begin{bmatrix} \mathbf{Q}_{1}^{+} \\ \mathbf{Q}_{N+1}^{-} \end{bmatrix} = \begin{bmatrix} \mathbf{q}_{0} \\ -\mathbf{f}_{0} \end{bmatrix} . \tag{4.156}$$

The minus sign in front of the force $\underline{\mathbf{f}}_0$ results from the fact that the force is applied to the left side of a unit cell.

Coupling of multiple wave guides

In general, it is possible to couple multiple periodic structures with interfaces defined by a change of the unit cell or by external loads. The following section explains the general procedure using a pinned beam that is loaded in the center.
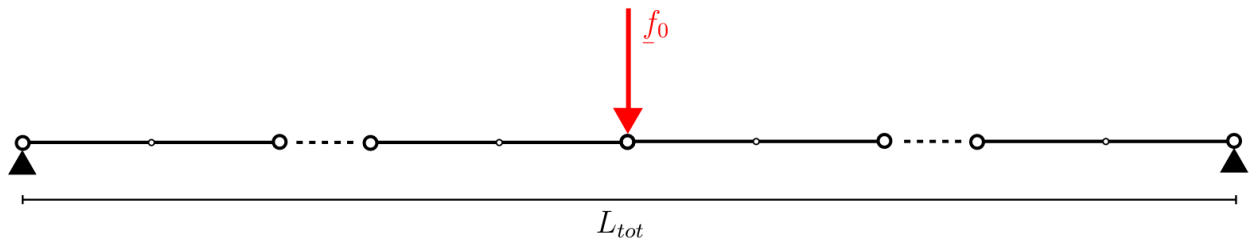
Figure 4.29: Model of a pinned beam that is loaded with a force.

To be able to define boundary conditions in the center of the beam, one divides the structure into two separate wave guides.
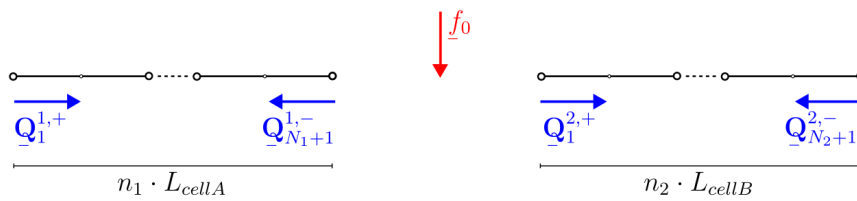
Figure 4.30: Division of the pinned beam into two segments.

At each interface, it is possible to prescribe displacements or forces. In this example the unit cell consists of two Euler-Bernoulli beams with a vertical and a rotational DOF at each node.
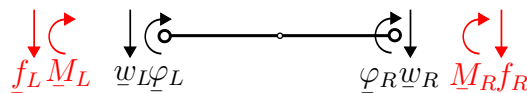
Figure 4.31: Degrees of freedom (DOF) and forces at the boundaries of the unit cell consisting of two Euler-Bernoulli beam.

Two degrees of freedom at each boundary result in four wave solutions: two positive and two negative going waves. Thus, there are four unknown wave amplitudes in each segment. The

eigenvectors (wave shapes) have the size 4×1, as they relate the wave amplitude of each wave shape to two displacements and two forces.

For the system described in figure 4.30, there are eight equations in the wave domain. The boundary conditions according to (4.154) at the left end of the structure are

$$
\begin{bmatrix} w_1^1 \\ \varphi_1^1 \\ -f_1^1 \\ -M_1^1 \end{bmatrix} = \underbrace{\begin{bmatrix} \boldsymbol{\Phi}_q^+ & \boldsymbol{\Phi}_q^-[\boldsymbol{\mu}^+]^{N_1} \\ \boldsymbol{\Phi}_f^+ & \boldsymbol{\Phi}_f^-[\boldsymbol{\mu}^+]^{N_1} \end{bmatrix}}_{\mathbf{A}_L^1} \begin{bmatrix} \mathbf{Q}_1^{1,+} \\ \mathbf{Q}_{N_1+1}^{1,-} \end{bmatrix} = \begin{bmatrix} 0 \\ ? \\ ? \\ 0 \end{bmatrix} .
\tag{4.157}
$$

The rotation φ_1^1 and the vertical force f_1^1 are unknown. Accordingly, the boundary conditions for the right end of the structure are

$$
\begin{bmatrix} w_{N_2+1}^2 \\ \varphi_{N_2+1}^2 \\ f_{N_2+1}^2 \\ M_{N_2+1}^2 \end{bmatrix} = \underbrace{\begin{bmatrix} \boldsymbol{\Phi}_q^+[\boldsymbol{\mu}^+]^{N_2} & \boldsymbol{\Phi}_q^- \\ \boldsymbol{\Phi}_f^+[\boldsymbol{\mu}^+]^{N_2} & \boldsymbol{\Phi}_f^- \end{bmatrix}}_{\mathbf{A}_R^2} \begin{bmatrix} \mathbf{Q}_1^{2,+} \\ \mathbf{Q}_{N_2+1}^{2,-} \end{bmatrix} = \begin{bmatrix} 0 \\ ? \\ ? \\ 0 \end{bmatrix} .
\tag{4.158}
$$

Further equations result from the continuity of the deformation and the force equilibrium at the interface

$$
\begin{bmatrix} w_{N_1+1}^1 \\ \varphi_{N_1+1}^1 \end{bmatrix} + \begin{bmatrix} -w_1^2 \\ -\varphi_1^2 \end{bmatrix} = \begin{bmatrix} 0 \\ 0 \end{bmatrix} ,
\tag{4.159}
$$

$$
\begin{bmatrix} f_{N_1+1}^1 \\ M_{N_1+1}^1 \end{bmatrix} + \begin{bmatrix} f_1^2 \\ M_1^2 \end{bmatrix} = \begin{bmatrix} -f_0 \\ 0 \end{bmatrix} .
\tag{4.160}
$$

The following expression summarizes the coupling conditions in the wave domain

$$
\underbrace{\begin{bmatrix} \boldsymbol{\Phi}_q^+[\boldsymbol{\mu}^+]^{N_1} & \boldsymbol{\Phi}_q^- \\ \boldsymbol{\Phi}_f^+[\boldsymbol{\mu}^+]^{N_1} & \boldsymbol{\Phi}_f^- \end{bmatrix}}_{\mathbf{A}_R^1} \begin{bmatrix} \mathbf{Q}_1^{1,+} \\ \mathbf{Q}_{N_1+1}^{1,-} \end{bmatrix} - \underbrace{\begin{bmatrix} \boldsymbol{\Phi}_q^+ & \boldsymbol{\Phi}_q^-[\boldsymbol{\mu}^+]^{N_2} \\ \boldsymbol{\Phi}_f^+ & \boldsymbol{\Phi}_f^-[\boldsymbol{\mu}^+]^{N_2} \end{bmatrix}}_{\mathbf{A}_L^2} \begin{bmatrix} \mathbf{Q}_1^{2,+} \\ \mathbf{Q}_{N_2+1}^{2,-} \end{bmatrix} = \begin{bmatrix} 0 \\ 0 \\ -f_0 \\ 0 \end{bmatrix} .
\tag{4.161}
$$

The minus sign in front of matrix $\mathbf{A}_L^2$ comes from the fact that the displacement at the interface should be equal and that the forces of the left and right of the interface have opposite sign (see (4.150)).

Summarizing the boundary conditions of the left end (4.154) and of the right end (4.155) with the coupling conditions (4.161) yields the following system of equations

$$
\begin{bmatrix}
\mathbf{A}_L^1(1,:) & \mathbf{0} \\
\mathbf{A}_L^1(4,:) & \mathbf{0} \\
\hdashline
\mathbf{A}_R^1 & -\mathbf{A}_L^2 \\
\hdashline
\mathbf{0} & \mathbf{A}_R^2(1,:) \\
\mathbf{0} & \mathbf{A}_R^2(4,:)
\end{bmatrix}
\begin{bmatrix}
\underline{\mathbf{Q}}_1^{1,+} \\
\underline{\mathbf{Q}}_{N_1+1}^{1,-} \\
\underline{\mathbf{Q}}_1^{2,+} \\
\underline{\mathbf{Q}}_{N_2+1}^{2,-}
\end{bmatrix}
=
\begin{bmatrix}
0 \\
0 \\
\hdashline
0 \\
0 \\
-\underline{f}_0 \\
0 \\
\hdashline
0 \\
0
\end{bmatrix} .
\tag{4.162}
$$

Figure 4.32 shows the frequency response function of the pinned beam evaluated at different locations L of the beam. It illustrates the response of the structure from 0 to 1000 Hz in discrete steps of 1 Hz. The length of the beam L_{tot} is 1 m and the load $\underline{f}_0$ equals 100 N. The left and right segments both consist of 20 unit cells ($n_1 = n_2 = 20$) and each unit cell comprises two Euler-Bernoulli beam elements. The cross section A of the beam is rectangular and measures 10^{-4} m^2. The material's density ρ and Young's modulus E are 7800 kg/m^3 and $2 \cdot 10^{11}$ N/m^2, respectively.
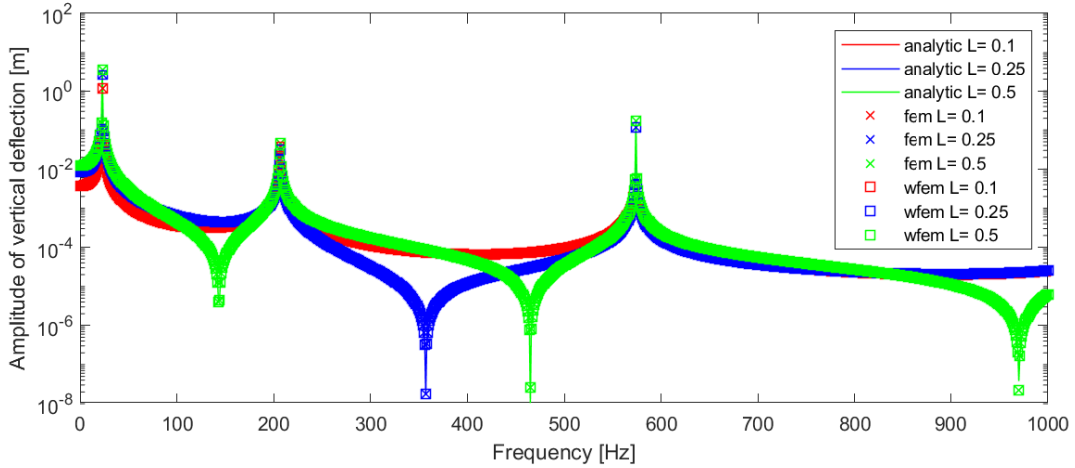
Figure 4.32: Frequency response at different positions of the pinned beam loaded with a central force; analytical solution and numerical solutions with FEM and WFEM.
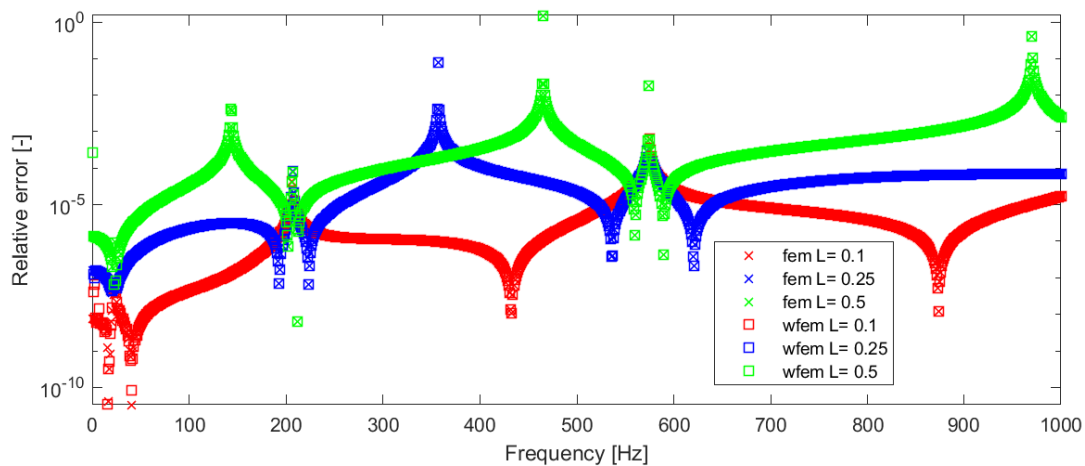
Figure 4.33: Error plot of the solution from FEM and WFEM.

Both the WFEM and the FEM solution converge to the analytical solution. The analytical solution is extracted from [Blevins 2016]. The wave solutions are computed using Duhamel's formulation. Figure 4.33 shows the relative error between the analytical solution and the numerical methods. Besides the frequency range from 0 to 50 Hz, the error of the WFEM and FEM is almost identical for all frequencies. The relative error is computed using

$$error = \frac{\|u_{numerical} - u_{analytical}\|}{\|u_{analytical}\|} \tag{4.163}$$

The previous procedure also holds for more complex unit cells. The following example shows the effect of a periodic resonator. Figure 4.34 illustrates the modified unit cell. The mass of the resonator is 5% of the mass of the unit cell. The target frequency of the resonator (207 Hz) determines the spring stiffness k_s. The damping ratio of the resonator is 0.01. Figure 4.35 compares the FRF function of the pinned beam with periodic resonators using WFEM and FEM. Both methods capture the effect of the resonator. The resonator reduces the vibration of the beam at 207 Hz and splits the resonance peak of the original structure into two resonance peaks at 185 Hz and 231 Hz.
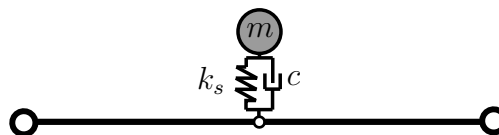
Figure 4.34: Modified unit cell.
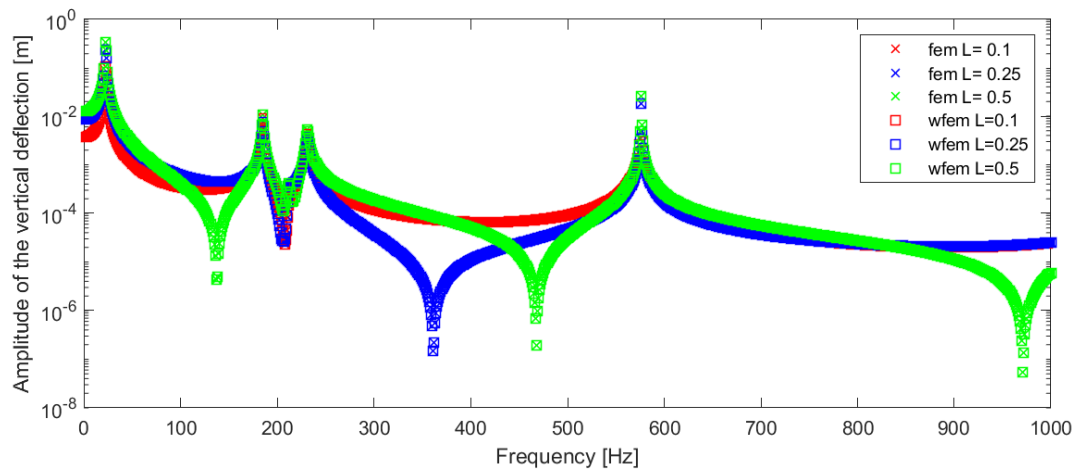
Figure 4.35: Frequency response at different positions of the pinned beam loaded with a central force and applied resonators; numerical solutions with FEM and WFEM.

5 Numerical studies

The following chapter discusses several numerical studies. The first part focuses on the acoustic black hole (ABH) effect. The author compares various ABH configurations and evaluates their vibroacoustic performance in terms of vibration suppression and sound radiation. The second part presents numerical studies for the design of locally resonant materials. The focus of this part is the study of periodic resonators. Besides the dimensioning of the resonators based on the wave solutions, additional studies explain the effect of the resonators on the radiated sound power.

5.1 Studies on the acoustic black hole effect

The author published some preliminary results of the following section in various publications [Miksch 2017; Miksch et al 2018a,b]. Section 5.1.1 demonstrates the focalization effect of ABH. Section 5.1.2 investigates different thickness profiles in beams. This chapter focus on the general effect of the different profiles on the vibration and the sound radiation. Section 5.1.3 evaluates the energy levels of single and multiple ABH configurations in plates. The studies presented in this chapter spawn design criteria for ABH in plate-like structures. Section 5.1.4 summarizes the results of the numerical studies about the ABH effect.

5.1.1 The focalization property of acoustic black holes

This section demonstrates the focalization effect of a single ABH embedded in the middle of a plate. To show the focalization characteristic of a smooth thickness profile the structural intensity (STI) is a suitable quantity to describe the response. It gives directional information about the power flow and its magnitude. The STI is computed by a multiplication of the stress tensor with the complex conjugate of the velocity vector [Pavic 1987]: $\mathbf{I} = -\frac{1}{2}\operatorname{Re}\{\underline{\boldsymbol{\sigma}}\,\underline{\mathbf{v}}^*\}$. In the appendix A.6, there is a detailed description how to evaluate the STI using a discretized finite element model.

(a) Numerical model of a plate with an embedded ABH.

(b) Numerical model of a uniform plate.
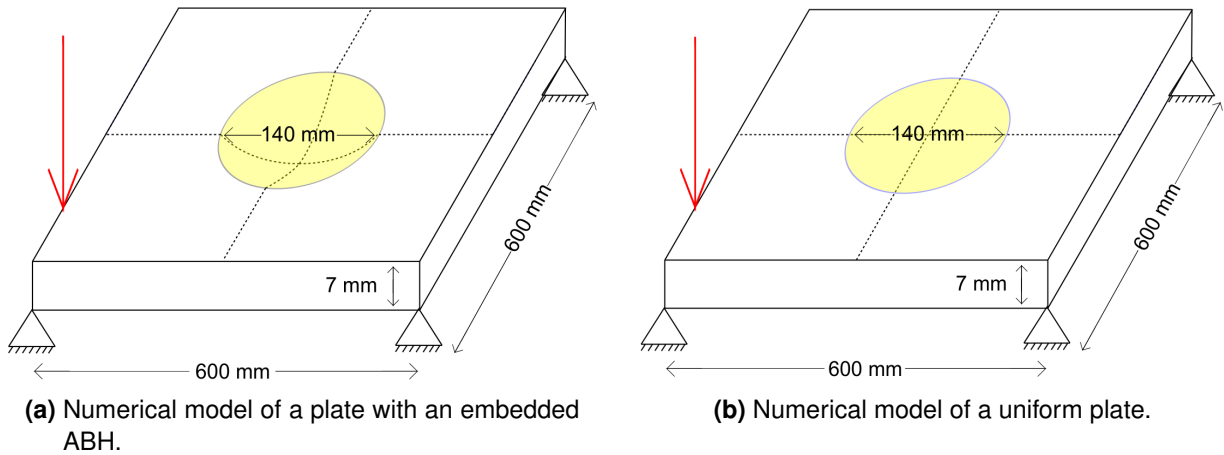
Figure 5.1: Comparison of a ABH and uniform plate; the ABH region is marked yellow.

To demonstrate the focalization of an ABH, the following section compares the STI of an ABH plate and a uniform plate of similar dimensions. The dimensions of the plates are $600 \times 600 \times 7$ mm and the plates are clamped at all four corners. A harmonic point load at one edge (200 mm shifted from the corner) excites the plate. Table 5.1 lists the material properties of the plate. The thickness profile of the ABH is rotational symmetric and has the form: $h(r) = \epsilon x^{2.2} + h_{min}$. ϵ is adjusted such that the diameter of the ABH is 140 mm and the residual thickness h_{min} is 2 mm.

Density	2770 kg/m^3
Young's Modulus	$7.1 \cdot 10^{10}$ Pa
Poisson's ratio	0.33
Damping coefficient	0.001

Table 5.1: Material properties of the plate.

Figure 5.2 visualizes the STI at 2881 Hz and 4301 Hz. The vector plots at the top of the figure show the STI of the ABH plates and the plots on the bottom the STI of the uniform plate, respectively. The vector plots on the left are related to the frequency of 2881 Hz and the plots on the right correspond to the excitation frequency of 4301 Hz. The plot in the middle shows the percentage of energy located in the middle region of the plate. This region is marked with yellow color in figure 5.1.
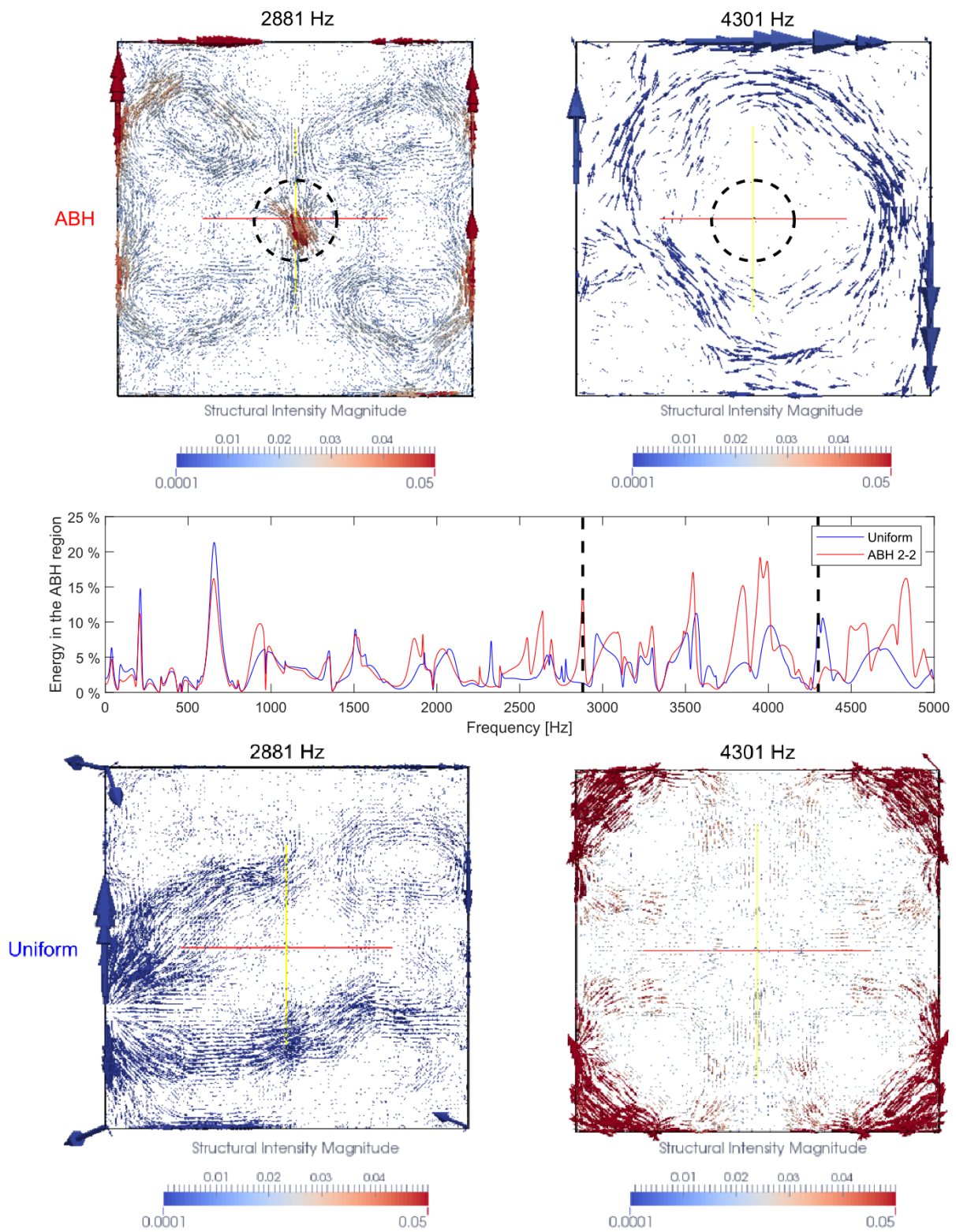
Figure 5.2: Structural intensities of the ABH plate (top) and the uniform plate (bottom) at 2881 Hz and 4301 Hz.

At 2881 Hz, the ABH plate focuses more energy in the ABH region than the uniform plate (see middle plot in figure 5.2). The ABH here works as a focusing lens for the energy. The STI indicate that the power is guided towards the center of the ABH while the magnitude of the STI increases. The boundary conditions of the plate explain the large intensities at the edges of the plate. Due to the fixed supports at the four corners of the plate, a large amount of the energy flows towards the corners of the plate. At 4301 Hz, the uniform plate accumulates more energy in the center area of the plate. The amount of energy is comparable to the amount of energy of the ABH plate at 2881 Hz, but the STI vector plot of the uniform plate at 4301 Hz does not show any focalization characteristic in the power flow. The STI of the ABH plate show a circulation of the power flow around the ABH.

Concluding, there exist frequencies where the ABH plate works as a focusing lens for the energy. Nevertheless, it is difficult to identify spots for potential ABH placements. The example shows that locations, where the uniform plate shows an increased energy accumulation, are not generally beneficial placing locations for ABH. An ABH that strongly influences the overall behavior of the structure can also result in a smaller energy accumulation at the desired location. Consequently, it is difficult to derive the optimal locations of an ABH from the original unmodified structures.

5.1.2 Beam-like structures with local thickness variations

The following section investigates different one dimensional ABH configurations and their influence on the vibrational behavior of the structure and the radiated sound power. Figure 5.3 shows the investigated thickness profiles.

Figure 5.3: Labeling of the different thickness profiles made of titanium (black) and a damping material (green).

The beams have a length of $800\,\mathrm{mm}$ and a thickness of $3\,\mathrm{mm}$. The beams consist of titanium. The thickness profiles follow the mathematical expression $h(x) = \epsilon x^\beta + h_{min}$ with $h_{min} = 1\,\mathrm{mm}$. The diameter of $200\,\mathrm{mm}$ defines the parameter ϵ. The following paragraph compares the performance of a uniform beam, a beam modified by an abrupt thickness reduction

with $\beta = \infty$ (ABH step) and a smooth thickness reduction with $\beta = 2.2$ (ABH 2.2). The investigation includes the influence of an additional constrained layer damping (CLD) in the vicinity of the thickness profiles. The CLD consists of a $1\,\mathrm{mm}$ layer of damping material covered by an $1\,\mathrm{mm}$ layer of titanium. Table 5.2 lists the material properties of titanium and the applied damping material. Damping is introduced using a structural loss factor. The loss factor of titanium is 0.001 and the loss factor of the damping material is 0.1.

Table 5.2: Material properties of titanium and the damping material.

	Titanium	Damping material
E	$104\,\mathrm{GPa}$	$0.01\,\mathrm{GPa}$
ρ	$4430\,\mathrm{kg\,m^{-3}}$	$1000\,\mathrm{kg\,m^{-3}}$
ν	0.31	0.45
η	0.001	0.1

The beams are modeled using two dimensional plane stress elements. The FE-models have ten elements through the thickness of the beam. The computation of the FRF follows the approach of the modal superposition. This offers the opportunity to apply the load in the modal space. A unit modal force for each mode ($\mathbf{\Phi}^T \underline{\mathbf{f}} = \mathbf{1}$) excites all modes. The eigenvectors are mass-normalized ($\mathbf{\Phi}_i^T \mathbf{M} \mathbf{\Phi}_i = 1$).
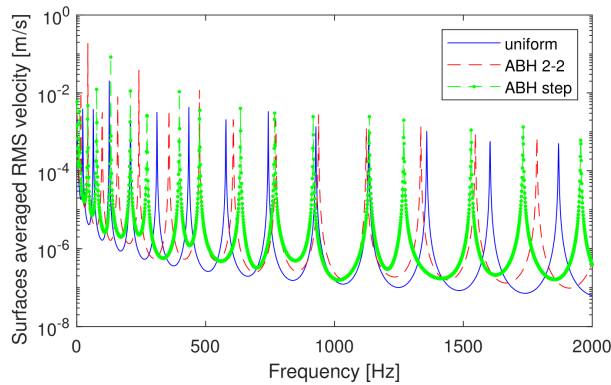
Figure 5.4: Surface integrated vertical velocity for beams with different thickness profiles without CLD.
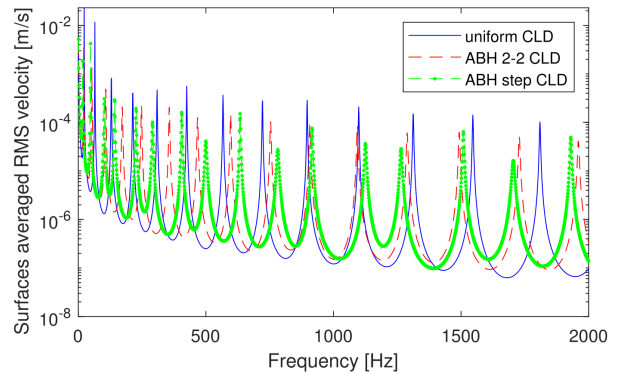
Figure 5.5: Surface integrated vertical velocity for beams with different thickness profiles with CLD.

Figure 5.4 and figure 5.5 show the surface integrated root mean squared (RMS) velocity.

$$v_{RMS} = \sqrt{\frac{1}{A} \int_A \underline{v}(x,y)^2 \, dA} \; . \tag{5.1}$$

Due to the fact that the structure is a one dimensional beam along the x-direction, the vibroacoustic properties are evaluated per unit meter in the y-direction.

The beam with the abrupt thickness reduction (and without CLD) shows slightly higher surface velocities at the resonance peaks than the smooth reduction and the uniform beam (see figure 5.4). Especially in the low frequency region up to 500 Hz, the thickness reductions yield an increase of the surface velocities. Besides the slight increase of the peak values, the thickness reduction also increase the modal density. The reason is the reduced stiffness due to the removal of material. Therefore, one observes that the thickness reductions reduce the eigenfrequencies of the structure. Figure 5.6 shows the comparison of three exemplary modes. With increasing mode number, the beams with a local thickness reduction evolve a locally pronounced modeshape. At mode four, the deformation amplitudes at the indentations are comparable to the deformation amplitudes in the rest of the structure. Comparing mode eight of the different configuration, the local thickness reduction increase the deformation at the indentation compared to the rest of the beam. For mode twelve both beams with thickness reduction show a locally pronounced mode at the thickness reduction. Appendix A.7 shows the effect of the thickness reduction on the first twelve mode shapes. The localized mode of the abrupt profile (ABH step) is more pronounced than the localized modes of the smooth profile (ABH 2-2).
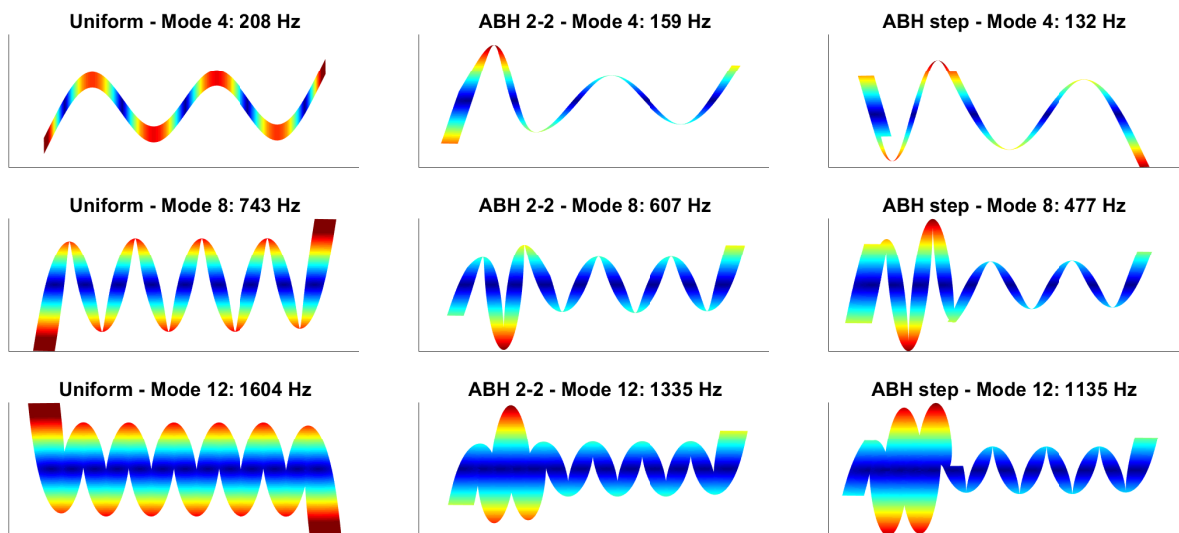
Figure 5.6: Modeshapes of Mode 4, 8 and 12 for the different thickness profiles (exemplarily shown without CLD). *Remark: The strongly varying thickness of the beams is an artifact that results from squeezing the deformation pattern along the beam axis.*

Figure 5.5 illustrates the respective surface velocity for the different thickness profiles with additional CLD. Both thickness profiles combined with a CLD show a reduction of the surface

velocities compared to the uniform beam with CLD. The abrupt profile with CLD yield a lower surface velocity than the other measures. The reason is the larger deformation at the location where the damping measure is applied. The eigenfrequencies of the abrupt thickness profile are lower compared to the eigenfrequencies of the other configurations (see figure 5.6). Therefore, the abrupt thickness profiles yield larger curvatures at lower frequencies than the smooth thickness profile. This effect strongly increases the energy dissipation of the CLD which results in stronger reduction of the peak amplitudes.

Besides the surface velocity, the radiated sound is also a relevant quantity to evaluate the vibroacoustic performance of lightweight components. Therefore, the following section elaborates on the influence of local thickness reductions on the sound radiation. The radiated power P is computed per unit meter using 100×100 elementary radiators (see 2.5.2). Figure 5.7 and figure 5.8 show the sound power level L_W for the beams without and with CLD.

$$L_W = 10 \log_{10} \left(\frac{P}{P_0} \right) \quad \text{with} \quad P_0 = 10^{-12} \text{W} . \tag{5.2}$$
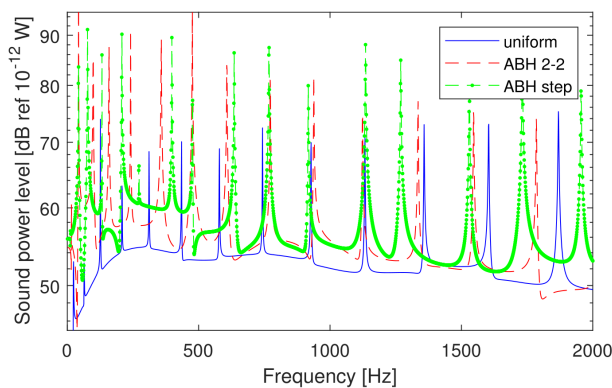
Figure 5.7: Sound radiation for beams with different thickness profiles without CLD.
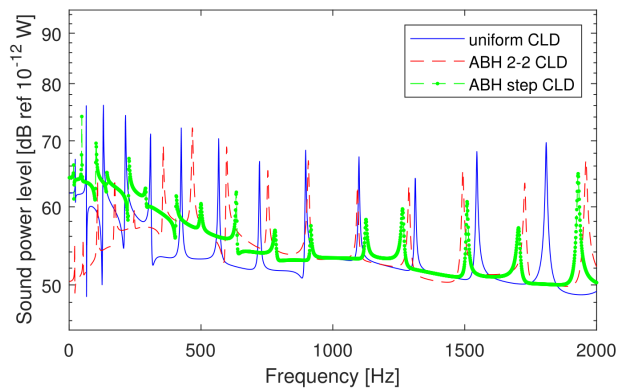
Figure 5.8: Sound radiation for beams with different thickness profiles with CLD.

From figure 5.7, one observes that the thickness reductions without CLD generally increase the sound radiation of the beam. For frequencies below 1 kHz, the uniform beam radiates significantly less power than the beams with thickness indentations. For frequencies above 1 kHz, the sound power level in the resonance peaks of the different beams decreases. Nevertheless, the peaks of the sound power level of the abrupt thickness reduction remains relatively large compared to the uniform beam. Figure 5.8 shows the effect of an additional CLD. For the uniform beam with attached CLD, the radiated sound power does not decrease for all peaks. In the frequency range up to 700 Hz, the uniform beam with CLD radiates more

power than the uniform beam without CLD. Responsible for this increase is the increased mass of the structure. Above 700 Hz the CLD yields a slightly lower sound power level. In general, the beams with reduced thickness and CLD yield a lower sound radiation for all resonance peaks compared to the corresponding beam without CLD. For frequencies below 300 Hz the smooth thickness reduction radiates less power than the abrupt thickness reduction. With increasing frequency the power radiated by the beam with an abrupt thickness reduction decreases. Comparing the radiation in the resonance peaks for frequencies above 300 Hz, the beam with the abrupt thickness profile radiates the least amount. Whereas, the beam without thickness reduction shows the greatest sound radiation in the resonance peaks.

For a better understanding, how the different thickness profiles influence the sound radiation, the following paragraph evaluates the wavenumber spectra of the vertical surface velocities. Figure 5.9 and 5.10 demonstrate the wavenumber spectra at three different frequencies. The selected frequencies correspond to the eigenfrequency of mode four, eight and twelve. The vertical lines indicate the wavenumber of the air. Consequently, the wavenumber components smaller than the wavenumber of air contribute to the radiated sound power. The maximum of the wavenumber spectra corresponds to the dominant structural wavenumber. The smaller side lobes are linked to the fact that the host structure is finite, resulting in a multiplication with a window function in the spatial domain. This is linked to a convolution with the sinc function in the wavenumber domain. Appendix A.8 explains the computation of the wavenumber spectra in detail and illustrates the spectra for the first twelve modes.

Figure 5.9 shows the impact of the thickness reduction. For the fourth mode, the thickness profiles result in a scaling of the wavenumber spectra. The dominant structural wavenumber does not change. Comparing the mode shapes of the fourth mode (see figure 5.6), one can see that the wavenumber in the structure is almost unchanged. For higher modes, the wavenumber spectra shows a distinct diversification. The reason is that for higher frequencies the wavelength of the bending waves matches the dimension of the diameter of the thickness reduction [Conlon and Fahnline 2015]. In that case, the locally reduced stiffness of the structure locally modifies the wavenumber of the bending waves. This results in a distinct broadening of the wavenumber spectra. Looking at the mode shapes (figure 5.6), one can see that for mode eight and twelve, the wavenumber at the thickness reduction is different than the wavenumber in the rest of the structure. The local wavenumber increases compared to the wavenumber in the rest of the structure. In general, this could transfer some of the energy of the vibration to subsonic wavenumbers that do not radiate to the far field [Zhao et al 2015]. However, figure 5.9 also illustrates that for higher modes the energy partition between lower and higher wavenumbers is more balanced than for the uniform beam. Consequently, the
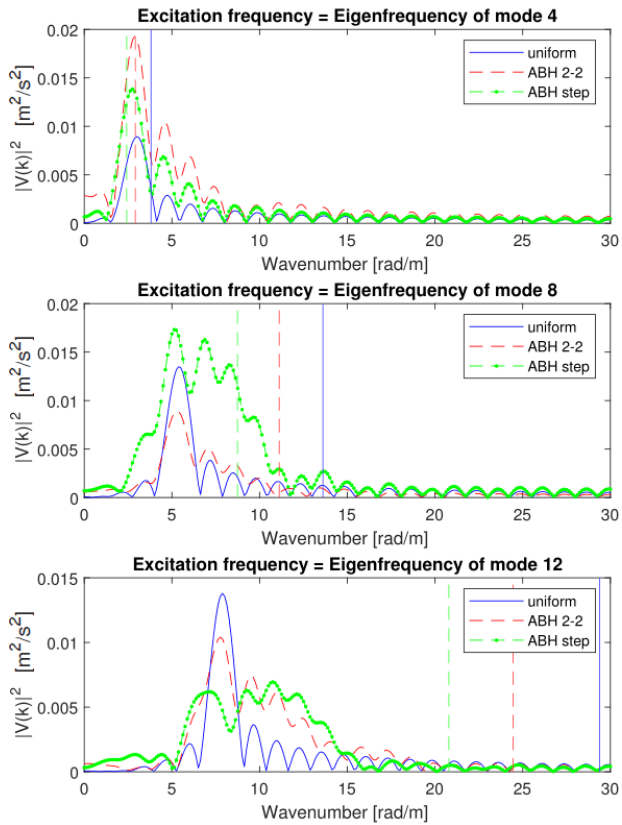
Figure 5.9: Wavenumber spectra of the vertical surface velocity for beams with different thickness profiles (without CLD) at different frequencies; the vertical lines mark the corresponding wavenumber of the air.
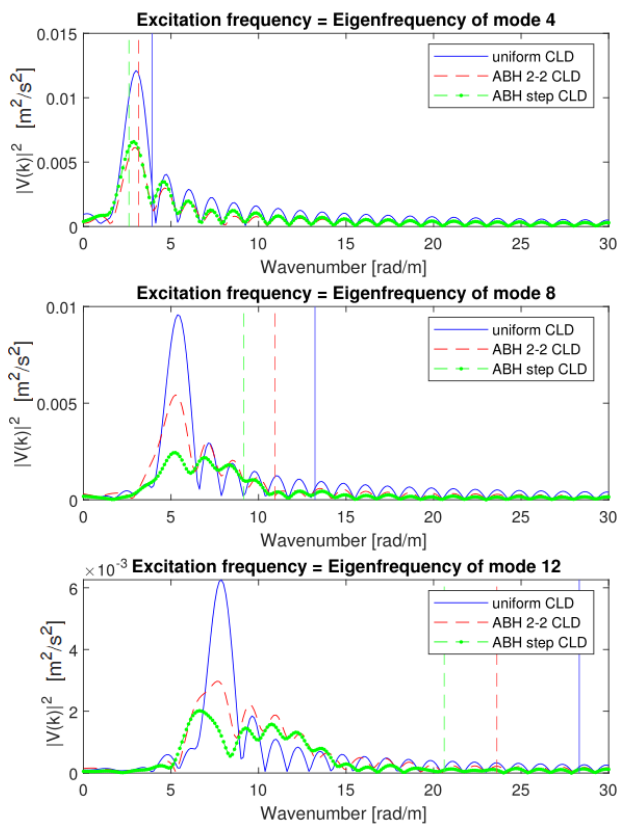
Figure 5.10: Wavenumber spectra of the vertical surface velocity for beams with different thickness profiles with CLD at different frequencies; the vertical lines mark the corresponding wavenumber of the air.

increase of the level and the diversification of the spectra explains the increase of the radiated sound power.

Figure 5.10 shows the respective wavenumber spectra for mode four, eight and twelve for the structure modified with CLD. For the uniform beam with CLD, the level of the wavenumber spectra of mode four increases compared to the respective spectra without CLD. Therefore, the sound radiation of the uniform beam with CLD increases for lower frequencies. Comparing the beams with indentations, the benefit of a CLD becomes clear. For the beams with local thickness variations, the CLD reduces the vibrational level for all reasonance peaks. The lower level of the wavenumber spectra explains the reduced radiated power. The abrupt thickness reduction shows a lower level of the wavenumber spectra than the smooth thickness and consequently yields a lower radiated sound level.

Summarizing, the combination of local thickness reduction with CLD show improved vibrational behavior in terms of vibration amplitudes as well as radiated sound power. The

benefit of an ABH configuration with a smooth thickness profile does not show any benefit compared to an ABH configuration with an abrupt profile.

5.1.3 Energetic evaluation of two dimensional acoustic black holes

The following section focuses on two dimensional ABH in plates. To evaluate the performance of the ABH configurations, the author compares the different configurations to the uniform plate. For the energetic evaluation, the energies are normalized with respect to the input power. This is necessary to avoid an overlaying interpretation linked to a changes in the input power due to a simple modal shift. The energetic insertion loss is

$$\Delta L = 10 \log \left(\frac{E_{uni}/P_{uni}}{E_{...}/P_{...}} \right) \quad [\text{dB}] . \tag{5.3}$$

In this chapter, the thickness profiles are two dimensional circular indentations in a rectangular plate. The investigated profiles have the same form as previously (compare to figure 5.3). However, in two dimensions the thickness profiles are rotational symmetric with respect to the center of the indentation. As previously, the thickness profiles follow the expression $h(r) = \epsilon r^\beta + h_{min}$. The minimum thickness at the center of the circular indentation is 1 mm and the diameter of 200 mm defines the parameter ϵ. Figure 5.11 illustrates an exemplary configuration. The plate's dimension is $600 \times 500 \times 3$ mm. The material of the plate is titanium. Table 5.2 lists the material properties of titanium. A harmonic surface load which covers the area of 20×20 mm excites the plates. The plates are modeled using the commercial software package ANSYS®. Convergence studies ensuring a correct modeling of the respective phenomena are covered in Miksch [2017].
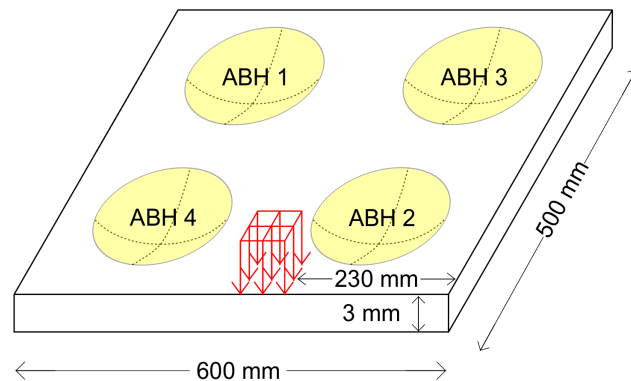
Figure 5.11: Model of an exemplary plate with circular indentations excited by a harmonic distributed load.

The following section investigates various configurations of single and multiple ABH. The numbering of the ABH in figure 5.11 determines the order in which the ABH are allocated. The following labeling helps to distinguish the different configurations:

$$\underbrace{4}_{\substack{\text{\# of}\\\text{indentation}}} \quad \underbrace{\text{ABH}}_{\substack{\text{ABH or}\\\text{uniform}}} \quad \underbrace{2.2}_{\substack{\text{exponent}\\\beta}} \quad \underbrace{\text{CLD}}_{\substack{\text{additional CLD}\\\text{at indentation}}}$$
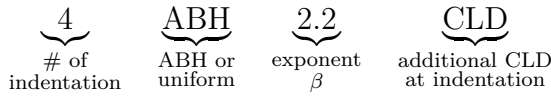
The insertion loss is computed from 0 to 2 kHz in discrete steps of 1 Hz. Afterwards, the insertion loss is averaged over third-octave bands. Appendix A.9 lists the unaveraged insertion loss of the following comparisons.
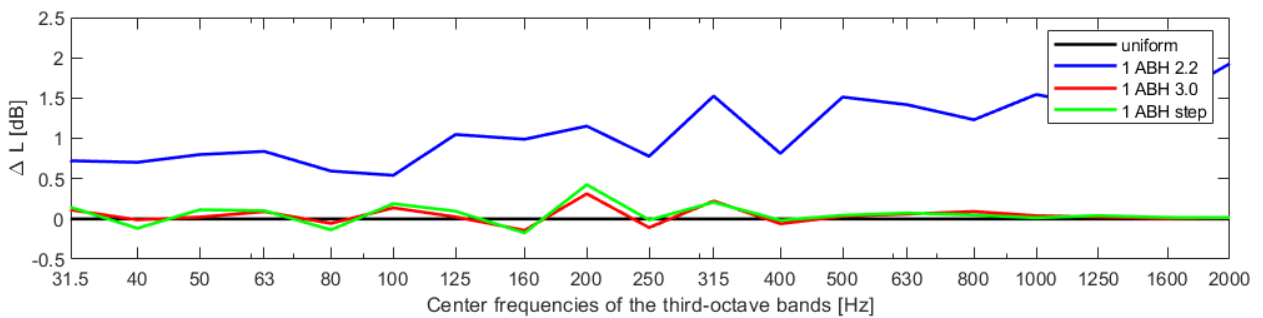
Figure 5.12: Insertion loss of a plate with a single ABH profile with different exponents β (without CLD).

Figure 5.12 shows the insertion loss as defined in (5.3) for a single ABH with three different thickness profiles. Below, 31.5 Hz, the insertion loss is driven be the appearance of the first resonance frequency of the structure. Therefore, these bands are excluded in the following. The profiles with $\beta = 3$ and $\beta = \infty$ do not provide a significant increase of the insertion loss. However, a smooth thickness profile with $\beta = 2.2$ yields a positive insertion loss over all bands. The depicted configuration increases the averaged insertion loss by 1.6 dB. In addition, such a profile reduces the mass of the plate by 3.7 %.
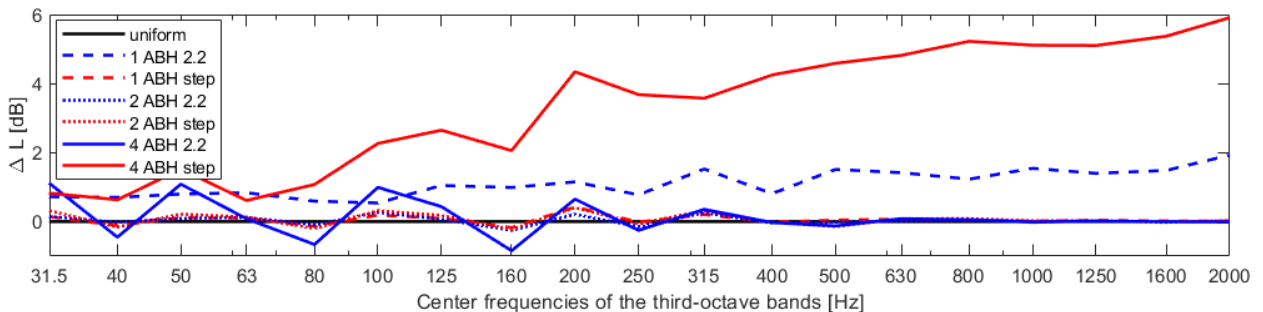
Figure 5.13: Insertion loss of a plate with multiple ABH profiles (without CLD).

In general, increasing the number of ABH does not yield an increase in the insertion loss (see

figure 5.13). Applying two or four identical profiles with an exponent $m = 2.2$, the insertion loss decreases compared to the single ABH. In contrast, four ABH with an abrupt thickness reduction result in a higher insertion loss compared to a single or two of such profiles. The averaged insertion loss for the plate with four abrupt thickness profiles is slightly above 3 dB.

In the following, an additional CLD increases the energy dissipation. The CLD is located at the indentations and consists of a 1 mm damping layer and an 1 mm cover layer made of titanium. Table 5.2 lists the material properties of the plate and the damping material. To distinguish the impact of the thickness reduction and the CLD, figure 5.14 compares the configurations with and without CLD. The dashed curves indicate the configurations without CLD and the continuous lines mark the corresponding results with additional CLD. The additional CLD increases the insertion loss for all configurations. The strongest increase experiences the ABH with the abrupt thickness reduction ($\beta = \infty$). In the third octave bands up to 125 Hz, both ABH with CLD behave similarly and oscillate around the insertion loss of the uniform plate with CLD. Thus, in this frequency range, the increased insertion loss mainly results from the CLD. With increasing frequency, the thickness reduction results in an improved insertion loss compared to the uniform plate. For the octave bands above 125 Hz, the abrupt ABH outperforms the smooth ABH.
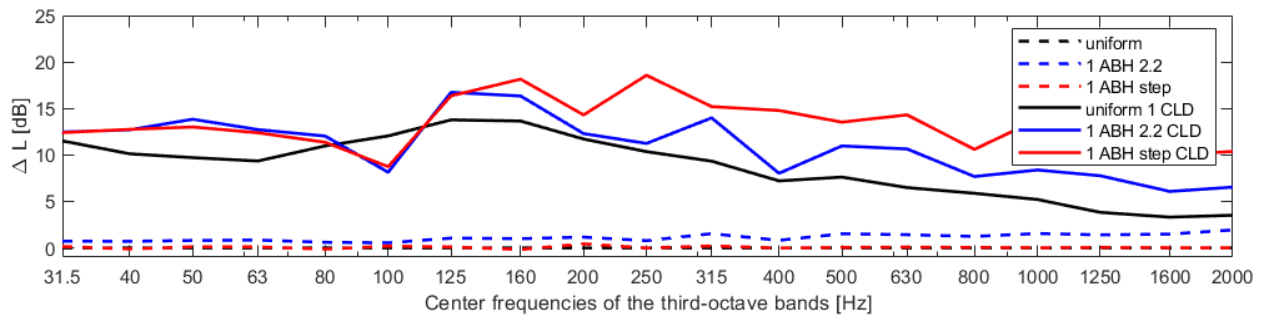
Figure 5.14: Insertion loss of a plate with two different ABH profile with and without additional CLD.

The previous investigation shows that using CLD, a smooth thickness reduction is not necessary to maximize the performance. Following the theoretical derivation of Mironov [1988], a CLD that introduce a non-smooth transition deteriorate the ABH effect. To investigate the effect of a smooth CLD, the following paragraph compares two configurations of sandwich layer damping (SLD). Figure 5.15 shows the SLD configurations. The plate minimal thickness at the top and the bottom is 1 mm. The damping pads are rotational symmetric and follow the same power laws as previously.

Figure 5.16 compares the SLD configurations and the respective CLD configurations. In the

ABH 2.2 SLD :

ABH step SLD :

Figure 5.15: Two different thickness profiles that follow an integrated sandwich layer damping (SLD).
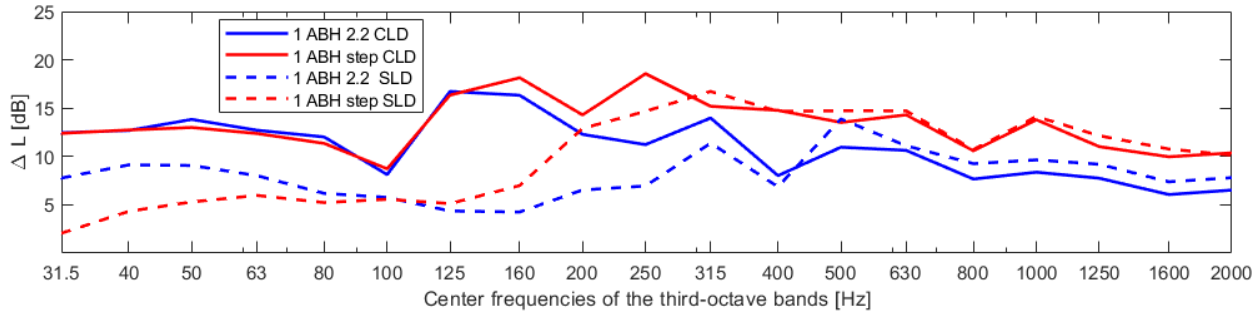
Figure 5.16: Insertion loss of a plate with two different ABH profile with CLD and SLD.

low frequency range up to 250 Hz, the CLD configuration with the step profile has a larger insertion loss than the respective SLD configurations. Above 250 Hz, the abrupt configurations have almost the same insertion loss. Comparing the performance of the smooth ABH with SLD and CLD, the SLD shows a slightly larger insertion loss for the bands above 400 Hz than the respective CLD configuration. Neither the smooth CLD, nor the smooth SLD configuration outperforms the respective abrupt CLD or SLD configuration. In fact, the abrupt SLD configuration is superior to the smooth SLD except for frequencies below 100 Hz. Concluding, also for the presented SLD configuration, there is no general benefit of a smooth profile compared to an abrupt profile.

Finally, the impact of multiple ABH with CLD on the insertion loss is discussed. Increasing the number of ABH increases the insertion loss (see figure 5.17). Using CLD, the insertion loss is larger for the plates with indentations. The thickness profiles enhances the dissipation effect of the CLD. The first ABH embedded in the plate has the strongest impact. With increasing number of ABH the insertion loss increases. For third octave bands below 100 Hz, the smooth profiles generates the largest insertion loss for configurations with one, two, and four ABH. For frequencies above 100 Hz, the abrupt thickness reduction yields a larger insertion loss than the respective ABH with smooth profiles.

5.1.4 Summary

The previous investigations show how different thickness profiles influence the wavenumber spectra of the surface velocity of beam-like structures. Based on the impact on the wavenumber spectra the sound radiation varies for the different configurations. For low frequencies,
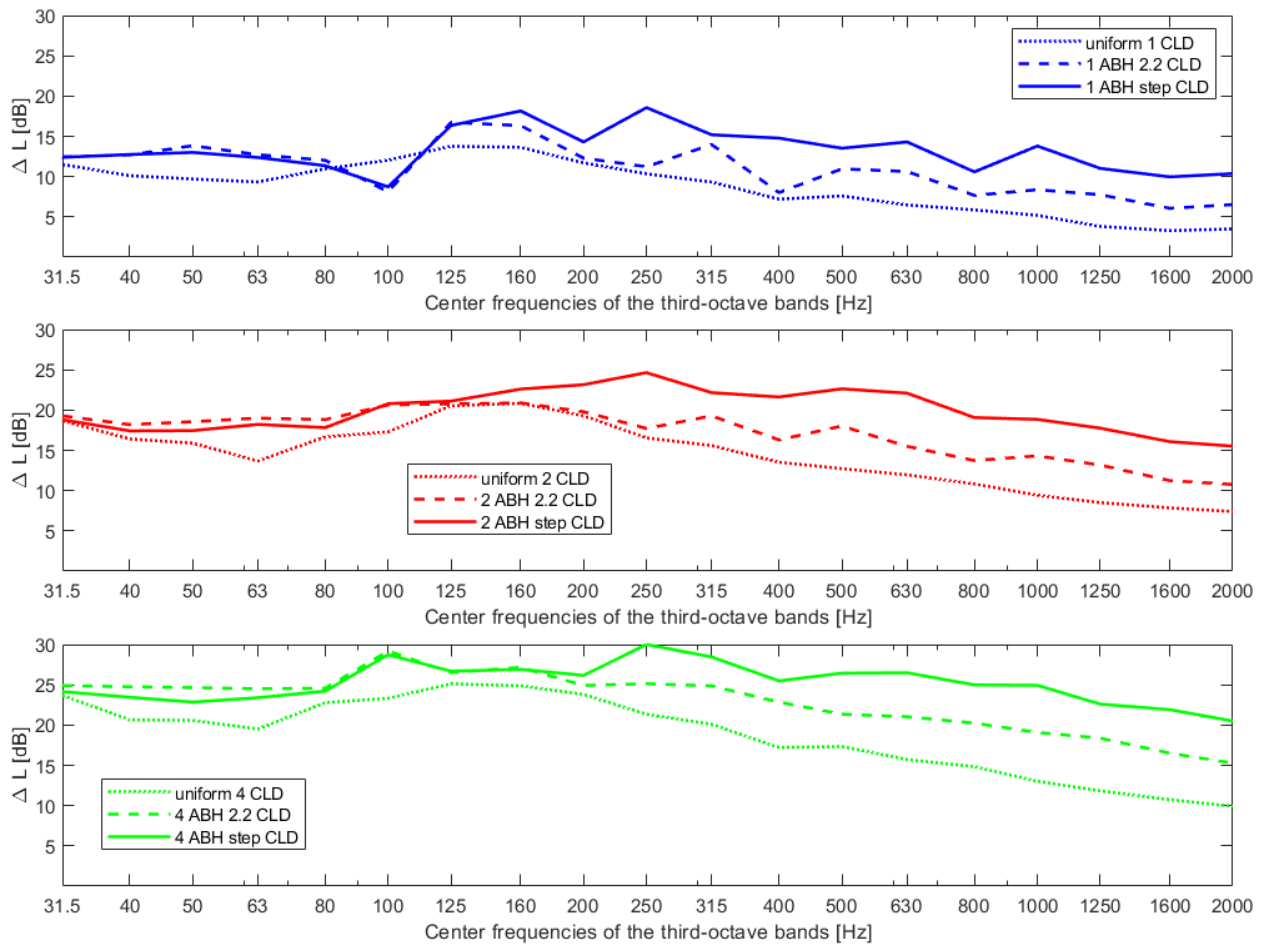
Figure 5.17: Insertion loss of a plate with multiple ABH with different profiles and CLD; Comparison of one (top), two (middle) and four (bottom) incorporated ABH.

a thickness reduction scales up the wavenumber spectra which results in an increase of the radiated sound power level. For higher frequencies, the wavelength of the vibration patterns fit in the thickness indentation. This results in a broadening of the wavenumber spectra which transfers some of the vibrational energy towards higher and lower wavenumbers. Using additional CLD in the vicinity of the indentations result in a strong decrease of the level of the wavenumber spectra which decreases the sound radiation. The abrupt profile outperforms the smooth profile in terms of surface velocities and radiated sound power, except for very low frequencies where the wavelength is larger than the diameter of the profile.

The evaluation of the insertion loss of plate-like structures modified by ABH confirms the results of the investigations of the beam-like structures. Various studies reinforce the proposition that an abrupt thickness profile with damping treatment that enhance the energy dissipation outperforms smooth profiles. The reason are the larger deformation that occur due to the abrupt profiles. The larger deformation increase the shear deformation in the

CLD. This proposition holds for multiple indentations as well as for sandwich composites with integrated damping layers. The benefit of a smooth profile is only obvious for bending waves whose wavelength are relatively large compared to the diameter of the profile.

5.2 Studies on locally resonant materials

The following section focuses on the design of locally resonant materials based on periodic resonators. The author published some preliminary results of the following section in various publications [Miksch et al 2018c; Miksch and Müller 2019; Miksch et al 2019]. First, section 5.2.1 discusses the design of beam-like resonators. For an exemplary beam-like resonator, it elaborates on the influence of different design parameters on the performance of the resonator. Second, section 5.2.2 demonstrates the influence of periodic resonators on the wave solutions of beams. Subsequently, section 5.2.3 discusses the relation between the wave solutions and the frequency response function (FRF) of a finite structure. Section 5.2.4 assesses the performance of the resonators based on the wave solutions. Finally, section 5.2.5 evaluates the vibroacoustic performance of locally resonant beams. The studies presented in this chapter spawn design criteria for resonant structures. Finally, section 5.2.6 summarizes the results of the numerical studies.

5.2.1 Designing beam-like resonators

In general, the manufacturing capabilities and the installation space in the host structure restricts the design space of beam-like resonators. The following section investigates a potential design of a beam-like resonator that could be manufactured using additive layer manufacturing (ALM) and is than integrated in the cavities of a honeycomb panel. The design is proposed by Müller and Faulhaber [2018]. Six independent parameters define the geometry (see figure 5.18).
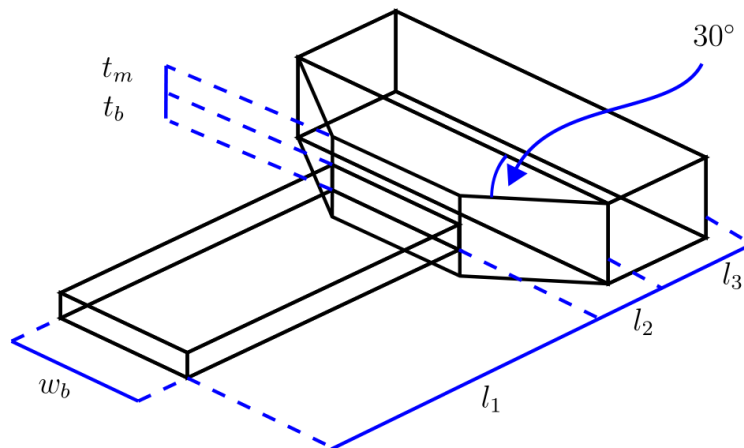
Figure 5.18: Geometric parameters of the beam-like resonator.

The beam-like resonator consists of three segments: a beam segment of length l_1, a transition segment of length l_2 and an end mass of length l_3. The ALM process limits the overhang thickness t_m to 1 mm and the transition angle to 30°. Additionally, the installation space is restricted to

$$l_1 + l_2 + l_3 \leq 25 \text{ mm} , \tag{5.4}$$

$$t_b + 2t_m \leq 5 \text{ mm} , \tag{5.5}$$

$$w_m = w_B + 2\tan(60°)l_2 \leq 25 \text{ mm} . \tag{5.6}$$

The following investigation assesses the influence of the geometry on the eigenfrequency, the mass of the resonator, and the amplification functions V. A coupled beam model (presented in section 4.1.1) evaluates the eigenfrequency and the amplification function. The beam-like resonator is coupled to a simple mass-spring system to compute the characteristics of the amplification function (see figure 5.19). The displacement of the main mass w determines the amplification function

$$V = \frac{w}{w_{stat}} \quad \text{with} \quad w_{stat} = \frac{|f|}{k_s} . \tag{5.7}$$
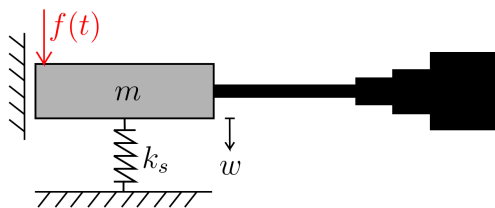
Figure 5.19: Beam-like resonator consisting of coupled beams connected to a discrete mass-spring system.
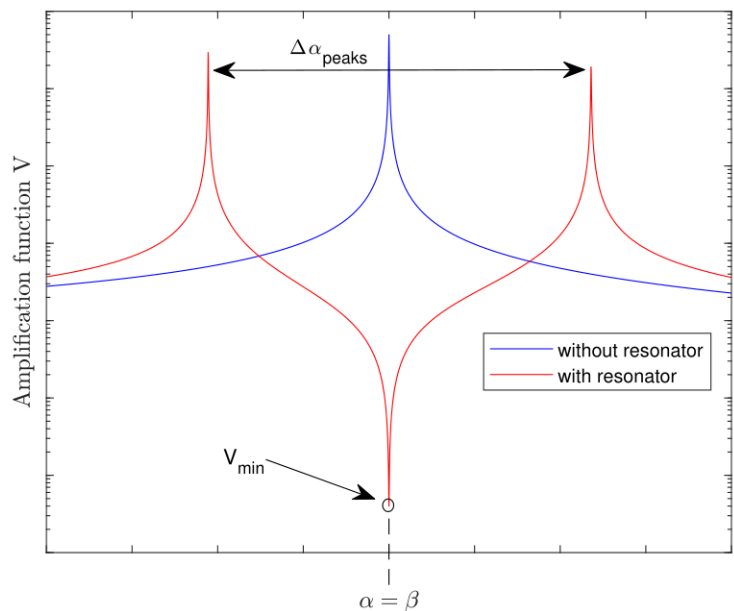
Figure 5.20: Characteristics of the amplification function, $\alpha = \frac{\Omega}{\omega}$ is the frequency ratio of the excitation and $\beta = \frac{\omega_{1,beam}}{\omega}$ is the tuning frequency ratio of the resonator.

There are two relevant quantities of the amplification function V: the minimum value of the amplification function V_{min} which occurs in the vicinity of the local resonance of the beam and the frequency range between the two resonance peaks $\Delta\alpha$ (see figure 5.20). The minimum value is important for the maximal reduction of the vibrations at the tuning frequency (narrow band performance). The distance between the resonance peaks reveals the broadband performance. The larger the distance the greater the frequency range in which the vibration can be reduced. In general a larger mass improves both of these characteristics. However, section 4.1.2 shows that besides the overall mass, other quantities as the ratio of tip mass and beam mass as well as the ratio of the mass moment inertias influence the amplification function. Therefore, this investigation directly focus on the geometric parameters of the beam-like resonator. The resonator consists of Titanium, whose material properties are listed in table 5.2.
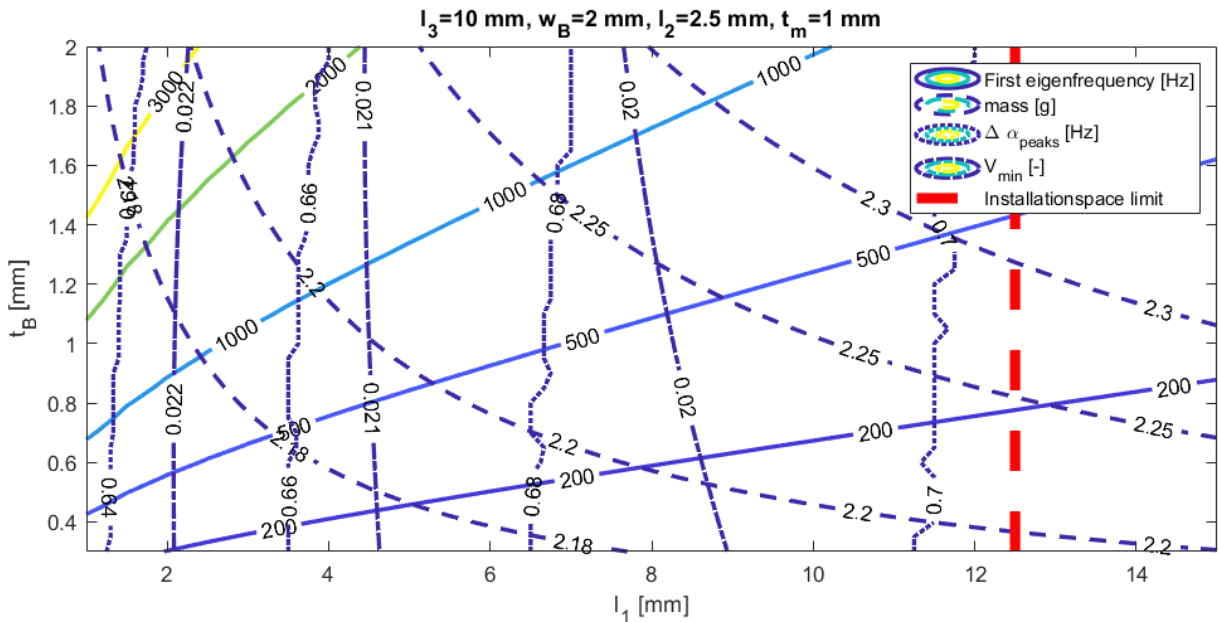
Figure 5.21: Influence of l_1 and t_b on the first eigenfrequency, the mass and the distance of the resonance peaks and the minimal value of the amplification function.

At first, the design of the beam segment (l_1, t_B) will be investigated. Figure 5.21 shows the influence of the length l_1 and the thickness t_B of the beam segment on the characteristic values of the resonator. The continuous curves mark the first eigenfrequency in Hertz, the dashed curves mark the mass in grams. The dotted line indicates the dimensionless frequency range of the resonance peaks $\Delta\alpha_{peaks}$ and the dashed-dotted line the minimum value of the amplification function V_{min}. To find an optimal design for a specific beam-like resonator, one

first defines the frequency of operation. Moving along the curve of a specific eigenfrequency, the respective characteristics of the amplification function change. For an maximal $\Delta\alpha$ and a minimum V_{min}, the beam length l_1 should be as large as possible. The installation space restricts the optimal length l_1. The optimal designs for various target frequencies lay on the dotted red line. The reason is that these designs maximize the total mass of the beam-like resonators.
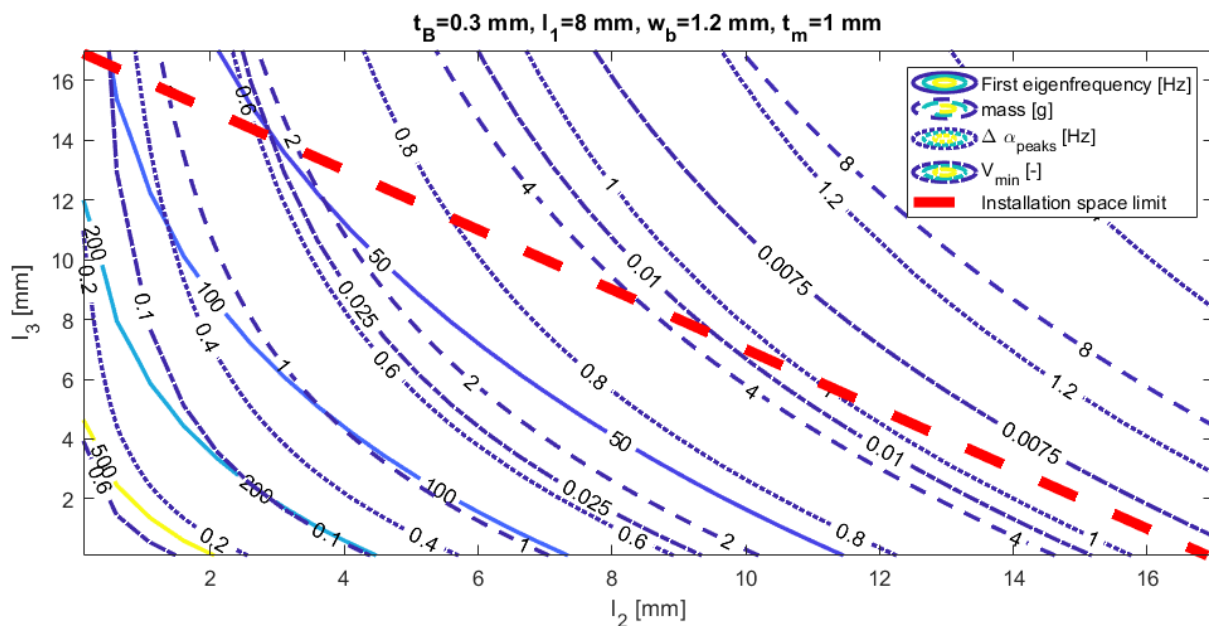
Figure 5.22: Influence of l_2 and l_3 on the first eigenfrequency, the mass and and the distance of the resonance peaks and the minimal value of the amplification function.

Second, figure 5.22 investigates the design of the tip mass. Therefore, the length of the transition segment l_2 and the length of the end mass l_3 is considered. Due to the fixed transition angle of 30°, the length l_2 defines the width of the end mass (5.6). The optimal designs that maximize $\Delta\alpha$ and a minimize V_{min} lie on the x-axis of the graph. That means, choosing l_3 as small as possible and adjust l_2 to meet the required resonance frequency. Increasing l_2 or l_3 increases the mass of the tip mass but it also moves the center of gravity which shifts the resonance frequency. Therefore, the optimal design accumulates as much mass as possible at the transition segment and minimizes l_3.

Finally, Figure 5.23 shows the influence of the length of the beam segment l_1 and the length of the transition segment l_2 on the performance of the resonator. As described l_2 determines the width of the tip mass (5.6). For the presented parameter configuration, moving to the top left corner of the graph optimizes both the characteristics of the amplification function V_{min}
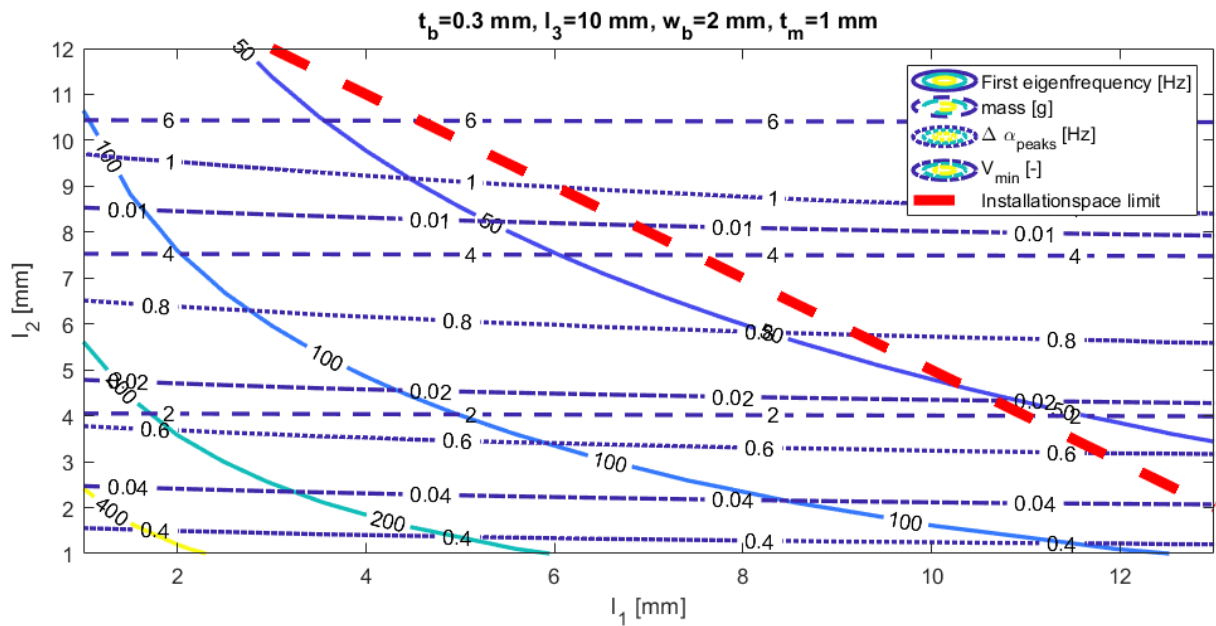
Figure 5.23: Influence of l_1 and l_2 on the first eigenfrequency, the mass and and the distance of the resonance peaks and the minimal value of the amplification function.

and $\Delta\alpha_{peaks}$. This holds for all frequency curves. Thus, minimizing l_1 and maximizing l_2 until the limit of the design space yields the optimal performance of the beam-like resonator. The same holds for the parameter dependency of l_1 and l_3 (see Appendix A.19). The reason is that for a fixed eigenfrequency, a short beam section and a very large tip mass maximizes the overall mass of the resonator.

5.2.2 Wave solutions of Euler-Bernoulli beams with discrete resonators

The following section elaborates on the wave solutions of an Euler-Bernoulli beam. The wave solutions are computed with Duhamel's formulation of the Wave Finite Element Method (WFEM) described in section 4.2.2. As shown in figure 5.24, the beam has two degrees of freedom at each node (vertical deflection and rotation). Figure 5.24 also lists the material parameters and the geometric parameters of the beam.

E	210 GPa
ρ	7800 kg/m^3
ν	0.3
L	10 cm
A	1 cm^2
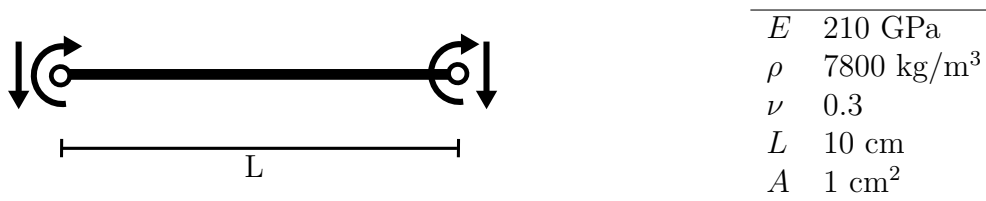
Figure 5.24: Model of an Euler-Bernoulli beam with vertical and rotational degrees of freedom at each node with corresponding material and geometric properties.
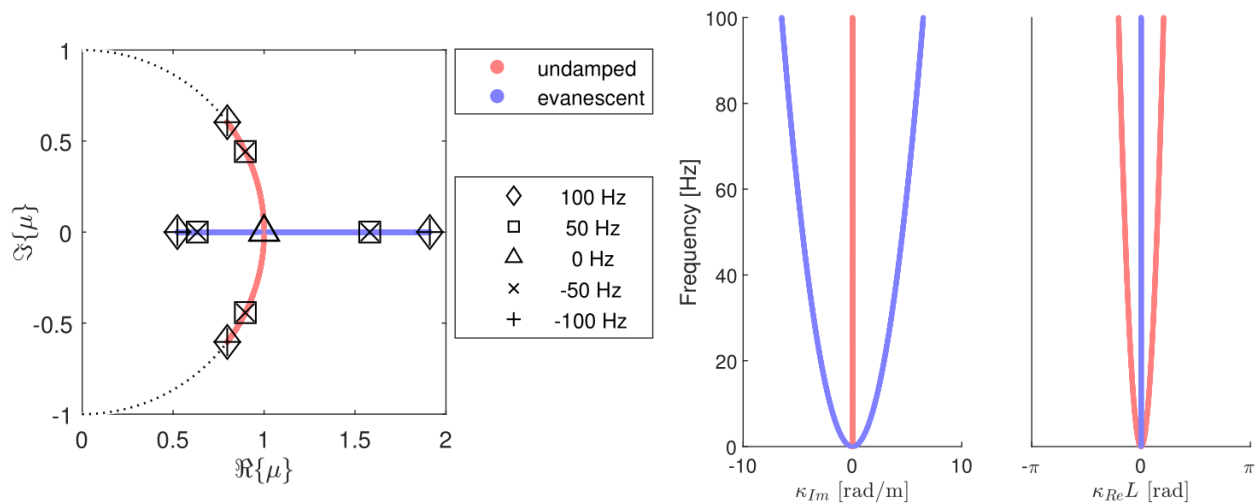
Figure 5.25: Solution of the eigenvalue problem for the Euler-Bernoulli beam and corresponding spatial decay and phase information.

For an undamped Euler-Bernoulli beam, there are four fundamental wave solutions for each frequency: two evanescent waves and two undamped waves [Cremer and Heckl 1967]. Each wave solution has a decay characteristic and a phase that can be extracted from the complex eigenvalue μ. The eigenvalue μ is an exponential function

$$\mu = \mathrm{e}^{-i(\kappa_{Re}+i\kappa_{Im})L} = \mathrm{e}^{-i\kappa_{Re}L}\mathrm{e}^{\kappa_{Im}L} \ . \tag{5.8}$$

As shown in figure 4.14, undamped waves do not show a decay characteristic ($\kappa_{Re} \neq 0, \kappa_{Im} = 0$) whereas evanescent wave have decay but no phase ($\kappa_{Re} = 0, \kappa_{Im} \neq 0$). In the following, the decay characteristic is denoted κ_{Im}. This quantity describes the spatial decay in radians per meter. The phase characteristic of the wave solution is expressed in radians and is determined by $\kappa_{Re}L$. Figure 5.25 shows the eigenvalues (left) and the wave characteristics (right) of the Euler-Bernoulli beam computed from -100 Hz to 100 Hz in frequency steps of 0.1 Hz. The dashed line in the eigenvalue plot marks the unit circle which indicates possible locations of eigenvalues representing undamped waves. The eigenvalues on the real axis correspond to the evanescent waves. In general, eigenvalues located inside of the unit circle represent waves traveling in the positive direction, whereas eigenvalues located outside of the unit circle represent waves traveling in the negative direction. Eigenvalues located on the unit circle are either waves traveling in positive or negative direction. The markers highlight the wave solutions at ± 100, ± 50 and 0 Hz. The wave solutions for positive and negative frequencies are the same. Figure 5.25 also illustrates the decay and phase information that can be extracted from the eigenvalues μ (see (5.8)). These plots are preferably used to show the information about the frequency dependency of the wave solutions. The red curves indicate the undamped wave solutions ($\kappa_{Re} \neq 0$, $\kappa_{Im} = 0$), whereas the blue curves indicate the evanescent wave solutions ($\kappa_{Re} = 0$, $\kappa_{Im} \neq 0$). For a later the comparison of various configurations, the decay characteristic is normalized with the length of the unit cell.

The following paragraph shows the effect of a discrete resonator on the wave solutions of the beam structure. Figure 5.26 illustrates the resonator and its parameters. The properties of the beam are the same as in the previous model.

$m_{add} = m/m_{beam}$	5 %
$f_{res} = \frac{1}{2\pi}\sqrt{k_s/m}$	50 Hz
$D_{res} = c/(2\sqrt{k_s m})$	1 %
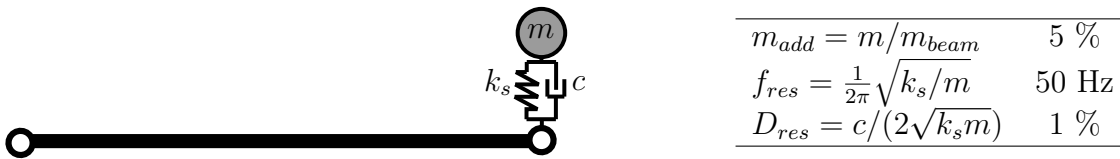
Figure 5.26: Euler-Bernoulli beam with attached resonator and corresponding properties of the resonator; properties of the beam are the same as described in figure 5.24.

In this example, the mass m of the resonator amounts to $5\,\%$ of the mass of the beam. Furthermore, the eigenfrequency of the resonator f_{res} is 50 Hz. Additionally, a critical damping ratio D_{res} of $1\,\%$ is introduced that defines the damping constant ($c = D_{res}2\sqrt{k_s m}$. As soon as energy dissipation occurs, in general undamped waves do not exist. To distinguish strongly damped waves from nearly undamped waves, the author defines undamped waves as waves having a spatial decay of less than 1% per meter.

Figure 5.27: Eigenvalues describing the wave solutions of an Euler-Bernoulli beam with an attached resonator and corresponding spatial decay and phase information.

Figure 5.27 illustrates the influence of the resonator on the four wave solutions of the beam. In the frequency range of the target frequency of the resonator, there only occur damped waves. This frequency range is identified as stop band. One can observe the stop band in both the decay characteristics and the phase characteristics of the wave solutions. The maximum spatial decay (5.82 rad/m) due to the resonator appears at a frequency slightly below the resonance frequency (at 49.7 Hz). Additionally, the damped wave solutions (black curves) that evolve from the originally undamped wave solutions only experience a maximum attenuation of 2.10 rad/m at a frequency slightly higher than the target frequency of the resonator.
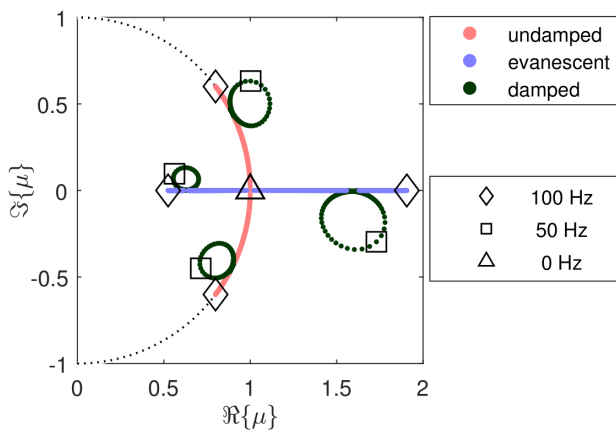
Figure 5.28: Eigenvalues describing the wave solutions of an Euler-Bernoulli beam with an attached resonator with complex spring stiffness $\hat{k}_s = k_s(1 + i0.02)$.
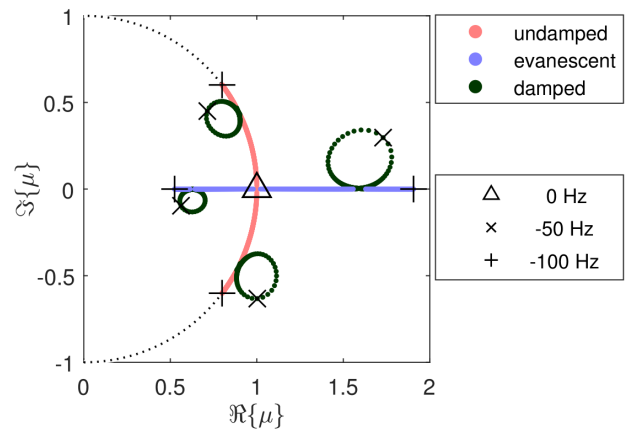
Figure 5.29: Eigenvalues describing the wave solutions of an Euler-Bernoulli beam with an attached resonator with complex spring stiffness $\hat{k}_s = k_s(1 - i0.02)$.

The eigenvalue plots (left plot) in figure 5.25 show that for undamped structures, it is sufficient to compute the wave solutions for positive frequencies. If the model includes energy dissipation, damped waves having both a phase and a decay characteristic occur ($\kappa_{Re} \neq 0$, $\kappa_{Im} \neq 0$). To incorporate all possible combinations of phase and decay, the wave solutions computed for negative frequencies yield the complex conjugated wave solutions (see the eigenvalue plot in figure 5.27). If energy dissipation occurs due to a frequency independent structural loss factor η, the computation with positive frequencies and a positive structural loss factor yields one set of wave solutions and the computation with negative frequencies and a negative structural loss factor yields the complex conjugated wave solutions (compare figures 5.28 and 5.29). In general, there exist wave pairs traveling in opposite direction. These pairs have an opposite sign in the relative phase shift and the spatial decay. These pairs correspond to the eigenvalues μ and $1/\mu$.

In practice, a resonator also introduces a rotational inertia, which yields an additional decaying effect. Therefore, the following paragraph presents the wave solutions for a rotational resonator as described in figure 5.30.

| $m_{add} = m/m_{beam}$ | 5 % |
$f_{res} = \frac{1}{2\pi}\sqrt{k_\Phi/(mr^2)}$	50 Hz
$D_{res} = c_\Phi/(2\sqrt{k_\Phi mr^2})$	1 %
r	20 cm
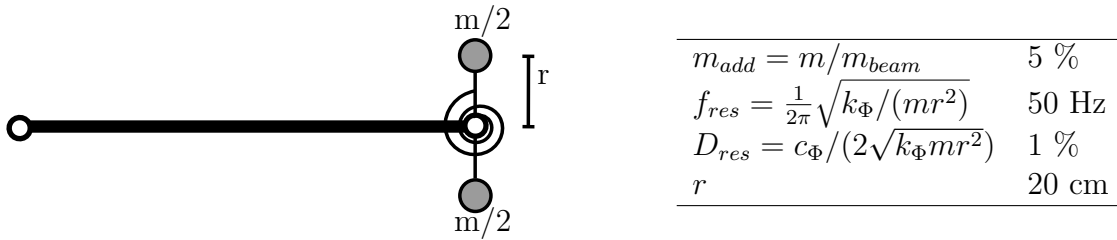
Figure 5.30: Euler-Bernoulli beam with attached rotational resonator and corresponding properties of the resonator; properties of the beam are the same as described in figure 5.24.
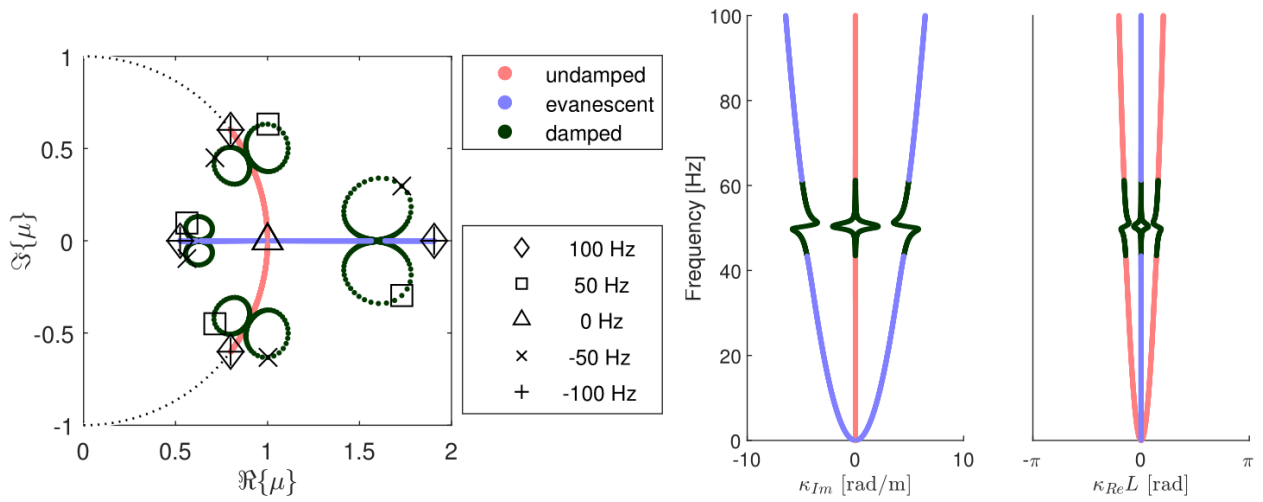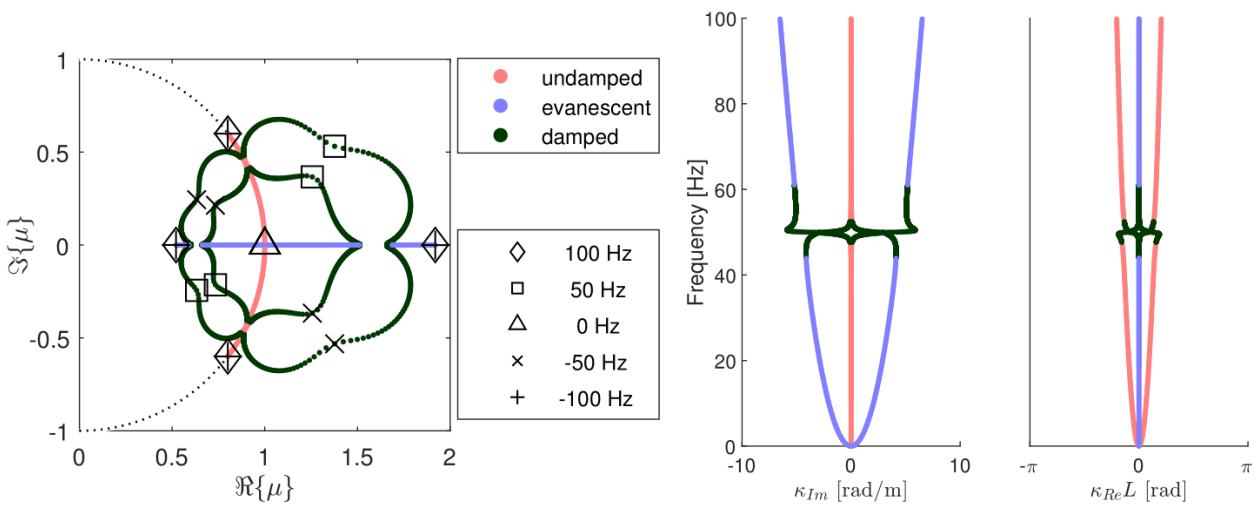

Figure 5.31: Eigenvalues describing the wave solutions of an Euler-Bernoulli beam with an attached rotational resonator and corresponding spatial decay and phase information.

Figure 5.31 shows the wave solutions. The maximum spatial decay of the damped waves appears slightly above the resonance frequency of the resonator (50.5 Hz). The maximum spatial decay is 5.89 rad/m. Comparing the evolution of the damped waves solutions, the rotational resonator modifies the wave solution of the beam differently than the vertical resonator. The damped wave branches that evolve due to the rotational resonator show a transitional behavior between undamped and evanescent wave solutions and vice versa. This can be observed in the eigenvalue plot: The side loops of undamped and evanescent waves overlap.
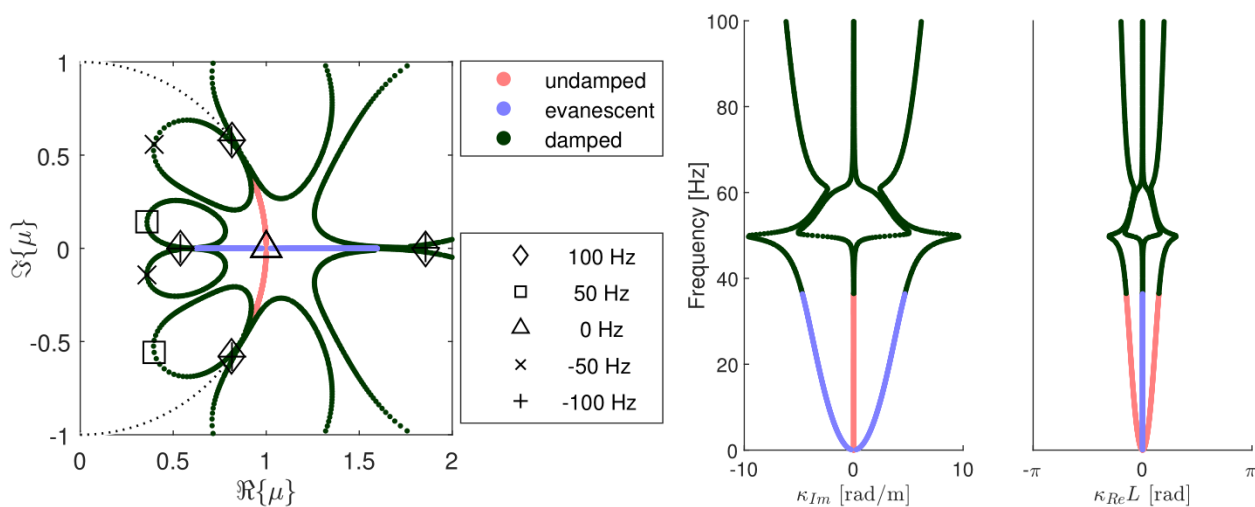
Figure 5.32: Eigenvalues describing the wave solutions of an Euler-Bernoulli beam with an attached vertical resonator with increased mass (50 % of the mass of the beam) and corresponding spatial decay and phase information.

The undamped wave branches of the vertical resonator remain separate. Figure 5.32 shows the wave solutions of a vertical resonator with a mass equal to 50 % of the beam mass. The side loops of damped waves that occur due to the resonator do not overlap because the corresponding wave solutions result from excitation frequencies with opposite sign. Comparing figures 5.27 and 5.32, one observes that a larger mass enhance the stop band and increases the maximum spatial decay at the target frequency. Furthermore, it increases the averaged spatial decay in the stop band.

5.2.3 Relation between wave solutions and frequency response function of a finite structure

The following section explains the link between the characteristics of the wave solutions and the characteristics of the FRF of a finite structure. The main characteristic of the FRF

are the resonance peaks. These peaks occur due to an interference of incident waves and reflected waves. Depending on the phase change of the unit cell and the total length of the structure, standing waves occur. Each reflection amplifies the standing wave which results in the resonance peaks in the FRF. The phase change ϕ that a wave experience traveling to the boundary and back depends on the phase change over the length of the beam structure and the phase change ϕ_{BC} that the wave experiences due to the boundary condition

$$\phi = N\kappa_{Re}L + \phi_{BC} \ . \tag{5.9}$$

N are the number of unit cells that built up the finite structure. A resonance peak occurs if the phase change that a wave experiences when traveling to the boundary an back equals $(n + \frac{1}{2})\pi$ where $n \in \mathbb{N}$. In the following, these phase changes are named critical phases. Table 5.3 lists the critical phases for beams with different boundary conditions.

Table 5.3: Critical phase characteristics of the wave solutions for various boundary conditions; host structure consists of N unit cells of length L.

Boundary conditions	Critical phase ϕ_{crit}
free - free clamped - clamped	$\pm(n + \frac{1}{2})\pi/N, \quad n \in \mathbb{N}$
pinned - pinned	$\pm n\pi, \quad n \in \mathbb{N}$
clamped - pinned free - pinned	$\pm(n + \frac{1}{4})\pi/N, \quad n \in \mathbb{N}$

Figure 5.33 shows a free-free beam with a length of 1 m. A harmonic force in the vertical direction excites the beam. The beam structure consists of $N = 10$ identical unit cells of length $L = 10$ cm. The unit cell is discretized with five Euler-Bernoulli beam elements. The beam's material is aluminum (see table 5.4).

Figure 5.33: Model of a free-free beam that consists of ten identical unit cells of length L = 10 cm.

Figure 5.34 relates the FRF and the phase change of the unit cell. In the phase plot, there are two branches of undamped waves. The upper branch with positive slope describes the wave that propagate in positive direction. The lower branch describes similar waves traveling in negative direction. The vertical lines in figure 5.34 mark the resonance peaks of the FRF and the corresponding critical phase characteristics of the wave solutions.

Young's modulus	64 GPa
Density	2700 kg/m^3
Poisson ratio	0.34
Loss factor	0.01

Table 5.4: Material properties of aluminum.
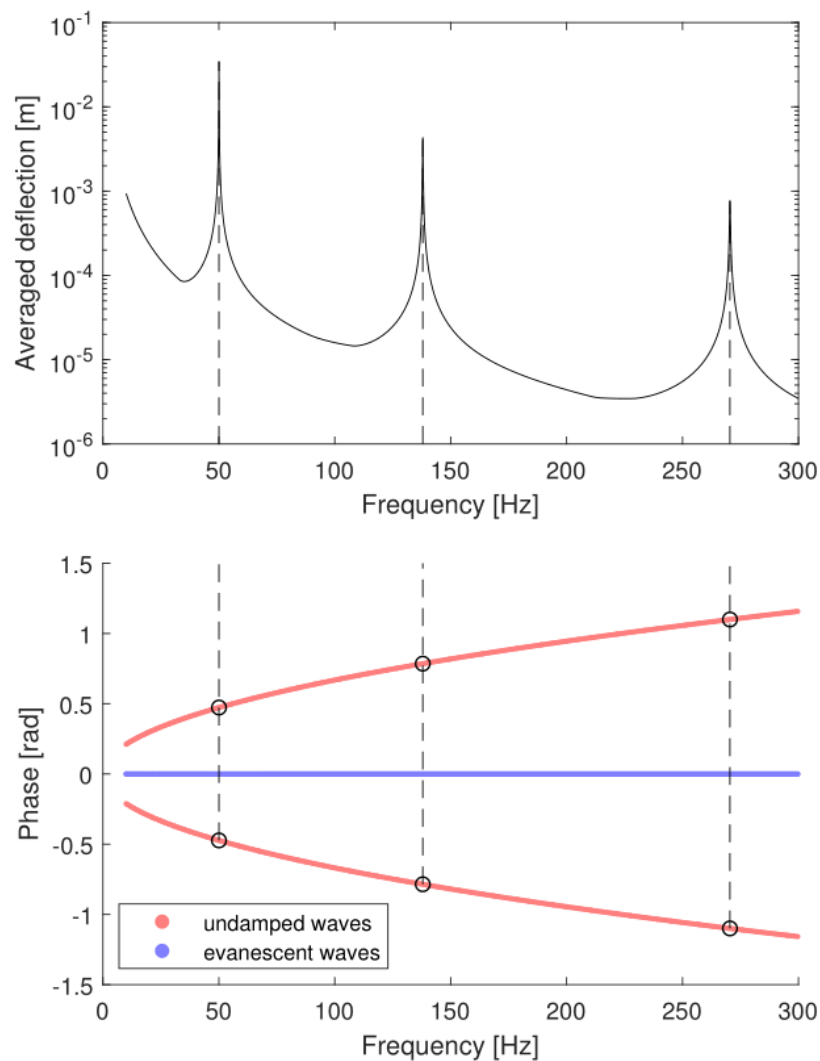
Figure 5.34: Averaged displacement of the beam (top) and the phase change ($\kappa_{Re}L$) of the unit cell (bottom); red curves identify undamped waves and the blue curves the evanescent waves.

Besides the phase characteristic, wave solutions also possess a decay characteristic. The decay characteristic limits the amplitude in the resonance peaks. For undamped structures, the propagating wave solutions do not decay. Therefore, the displacements at the resonance frequencies go to infinite. Assuming that the response of the structure results from the interference of the initial wave and an infinite number of reflections, there exists an upper

bound

$$Q \sum_{r=0}^{\infty} \mathrm{e}^{rk_I LN} \; . \tag{5.10}$$

Q is the amplitudes of the initial wave and r counts the number of reflections of the initial wave. The assumption for (5.10) is that the original wave ($r = 0$) ideally aligns with each reflected wave. For waves that decay in the direction of propagation, (5.10) is limited

$$Q \sum_{r=0}^{\infty} \mathrm{e}^{rk_I LN} = Q \frac{\mathrm{e}^{k_I LN}}{\mathrm{e}^{k_I LN} - 1} \quad \text{with} \quad k_I LN < 0 \; . \tag{5.11}$$

Using local resonators, it is possible to manipulate the phase and the decay characteristics of the wave solutions. This is linked with a change of the resonance frequencies as well as the vibration amplitudes at the resonance frequencies. To demonstrate this, the unit cell of the beam structure from figure 5.33 is modified. Each unit cell comprises a resonator with the following characteristics:

$$m_{res} = 5 \% \; m_{unit\;cell} \; ,$$
$$f_{res} = 138 \; \text{Hz} \; ,$$
$$D_{res} = 1 \% \; .$$
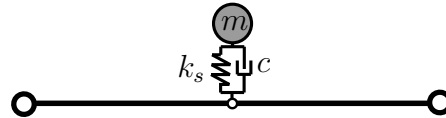
Figure 5.35: Modified unit cell.

The mass is fixed such that the resonator adds 5 % mass to the structure. The resonance frequency f_{res} determines the stiffness constant k_s. Finally, the damping constant c results from the damping ratio D_{res}. The periodic resonators change the eigenfrequencies and therefore the resonance peaks of the FRF. Table 5.5 compares the eigenfrequencies of the beam structure with and without resonators. The resonators splits the resonance at 138 Hz into multiple resonances between 124 and 154 Hz.

	Eigenfrequencies of the beam structure in Hz											
no resonator	50					138						270
ten resonators	49	124	137	138	138	138	138	138	141	141	141	154	273

Table 5.5: Eigenfrequencies of the beam structure with and without resonators.

Figure 5.36 shows the FRF of the beam structure with attached resonators. The dashed vertical lines mark the eigenfrequencies of the beam structure. For each frequency there exist a corresponding phase and decay characteristic of the wave solutions (see spherical

markers). Due to the symmetry of the phase and decay plot, figure 5.36 contains only the absolute values of the phase and decay information. The different colors mark the different wave types. As previously illustrated, undamped waves are defined as having a spatial decay of less than 1% per meter. The resonators modify the phase and the decay characteristics. The dotted lines indicate the phase and decay curves of the unmodified unit cell.
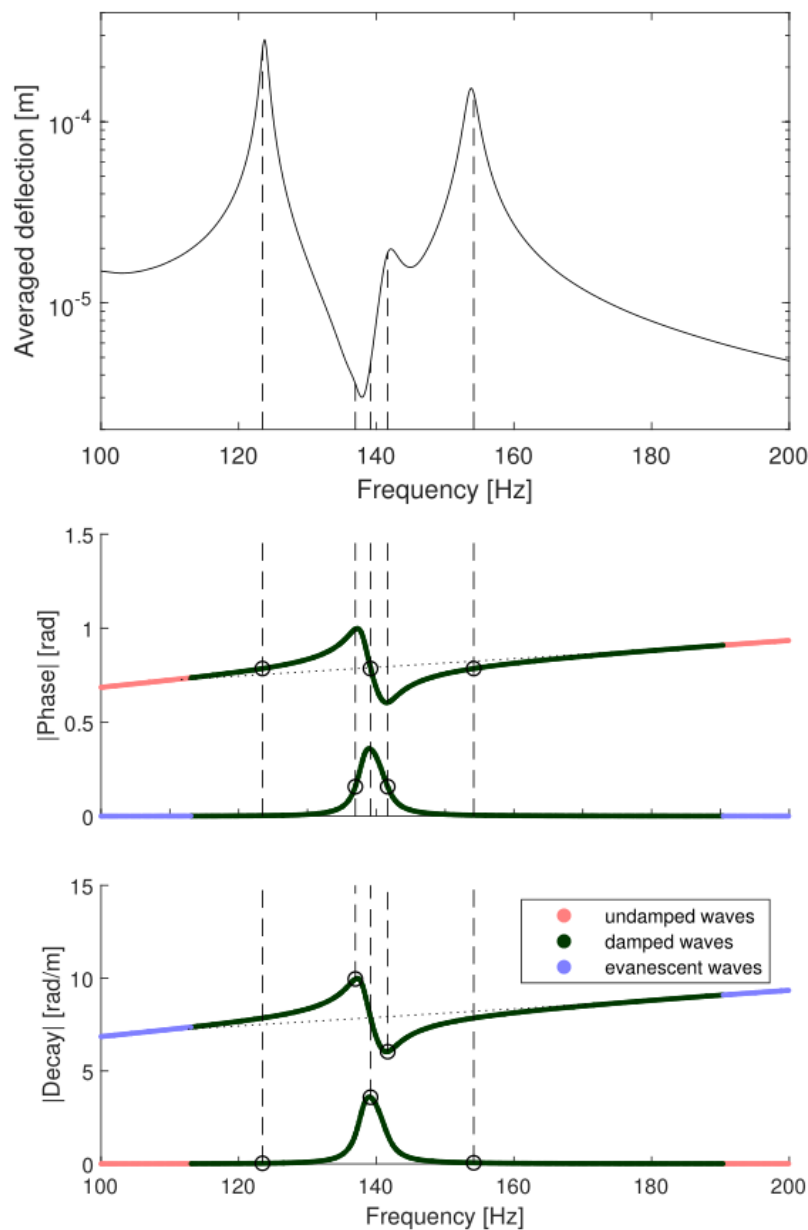
Figure 5.36: Frequency response function of beam structure with periodically attached resontors (top) and the phase $\kappa_{Re}L$ (middle) and decay κ_{Im} (bottom) characteristics from the wave solutions of the unit cell.

The change in the phase plot due to the resonators explains the splitting of the resonance frequencies. In contrast to the unit cell without resonator, the resonators generate five

critical phase shifts in the vicinity of the tuning frequency. Depending on the respective decay constant, the FRF emerges a resonance peak or not. A critical phase of $\frac{3}{2}\pi/N$ occurs at three different frequencies (124, 138 and 154 Hz). At 124 and 154 Hz, the decay constants are almost vanishing and therefore the FRF reveals resonance peaks at 124 and 154 Hz. Around the tuning frequency of the resonators, the resonators increase the decay constant from 0 to 3.6 rad/m. This results in a reduction of the FRF. Two additional critical phases of $\frac{1}{2}\pi/N$ appear at 138 and 142 Hz. These resonances emerge from the transformation of the originally evanescent waves. The corresponding decay constant (10.0 rad/m) at 138 Hz is larger compared to the respective decay constant of the unmodified unit cell (7.8 rad/m). At 138 Hz, there is no resonance peak observable in the FRF. However, at 142 Hz the respective decay constant (6.0 rad/m) decreases compared to the unmodified unit cell (8.0 rad/m), which yields a small peak in the FRF.

The previous investigation demonstrates that modifications of the wave solutions by local resonators directly effect the frequency dependent performance of the structure. The occurrence of resonance peaks is strongly influenced by the boundary conditions of the host structure. Nevertheless, an increased decay constant is important to reduce the motion of the host structure. Consequently, to optimize the design of a resonator without including the effect of the boundary conditions of the host structure can be performed based on the wave solutions of the unit cell. This approach is for example very useful to evaluate designs in an early stage of development, where the exact boundary conditions are not defined yet. In general a larger spatial decay at the target frequency reduces the vibration. Furthermore, a larger stop band yields a larger separation of the critical phase characteristics. This leads to an improvement of the broadband performance. Therefore, the maximal spatial decay and the stop band size are relevant quantities that assess the performance of local resonators.

5.2.4 Influence of the resonator spacing on the wave solutions

The following section investigates different configurations of the unit cell to asses the effect of the resonator spacing on the wave solutions. First, the influence of the length of the unit cell is considered for a discrete resonator. The total mass added by the resonator is 5 % of the beam mass. Thus, the overall mass added per unit length is constant. Varying the length L is equivalent to compare different resonator spacings for a fixed percentage of additional mass. The following section both investigates the spacing of vertical and rotational resonators as described in figures 5.26 and 5.30, respectively.
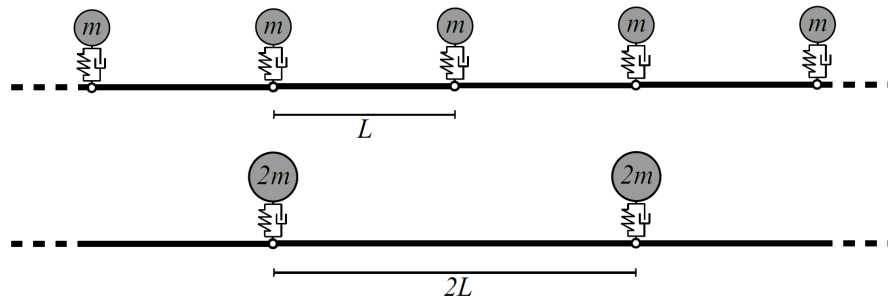
Figure 5.37: What is the optimal resonator spacing? Effect of doubling the beam length L on the mass of each individual resonator while the percentage of added mass remains constant.
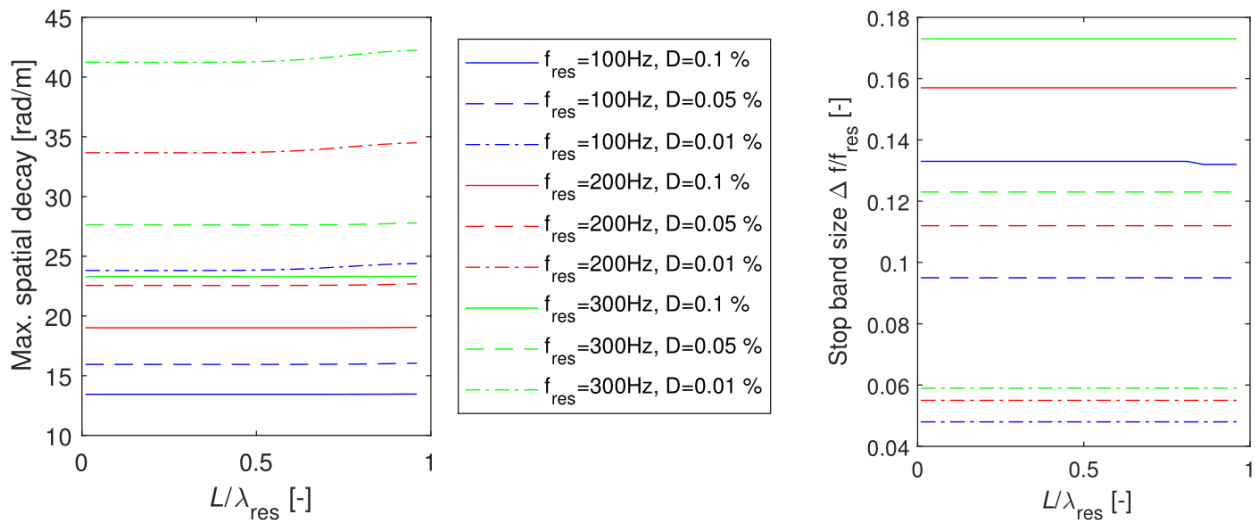
Figure 5.38: Influence of the resonator spacing on the stop band characteristics for a discrete vertical resonator.

Figure 5.38 illustrates the dependency of the stop band characteristics on the resonator spacing L for the beam with vertical resonators. The color of the curves indicate the frequency of the resonator and the line style the damping ratios. The mass ratio of the resonators m_{add} is 5 %. The left graph shows the maximal spatial decay ($\max \kappa_{Im}$) that occurs at the target frequency of the resonator. The right graph illustrates the stop band size (frequency range where only damped waves occur). To compare the different resonator configurations, the length of the beam is normalized by the wavelength of the bending wave at the eigenfrequency of the resonator λ_{res}. The size of the stop band Δf is normalized by the resonator frequency f_{res}. One observes that the spacing of the vertical resonators does not influence the stop band characteristics. The spatial decay and the stop band size are almost constant for all resonator configurations. A larger target frequency increases the maximal spatial decay and the stop band size. Increasing the damping decreases the maximal spatial decay of the resonator and increases the stop band size.
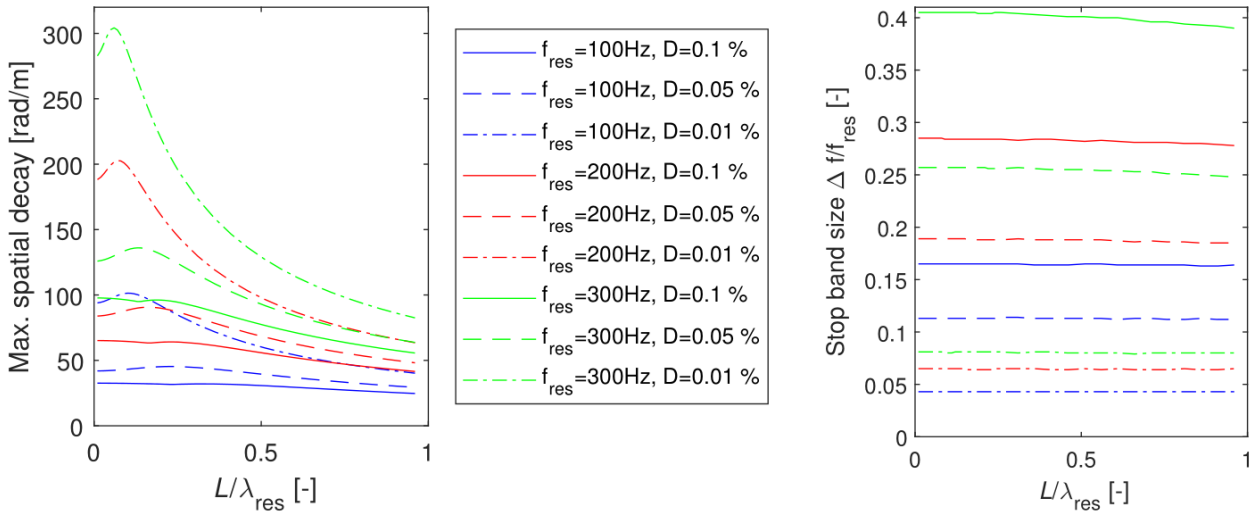
Figure 5.39: Influence of the resonator spacing on the stop band characteristics for a discrete rotational resonator.

Figure 5.39 shows the effect of rotational resonators. The parameters of the rotational resonators are listed in figure 5.30. In contrast to the vertical resonator, the maximal decay of the rotational resonator depends on the resonator spacing, whereas the stop band size is almost independent of the spacing. For larger frequencies and a lower damping ratios an optimal resonator spacing that maximizes the spatial decay evolves. A higher target frequency yields a lower optimal resonator spacing. Likewise, a lower damping ratio reduces the optimal resonator spacing. For low resonator frequencies and large damping ratio the maximal spatial decay is almost independent of the resonator spacing. The general observation that the spatial decay and the stop band size increase with increasing resonator frequency is also valid for the rotational resonators. Accordingly, a larger damping ratio results in a decrease of the maximal spatial decay and an increases of the stop band size.

In practice, locally resonant materials commonly consist of beam-like resonators integrated into the host structures. Therefore, in the following section the discrete resonators are replaced with beam-like resonators (see figure 5.40).

$f_{res} = \frac{1.875^2}{2\pi L_{res}^2} \sqrt{\frac{EI_{res}}{\rho A_{res}}}$	200 Hz
$m_{add} = m_{res}/m_{beam}$	5 %
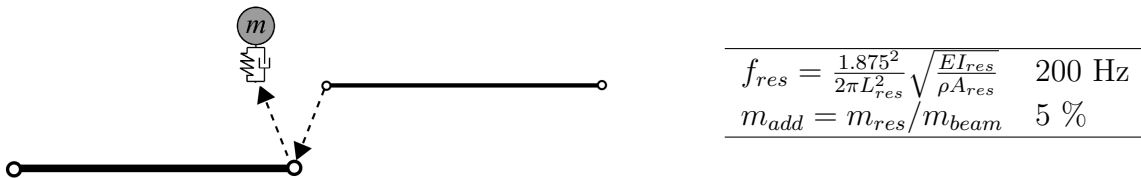
Figure 5.40: Model of an Euler-Bernoulli beam with attached Euler-Bernoulli beam that acts as a resonator; cross section A of the main beam is 1 cm^2.

The material and geometric properties of the host beam and the beam resonator are the

same as previously (compare to figure 5.24), except that the resonators Young's modulus is complex $\hat{E} = E(1 + i\eta)$, where η is the structural loss factor (for positive frequencies). The desired (first) eigenfrequency and the mass of the resonator beam determine the length and the cross section of the resonator. To derive the dependence between the geometry and the resonance frequency, the resonator beam is assumed to behave as a clamped-free Euler-Bernoulli beam [Blevins 2016].

Figure 5.41: Influence of the resonator spacing on the stop band characteristics for the beam resonator with varying loss factor.

Figure 5.42: Influence of the resonator spacing on the geometry of the beam resonator.

Figure 5.41 shows the maximal decay and the size of the stop band for the beam resonator shown in figure 5.40. The structural loss factor of the resonator material varies from 0.1% to 0.3%. With increasing loss factor the maximal spatial decay decreases while the stop band size increases. Increasing the damping results in a decrease of the maximal spatial

decay. The reason is that with increasing damping, the evanescent waves disappear. For the maximal decay, there exists an optimal resonator spacing that depends on the damping of the resonator. The stop band size is slightly increasing with increasing resonator spacing. Due to the fact that the amount of added mass by the beam resonator is fixed to 5 %, the geometry of the beam resonators changes when the spacing of the resonator varies. This is necessary to ensure that the eigenfrequency of the resonator remains the same. The resonator beam has a rectangular cross section. Figure 5.42 illustrates the changes in the geometry of the beam. The changes are independent of the damping. The length and the cross section of the beam resonator increases with the spacing. The reason is that a single resonator beam has a larger absolute mass for an increased spacing. Due to the change in geometry, the second moment of area changes and therefore the energy dissipation might vary as well. The reason is the direct link between the stiffness of the structure and the energy dissipation due to the structural loss factor. Therefore, it is difficult to separately investigate the influence of the spacing and the damping.
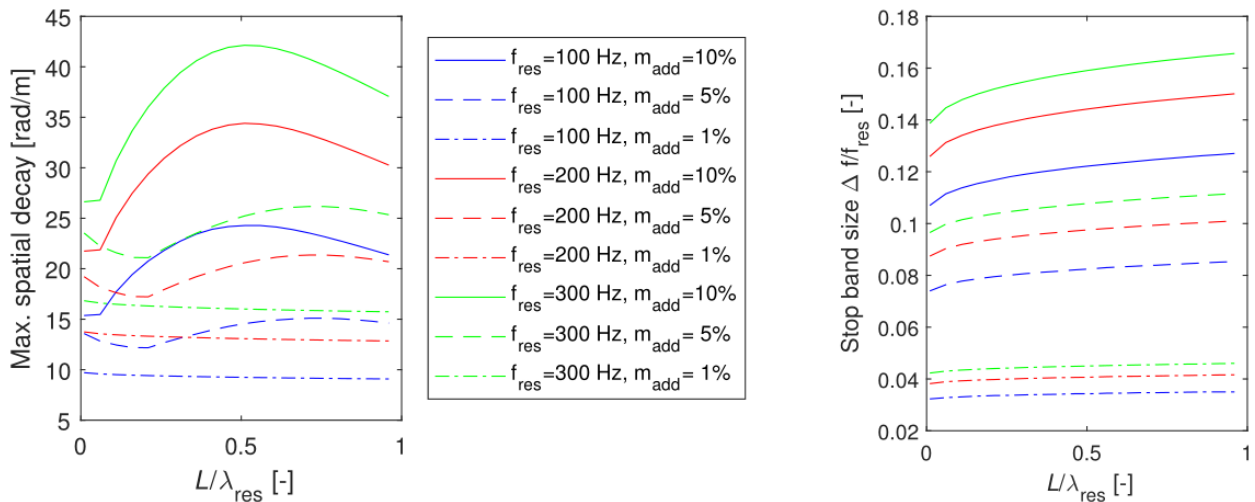
Figure 5.43: Influence of the resonator spacing on the stop band characteristics for the beam resonator with varying resonator mass ratio.

The next paragraph investigates the impact of the resonator mass ratio $m_{add} = m_{res}/m_{beam}$ and resonator frequency f_{res} for a fixed structural loss factor of 0.1 % of the resonator. Figure 5.43 shows the stop band characteristics. It is obvious that a larger mass ratio result in an increased maximal spatial decay and an increased stop band size. As previously, the stop band size is slightly increasing with increasing resonator spacing. Furthermore, the optimal spatial decay only depends on the mass ratio not on the resonator frequency. For a mass ratio of 10 % the maximal spatial decay is maximized for a resonator spacing that matches half the length of the bending wave at the resonator frequency. For 5 % additional
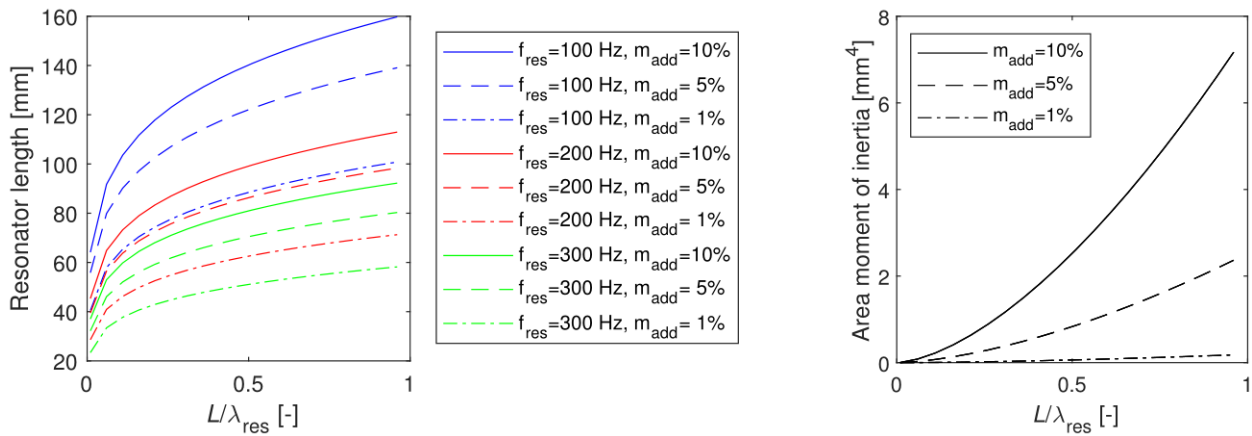
Figure 5.44: Influence of the resonator spacing on the geometry of the beam resonator. The beam geometry is defined by the rectangular cross section and the length of the beam resonator.

mass, the optimal spacing increases to three quarters of the bending wave at the resonator frequency. For a mass ratio of 1 %, the maximal spatial decay is almost constant for all resonator spacings. It slightly decreases with increasing spacing. The previous investigation revealed that the optimal resonator spacing also depends on the energy dissipation in the resonator beam. Figure 5.44 shows the variation of the length and the area moment of inertia of the beam resonator for the different spacings. The area moment of inertia is the same for all resonator frequencies. It only depends on the mass ratio. Thus, the cross section is adjusted to match the required mass of the beam resonator, while the length of the beam determines the resonator frequency.

$$f_{res} = \frac{1}{2\pi} \sqrt{\frac{3EI_{res-beam}}{L^3_{res-beam}(m+0.24m_{res-beam})}} \qquad 200 \text{ Hz}$$

$$m_{add} = (m + m_{res-beam})/m_{beam} \qquad 5 \text{ \%}$$
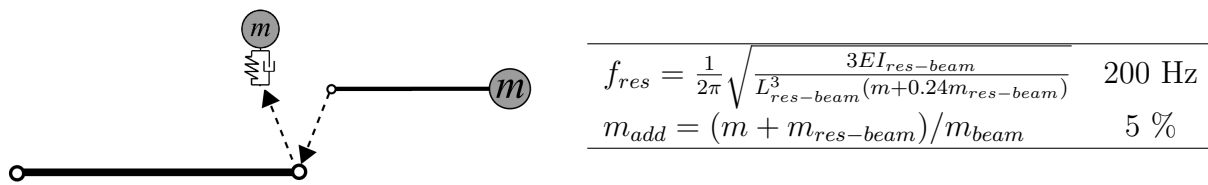
Figure 5.45: Euler-Bernoulli beam with attached resonator beam with additional end mass and corresponding properties of the resonator beam.

For beam-like resonators tackling low frequency structure borne noise, the resulting resonator beam is relatively long compared to the resonator spacing. This might be infeasible for practical applications. An additional mass located at the end of the beam resonator can avoid that: the larger the end mass, the shorter the resonator beam becomes (assuming the resonance frequency remains unchanged). Following this, the same investigation are performed on resonator beams with varying ratio of end mass to resonator beam mass $m/m_{res-beam}$ (see figure 5.45). As previously, the structural loss factor of the resonator beam is 0.1 %. The total added mass of the resonator is 5 % and the resonator frequency is
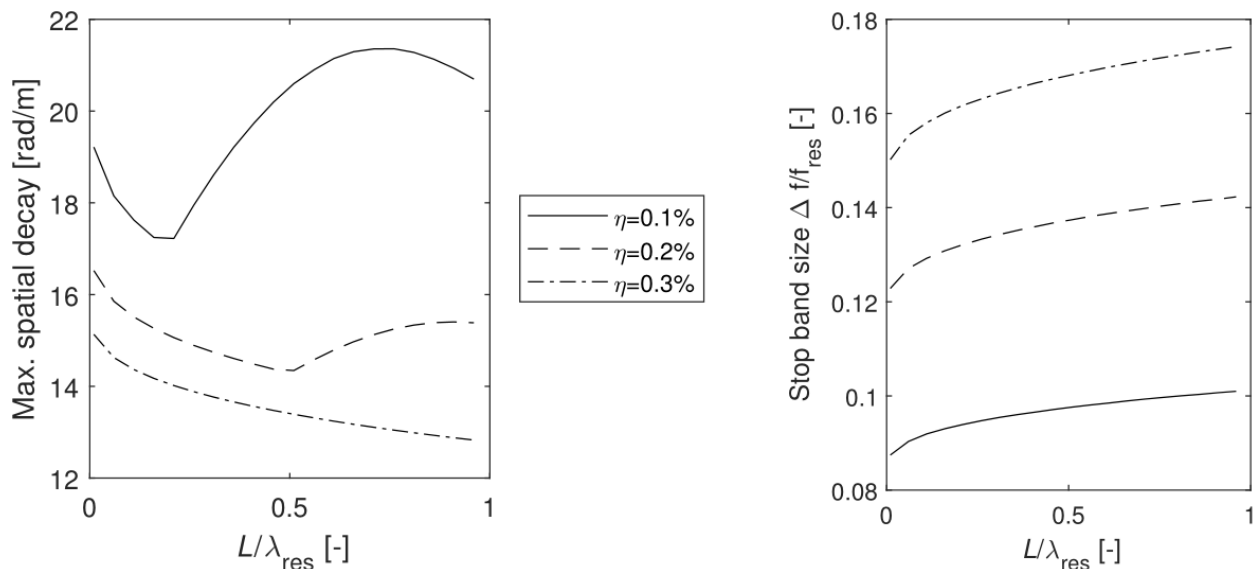
200 Hz.
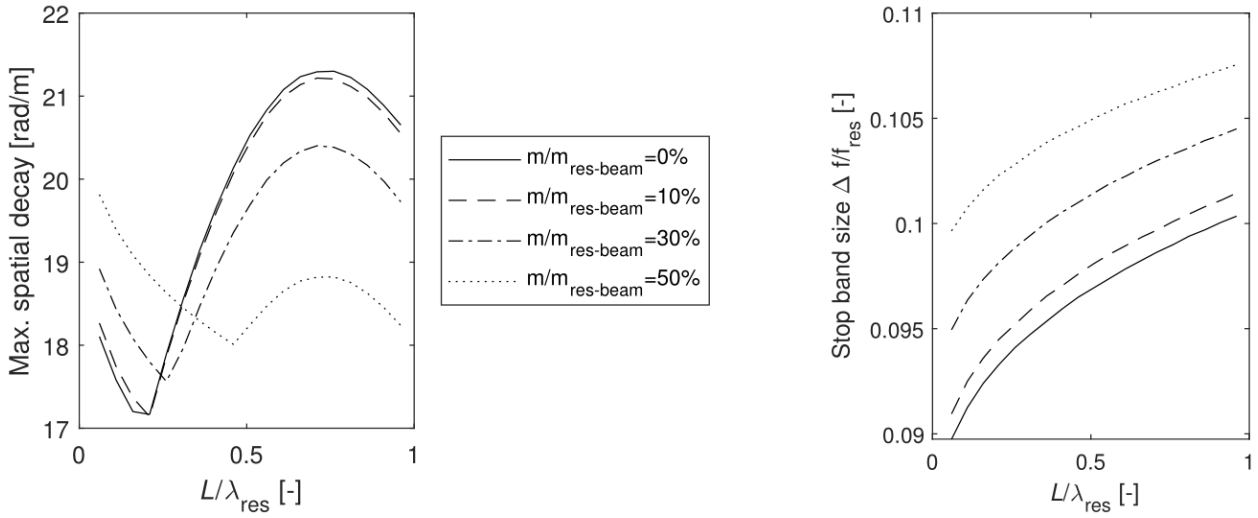
Figure 5.46: Influence of the resonator spacing on the stop band characteristics for the beam resonator with varying end mass ratio.
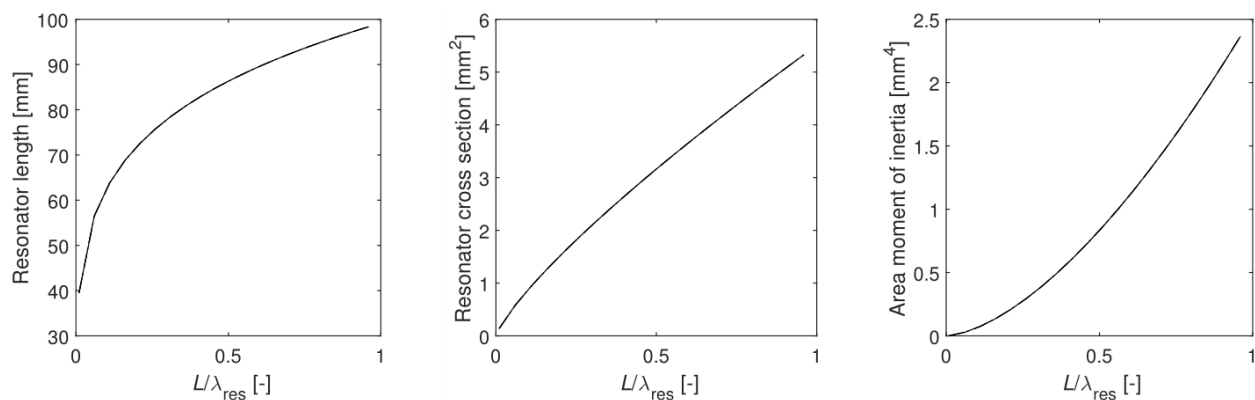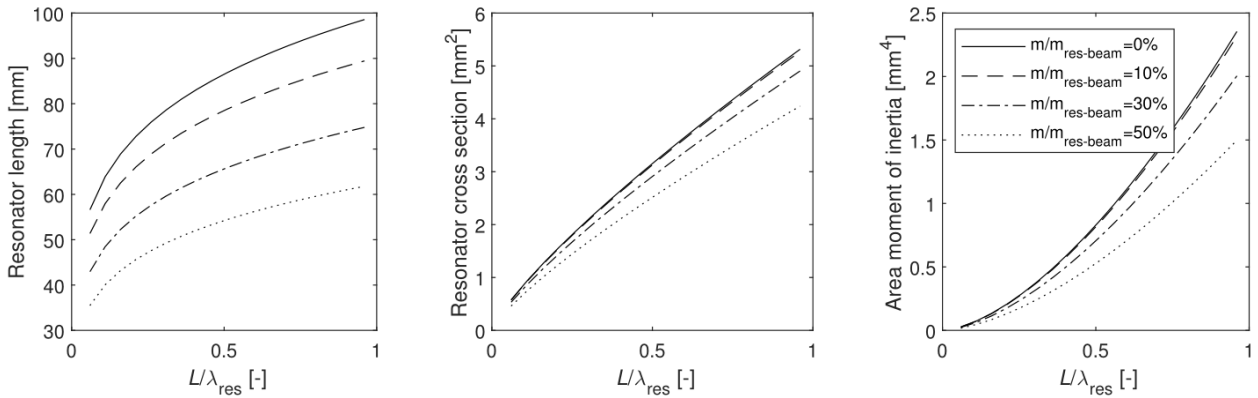

Figure 5.47: Influence of the resonator spacing on the geometry of the beam resonator with end mass.

Figure 5.46 illustrates the stop band characteristics for beam resonators with various end mass ratios. As shown in previous investigation, the beam without end mass shows a optimal resonator spacing that maximizes the decay at three quarters of the bending wavelength of at the resonators eigenfrequency. Increasing the end mass ratio the maximal spatial decay for larger resonators spacings ($L/\lambda_{res} > 0.3$) decreases and for lower spacings ($L/\lambda_{res} < 0.3$) it increases. This trend continues until the optimal resonator spacing shifts towards lower spacings for an end mass ratio of 50 %. However, the maximal decay at the optimal spacing is higher for the beam without end mass. In contrast to the spatial decay characteristics, the stop band size increases with increasing end mass ratio for all resonator spacings. Figure 5.47 shows the resulting geometric parameters of the resonator beam.

Concluding, both discrete and beam resonator show that with increasing target frequency of the resonator the maximal spatial decay and the stop band size increases. For the vertical discrete resonators, the wave characteristics are independent of the spacing. In contrast, the rotational and beam-like resonators have an optimal resonator spacing that maximizes the spatial decay at the target frequency of the resonator. The optimal resonator spacing depends on the target frequency and the damping of the resonator. In contrast, the spacing does not strongly influence the stop band size. It slightly increases with increasing resonator spacing. Furthermore, beam-like resonators with additional end mass generate shorter beam resonators. The more resonator mass is located at the end of the beam the larger the stop band size. Depending on the resonator spacing, the maximal spatial decay increases or decreases with increasing tip mass ratio. However, the maximal possible decay of a beam resonator without end mass is larger than the maximal possible spatial decay of a resonator beam with end mass.

5.2.5 Sound radiation of finite beams with discrete resonators

The following section investigates the impact of resonators on the vibration of the structure and the radiated sound power. The host structure is a beam made of aluminum and has a length of 1 m and a thickness of 1 cm. Table 5.4 lists the material properties of aluminum. The beam consists of 100 beam elements. 30 periodic resonators complement the beam.
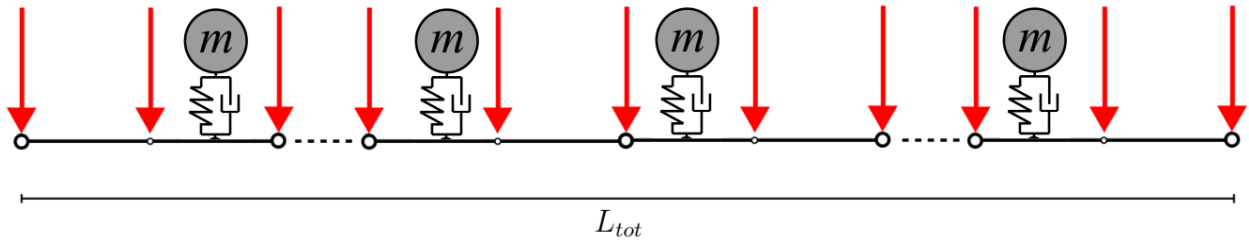
Figure 5.48: Model of a beam with 30 periodically attached resonators.

The discrete resonators are added as additional DOF (see section 4.1.3). All vertical degrees of freedom of the beam are loaded by a single load. Each single load has an amplitude of 1 N and random phase drawn from the uniform distribution between $-\pi$ and $+\pi$. This ensures that all bending modes are excited.
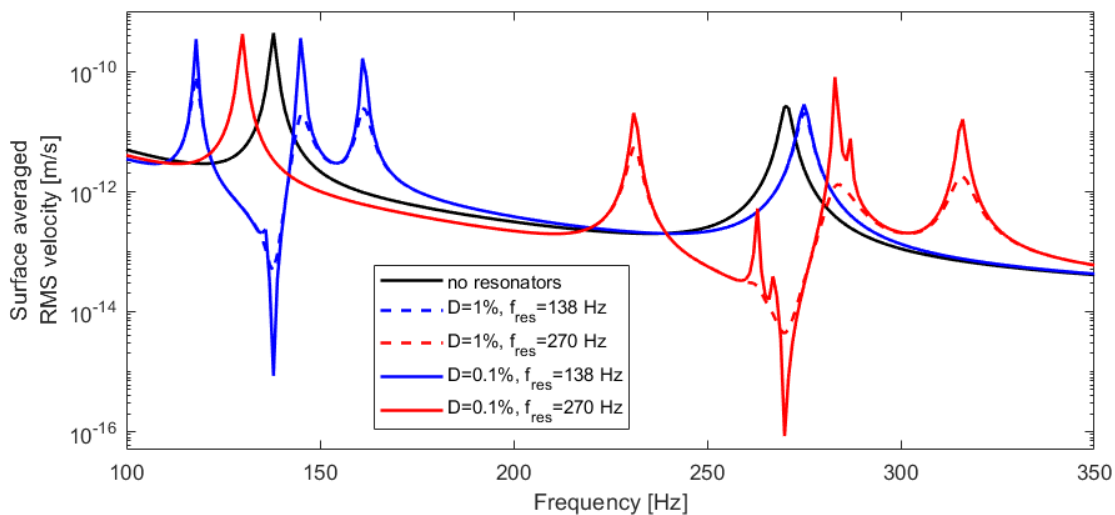
Figure 5.49: Surface averaged vertical velocity for beams with 30 periodically attached resonators with different parameters of the resonators.

Figure 5.49 compares the integrated vertical surface velocity of four different sets of resonators. The black curve indicates the velocity of the host structure without resonators. The blue and red curves illustrate the impact of the resonators with tuning frequency $f_{res} = 138$

Hz and $f_{res} = 270$ Hz, respectively. The overall mass of the resonators equals 10 % of the mass of the host structure and each resonator has the same mass. The colored straight lines mark resonators with a damping ratio $D = 0.1\%$ and the respective dashed lines indicate the resonators with a damping ratio $D = 1\%$. The resonators yield a significant reduction of the averaged velocity curves at the target frequency. However, there occur multiple resonance peaks around the target frequency. These peaks occur due to the additional modes that the resonators cause. In fact, closed to the target frequency of the resonators there occur $n - 1$ eigenfrequencies, where n is the number of resonators added to the structure. Some of these modes are observable as peaks in the frequency spectrum of the surface velocity. For the resonators with frequency $f_{res} = 138$ Hz, these peaks occur at 118 Hz, 145 Hz and 161 Hz, for the resonators with frequency $f_{res} = 270$ Hz at 231 Hz, 283 Hz and 316 Hz. The resonators with the larger damping ratio (dashed curves) show a reduction of the resonance peaks as well as a smaller dip at the target frequency of the resonators.
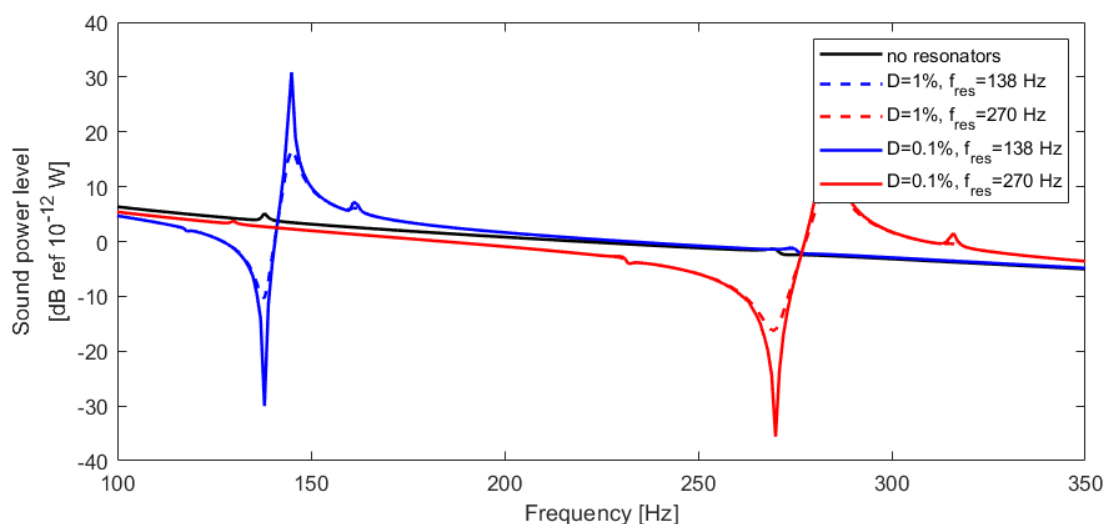
Figure 5.50: Sound power level of the radiated sound for beams with 30 periodically attached resonators with different parameters of the resonators.

Figure 5.50 shows the sound power level for the different configurations. The sound power is computed per unit meter along the width of the beam using 100×100 discrete elementary radiators (see section 2.5.2). For the host structure without resonators, there are no strong peaks in the observed frequency range. The main influence of the resonators is a strong dip at the target frequency of the resonators followed by a peak. The resonators reduce the sound radiation at the target frequency, however for frequencies slightly above the resonance frequency, the sound radiation significantly increases. Increasing the damping ratio of the resonators results in a smoothing of the dip and the peak. To explain the occurrence of the

peaks and the dips, the following passage discusses the wavenumber spectra of the vertical surface velocity at the respective excitation frequencies.
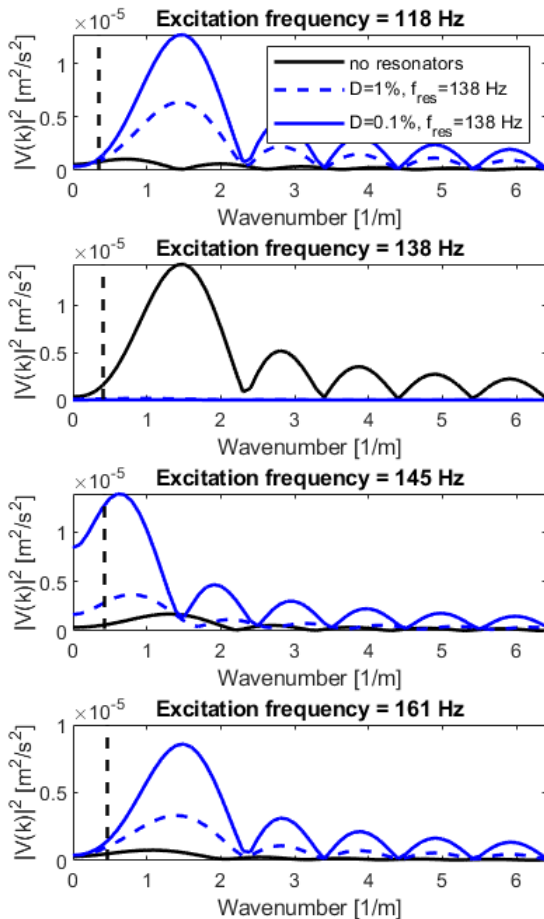
Figure 5.51: Wavenumber spectra of the lateral surface velocity for beams with 30 periodically attached resonators (f_{res} = 138 Hz) at different excitation frequencies; the vertical line marks the corresponding wavenumber of the air.
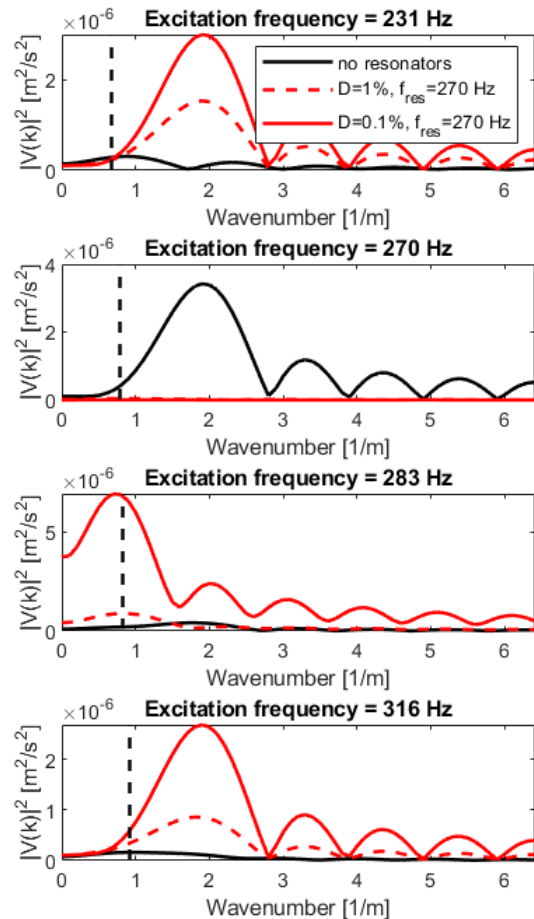
Figure 5.52: Wavenumber spectra of the lateral surface velocity for beams with 30 periodically attached resonators (f_{res} =270 Hz) at different excitation frequencies; the vertical line marks the corresponding wavenumber of the air.

Figure 5.51 and figure 5.52 compare the wavenumber spectra of the surface velocity at the resonance peaks observed in the FRF of the averaged surface velocity. The vertical line indicates the wavenumber of air at the respective frequency. Thus, wavenumbers smaller than the vertical line contribute to the radiated sound. The maximum of the wavenumber spectra corresponds to the dominant structural wavenumber. The smaller side lobes result

from the Fourier transformation of the window function linked with the finite beam. Since the multiplication with a window function in the spatial domain is equivalent to a convolution with the sinc function in the wavenumber domain.

At the target frequencies (138 Hz and 270 Hz), the resonators strongly reduce the energy of the wavenumber spectra which strongly reduce the radiated sound power. For the other resonance peaks below and above the target frequencies, the resonators increase the level of the spectra. For the resonance peaks below the target frequencies of the resonators (118 Hz and 231 Hz), the beams with resonators have a larger dominant structural wavenumber. Therefore, the increased vibration level does not yield an increased radiated sound power because most of the wavenumber components are above the wavenumber of the air (subsonic) and do not contribute to the radiation. At the resonance peaks above the target frequencies (145 Hz and 283 Hz), the resonators decrease the dominant structural wavenumber. The increased power in the wavenumber spectra and the shift of the dominant structural wavenumber towards the supersonic part of the spectra strongly increase the radiated sound power. A larger damping ratio reduces this shift with respect to the wavenumber spectra of the host structure without resonators. Therefore, increasing the damping is a effective measure to reduce the sound radiation peak that occurs slightly above the target frequency of the resonators. On the one hand, it reduces the power of the spectra. On the other hand, it shifts the dominant structural wavenumber further away from the supersonic part of the spectra. The second resonance peak that occurs in the averaged surface velocity (at 161 Hz and 316 Hz) does not appear in the sound radiation. The reason is the same as for the resonance peak below the target frequency of the resonators: the dominant structural wavenumber is shifted towards the subsonic part of the spectra.

The next section investigates the same data for other tuning frequencies of the resonators. The setup for the host structure is the same as previously. The coincidence frequency of the structure is 1323 Hz. The investigated resonator frequencies are 668 Hz, 1242 Hz and 1595 Hz. In the following plots, the color of the curves indicate the target frequency of the resonators. The line style marks different configurations for the mass ratio and the damping ratio of the resonator:

- straight line: $m_{add} = 10\%$, $D_{res} = 0.1\%$

- dashed line: $m_{add} = 10\%$, $D_{res} = 1\%$

- dotted line: $m_{add} = 5\%$, $D_{res} = 1\%$

Figure 5.53 illustrates the surface velocities. As previously observed, the resonators split up the peak of the unmodified host structure in several other resonance peaks, whereas at the

target frequency a dip appears. For the configurations with the lower damping ratio (straight lines), there appear multiple resonance peaks in the vicinity of the target frequency. With increasing target frequency the width of the reduction dip increases. In general, the mass of the resonators influence the width and the depth of the dip. A larger mass results in a more broadband and deeper dip of vibration suppression, but the resonance peaks next to the dip increase as well. In contrast, a larger damping ration reduces the depth of the dip and also decreases the resonance peaks around the target frequency.
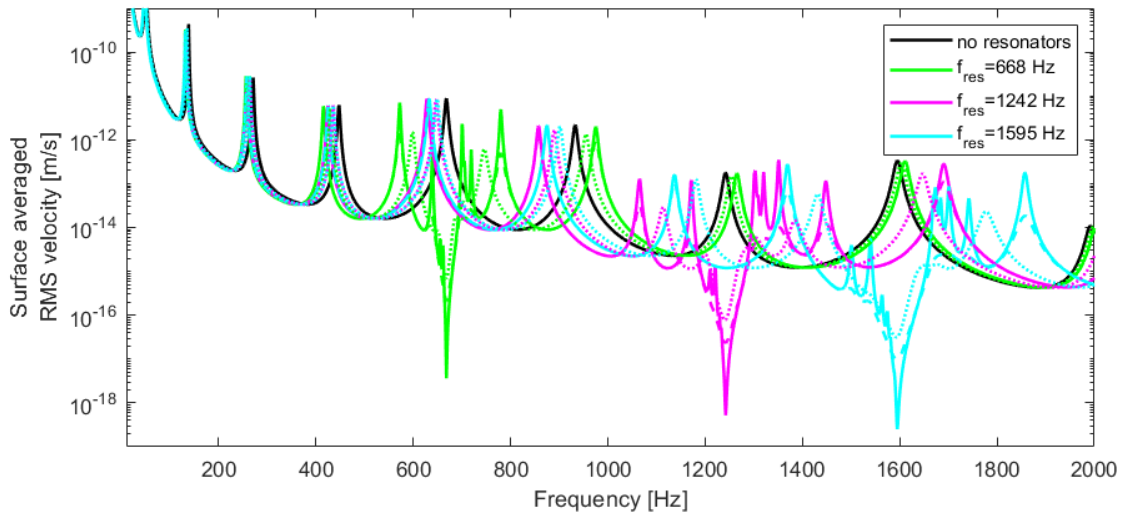
Figure 5.53: Surface averaged vertical velocity for beams with 30 periodically attached resonators with different parameters of the resonators; straight lines indicates resonators with a total mass of 10 % of the mass of the host structure and the dotted lines indicates the set of resonators with a total mass of 5 % of the host structure.
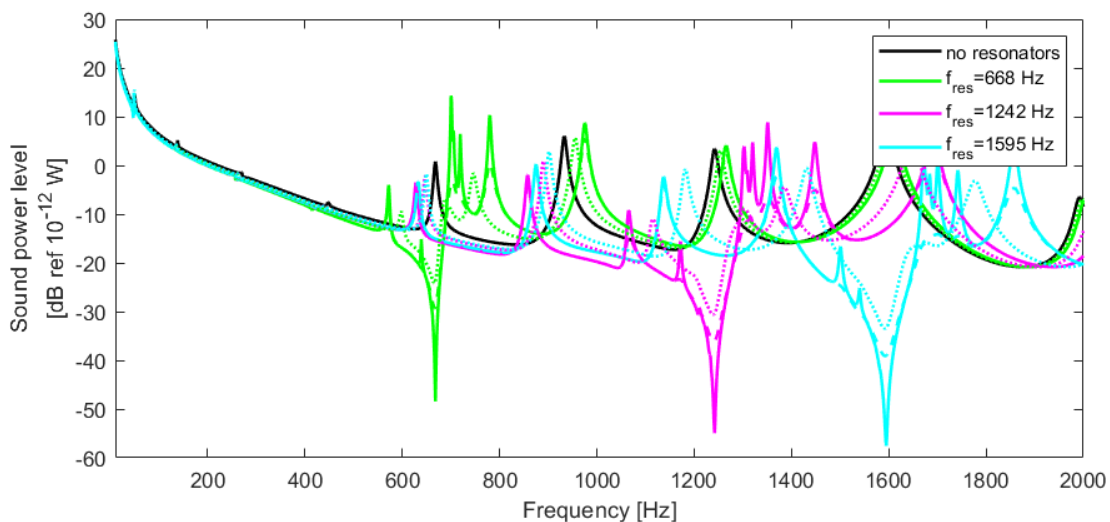
Figure 5.54: Sound power level of the radiated sound for beams with 30 periodically attached resonators with different parameters of the resonators.

Figure 5.54 shows the sound power level for the respective configurations. Up to 500 Hz, there are no peaks of increased sound radiation. The reason is that the structural wavenumber is larger than the corresponding wavenumber of the air. Besides a very small decrease (<1 dB), the resonators have no significant effect on the sound radiation up to 500 Hz.

For the resonators with target frequency 668 Hz (green curves), there is a small peak in front of the dip of reduced sound radiation. After the dip two larger peaks appear at 700 Hz and 780 Hz. For the resonators with the lower damping ratio and the larger mass (straight green line), these peaks are strongly developed and there exist additional side peaks at 639 Hz and 719 Hz. Decreasing the mass or increasing the damping ratio results in reduction of the peaks that are adjacent to the dip of reduced sound radiation. The wavenumber spectra gives information about the appearance of these peaks.
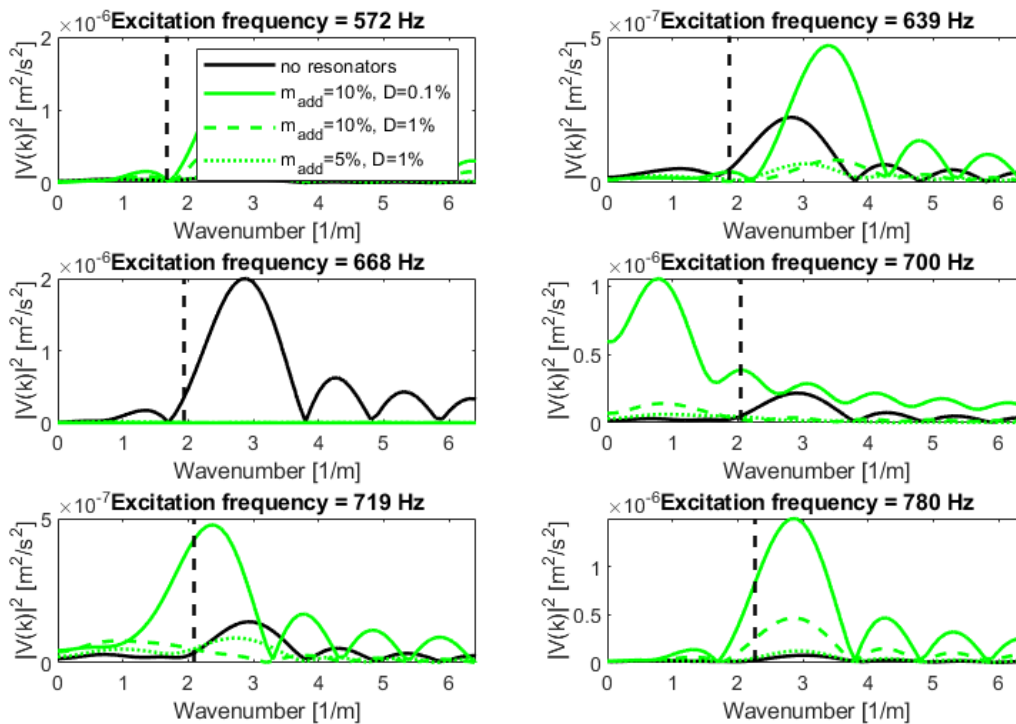
Figure 5.55: Wavenumber spectra of the vertical surface velocity for beams with 30 periodically attached resonators (f_{res} = 668 Hz) at different excitation frequencies; the vertical line marks the corresponding wavenumber of the air.

Figure 5.55 shows the wavenumber spectra at the peaks observed in the sound power level. In general, one observes two main aspects in the wavenumber spectra: First the resonators change the over all power level of the wavenumber spectra and second, the resonators shift the wavenumber spectra. Depending on the parameters of the resonators the power level of

the wavenumber spectra increases or decreases for different frequencies of excitation. At 572 Hz, the wavenumber spectra increases, however, this merely results in a small increase of the radiated sound power. The reason is that the main structural wavenumber is notably larger than the wavenumber of the air (vertical line). At 639 Hz, the resonators shift the main wavenumber of the structure towards a larger wavenumber (compared to the host structure without resonators). Therefore, the sound radiation is smaller for the configurations with resonators, even though the resonators with a damping ratio of $D = 0.1\%$ show a strongly increased power level of the wavenumber spectra. Comparing the shift and the level of the spectra of different resonators, a larger mass of the resonators yields a larger shift in the wavenumber domain and an increased power level. Increasing the damping ratio reduces the level but has no observable effect on the shift. If the excitation frequency matches the eigenfrequency of the resonators, the level of the wavenumber spectra is strongly reduced which results in the strong reduction of radiated sound power. The strong shift of the wavenumber spectra towards lower wavenumber at 700 Hz explains the peak of sound radiation. Due to the shift, the main structural wavenumber is below the wavenumber of air. As previously, a higher mass yields a stronger shift as well as an increased power level of the wavenumber spectra. The wavenumber spectra at 719 Hz show similar characteristics but the shift towards lower wavenumbers is reduced. The resonators with large mass and low damping ratio show a strong increase of the level, which results in an additional side peak in the sound power level. At 780 Hz, there is no longer a shift in the spectra. One observes the effect of the resonators in the increased level of the wavenumber spectra, which again yield a peak in the sound radiation. The respective wavenumber spectra for the resonators targeting 1242 Hz agree with the above described observation. Figure A.20 in the appendix lists the respective spectra.
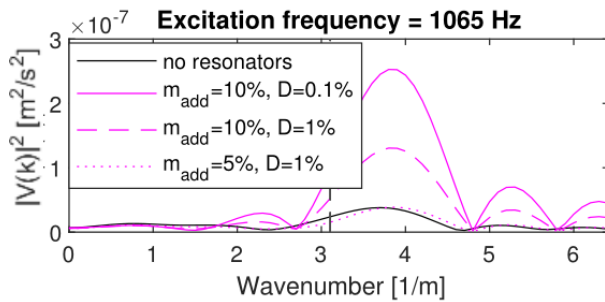
Figure 5.56: Wavenumber spectra of the lateral surface velocity for beams with 30 periodically attached resonators (f_{res} = 1242 Hz) at 1065 Hz; the vertical line marks the corresponding wavenumber of the air.
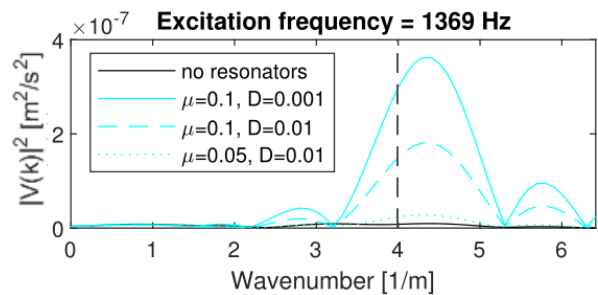
Figure 5.57: Wavenumber spectra of the lateral surface velocity for beams with 30 periodically attached resonators (f_{res} =1595 Hz) at 1369 Hz; the vertical line marks the corresponding wavenumber of the air.

Comparing the sound power levels, the beam with resonators tuned to 1595 Hz show a more pronounced peak at frequencies slightly below the dip of radiation suppression compared to the other resonator configurations. The reason is that the coincidence frequency of the structure (1323 Hz) is close to the excitation frequency of 1369 Hz. Therefore, a large amount of the wavenumber spectra at 1369 Hz contributes to the sound radiation. As the resonator increase the level in the spectra, the radiated sound power increases for frequencies above the coincidence frequency (compare figure 5.56 and 5.57).

Summarizing, resonators tuned to a fixed frequency generate multiple resonance peaks in the averaged surface velocities. For low frequency resonators, the sound power level only shows a characteristic dip of sound reduction followed by a peak in the sound radiation. The reason for the increased sound radiation is the increase of the vibration level as well as a shift of the wavenumber spectra towards the supersonic part of the spectra. For resonators tuned to higher frequencies, the additional peaks in the surface velocity also appears in the sound power level. The peaks increase with increasing resonator mass. Increasing the damping helps to reduce these peaks, however, it also deteriorates the vibration reduction and sound reduction at the target frequency of the resonator.

5.2.6 Summary

The previous investigations demonstrate how the Wave Finite Element Method (WFEM) can be applied to design locally resonant materials. Besides the location of the stop band, the spatial decay characteristics also provide information about the wave solutions that exist in the frequency range of stop bands. This helps to design the frequency dependent performance of locally resonant materials. The link between wave solutions and the motion of the structure explains why the spatial decay reproduces well known characteristic properties of resonant materials. Parameter studies performed on the wave solutions yield design rules for locally resonant materials. The advantage of this approach is that the design of the resonant material are related to the wave solutions which are independent of the boundary conditions of the host structure. Consequently, optimizing the design based on the wave solution can also be done in an early stage of development where the exact boundary conditions of the structural components are unknown.

The presented work shows how the beam resonators can be dimensioned to generate mass optimized acoustic metamaterial with beneficial vibroacoustic performance. There are two quantities that determine the performance of the metamaterial. First, the broadband performance which is determined by the frequency range in which the local resonance suppresses

the propagation of undamped waves. The larger this frequency range, the better is the broadband performance. Second, the maximum spatial decay that occurs at the eigenfrequency of the resonator. This is denoted as the narrowband performance. A larger spatial decay at the target frequency of the resonator yields a better narrowband performance. Table 5.6 visualizes the influence of different parameters on the broad- and narrowband performance. There are four different parameters:

- the total mass of the beam resonator

- the damping of the beam resonator

- the endmass ratio of the beam resonator

- the spacing of the beam resonator

The diagonal entries of the matrix (table 5.6) show the general influence of the parameter on the performance. The following color show a beneficial or disadvantageous influence:

■ beneficial

■ disadvantageous

The off-diagonal entries demonstrate which of the parameters is more relevant for the respective performance. For the comparison the following color scheme is used:

■ more beneficial

▮▮▮ equally beneficial

▮▮▮ equally disadvantageous

■ less beneficial

Each entry in the matrix contains two colors. The first is related to the broadband performance, whereas the second is related to the narrowband performance.

broadband / narrowband	↑ total mass	↑ damping	↑ endmass ratio	opt. spacing
↑ total mass	■ / ■	▮▮ / ■	■ / ■	■ / ■
↑ damping	▮▮ / ■	■ / ■	■ / ▮▮	■ / ■
↑ endmass ratio	■ / ■	■ / ▮▮	■ / ■	■ / ■
opt. spacing	■ / ■	■ / ■	■ / ■	■ / ■

Table 5.6: Influence of the different parameters of the local resonator on the broad- and narrowband performance.

The following section explains the information that is summarized in table 5.6. The information about the influence of the effect of increasing the total mass of the resonator is contained in the first row. The first entry indicates that increasing the total mass of the

resonator is beneficial for the broad and narrowband performance. Comparing the influence of the total mass to the influence of the damping (second entry in the first row), the effect on the broadband performance is equally beneficial. However, for the narrowband performance the total mass of the resonator is of greater importance than the damping. Looking at the other entries of the first row, one can see that the effect of the total mass is more beneficial for the broad- and narrowband performance than the endmass ratio or the optimal resonator spacing. Concluding, increasing the total mass of the resonator has the strongest influence on the broad- and narrowband performance. Therefore, the mass of the resonator should be as large as possible.

The second row shows the impact of increasing the damping. An increased damping improves the broadband performance and the benefit of an increased damping is larger then the benefit of an increased endmass ratio or an optimal resonator spacing. For the narrowband performance, the damping is disadvantageous. Similarly, the endmass ratio does not improve the narrowband performance (row three). However, the impact of the endmass ratio is less significant than the total mass or the damping. In contrast to that, the optimal resonator spacing improves both the broad and the narrowband performance (row four). However, for the broadband performance, it is less effective than the other parameters. If an increase of the total mass of the resonator is impossible, the optimal resonator spacing is the only alternative to improve the narrowband performance. Although, the benefit is smaller than the benefit of an increased mass. The optimal resonator spacing depends on the target frequency and the damping of the resonator.

Besides the investigation of the wave solution, further studies investigated the vibroacoustic behavior of locally resonant materials. In general, resonant materials tuned to a single frequency generate multiple resonance peaks in the vicinity of the target frequency. The reason for that are the multiple eigenfrequencies due to the local resonators. These additional resonances can increase the radiated sound power for some frequencies. Parameters as the mass or the damping of the resonators can be adjusted to avoid spectral peaks of increased sound radiation, however, this also deteriorates the vibration reduction and sound reduction at the target frequency of the resonator. Therefore, one has to gauge the parameters of the resonators.

6 Conclusion

The trade-off between reduced mass and reduced acoustic performance of conventional lightweight components is crucial for future aircraft and vehicle applications. Innovative high-efficient propulsion might intensify this trade-off. Conventional measures are only effective for higher frequencies and implicate an increase of the mass of the overall structure. Therefore, there is a need for novel lightweight metamaterials that improve the vibroacoustic performance without a notable increase of the overall mass. Acoustic metamaterials show great potentials for low mass lightweight structures with improved vibroacoustic properties. In many examples, acoustic metamaterials have dynamically modified properties as negative density, negative compressibility, or negative refraction. The general idea of negative effective material constants offers novel design opportunities for future lightweight components. Such unconventional material properties result from the evaluation of the material properties on the macro scale. However, metamaterials consists of sub elements scaled below the wavelength of the media it interferes with. This microscopic dimensioning yields macroscopic properties that seems to be beyond the limits of conventional materials.

In general, there are many different concepts of acoustic metamaterials. This thesis focuses on two concepts for the design of novel lightweight structures with beneficial vibroacoustic properties. The first concept is based on the idea of so called "acoustic black holes". The idea is to capture bending waves at predefined locations to reduce structure borne noise. Local thickness reductions with additional damping treatment effectively dissipate large amounts of vibrational energy. An advantage of this concept is the potential to reduce the mass of the overall structure, while the vibroacoustic properties improve on a large frequency range. In this work, comparisons between structural components with and without local thickness reduction demonstrate the increased energy dissipation at localized damping treatments and explain the resulting lower amplitudes of the vibration and the reduction of the radiated sound power. Beyond that, the presented numerical studies reveal that a smooth thickness profile generating a smooth impedance transition is not generally necessary to maximize the performance. Studies of different thickness profiles explain the particular influence on the macroscopic behavior of the structure. Based on that, the presented studies show that

an abrupt thickness profile with localized damping measures outperforms smooth profiles with similar damping measures on a wide frequency range. The benefit of a smooth ABH configuration only emerge for low frequencies.

The second concept, which is investigated in detail, are locally resonant materials. The advantage of this concept is that local resonances modify the vibroacoustic properties of the host structure in desired frequency ranges. Such materials are suitable for specific narrow-band excitation scenarios. In vehicles, such phenomena result from the blade passing frequency of propellers, the gear mechanism or other narrow-band noise induced by the engines. Due to the different scales of the resonating sub structures and the host structure, various modeling aspects for locally resonant materials are covered. The focus of this work are beam-like resonators. The author derives the relation between the dynamic behavior of beam-like resonators and simple SDOF systems. In general, resonant materials strongly improve the vibroacoustic performance at the target frequency of the resonators. However, slightly below and above the target frequency, multiple additional resonances occur. The reason for that are the multiple eigenfrequencies due to the local resonators. A detailed discussion about the sound radiation of such materials clarifies under which circumstances the additional resonances result in an increased sound radiation.

It was shown that parameter studies based on the unit cell are suitable to evaluate the performance of periodic materials. Applying the Wave Finite Element Method to compute the wave solutions, it is possible to identify the stop band characteristics.

The novelty of the presented methodology is the computation of the spatial decay characteristics in the stop band. It is shown how the spatial decay is linked to the motion of the structure in the vicinity of the target frequency. Therefore, the spatial decay can be used to evaluate the performance of the resonators and derive design criteria for optimized resonant materials. The benefit of this procedure is that it only requires a detailed model of a single unit cell. This reduces the computational effort and offers the possibility to directly link the dimensioning of the local resonances to the wave propagation that occurs in the material. As the procedure does not require knowledge of the boundary conditions of the host structure it can be used in an early stage of development. The procedure is applied for mass optimized locally resonant materials. For beam-like resonators, an optimal resonator spacing exists that maximizes the spatial decay at the target frequency of the resonator. Furthermore, it is also possible to maximize the stop band size based on the dimensioning of the resonators.

A Appendix

A.1 Derivation of solution for the beam in bending with varying thickness

The force equilibrium at an infinitesimal beam element yields the governing equation for the beam in bending.
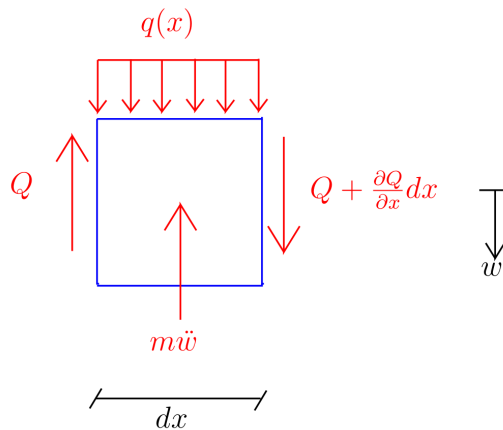
Figure A.1: Force equilibrium at the infinitesimal beam element.

The shear forces Q changes by $\frac{\partial Q}{\partial x}dx$. The inertia term consists of the mass m of the element and the acceleration $\ddot{w}$. Balancing all forces along the infinitesimal element yields

$$-m\ddot{w} + q(x)dx + (Q + \frac{\partial Q}{\partial x}dx) - Q = 0 \tag{A.1}$$

with

$$m(x) = \rho\, A(x)\, dx \ . \tag{A.2}$$

The cross section A of the beam and the mass m vary with spatial coordinate x. ρ is the density of the material. Inserting the varying mass $m(x)$, the force equilibrium (A.1) results in

$$-\rho A(x)dx\, \ddot{w} + q(x)dx + \frac{\partial Q}{\partial x}dx = 0 \ . \tag{A.3}$$

Subsequently, (A.3) is divided by dx:

$$-\rho A(x)\ddot{w} + q(x) + \frac{\partial Q}{\partial x} = 0 \ . \tag{A.4}$$

According to Euler-Bernoulli beam theory, the shear force Q is

$$Q = -\frac{\partial}{\partial x}\left(EI(x)\frac{\partial^2 w}{\partial x^2}\right) \ , \tag{A.5}$$

with E being the Young's modulus. Inserting (A.5) in (A.4) yields

$$-\rho A(x)\ddot{w} + q(x) - \frac{\partial^2}{\partial x^2}\left(EI(x)\frac{\partial^2 w}{\partial x^2}\right) = 0 \ . \tag{A.6}$$

In the following, it is assumed that the external loading $q(x)$ is zero and that the beam oscillates harmonically with a frequency Ω.

$$w = \underline{w}e^{i\Omega t} \tag{A.7}$$

$\underline{w}$ is a complex amplitude. i is the imaginary unit and t is the time variable. The acceleration $\ddot{w}$ is computed by deriving w twice with respect to time t

$$\dot{w} = i\Omega\underline{w}e^{i\Omega t} = i\Omega w \ ,$$
$$\ddot{w} = -\Omega^2\underline{w}e^{i\Omega t} = -\Omega^2 w \ . \tag{A.8}$$

Consequently, (A.6) transforms to

$$\rho A(x)\Omega^2\underline{w} - \frac{\partial^2}{\partial x^2}\left(EI(x)\frac{\partial^2 \underline{w}}{\partial x^2}\right) = 0 \ . \tag{A.9}$$

In the next step, one defines the varying thickness and width as presented in [Mironov and Gladilin 2016]

$$h(x) = h_0(x/x_0)^2 \ , \tag{A.10}$$

$$d(x) = d_0(x/x_0)^\alpha \ . \tag{A.11}$$

h_0 and d_0 describe the initial thickness and initial width, receptively. x_0 marks the location where the uniform cross section ends and the profile reduction starts. Consequently, the cross section A and the area moment of inertia I are

$$A(x) = \frac{h_0 d_0}{x_0^{2+\alpha}} x^{2+\alpha} \tag{A.12}$$

$$I(x) = \frac{h_0^3 d_0}{12 x_0^{6+\alpha}} x^{6+\alpha} \ . \tag{A.13}$$

Inserting (A.12) and (A.13) in the equation of motion (A.9) yields

$$\rho \frac{h_0 d_0}{x_0^{2+\alpha}} x^{2+\alpha} \Omega^2 \underline{w} - \frac{\partial^2}{\partial x^2} \left(\frac{E h_0^3 d_0}{12 x_0^{6+\alpha}} x^{6+\alpha} \frac{\partial \underline{w}^2}{\partial x^2} \right) = 0 \ . \tag{A.14}$$

After dividing both sides with $\frac{E h_0^3 d_0}{12 x_0^{6+\alpha}}$ the expression simplifies

$$\frac{12 \rho \Omega^2}{E} \left(\frac{x_0^2}{h_0} \right)^2 x^{2+\alpha} \underline{w} - \frac{\partial^2}{\partial x^2} \left(x^{6+\alpha} \frac{\partial^2 \underline{w}}{\partial x^2} \right) = 0 \ . \tag{A.15}$$

The solution of (A.15) has the form [Mironov and Gladilin 2016]

$$\underline{w}(x) = x^\gamma \ . \tag{A.16}$$

Inserting this approach results in

$$\frac{12 \rho \Omega^2}{E} \left(\frac{x_0^2}{h_0} \right)^2 x^{2+\alpha+\gamma} - \frac{\partial^2}{\partial x^2} \left(x^{4+\alpha+\gamma} \gamma \left(\gamma - 1 \right) \right) = 0 \ . \tag{A.17}$$

Resolving the second derivative with respect to x simplifies the expression

$$\frac{12 \rho \Omega^2}{E} \left(\frac{x_0^2}{h_0} \right)^2 x^{2+\alpha+\gamma} - x^{2+\alpha+\gamma} \left((4 + \alpha + \gamma)(3 + \alpha + \gamma) \gamma (\gamma - 1) \right) = 0 \ . \tag{A.18}$$

A division with $x^{2+\alpha+\gamma}$ leads to an forth order expression for ν

$$\frac{12\rho\Omega^2}{E}\left(\frac{x_0^2}{h_0}\right)^2 - (4+\alpha+\gamma)(3+\alpha+\gamma)\gamma(\gamma-1) = 0 \ . \tag{A.19}$$

To simplify this expression, [Mironov and Gladilin 2016] substitute γ with $\chi - \frac{\alpha+3}{2}$

$$\frac{12\rho\Omega^2}{E}\left(\frac{x_0^2}{h_0}\right)^2 - \left(\chi+\left(\frac{5}{2}+\frac{\alpha}{2}\right)\right)\left(\chi+\left(\frac{3}{2}-\frac{\alpha}{2}\right)\right)\left(\chi-\left(\frac{3}{2}+\frac{\alpha}{2}\right)\right)\left(\chi-\left(\frac{5}{2}+\frac{\alpha}{2}\right)\right) = 0 \ . \tag{A.20}$$

Applying $(a-b)(a+b) = a^2 - b^2$ twice reveals a further simplification to

$$\frac{12\rho\Omega^2}{E}\left(\frac{x_0^2}{h_0}\right)^2 - \left(\chi^2-\left(\frac{\alpha+5}{2}\right)^2\right)\left(\chi^2-\left(\frac{\alpha+3}{2}\right)^2\right) = 0 \ . \tag{A.21}$$

This leads to a bi-quadratic equation for χ

$$\chi^4 - \chi^2\left(\left(\frac{\alpha+5}{2}\right)^2+\left(\frac{\alpha+3}{2}\right)^2\right) + \left(\frac{\alpha+5}{2}\right)^2\left(\frac{\alpha+3}{2}\right)^2 - \frac{12\rho\Omega^2}{E}\left(\frac{x_0^2}{h_0}\right)^2 = 0 \ . \tag{A.22}$$

An additional substitution of $\iota = \chi^2$ leads to two solutions

$$\iota_{1,2} = \frac{1}{2}\left(\left(\frac{\alpha+3}{2}\right)^2+\left(\frac{\alpha+5}{2}\right)^2\right) \tag{A.23}$$

$$\pm\sqrt{\frac{1}{4}\left(\left(\left(\frac{\alpha+3}{2}\right)^2+\left(\frac{\alpha+5}{2}\right)^2\right)^2-\left(\frac{\alpha+5}{2}\right)^2\left(\frac{\alpha+3}{2}\right)^2\frac{12\rho\Omega^2}{E}\left(\frac{x_0^2}{h_0}\right)^2\right)} \ . \tag{A.24}$$

Consequently, there exist four solution for $\gamma = \chi - \frac{\alpha+3}{2}$

$$\gamma_{1,2,3,4} = -\frac{\alpha+3}{2} \pm \left[\frac{1}{2}\left(\left(\frac{\alpha+3}{2}\right)^2+\left(\frac{\alpha+5}{2}\right)^2\right)\right. \tag{A.25}$$

$$\left.\pm\sqrt{\frac{1}{4}\left(\left(\left(\frac{\alpha+3}{2}\right)^2+\left(\frac{\alpha+5}{2}\right)^2\right)^2-\left(\frac{\alpha+5}{2}\right)^2\left(\frac{\alpha+3}{2}\right)^2\frac{12\rho\Omega^2}{E}\left(\frac{x_0^2}{h_0}\right)^2\right)}\right]^{\frac{1}{2}} \tag{A.26}$$

A.2 Derivation of the amplification functions for the two-DOF-oscillator
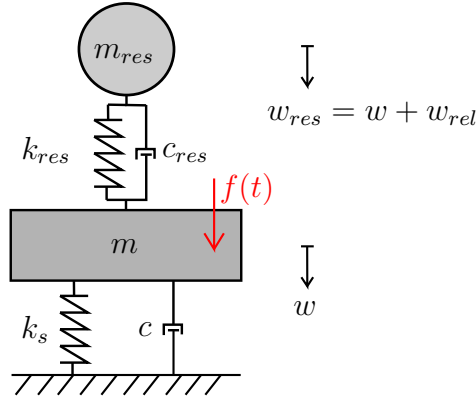
Figure A.2: The two-DOF-oscillator.

The differential equation describing the two-DOF-oscillator is

$$f(t) - m\ddot{w} - c\dot{w} - k_s w + c_{res}\dot{w}_{rel} + k_{res}w_{rel} = 0 \; , \tag{A.27}$$

$$-m_{res}(\ddot{w}_{rel} + \ddot{w}) - c_{res}\dot{w}_{rel} - k_{res}w_{rel} = 0 \; . \tag{A.28}$$

Reordering and a further division of A.27 by m and A.28 by m_{res} leads to

$$\ddot{w} + \frac{c}{m}\dot{w} + \frac{k_s}{m}w - \frac{c_{res}}{m}\dot{w}_{rel} - \frac{k_{res}}{m}w_{rel} = \frac{f(t)}{m} \; , \tag{A.29}$$

$$\ddot{w}_{rel} + \ddot{w} + \frac{c_{res}}{m_{res}}\dot{w}_{rel} + \frac{k_{res}}{m_{res}}w_{rel} = 0 \; . \tag{A.30}$$

With the definition of the eigenfrequency $\omega = \frac{k_s}{m}$ and the damping ratio $D = \frac{c}{c_{crit}} = \frac{c}{2m\omega}$ the eigenfrequency and damping ratio of the main structure and of the resonator can be introduced

$$\ddot{w} + 2\omega D\dot{w} + \omega^2 w - 2\frac{m_{res}}{m}\omega_{res}D_{res}\dot{w}_{rel} - \frac{m_{res}}{m}\omega_{res}^2 w_{rel} = \frac{f(t)}{m} \; , \tag{A.31}$$

$$\ddot{w}_{rel} + \ddot{w} + 2\omega_{res}D_{res}\dot{w}_{rel} + \omega_{res}^2 w_{rel} = 0 \; . \tag{A.32}$$

In the next step the mass ratio $\mu = \frac{m_{res}}{m}$ is introduced

$$\ddot{w} + 2\omega D\dot{w} + \omega^2 w - 2\mu\omega_{res}D_{res}\dot{w}_{rel} - \mu\omega_{res}^2 w_{rel} = \frac{f(t)}{m} \; , \tag{A.33}$$

$$\ddot{w}_{rel} + \ddot{w} + 2\omega_{res}D_{res}\dot{w}_{rel} + \omega_{res}^2 w_{rel} = 0 \; . \tag{A.34}$$

The two force balances (A.33) and (A.34) can be written in matrix notation

$$
\underbrace{\begin{bmatrix} 1 & 0 \\ 1 & 1 \end{bmatrix}}_{\mathbf{M}} \underbrace{\begin{bmatrix} \ddot{w} \\ \ddot{w}_{rel} \end{bmatrix}}_{\ddot{\mathbf{w}}} + \underbrace{\begin{bmatrix} 2\omega D & -2\mu\omega_{res}D_{res} \\ 0 & 2\omega_{res}D_{res} \end{bmatrix}}_{\mathbf{C}} \underbrace{\begin{bmatrix} \dot{w} \\ \dot{w}_{rel} \end{bmatrix}}_{\dot{\mathbf{w}}} + \underbrace{\begin{bmatrix} \omega^2 & -\mu\omega^2_{res} \\ 0 & \omega^2_{res} \end{bmatrix}}_{\mathbf{K}} \underbrace{\begin{bmatrix} w \\ w_{rel} \end{bmatrix}}_{\mathbf{w}} = \underbrace{\begin{bmatrix} \frac{f(t)}{m} \\ 0 \end{bmatrix}}_{\mathbf{f}} . \quad (A.35)
$$

The matrices $\mathbf{M}$, $\mathbf{C}$ and $\mathbf{K}$ are named mass, damping and stiffness matrix. The external force $f(t)$ is an harmonic force with frequency Ω that acts on the main structure

$$
f(t) = \underline{f}e^{i\Omega t} . \quad (A.36)
$$

The steady state solution will oscillate with the same frequency as the excitation frequency. Therefore, for the particular solution, the following approach is applied [Petersen 1996]

$$
\mathbf{w} = \underline{\mathbf{w}}e^{i\Omega t} . \quad (A.37)
$$

Inserting (A.36), (A.37) and the respective time derivatives in (A.35) yields

$$
\left(-\Omega^2 \begin{bmatrix} 1 & 0 \\ 1 & 1 \end{bmatrix} + i\Omega \begin{bmatrix} 2\omega D & -2\mu\omega_{res}D_{res} \\ 0 & 2\omega_{res}D_{res} \end{bmatrix} + \begin{bmatrix} \omega^2 & -\mu\omega^2_{res} \\ 0 & \omega^2_{res} \end{bmatrix} \right) \underline{\mathbf{w}}e^{i\Omega t}
$$
$$
= \begin{bmatrix} \frac{\underline{f}}{m} \\ 0 \end{bmatrix} e^{i\Omega t} .
$$

The exponential terms $e^{i\Omega t}$ cancel

$$
\begin{bmatrix} -\Omega^2 + i2\Omega\omega D + \omega^2 & -i2\Omega\mu\omega_{res}D_{res} - \mu\omega^2_{res} \\ -\Omega^2 & -\Omega^2 + i2\Omega\omega_{res}D_{res} + \omega^2_{res} \end{bmatrix} \underbrace{\begin{bmatrix} \underline{w} \\ \underline{w}_{rel} \end{bmatrix}}_{\underline{\mathbf{w}}} = \begin{bmatrix} \frac{\underline{f}}{m} \\ 0 \end{bmatrix} . \quad (A.38)
$$

From the second line in (A.38), we can relate $\underline{w}_{rel}$ to $\underline{w}$

$$
\underline{w}_{rel} = \frac{\Omega^2}{-\Omega^2 + i2\Omega\omega_{res}D_{res} + \omega^2_{res}} \underline{w} . \quad (A.39)
$$

Inserting this into the first line of (A.38), yields

$$
\left(-\Omega^2 + i2\Omega\omega D + \omega^2 + \frac{(-i2\Omega\mu\omega_{res}D_{res} - \omega^2_{res}\mu)\Omega^2}{-\Omega^2 + i2\Omega\omega_{res}D_{res} + \omega^2_{res}} \right) \underline{w} = \frac{\underline{f}}{m} . \quad (A.40)
$$

Thus, the solution of $\underline{w}$ and $\underline{w}_{rel}$ are

$$\underline{w} = \frac{\underline{f}}{m}\frac{a+ib}{c+id} \; , \tag{A.41}$$

$$\underline{w}_{rel} = \frac{\underline{f}}{m}\frac{\Omega^2}{c+id} \; , \tag{A.42}$$

with

$$a = \omega_{res}^2 - \Omega^2 \; , \tag{A.43}$$

$$b = 2\Omega\omega_{res}D_{res} \; , \tag{A.44}$$

$$c = \Omega^4 - \Omega^2(\omega^2 + \omega_{res}^2 + \mu\omega_{res}^2 + 4\omega\omega_{res}DD_{res}) + \omega_1^2\omega_{res}^2 \; , \tag{A.45}$$

$$d = 2\Omega\left(\omega D(\omega_{res}^2 - \Omega^2) + \omega_{res}D_{res}(\omega^2 - \Omega^2 - \mu\Omega^2)\right) \; . \tag{A.46}$$

The absolute value of the deflections $|w|$ and $|w_{rel}|$ depends on the amplitude f_0 of the excitation

$$|\underline{w}| = \frac{f_0}{m}\sqrt{\frac{a^2+b^2}{c^2+d^2}} \; , \tag{A.47}$$

$$|\underline{w}_{rel}| = \frac{f_0}{m}\sqrt{\frac{\Omega^4}{c^2+d^2}} \; . \tag{A.48}$$

In a next step, the displacement amplitudes are normalized with the static deflection $w_{stat} = \frac{f_0}{k_s}$. Furthermore, one introduces the frequency ratio $\alpha = \frac{\Omega}{\omega}$ and $\beta = \frac{\omega_{res}}{\omega}$. This results in the amplifications functions V and V_{rel}

$$V = \frac{|\underline{w}|}{w_{stat}} = \sqrt{\frac{e^2+f^2}{g^2+h^2}} \; , \tag{A.49}$$

$$V_{rel} = \frac{|\underline{w}_{rel}|}{w_{stat}} = \sqrt{\frac{\alpha^4}{g^2+h^2}} \; . \tag{A.50}$$

with

$$e = \beta^2 - \alpha^2 \; , \tag{A.51}$$

$$f = 2\alpha\beta D_{res} \; , \tag{A.52}$$

$$g = \alpha^4 - \alpha^2(1 + \beta^2 + \mu\beta^2 + 4\beta DD_{res}) + \beta^2 \; , \tag{A.53}$$

$$h = \alpha[2D(\beta^2 - \alpha^2) + 2\beta D_{res}(1 - \alpha^2 - \mu\alpha^2)] \; . \tag{A.54}$$

A.3 Influence of the damping and the tuning of the two-DOF-oscillator

This section discusses the influence of the damping D_{res} and the tuning β of the resonator.
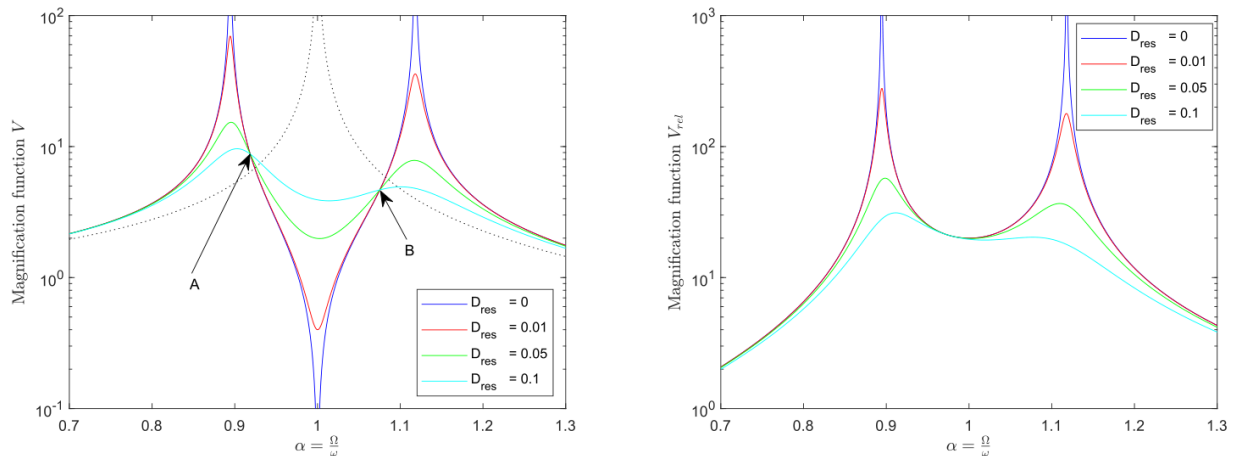
Figure A.3: Influence of the damping ratio of the resonator on the amplification functions; damping ratio of the main structure $D = 0$, mass ratio $\mu = 0.05$ and frequency tuning of the resonator $\beta = 1$; the dashed line indicates the original structure without the resonator.

Figure A.3 shows the amplification functions for a varying damping ratio. The mass ratio μ is 0.05. The main structure is undamped $(D = 0)$ and the resonator frequency is equal to the resonance frequency of the host structure $(\beta = 1)$. In theory, an undamped resonator $(D_{res} = 0)$ is able to reduce the vibration amplitude of the main structure at the resonance frequency ω to zero. Nevertheless, two peaks of large deflection of the main structure appear for excitation frequency slightly smaller and higher than ω. The larger the damping ratio, the larger the deflection of the main structure at the resonance frequency. The advantage of an increasing damping is that the two peaks that split up the resonance peak of the main structure also decreases. As previously, the relative motion of the resonator is larger than the motion of the main structure.

In the following, the influence of the frequency tuning of the resonator is investigated. Figure A.4 shows the influence of three different frequency tunings: one tuning where the resonance frequency of the resonator is slightly lower, the second tuning where the resonance frequency of the resonator is equal to the resonance of the main structure and a third tuning with a resonance frequency slightly higher than the resonance frequency of the main structure. With the tuning, the two frequency peaks and the minimum are shifted.

In general, one might be interested in optimal choices of parameters of the resonator. The optimal parameter set depends on the objective to minimize. For example, if the objective
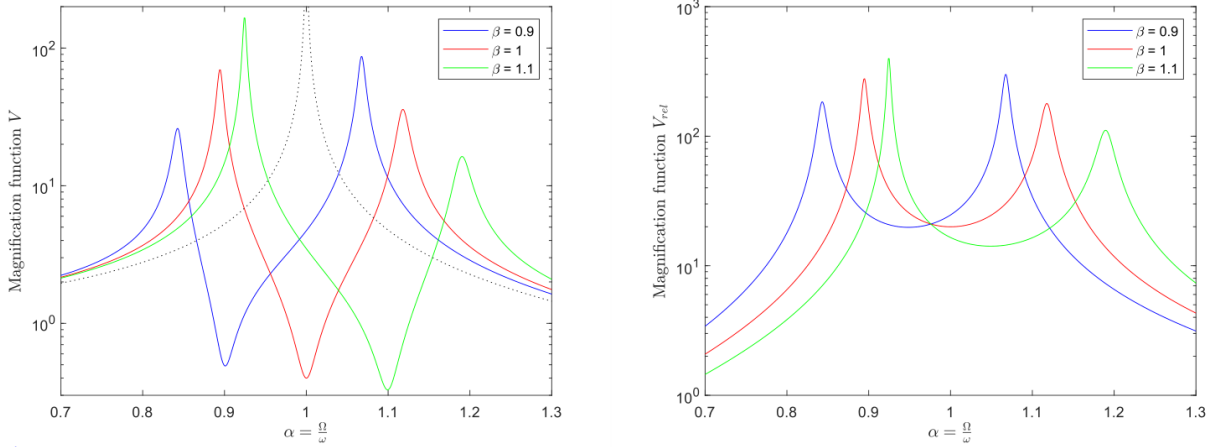
Figure A.4: Influence of the frequency of the res on the amplification functions; damping ratio of the main structure $D = 0$, damping ratio of the resonator $D_{res} = 0.01$ and mass ratio $\mu = 0.05$; the dashed line indicates the original structure without the resonator.

is to minimize the deflection at a specific frequency, one would prefer very low damping ratio of the resonator. Asami et al [2002] gives an overview of existing optimal parameters for different optimization objectives as well as optimal parameters of resonators for damped structures. In practice, undamped material does not exist. Furthermore, the accuracy of the manufacturing processes are limited. Therefore, the choice of optimal parameters should be investigated in the range of these limits.

Classically, the optimal tuning and damping of the resonator is assumed to be found when the two resonance peaks have the same height. This is achieved with setting the fix points A and B in figure A.3 to the same height [Hartog 1956]

$$\beta_{opt} = \frac{1}{1 + \mu} \ , \tag{A.55}$$

$$D_{res,opt} = \sqrt{\frac{3\mu}{8 \cdot (1 + \mu)^3}} \ . \tag{A.56}$$

In many applications, the material defines the damping constant and can not be chosen arbitrarily. In that case the (A.55) cannot be applied. For very low damping ratios as they might occur using a metamaterial based on alloys, the optimal tuning should be optimized separately. Table A.1 illustrates the improvement of the amplification function when the tuning β is optimized for a fixed damping ratio. The objective is to minimize the maximum value of the amplification factor. As previously, the main structure is undamped ($D_1 = 0$), the mass of the res is 5% of the main mass. The optimal tuning based on (A.55) for a mass ratio μ of 0.05 is 0.952.

D_D	β_{opt}	Improvement
0.1	0.955	>2%
0.05	0.961	>7%
0.02	0.964	>10%

Table A.1: Optimal tuning for a fixed damping ratio; the mass ratio μ is 5%.

A.4 Geometry parameters of beam-like resonators
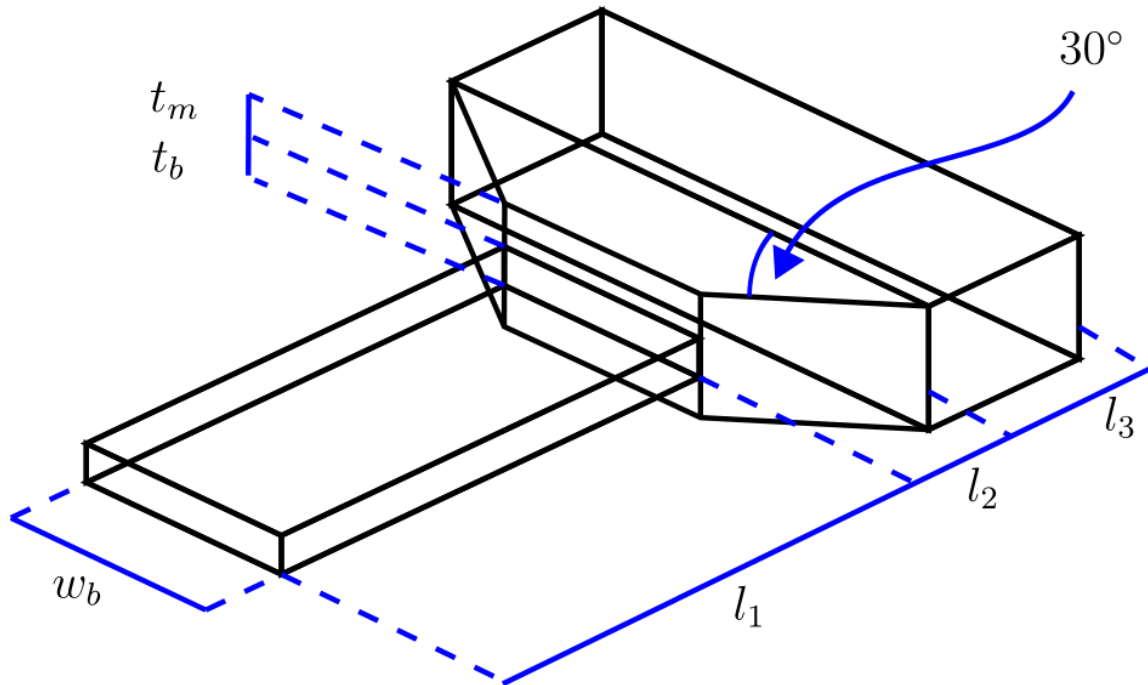
Design	t_B	w_B	l_1	l_2	l_3	t_m
1	0.3 mm	1.0 mm	15.8 mm	2.5 mm	5.0 mm	1.0 mm
2	0.3 mm	1.0 mm	13.3 mm	2.5 mm	5.0 mm	1.0 mm
3	0.3 mm	1.0 mm	10.3 mm	2.5 mm	5.0 mm	1.0 mm
4	0.3 mm	1.2 mm	10.9 mm	2.5 mm	5.0 mm	1.0 mm
5	0.3 mm	1.3 mm	11.1 mm	2.5 mm	5.0 mm	1.0 mm
6	0.3 mm	1.4 mm	8.2 mm	2.5 mm	5.0 mm	1.0 mm
7	0.3 mm	1.4 mm	8.0 mm	2.5 mm	3.9 mm	1.0 mm
8	0.3 mm	1.4 mm	7.5 mm	2.5 mm	3.9 mm	1.0 mm
9	0.3 mm	1.4 mm	7.2 mm	2.5 mm	3.9 mm	1.0 mm
10	0.3 mm	1.5 mm	6.9 mm	2.5 mm	3.5 mm	1.0 mm
11	0.3 mm	1.5 mm	6.7 mm	2.5 mm	2.9 mm	1.0 mm
12	0.3 mm	1.5 mm	6.2 mm	2.5 mm	2.9 mm	1.0 mm
13	0.4 mm	1.5 mm	7.9 mm	2.5 mm	2.9 mm	1.0 mm
14	0.3 mm	1.7 mm	6.0 mm	1.1 mm	3.8 mm	1.0 mm
15	0.3 mm	2.1 mm	8.7 mm	0.7 mm	0.7 mm	0.2 mm

A.5 Derivation of the amplification function of the beam-like resonator
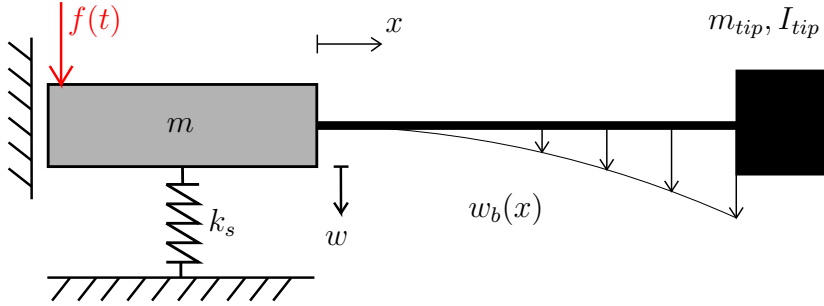
Figure A.5: Translation of the beam-like resonator with tip mass to a discrete mass-spring system.

The motion of the beam is described with the relative motion w_b, which can be described by a sum of the mode shapes of a clamped cantilever beam

$$\underline{w}_b(x) = \sum_{r=1}^{\infty} \underline{w}_{0,r} \Phi_r \ . \tag{A.57}$$

According to Erturk and Inman [2011], the mode shapes of a cantilever beam with tip mass are

$$\Phi_r = \cos \frac{\lambda_r}{L} x - \cosh \frac{\lambda_r}{L} x + Y_r \left(\sin \frac{\lambda_r}{L} x - \sinh \frac{\lambda_r}{L} x \right) \ , \tag{A.58}$$

with

$$Y_r = \frac{\sin \lambda_r - \sinh \lambda_r + \lambda_r \frac{m_{tip}}{m_{beam}} (\cos \lambda_r - \cosh \lambda_r)}{\cos \lambda_r + \cosh \lambda_r - \lambda_r \frac{m_{tip}}{m_{beam}} (\sin \lambda_r - \sinh \lambda_r)} \ . \tag{A.59}$$

The corresponding λ_r results from the solution of the equation

$$1 + \cos \lambda \cosh \lambda + \lambda \frac{m_{tip}}{m_{beam}} (\cos \lambda \sinh \lambda - \sin \lambda \cosh \lambda)$$

$$- \lambda^3 \frac{I_{tip}}{m_{beam} L^2} (\cosh \lambda \sin \lambda + \sinh \lambda \cos \lambda) + \lambda^4 \frac{m_{tip} I_{tip}}{m_{beam}^2 L^2} (1 - \cos \lambda \cosh \lambda) = 0 \ , \tag{A.60}$$

where I_{tip} is the mass moment of inertia of the tip mass at $x = L$. Figure 4.9 shows the influence of the tip mass and the mass moment of inertia on the mode shapes of the beam.

The generalized quantities for the base excited clamped beam with tip mass are

$$m_r = \rho A \int_0^L \Phi_r^2(x)dx + m_{tip}\Phi_r^2|_{x=L} + I_{tip}\frac{\lambda_r^2}{L^2}\tilde{\Phi}_r'^2|_{x=L} \ , \tag{A.61}$$

$$\text{with} \quad \tilde{\Phi}_r'|_{x=L} = -\sin\lambda_r - \sinh\lambda_r + Y_r(\cos\lambda_r - \cosh\lambda_r) \ , \tag{A.62}$$

$$k_r = EI \int_0^L \Phi_r''^2 dx = EI\frac{\lambda_r^4}{L^4}\int_0^L \tilde{\Phi}_r^2 dx \ , \tag{A.63}$$

$$\text{with} \quad \tilde{\Phi}_r'' = -\cos\frac{\lambda_r}{L}x - \cosh\frac{\lambda_r}{L}x + Y_r\left(-\sin\frac{\lambda_r}{L}x - \sinh\frac{\lambda_r}{L}x\right) \ , \tag{A.64}$$

$$p_r = \int_0^L p(x)\Phi_r dx = \Omega^2\left(\rho A \int_0^L \Phi_r dx + m_{tip}\Phi_r|_{x=L}\right)w_{base} \ . \tag{A.65}$$

In the example shown in figure A.5, the base excitation is the motion of the SDOF system ($w_{base} = w$). Using the generalized quantities, the following equation describes the steady state solution of the motion of the beam due to a harmonic base excitation $\underline{w}$

$$\left(-\Omega^2\left(\rho A \int_0^L \Phi_r^2(x)dx + m_{tip}\Phi_r^2|_{x=L} + I_{tip}\frac{\lambda_r^2}{L^2}\tilde{\Phi}_r'^2|_{x=L}\right) + EI\frac{\lambda_r^4}{L^4}\int_0^L \tilde{\Phi}_r''^2 dx\right)\underline{w}_{r,0}$$

$$-\Omega^2\left(\rho A \int_0^L \Phi_r dx + m_{tip}\Phi_r|_{x=L}\right)\underline{w} = 0 \ . \tag{A.66}$$

Dividing by $\rho A \int_0^L \Phi_r^2(x)dx$ yields

$$\left(-\Omega^2(1 + \zeta\xi_1 + \tau\xi_2) + \omega_{r,beam}\xi_3\right)\underline{w}_{r,0} - \Omega^2\left(\xi_4 + \zeta\xi_5\right)\underline{w} = 0 \ . \tag{A.67}$$

The parameters $\zeta = \frac{m_{tip}}{\rho AL}$ describes the mass ratio between tip mass and mass of the beam. Respectively, the ratio $\tau = \frac{I_{tip}}{m_{beam}L^2}$ describes the relation between the mass moments of inertia of the tip mass and the beam. The parameters ξ_i contain information about the shapes of the deformation. These parameters are dimensionless and are independent of the

geometry of the beam-like resonator. They only depend on the mode shape Φ_r

$$\xi_{1,r} = L \frac{\Phi_r^2|_{x=L}}{\int_0^L \Phi_r^2(x)dx} \ , \tag{A.68}$$

$$\xi_{2,r} = L\lambda_r^2 \frac{\Phi_r'^2|_{x=L}}{\int_0^L \Phi_r^2(x)dx} \ , \tag{A.69}$$

$$\xi_{3,r} = \frac{\int_0^L \tilde{\Phi}_r''^2 dx}{\int_0^L \Phi_r^2(x)dx} \ , \tag{A.70}$$

$$\xi_{4,r} = \frac{\int_0^L \Phi_r dx}{\int_0^L \Phi_r^2(x)dx} \ , \tag{A.71}$$

$$\xi_{5,r} = L \frac{\Phi_r|_{x=L}}{\int_0^L \Phi_r^2(x)dx} \ . \tag{A.72}$$

As previously, the division with the resonance frequency of the host structure in figure A.5 $\omega^2 = k_s/m$ enables the introduction of the dimensional frequency ratios $\alpha = \frac{\Omega}{\omega}$ and $\beta_r = \frac{\omega_{r,beam}}{\omega}$

$$\left(\beta_r^2\xi_{3,r} - \alpha^2(1 + \zeta\xi_{1,r} + \tau\xi_{2,r})\right)\underline{w}_{r,0} - \alpha^2\left(\xi_{4,r} + \zeta\xi_{5,r}\right)\underline{w} = 0 \ . \tag{A.73}$$

The derivation of the motion w of the mass m is similar as for the cantilever beam without end mass

$$\left(-\Omega^2 m + k_s\right)\underline{w} - Q(x = 0) = \underline{f} \ , \tag{A.74}$$

where the shear force at $x = 0$ is

$$Q(x = 0) = -EI\sum_{l=1}^{\infty}\underline{w}_{l,0}\frac{\lambda_l^3}{L^3}\left[\sin\frac{\lambda_l}{L}x - \sinh\frac{\lambda_l}{L}x + Y_l\left(-\cos\frac{\lambda_l}{L}x - \cosh\frac{\lambda_l}{L}x\right)\right]_{x=0}$$

$$= 2EI\sum_{l=1}^{\infty}\frac{\lambda_l^3}{L^3}Y_l\underline{w}_{l,0} \ . \tag{A.75}$$

Inserting the link between λ_l and the first eigenfrequency of the beam $\omega_{l,beam}^2 = \frac{\lambda_l^4}{L^4}\frac{EI}{\rho A}$, the shear force at the beginning is

$$Q(x = 0) = 2EI\sum_{l=1}^{\infty}\frac{\lambda_l^3}{L^3}\underline{w}_{l,0} = 2\rho AL\sum_{l=1}^{\infty}\frac{Y_l}{\lambda_l}\omega_{l,beam}^2\underline{w}_{l,0} \ . \tag{A.76}$$

Inserting (A.76) in (A.74) and dividing it by the mass of the host structure m results in

$$\left(-\Omega^2 + \frac{k_s}{m}\right)\underline{w} - 2\frac{\rho AL}{m}\sum_{l=1}^{\infty}\frac{Y_l}{\lambda_l}\omega_{l,beam}^2\underline{w}_{l,0} = \frac{f}{m} \ . \tag{A.77}$$

Again, the division by the square of the eigenfrequency of the main structure ω^2 enables the introduction of the dimensionless frequency ratios $\alpha = \frac{\Omega}{\omega}$ and $\beta_l = \frac{\omega_{l,beam}}{\omega}$

$$\left(1 - \alpha^2\right)\underline{w} - 2\frac{\rho AL}{m}\sum_{l=1}^{\infty}\frac{Y_l}{\lambda_l}\beta_l^2\underline{w}_{l,0} = \frac{f}{k_s} \tag{A.78}$$

Using the mass ratios $\mu = \frac{m_{tip}+m_{beam}}{m}$ and $\zeta = \frac{m_{tip}}{m_{beam}}$ the term $\frac{\rho AL}{m}$ equals $\frac{\mu}{1+\zeta}$

$$\left(1 - \alpha^2\right)\underline{w} - 2\frac{\mu}{1+\zeta}\sum_{l=1}^{\infty}\frac{Y_l}{\lambda_l}\beta_l^2\underline{w}_{l,0} = \frac{f}{k_s} \tag{A.79}$$

Consequently, the following two equations describe the motion of the mass and the beam-like resonator

$$\left(1 - \alpha^2\right)\underline{w} - 2\frac{\mu}{1+\zeta}\sum_{l=1}^{\infty}\frac{Y_l}{\lambda_l}\beta_l^2\underline{w}_{l,0} = \frac{f}{k_s} \ , \tag{A.80}$$

$$\left(\beta_r^2\xi_{3,r} - \alpha^2(1 + \zeta\xi_{1,r} + \tau\xi_{2,r})\right)\underline{w}_{r,0} - \alpha^2\left(\xi_{4,r} + \zeta\xi_{5,r}\right)\underline{w} = 0 \ . \tag{A.81}$$

$\underline{w}$ describes the amplitude of the displacement of host structure and $\underline{w}_r$ the amplitudes of mode r of the relative beam motion. Reformulating (A.81) yields

$$\underline{w}_{r,0} = \frac{\alpha^2\left(\xi_{4,r} + \zeta\xi_{5,r}\right)}{\beta_r^2\xi_{3,r} - \alpha^2(1 + \zeta\xi_{1,r} + \tau\xi_{2,r})}\underline{w} \ . \tag{A.82}$$

Inserting (A.82) in (A.80) results in

$$\left(1 - \alpha^2\right)\underline{w} - 2\frac{\mu}{1+\zeta}\sum_{l=1}^{\infty}\frac{Y_l}{\lambda_l}\frac{\beta_l^2\alpha^2\left(\xi_{4,l} + \zeta\xi_{5,l}\right)}{\beta_l^2\xi_{3,l} - \alpha^2(1 + \zeta\xi_{1,l} + \tau\xi_{2,l})}\underline{w} = \frac{f}{k_s} \ , \tag{A.83}$$

which can be rearranged to solve for $\underline{w}$

$$\underline{w} = \frac{f}{k_s}\frac{1}{\left(1 - \alpha^2\right) - 2\frac{\mu}{1+\zeta}\sum_{l=1}^{\infty}\frac{Y_l}{\lambda_l}\frac{\beta_l^2\alpha^2\left(\xi_{4,l}+\zeta\xi_{5,l}\right)}{\beta_l^2\xi_{3,l}-\alpha^2(1+\zeta\xi_{1,l}+\tau\xi_{2,l})}} \ . \tag{A.84}$$

Plugging in (A.84) in (A.82) solves for the unknown beam deflection $\underline{w}_{r,0}$

$$\underline{w}_{r,0} = \frac{\underline{f}}{k_s} \frac{\alpha^2 \left(\xi_{4,r} + \zeta\xi_{5,r}\right)}{\beta_r^2\xi_{3,r} - \alpha^2(1 + \zeta\xi_{1,r} + \tau\xi_{2,r})} \frac{1}{\left(1 - \alpha^2\right) - 2\frac{\mu}{1+\zeta}\sum_{l=1}^{\infty}\frac{Y_l}{\lambda_l}\frac{\beta_l^2\alpha^2\left(\xi_{4,l}+\zeta\xi_{5,l}\right)}{\beta_l^2\xi_{3,l}-\alpha^2(1+\zeta\xi_{1,l}+\tau\xi_{2,l})}} . \quad \text{(A.85)}$$

Around a resonance frequency of the beam ($\alpha \approx \beta_r$), a single term dominates the summation. Therefore, it is possible to simplify the summation in that frequency range

$$\sum_{l=1}^{\infty} \frac{Y_l}{\lambda_l} \frac{\beta_l^2\alpha^2 \left(\xi_{4,l} + \zeta\xi_{5,l}\right)}{\beta_l^2\xi_{3,l} - \alpha^2(1 + \zeta\xi_{1,l} + \tau\xi_{2,l})} \approx \frac{Y_r}{\lambda_r} \frac{\beta_r^2\alpha^2 \left(\xi_{4,r} + \zeta\xi_{5,r}\right)}{\beta_r^2\xi_{3,r} - \alpha^2(1 + \zeta\xi_{1,r} + \tau\xi_{2,r})} \quad \text{(A.86)}$$

Using this it is possible to approximate the displacement for frequencies around the target frequency of the resonator

$$\underline{w} \approx \frac{\underline{f}}{k_s} \frac{\beta_r^2\xi_{3,r} - \alpha^2(1 + \zeta\xi_{1,r} + \tau\xi_{2,r})}{\left(1 - \alpha^2\right)\left(\beta_r^2\xi_{3,r} - \alpha^2(1 + \zeta\xi_{1,r} + \tau\xi_{2,r})\right) - 2\frac{\mu}{1+\zeta}\frac{Y_r}{\lambda_r}\beta_r^2\alpha^2 \left(\xi_{4,r} + \zeta\xi_{5,r}\right)} , \quad \text{(A.87)}$$

$$\underline{w}_{r,0} \approx \frac{\underline{f}}{k_s} \frac{\alpha^2 \left(\xi_{4,r} + \zeta\xi_{5,r}\right)}{\left(1 - \alpha^2\right)\left(\beta_r^2\xi_{3,r} - \alpha^2(1 + \zeta\xi_{1,r} + \tau\xi_{2,r})\right) - 2\frac{\mu}{1+\zeta}\frac{Y_r}{\lambda_r}\beta_r^2\alpha^2 \left(\xi_{4,r} + \zeta\xi_{5,r}\right)} . \quad \text{(A.88)}$$

Again, normalizing the absolute values of the deflections with the static deflection $w_{stat} = \frac{|\underline{f}|}{k_s}$ results in the amplification function for the host structure and the relative motion of the beam

$$V \approx \sqrt{\frac{\left(\beta^2\xi_{3,r} - \alpha^2(1 + \zeta\xi_{1,r} + \tau\xi_2)\right)^2}{\left(\left(1 - \alpha^2\right)\left(\beta_r^2\xi_{3,r} - \alpha^2(1 + \zeta\xi_{1,r} + \tau\xi_{2,r})\right) - \frac{2Y_r}{\lambda_r}\frac{\mu}{1+\zeta}\beta_r^2\alpha^2 \left(\xi_{4,r} + \zeta\xi_{5,r}\right)\right)^2}} ,$$

$$\text{(A.89)}$$

$$V_{r,0} \approx \sqrt{\frac{\alpha^4 \left(\xi_{4,r} + \zeta\xi_{5,r}\right)^2}{\left(\left(1 - \alpha^2\right)\left(\beta_r^2\xi_{3,r} - \alpha^2(1 + \zeta\xi_{1,r} + \tau\xi_{2,r})\right) - \frac{2Y_r}{\lambda_r}\frac{\mu}{1+\zeta}\beta^2\alpha^2 \left(\xi_{4,r} + \zeta\xi_{5,r}\right)\right)^2}} .$$

$$\text{(A.90)}$$

A.6 Evaluation of the structural intensities (STI)

The STI represents the power flow in the material. It is useful to gain insights about the directional flow of energy of structure-borne sound. The STI is a non-complex vector quantity, which depends on the stresses and the velocities in the structure. The components of structural intensity are computed according to Pavic [1987] as

$$
\begin{aligned}
I_x &= -0.5\,\mathrm{Re}\{\underline{\sigma}_{xx}\underline{v}_x^* + \underline{\tau}_{xy}\underline{v}_y^* + \underline{\tau}_{xz}\underline{v}_z^*\}\ , \\
I_y &= -0.5\,\mathrm{Re}\{\underline{\tau}_{yx}\underline{v}_x^* + \underline{\sigma}_{yy}\underline{v}_y^* + \underline{\tau}_{yz}\underline{v}_z^*\}\ , \\
I_z &= -0.5\,\mathrm{Re}\{\underline{\tau}_{zx}\underline{v}_x^* + \underline{\tau}_{zy}\underline{v}_y^* + \underline{\sigma}_{zz}\underline{v}_z^*\}\ .
\end{aligned}
\tag{A.91}
$$

where $\underline{\sigma}_{ii}$ is the normal stress and $\underline{\tau}_{ij}$ is the shear stress. The first subscript indicates the direction of the surface normal and the second subscript relates to the direction of the stress. $\underline{v}_i^*$ is the complex conjugate of the velocity. Commercial software packages do not provide the STI directly. It can be calculated via the provided stresses and velocities. Before evaluating the STI, be aware of the fact that a standard finite element implementation computes the stresses accurately at the integration points, whereas the velocities are computed at the element nodes.
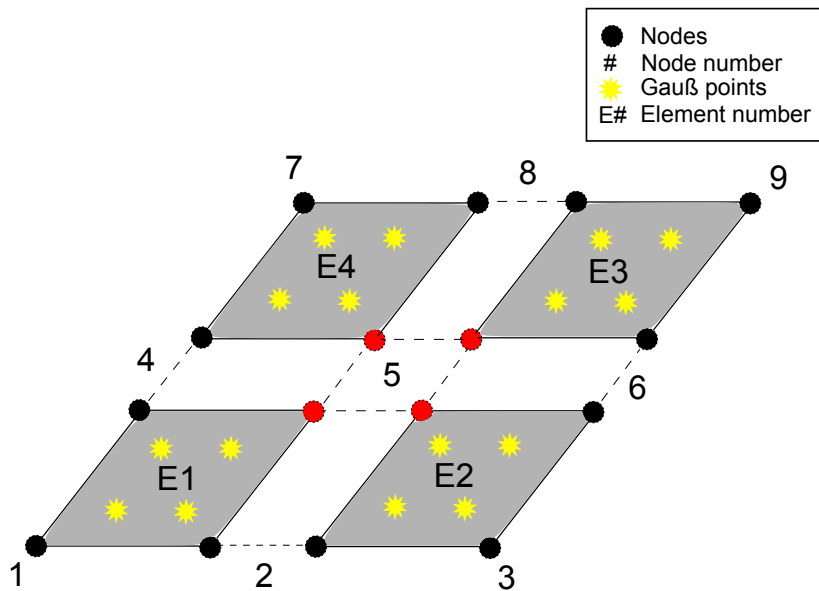
Figure A.6: Patch of four shell elements.

Before evaluating (A.91), it is necessary to compute stresses and velocities at the same location. A common way to compute the STI at the nodes is to extrapolate the stresses to

the nodes [Cook 1989]. As a node is adjacent to several elements, there are different stresses fields from different elements. For instance, node five (the red marked node in figure A.6) is connected to four elements. For each element, there exists a stress solution. The nodal stresses are estimated by averaging the stresses of the four adjacent elements at the location of node five. To get a reliable results one should check the difference in stress levels in the adjacent elements. If the stresses show large differences depending on the element, the averaging can result in inaccurate stresses at the nodes. Further mesh refinement increase the accuracy of the nodal stress computation. With the nodal stresses, it is possible to evaluate (A.91) to determine the STI at each node.

A.7 Modeshapes of beams with different thickness profiles

Figure A.7 shows the first twelve modes of three different beams. As expected, the indentation decreases the stiffness of the structure and reduce the eigenfrequencies of each mode. As the abrupt thickness profile (ABH step) has a stronger effect on the stiffness of the structure, the respective eigenfrequencies are lower than the eigenfrequencies of the respective modes of the beam with the smooth profile (ABH 2-2). Furthermore, the local thickness indentation generates a locally pronounced modeshape. These observation also hold for the beams with additional constrained layer damping (CLD). Figure A.8 shows the respective modes for the beams modified by a CLD.

Figure A.8 shows the impact of the CLD. First, the eigenfrequencies of the uniform beams are compared. Up to the forth mode, the beams with CLD have larger eigenfrequencies than the beams without the CLD. Thus, up to the forth mode the eigenfrequencies increase due to the increased stiffness. For higher modes, the beams with CLD have lower eigenfrequencies. For the larger modes the increased mass due to the CLD decreases the eigenfrequencies. Comparing the beams with indentations, the stiffening effect of the CLD holds for more modes. For the beam with the smooth thickness reduction (ABH 2-2), the stiffening of the CLD increases the eigenfrequencies up to the fifth mode, whereas for the abrupt thickness profile (ABH step), the eigenfrequencies increase up to the eighth mode.
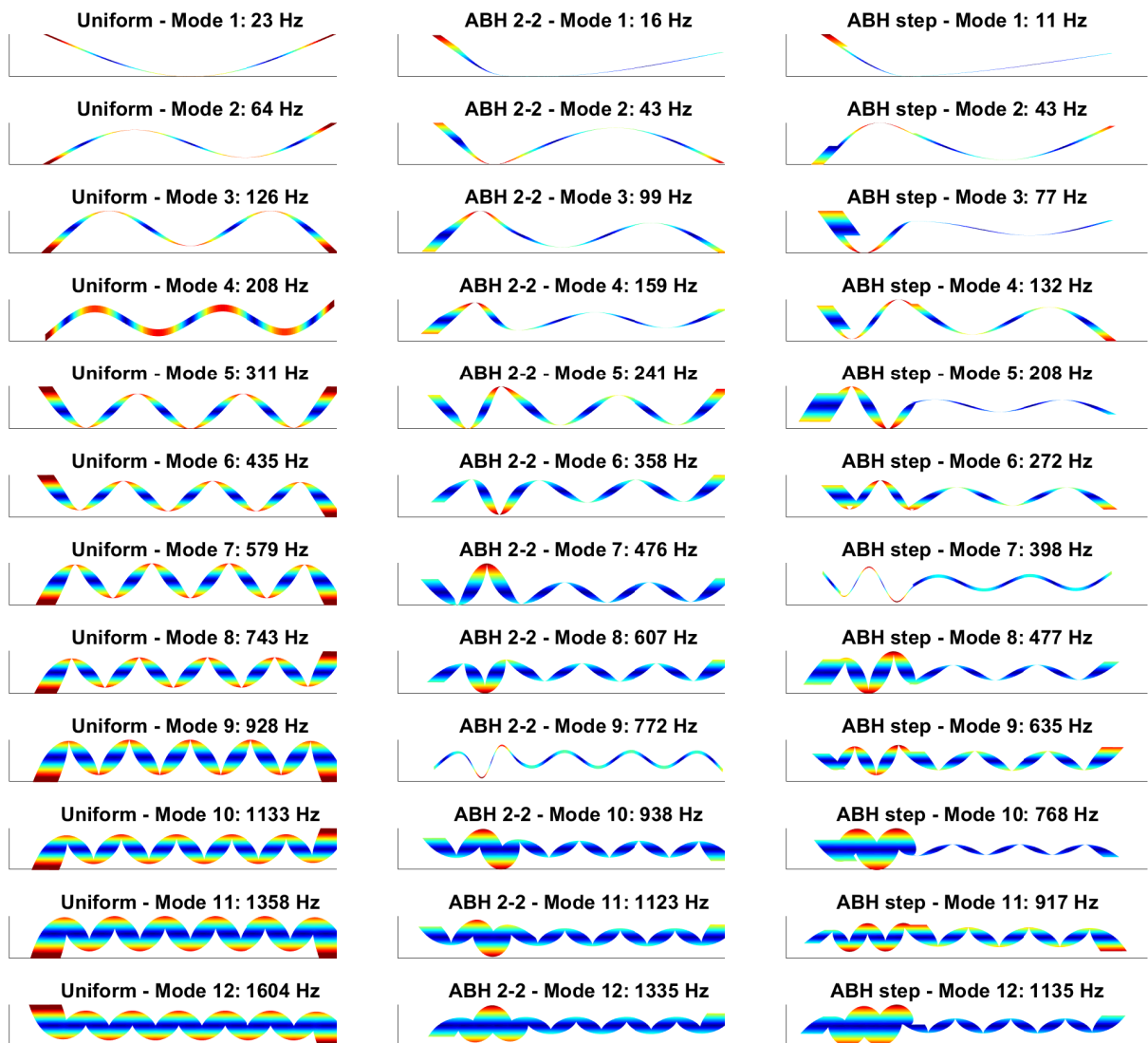
Figure A.7: Modeshapes of the first twelve modes of beams with different thickness profiles (without CLD). *Remark: The strongly varying thickness of the beams is an artifact that results from squeezing the deformation pattern along the beam axis.*

Uniform CLD - Mode 1: 23 Hz

ABH 2-2 CLD - Mode 1: 21 Hz

ABH step CLD - Mode 1: 17 Hz

Uniform CLD - Mode 2: 65 Hz

ABH 2-2 CLD - Mode 2: 53 Hz

ABH step CLD - Mode 2: 48 Hz

Uniform CLD - Mode 3: 130 Hz

ABH 2-2 CLD - Mode 3: 107 Hz

ABH step CLD - Mode 3: 102 Hz

Uniform CLD - Mode 4: 214 Hz

ABH 2-2 CLD - Mode 4: 172 Hz

ABH step CLD - Mode 4: 142 Hz

Uniform CLD - Mode 5: 309 Hz

ABH 2-2 CLD - Mode 5: 247 Hz

ABH step CLD - Mode 5: 226 Hz

Uniform CLD - Mode 6: 425 Hz

ABH 2-2 CLD - Mode 6: 357 Hz

ABH step CLD - Mode 6: 291 Hz

Uniform CLD - Mode 7: 567 Hz

ABH 2-2 CLD - Mode 7: 467 Hz

ABH step CLD - Mode 7: 405 Hz

Uniform CLD - Mode 8: 722 Hz

ABH 2-2 CLD - Mode 8: 597 Hz

ABH step CLD - Mode 8: 500 Hz

Uniform CLD - Mode 9: 897 Hz

ABH 2-2 CLD - Mode 9: 753 Hz

ABH step CLD - Mode 9: 634 Hz

Uniform CLD - Mode 10: 1099 Hz

ABH 2-2 CLD - Mode 10: 907 Hz

ABH step CLD - Mode 10: 782 Hz

Uniform CLD - Mode 11: 1312 Hz

ABH 2-2 CLD - Mode 11: 1093 Hz

ABH step CLD - Mode 11: 916 Hz

Uniform CLD - Mode 12: 1546 Hz

ABH 2-2 CLD - Mode 12: 1289 Hz

ABH step CLD - Mode 12: 1125 Hz

Figure A.8: Modeshapes of the first twelve modes of beams with different thickness profiles with CLD. *Remark: The strongly varying thickness of the beams is an artifact that results from squeezing the deformation pattern along the beam axis.*

A.8 Wavenumber spectra of beams with different thickness profiles

The following section explains the transformation of a variable into the Fourier domain

$$
\underline{v}(x) \quad \circ\!\!\!-\!\!\!\bullet \quad V(k) \,. \tag{A.92}
$$

The following derivations are based on the derivations in Müller [2019a].

The radiated power from a structure into the adjacent fluid depends on the velocity distribution of the structure. In general, only the vertical displacements significantly contribute to the sound power radiated into the far-field. Therefore, one only considers the velocity $\underline{v}(x)$ perpendicular to the surface. The vertical velocity $\underline{v}(x)$ results from a finite element model which therefore is a discrete function in space

$$
\begin{aligned}
\underline{v}\,(x)\,\Delta_0\,(x) &= \underline{v}\,(x)\sum_{n=-\infty}^{\infty}\delta^*\,(x-n\,X_s) \\
&= \sum_{n=-\infty}^{\infty}\underline{v}\,(n\,X_s)\,\delta^*\,(x-n\,X_s)
\end{aligned} \tag{A.93}
$$

with

$$
\delta^*\,(x) = \begin{cases} 1 & \text{for } x \;=\; 0 \\ 0 & \text{for } x \;\neq\; 0 \end{cases}. \tag{A.94}
$$

X_s is the spatial sampling period. As the beam structure is limited in space, the function is multiplied with a rectangular function $r\,(x)$

$$
r\,(x) = \begin{cases} 1 & -\frac{X_s}{2} \;<\; x \;<\; L_0 - \frac{X_s}{2} \\ 0 & \text{else} \end{cases}. \tag{A.95}
$$

L_0 is the length of the beam. The rectangular function $r(x)$ is chosen in such a way, that its limits do not coincide with a sampled value to avoid that the last value of a period coincides with the first value in the next period (these values would be summed up). $r(x)$ can be

imagined as the range of observation

$$
\underline{v}(x)\,\Delta_0(x)\,r(x) = \left[\sum_{n=-\infty}^{\infty} \underline{v}(n\,X_s)\,\delta^*(x - n\,X_s)\right] r(x)
$$
$$
= \sum_{n=0}^{N-1} h(n\,X_s)\,\delta^*(x - n\,X_s)
$$

(A.96)

Hint: There are N samples within the rectangle, which are equidistant $\left(N = \frac{L_0}{X_s}\right)$. The frequency spectrum of the finite length discrete spatial signal is still continuous. To calculate the values of this spectrum only at equidistant frequencies, it is discretized with $\Delta_1(x) = L_0 \sum_{m=-\infty}^{\infty} \delta^*(x - m\,L_0)$.

In the spatial domain, we obtain a convolution with $\Delta_1(x)$ leading to a periodic function, where the sampling frequency $f_s = \frac{1}{L_0}$ is chosen such that an overlap in the spatial domain is avoided.

$$
\underbrace{[\underline{v}(x)\,\Delta_0(x)\,r(x)] * \Delta_1(x)}_{\tilde{\underline{v}}(x)} = \left[\sum_{n=0}^{N-1} \underline{v}(n\,X_s)\,\delta^*(x - n\,X_s)\right] * L_0 \left[\sum_{m=0}^{N-1} \delta^*(x - m\,L_0)\right]
$$

(A.97)

$$
\tilde{\underline{v}}(x) = \ldots + L_0 \sum_{n=0}^{N-1} \underline{v}(n\,X_s)\,\delta^*(x + L_0 - n\,X_s) +
$$

(A.98)

$$
+ L_0 \sum_{n=0}^{N-1} \underline{v}(n\,X_s)\,\delta^*(x - n\,X_s) +
$$

$$
+ L_0 \sum_{n=0}^{N-1} \underline{v}(n\,X_s)\,\delta^*(x - L_0 - n\,X_s) + \ldots
$$

$\tilde{\underline{v}}(x)$ is the discrete approximation of $\underline{v}(x)$. Applying some algebraic transformations, (A.98) is written in a short form

$$
\tilde{\underline{v}}(x) = L_0 \sum_{m=-\infty}^{\infty} \left[\sum_{n=0}^{N-1} \underline{v}(n\,X_s)\,\delta^*(x - n\,X_s - m\,L_0)\right].
$$

(A.99)

Using a Fourier series, the Fourier transform of the discrete periodic function $\tilde{\underline{v}}(x)$ can be expressed as a sum of equidistant δ^* functions.

$$
V\left(\frac{r}{L_0}\right) = \sum_{r=-\infty}^{\infty} \alpha_r\,\delta^*(f - r\,f_0) \qquad \text{with:} \quad f_0 = \frac{1}{L_0}
$$

(A.100)

where

$$\alpha_r = \frac{1}{L_0} \int\limits_{-\frac{X_s}{2}}^{L_0 - \frac{X_s}{2}} \tilde{\underline{v}}(x)\, e^{-i2\pi r \frac{x}{L_0}}\, dx \qquad \text{with: } r = 0,\, \pm 1,\, \pm 2,\, \ldots \tag{A.101}$$

Inserting (A.99) leads to

$$= \frac{1}{L_0} \int\limits_{-\frac{X_s}{2}}^{L_0 - \frac{X_s}{2}} L_0 \sum_{m=-\infty}^{\infty} \sum_{n=0}^{N-1} \underline{v}(n\,X_s)\, \delta^*(x - n\,X_s - m\,L_0)\, e^{-i2\pi r \frac{x}{L_0}}\, dx \tag{A.102}$$

The integral is evaluated over one period and the simplified equation is

$$\alpha_r = \int\limits_{-\frac{X_s}{2}}^{L_0 - \frac{X_s}{2}} \sum_{n=0}^{N-1} \underline{v}(n\,X_s)\, \delta^*(x - n\,X_s)\, e^{-i2\pi r \frac{x}{L_0}}\, dx \tag{A.103}$$

$$= \sum_{n=0}^{N-1} \underline{v}(n\,X_s) \int\limits_{-\frac{X_s}{2}}^{L_0 - \frac{X_s}{2}} \delta^*(x - n\,X_s)\, e^{-i2\pi r \frac{x}{L_0}}\, dx$$

$$= \sum_{n=0}^{N-1} \underline{v}(n\,X_s)\, e^{-i2\pi n r \frac{X_s}{L_0}} \tag{A.104}$$

with: $L_0 = N\,X_s$

$$\alpha_r = \sum_{n=0}^{N-1} \underline{v}(n\,X_s)\, e^{-i2\pi n \frac{r}{N}}; \qquad r = 0,\, \pm 1,\, \pm 2,\, \ldots \tag{A.105}$$

Finally, we obtain for (A.100):

$$V\left(\frac{r}{N\,X_s}\right) = \sum_{r=-\infty}^{\infty} \sum_{n=0}^{N-1} \underline{v}(n\,X_s)\, e^{-i2\pi n \frac{r}{N}} \delta(f - r f_0) \tag{A.106}$$

$V\left(\dfrac{r}{N X_s}\right)$ is periodic with respect to a period N

$$V\left(\frac{r}{N\,X_s}\right) = \sum_{n=0}^{N-1} \underline{v}(n\,X_s)\, e^{-i2\pi n \frac{r}{N}} \qquad r = 0, 1,\, \ldots\, N - 1\,. \tag{A.107}$$

(A.107) is the *discrete Fourier transform*, which assigns N sampled values of a function in the transformed domain to N sampled values of an original function in the spatial domain using the continuous Fourier transform.

Using this transformation, the discrete vertical velocity of the beam is transformed into the discrete wavenumber domain.

$$\underline{\tilde{v}}(x) \quad \overset{\mathcal{F}}{\circ\!\!-\!\!\bullet} \quad V(k) \, . \tag{A.108}$$

As demonstrated in section 2.5.1, the wavenumber spectrum of the structural motion gives information about the sound radiation. For the sound radiation, the squared absolute value is required (see (2.39)). The squared absolute value of a complex spectra is

$$|V(k)|^2 = V(k)V(k)^* \, . \tag{A.109}$$

Wavenumber components smaller than the respective wavenumber of the air contribute to the sound radiation. In the following graphs, the wavenumber of the air is marked with the respective vertical line.

Figure A.9: Wavenumber spectra of the vertical surface velocity for beams with different thickness profiles (without CLD) at different frequencies; the vertical lines mark the corresponding wavenumber of the air.
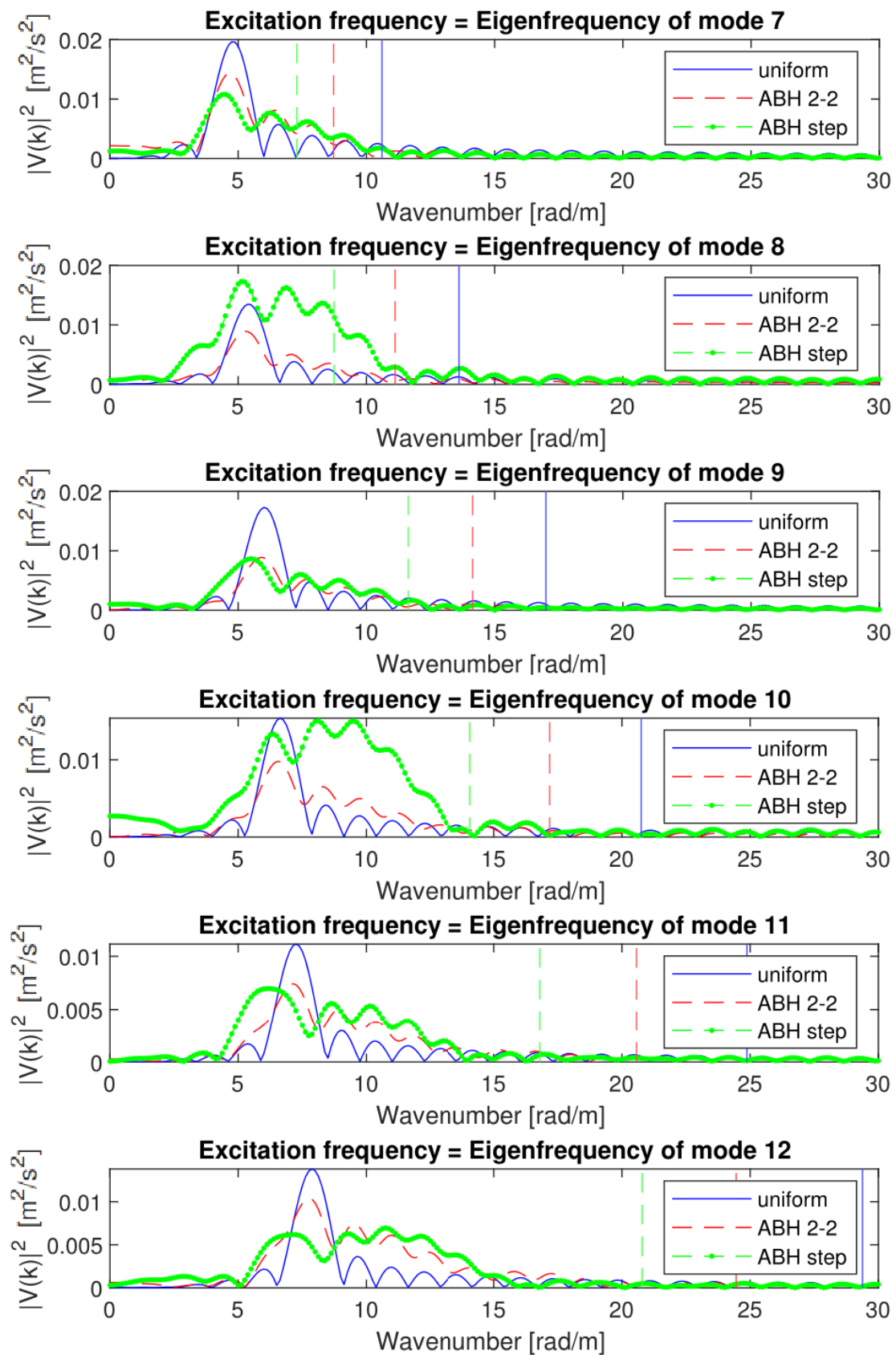
Figure A.10: Wavenumber spectra of the vertical surface velocity for beams with different thickness profiles (without CLD) at different frequencies; the vertical lines mark the corresponding wavenumber of the air.

Figure A.11: Wavenumber spectra of the vertical surface velocity for beams with different thickness profiles with CLD at different frequencies; the vertical lines mark the corresponding wavenumber of the air.
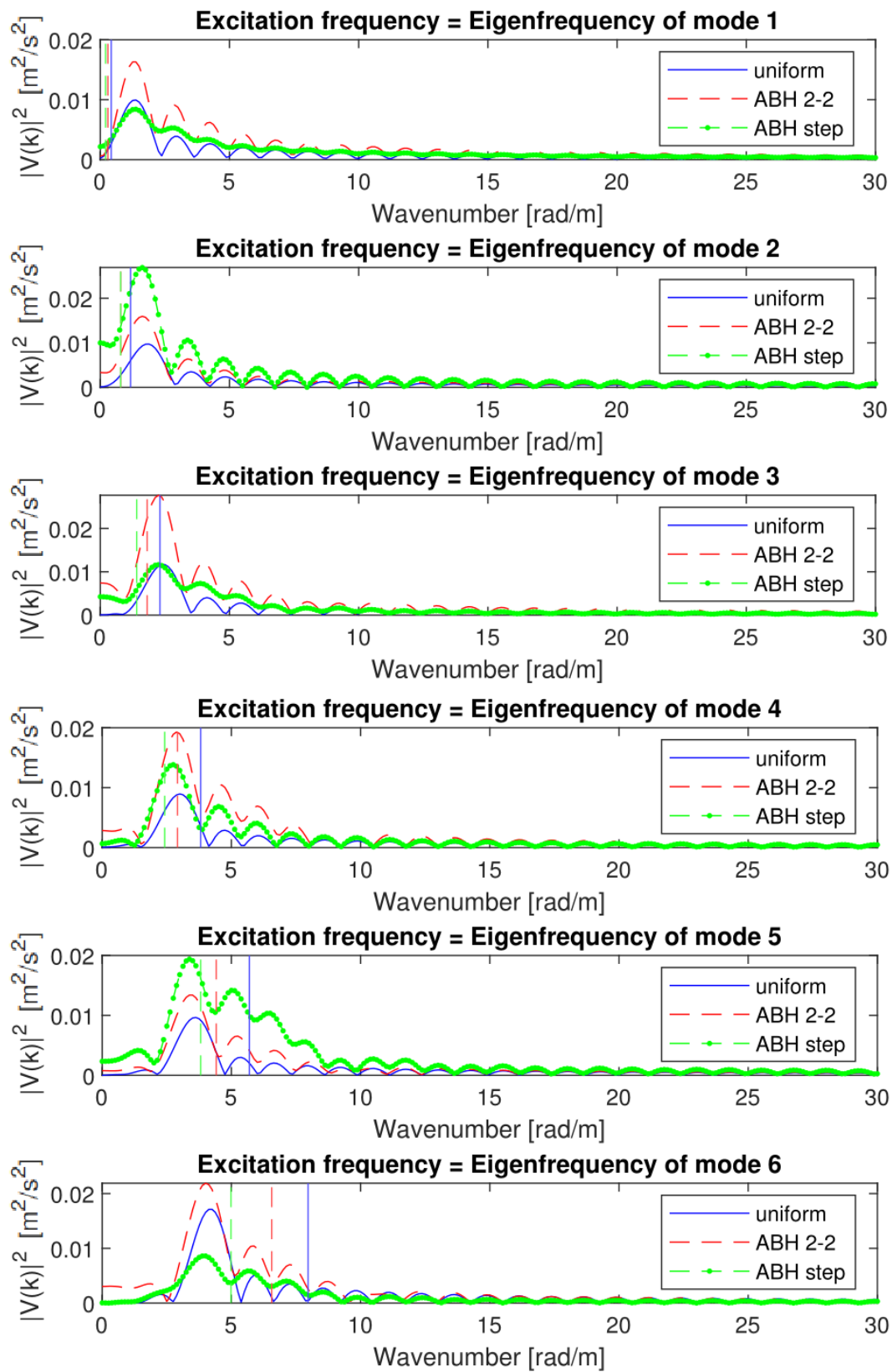
Figure A.12: Wavenumber spectra of the vertical surface velocity for beams with different thickness profiles with CLD at different frequencies; the vertical lines mark the corresponding wavenumber of the air.
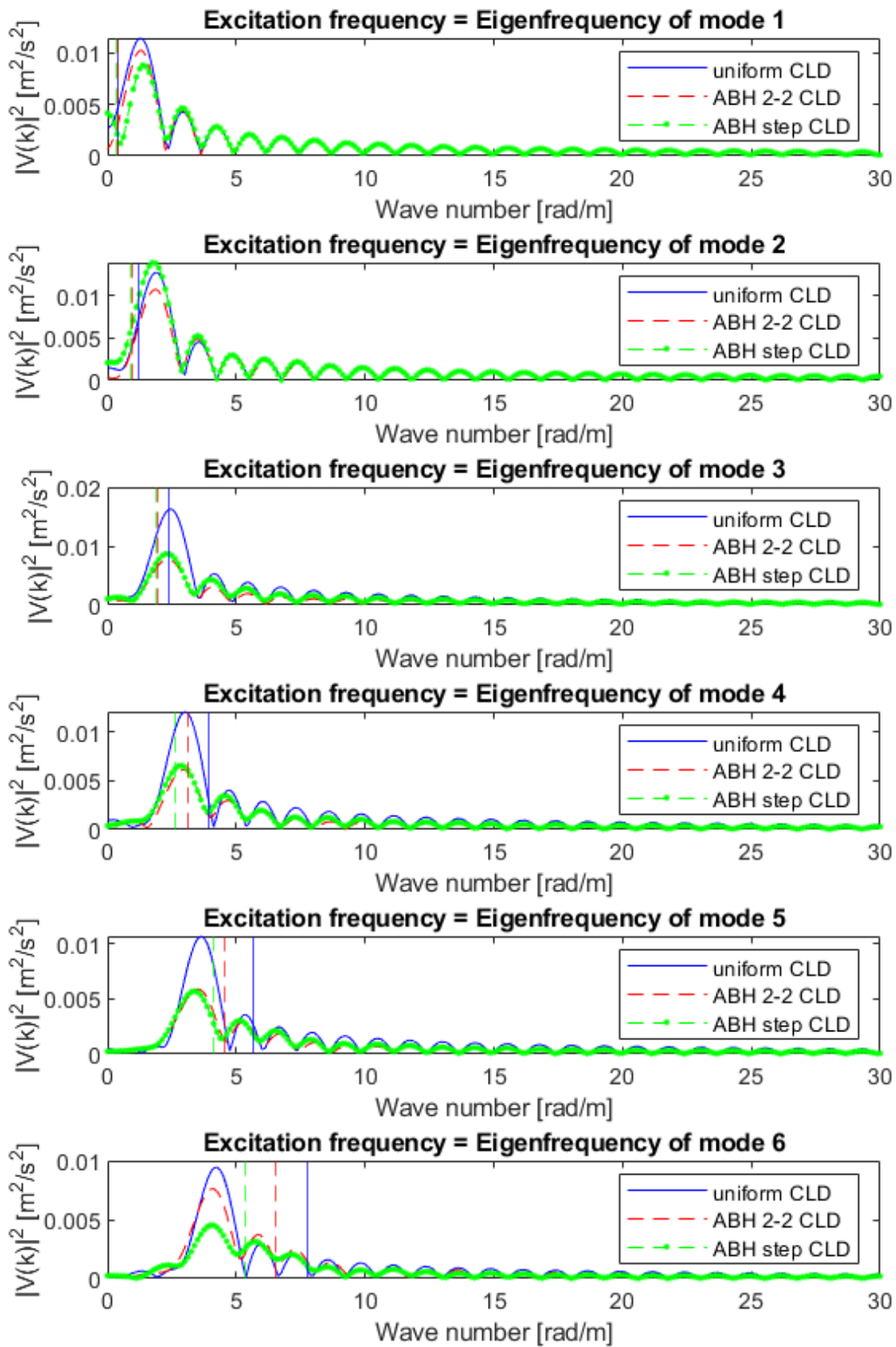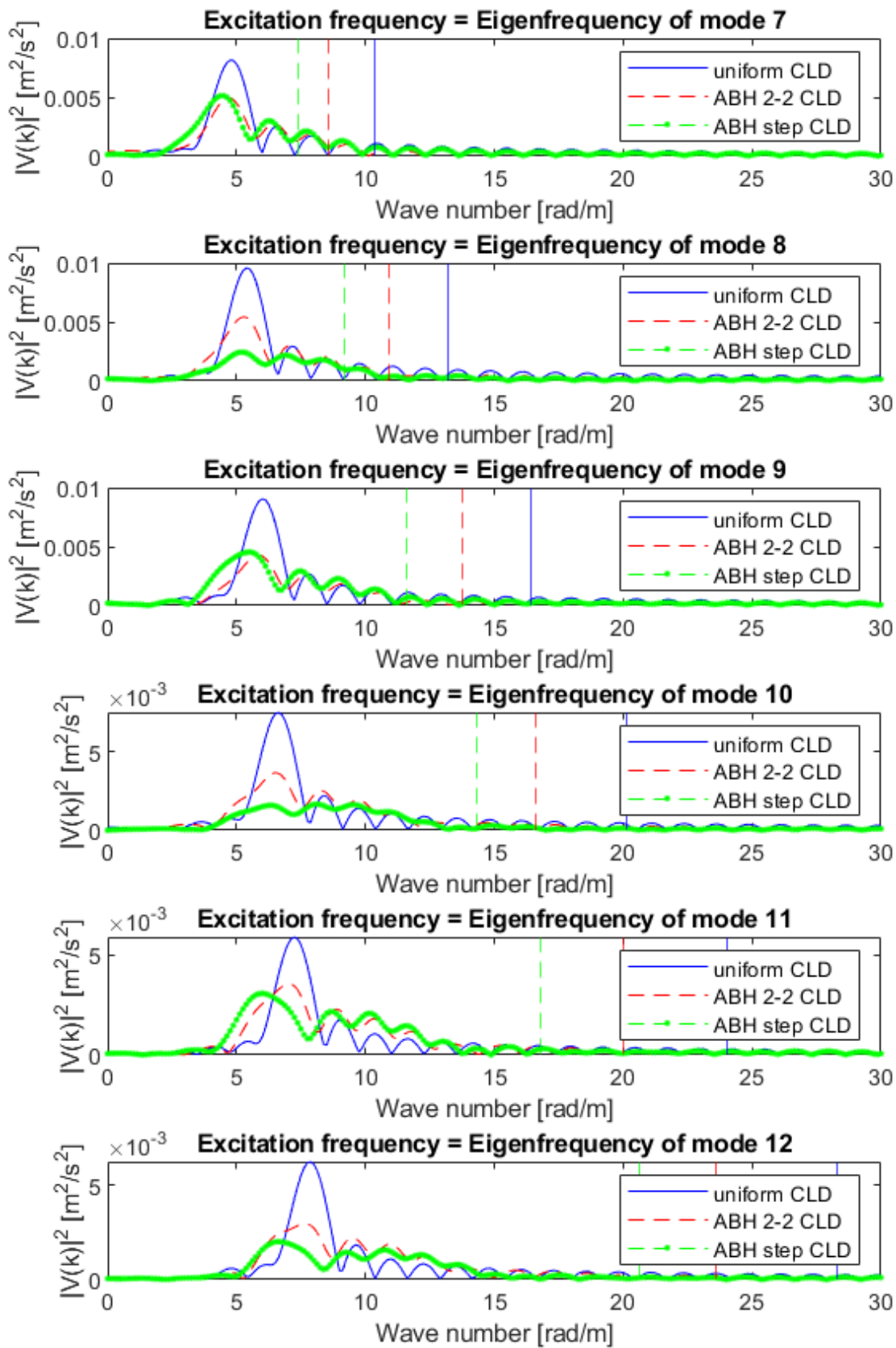
A.9 Insertion loss of plates with different ABH

The following section evaluates the performance of different ABH configurations in plates, the author compares the different configurations to the uniform plate. For the energetic evaluation, the energies are normalized with respect to the input power. This is necessary to avoid an overlaying interpretation linked to a changes in the input power due to a simple modal shift. The energetic insertion loss is

$$\Delta L = 10 \log \left(\frac{E_{uni}/P_{uni}}{E_{...}/P_{...}} \right) \quad [\text{dB}] \, . \tag{A.110}$$

The thickness profiles are two dimensional circular indentations in a rectangular plate. In two dimensions the thickness profiles are rotational symmetric with respect to the center of the indentation. The thickness profiles follow the expression $h(r) = \epsilon r^{\beta} + h_{min}$. The minimum thickness at the center of the circular indentation is 1 mm and the diameter of 200 mm defines the parameter ϵ. Figure 5.11 illustrates an exemplary configuration. The plate's dimension are $600 \times 500 \times 3$ mm. The material of the plate is titanium. Table 5.2 lists the material properties of titanium. A harmonic surface load which covers the area of 20×20 mm excites the plates.

The following section investigates various configurations of single and multiple ABH. The numbering of the ABH in figure 5.11 determines the order in which the ABH are allocated. The following labeling helps to distinguish the different configurations:

$$\underbrace{4}_{\substack{\# \text{ of} \\ \text{indentation}}} \quad \underbrace{\text{ABH}}_{\substack{\text{ABH or} \\ \text{uniform}}} \quad \underbrace{2.2}_{\substack{\text{exponent} \\ \beta}} \quad \underbrace{\text{CLD}}_{\substack{\text{additional CLD} \\ \text{at indentation}}}$$
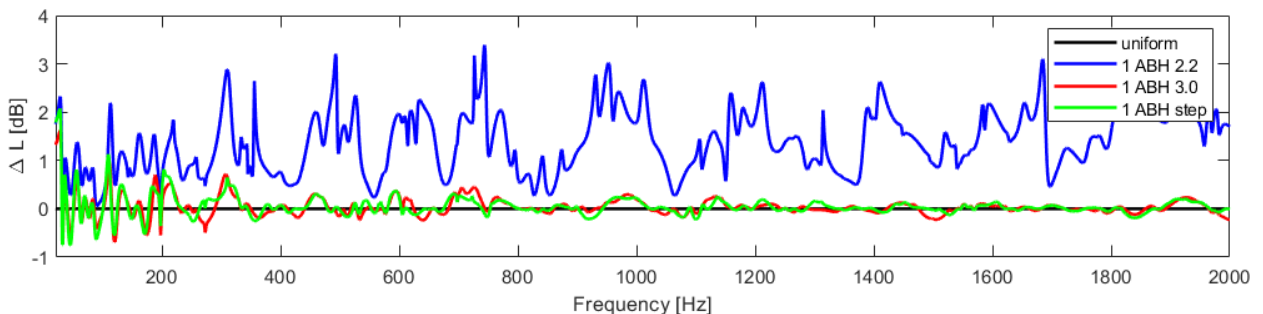
Figure A.13: Insertion loss of a plate with a single ABH profile with different exponents β (without CLD).
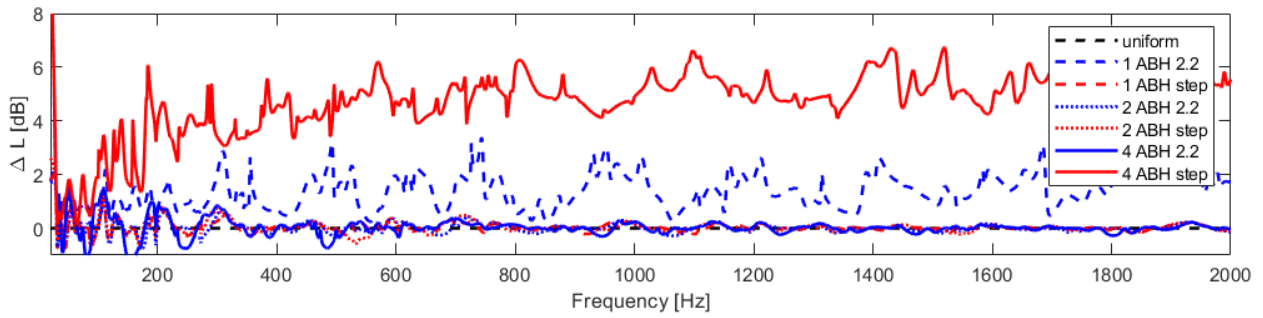
Figure A.14: Insertion loss of a plate with multiple ABH profiles (without CLD).
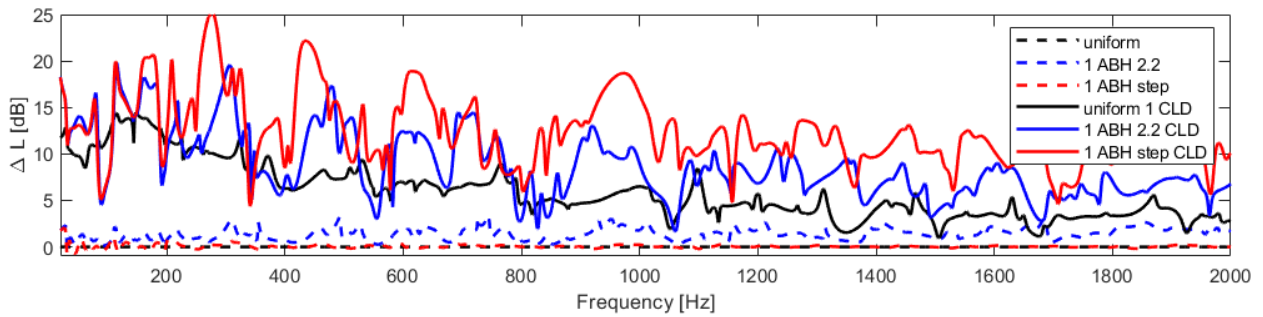
Figure A.15: Insertion loss of a plate with two different ABH profile with and without additional CLD.
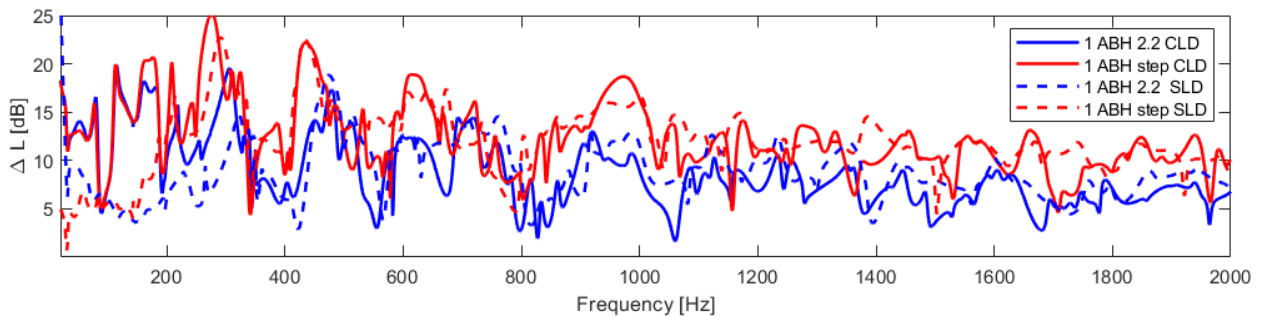
Figure A.16: Insertion loss of a plate with two different ABH profile with CLD and SLD.
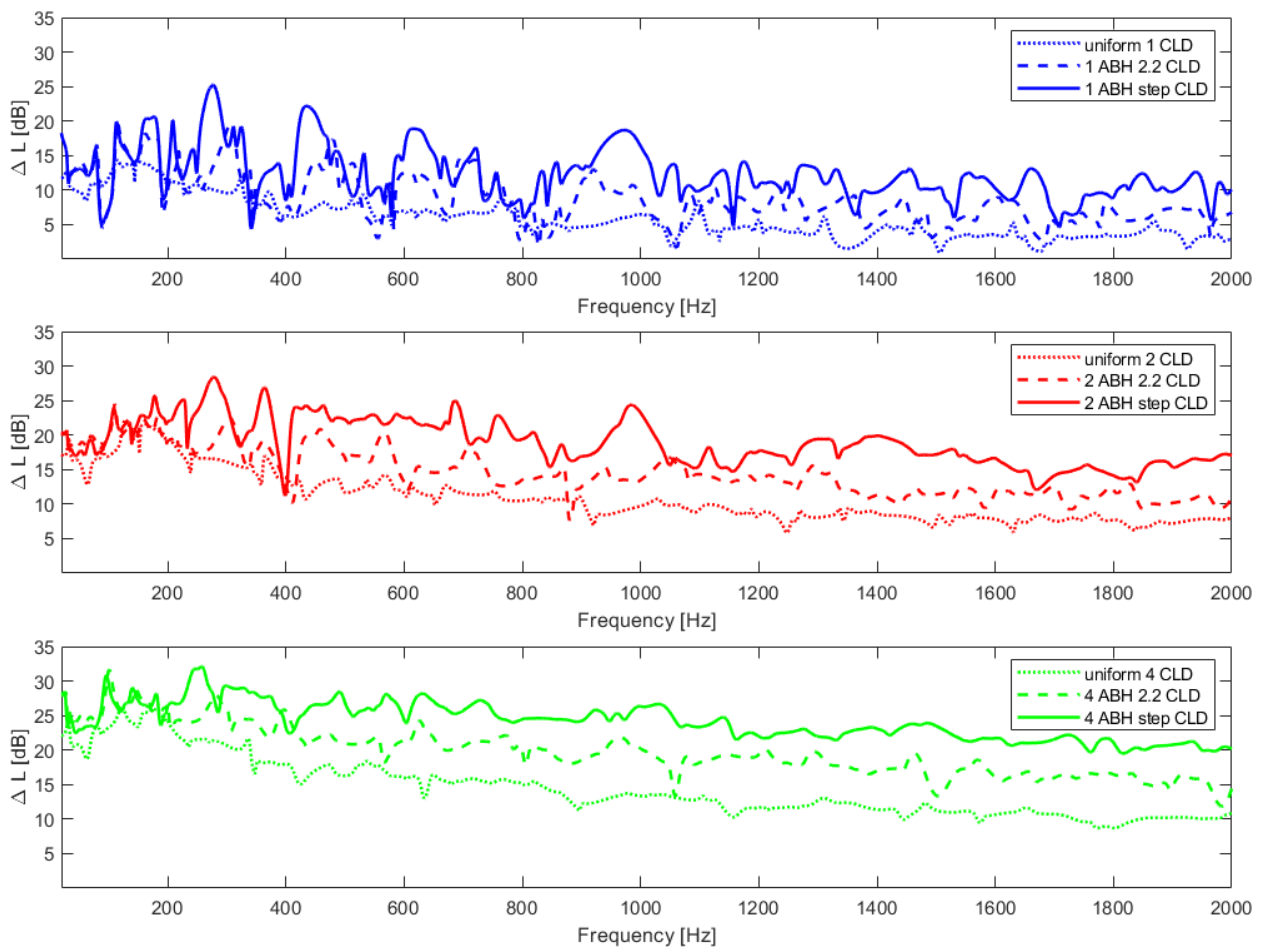
Figure A.17: Insertion loss of a plate with multiple ABH with different profiles and CLD; Comparison of one (top), two (middle) and four (bottom) incorporated ABH.

A.10 Influence of the geometry of a beam-like resonator

The following investigation assesses the influence of the geometry on the eigenfrequency, the mass of the resonator, and the amplification functions V. A coupled beam model (presented in section 4.1.1) evaluates the eigenfrequency and the amplification function. The beam-like resonator is coupled to a simple mass-spring system to compute the characteristics of the amplification function (see figure 5.19).
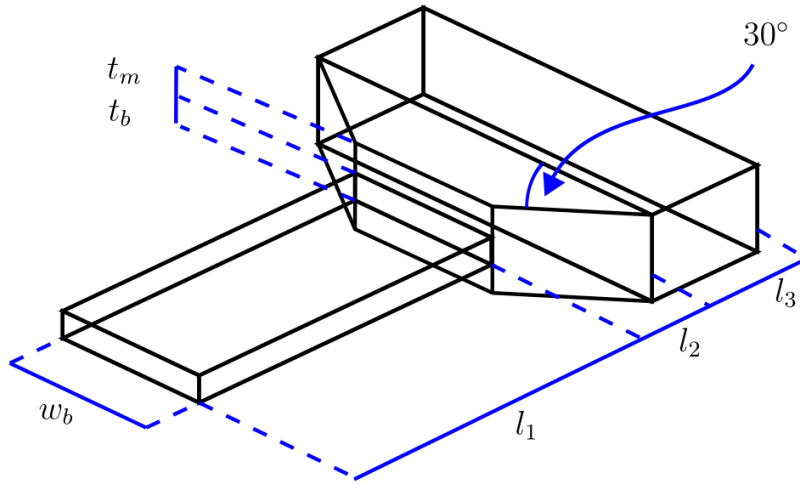
Figure A.18: Geometric parameters of the beam-like resonator.

The beam-like resonator consists of three segments: a beam segment of length l_1, a transition segment of length l_2 and an end mass of length l_3. The ALM process limits the overhang thickness t_m to 1 mm and the transition angle to 30°. Additionally, the installation space is restricted to

$$l_1 + l_2 + l_3 \leq 25 \text{ mm} , \tag{A.111}$$

$$t_b + 2t_m \leq 5 \text{ mm} , \tag{A.112}$$

$$w_m = w_B + 2\tan(60°)l_2 \leq 25 \text{ mm} . \tag{A.113}$$
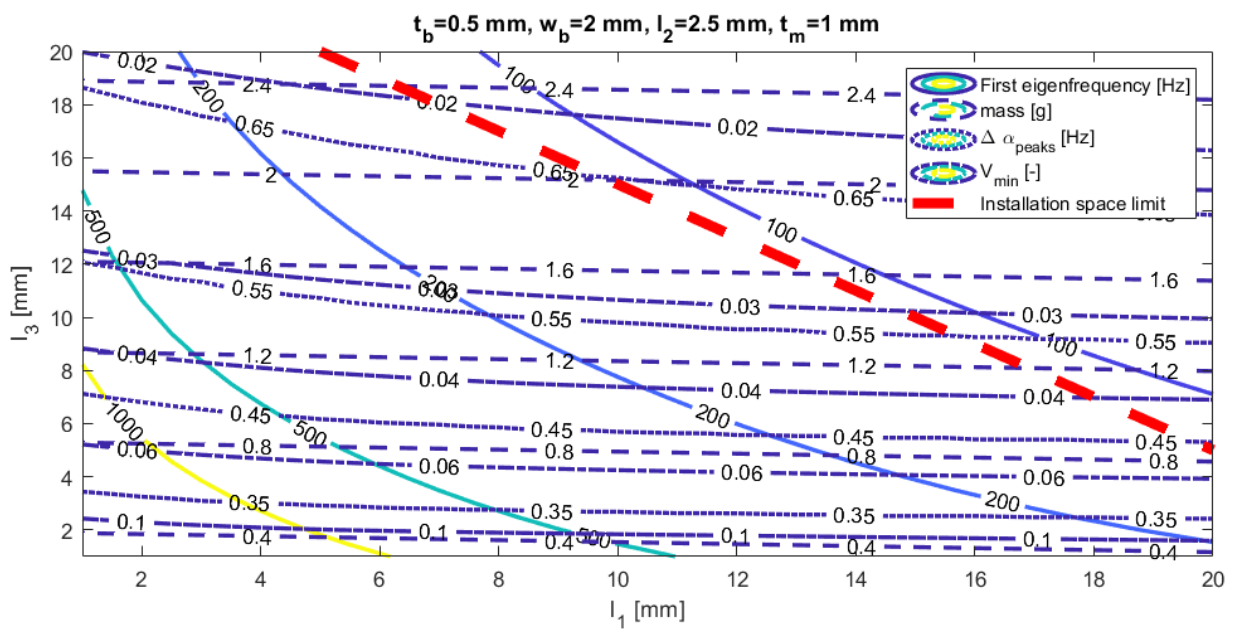
Figure A.19: Influence of l_1 and l_3 on the first eigenfrequency, the mass and and the distance of the resonance peaks and the minimal value of the amplification function.

A.11 Wavenumber spectra of beams with attached resonators

The following section investigates the impact of resonators on the vibration of the structure and the radiated sound power. The host structure is a beam made of aluminum and has a length of 1 m and a thickness of 1 cm. Table 5.4 lists the material properties of aluminum. The beam consists of 100 beam elements. 30 periodic resonators complement the beam. The model of the beam is shown in figure 5.48. The discrete resonators are added as additional DOF (see section 4.1.3). All vertical degrees of freedom of the beam are loaded by a single load. Each single load has an amplitude of 1 N and random phase drawn from the uniform distribution between $-\pi$ and $+\pi$. This ensures that all bending modes are excited.
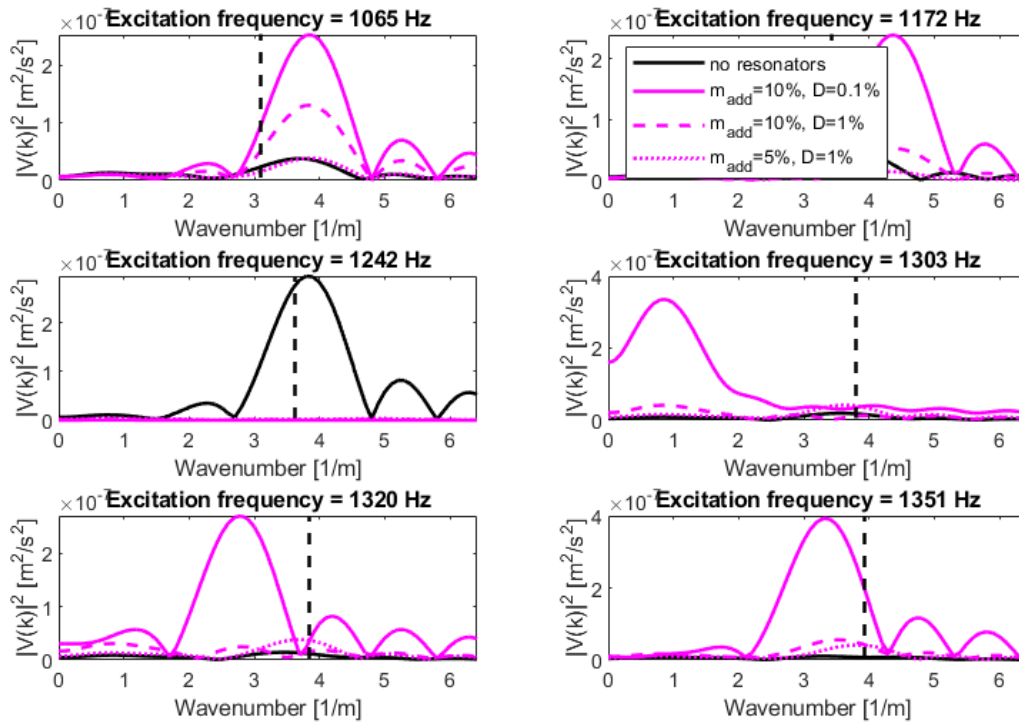
Figure A.20: Wavenumber spectra of the vertical surface velocity for beams with 30 periodically attached resonators (f_{res} = 1242 Hz) at different excitation frequencies; the vertical line marks the corresponding wavenumber of the air.
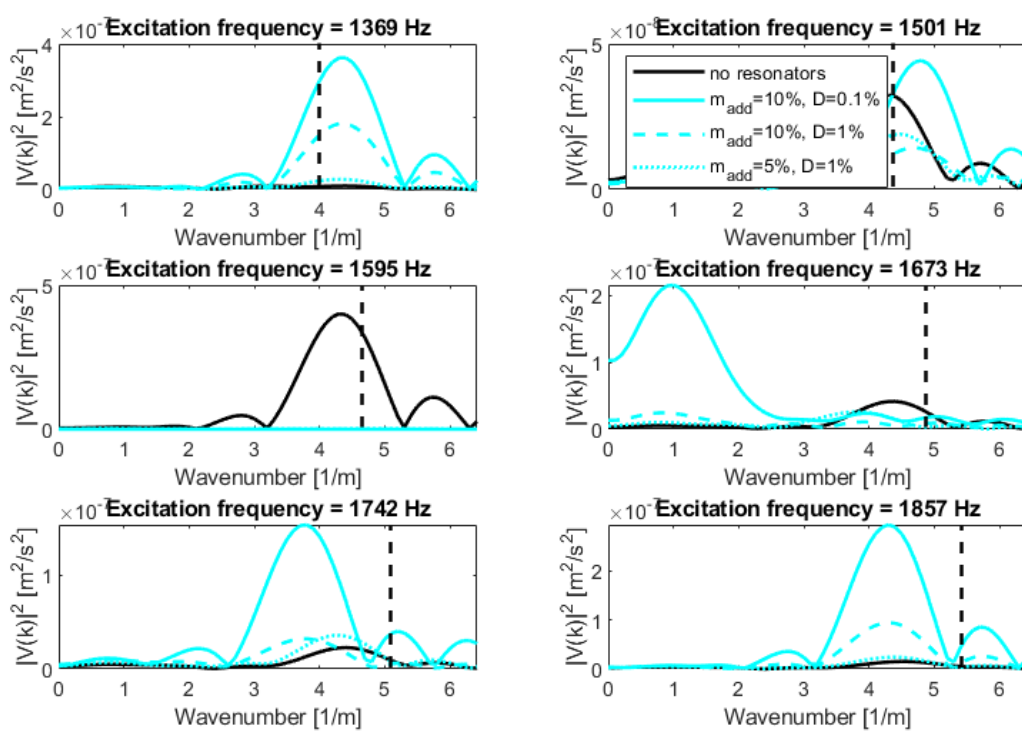
Figure A.21: Wavenumber spectra of the vertical surface velocity for beams with 30 periodically attached resonators (f_{res} = 1595 Hz) at different excitation frequencies; the vertical line marks the corresponding wavenumber of the air.

Bibliography

[Airoldi and Ruzzene 2011] AIROLDI, L. ; RUZZENE, M.: Design of tunable acoustic metamaterials through periodic arrays of resonant shunted piezos. In: *New Journal of Physics, vol. 13, no. 113010* (2011)

[Angrand 2019] ANGRAND, A.: Safran ponders open rotor options. In: *Air & Cosmos International, No. 7, pp. 22-23* (2019). – ISSN 1240-3113

[Arens et al 2012] ARENS, T. ; HETTLICH, F. ; KARPFINGER, C. ; KOCKELKORN, U. ; LICHTENEGGER, K. ; STACHEL, H.: *Mathematik*. Heidelberg: Spektrum Akademischer Verlag, 2. Edition, 2012

[Arfken and Weber 1995] ARFKEN, George B. ; WEBER, Hans J.: *Mathematical Methods for Physicists*. 4th edition. San Dieg0 : Academic Press, 1995

[Asami et al 2002] ASAMI, T. ; NISHIHARA, O. ; BAZ, A. M.: Analytical solutions to H_∞ and H_2 optimization of dynamic vibration absorbers attached to damped linear systems. In: *Journal of Vibration and Acoustics, vol. 124, pp. 284-295* (2002)

[Assouar et al 2012] ASSOUAR, M. B. ; SENESI, M. ; OUDICH, M. ; RUZZENE, M. ; HOU, Z.: Broadband plate-type acoustic metamaterial for low-frequency sound attenuation. In: *Applied physics letter, vol. 101, no. 173505* (2012)

[Bückmann et al 2014] BÜCKMANN, T. ; THIEL, M. ; KADIC, M. ; SCHITTY, R. ; WEGENER, M.: An elasto-mechanical unfeelability cloak made of pentamode metamaterials. In: *Nature Communications, vol 5, no. 4130* (2014)

[Benoît 1924] BENOÎT, C.: Note sur une méthode de résolution des équations normales provenant de l'application de la méthode des moindres carrés à un système d'équations linéaires en nombre inférieur à celui des inconnues (procédé du commandant Cholesky). In: *Bulletin géodésique, vol 2, pp. 67-77* (1924)

[Bishop and Welbourn 1952] BISHOP, R. E. D. ; WELBOURN, D. B.: The problem of the dynamic vibration absorber. In: *Engineering, vol. 174* (1952)

[Blevins 2016] BLEVINS, R. D.: *Formulas for Dynamics, Acoustics and Vibration*. Hoboken : Wiley, 2016

[Bloch 1929] BLOCH, F.: Über die Quantenmechanik der Elektronen in Kristallgittern. In: *Zeitschrift für Physik, vol. 52, issue 7, pp 555-600* (1929)

[Bowyer and Krylov 2016]   Bowyer, E. ; Krylov, V.: Acoustic black hole manufacturing for practical applications and the effect of geometrical and material imperfections. In: *Proceedings of Inter-Noise, Hamburg, pp. 2411-2421* (2016)

[Brock 1945]   Brock, J. E.: A Note on the Damped Vibration Absorber. In: *Journal of Applied Mechanics, vol 13, p. A284* (1945)

[Casadei et al 2009]   Casadei, F. ; Ruzzene, M. ; Dozio, L. ; Cunefare, K. A.: Broadband vibration control through periodic arrays of resonant shunts: Experimental investigation on plates. In: *Smart Materials and Strucutres, vol. 19* (2009)

[Chen and Wang 2014]   Chen, Y. ; Wang, L.: Periodic co-continuous acoustic metamaterials with overlapping locally resonant and Bragg band gaps. In: *Applied Physics Letter, vol. 105* (2014)

[Claeys et al 2017]   Claeys, C. C. ; Melo Filho, N. G. Rocha de ; Van Belle, L. ; Deckers, E. ; ; Desmet, W.: Design and validation of metamaterials for multiple structural stop bands in waveguides. In: *Extreme Mechanics Letters, vol. 12, pp. 7-22* (2017)

[Claeys et al 2016a]   Claeys, C. C. ; Melo Filho, N. R. de ; Deckers, Elke ; Pluymers, B. ; Sas, P. ; Desmet, W.: Experimental demonstrator of vibro-acoustic metamaterial for low frequent NVH insulation. In: *Proceedings of Inter-Noise, Hamburg, pp. 7451-7461* (2016)

[Claeys et al 2016b]   Claeys, C. C. ; Pluymers, B. ; Desmet, W.: A lightweight vibro-acoustic metamaterial demonstrator: Numerical and experimental investigation. In: *Mechanical Systems and Signal Processing, vol. 70-71, pp. 853-880* (2016)

[Claeys et al 2014a]   Claeys, C. C. ; Pluymers, B. ; Sas, P. ; Desmet, W.: Design of a resonant metamaterial based acoustic enclosure. In: *Proceedings of ISMA2014 including USD2014, pp. 3351-3358* (2014)

[Claeys et al 2011]   Claeys, C. C. ; Sas, P. ; Desmet, W.: On the potential of local resonators to obtain low-frequency band gaps in periodic lightweight structures. In: *3rd ECCOMAS, Corfu* (2011)

[Claeys et al 2014b]   Claeys, C. C. ; Sas, P. ; Desmet, W.: On the acoustic radiation efficiency of local resonance based stop band materials. In: *Journal of Sound and Vibration, vol. 333, issue 14, pp. 3203-3213* (2014)

[Claeys et al 2013]   Claeys, C. C. ; Vergote, K. ; Sas, P. ; Desmet, W.: On the potential of tuned resonators to obtain low frequency vibrational stop bands in periodic panels. In: *Journal of Sound and Vibration, vol. 332, issue 6, pp. 1418-1436* (2013)

[Conlon and Fahnline 2015]   Conlon, S. C. ; Fahnline, J. B.: Numerical analysis of the vibroacoustic properties of plates with embedded grids of acoustic black holes. In: *Journal of the Acoustical Society of America vol. 137, pp. 447-457* (2015)

[Conlon et al 2015]   CONLON, S. C. ; FAHNLINE, J. B. ; SHEPHERD, M. R. ; FEURTADO, P. A.: Vibration control using grids of Acoustic Black Holes: How many is enough? In: *Proceedings of Inter-Noise, San Francisco, pp. 6629-6642* (2015)

[Conlon and Feurtado 2018]   CONLON, S. C. ; FEURTADO, P. A.: Progressive phase trends in plates with embedded acoustic black holes. In: *The Journal of the Acoustical Society of America, vol. 143, no. 921* (2018)

[Cook 1989]   COOK, R. D.: *Concepts and applications for Finite Element Analysis.* New York: Wiley, 3rd edition, p.132, 1989

[Craster and Guenneau 2013]   CRASTER, R. V. ; GUENNEAU, S.: *Acoustic metamaterials - Negative Refraction, Imaging, Lensing and Cloaking.* Springer Series in Materials Science, no. 166, 2013

[Cremer and Heckl 1967]   CREMER, L. ; HECKL, M.: *Körperschall. Physikalische Grundlagen und Technische Anwendung.* Berlin : Springer, 1967

[Cummer et al 2008]   CUMMER, S. A. ; RAHM, M. ; SCHURIG, D.: Material parameters and vector scaling in transformation acoustics. In: *New Journal of Physics, vol. 10* (2008)

[Cummer and Schurig 2007]   CUMMER, S. A. ; SCHURIG, D.: One path to acoustic cloaking. In: *New Journal of Physics, vol. 9* (2007)

[Deymier 2013]   DEYMIER, P. A.: *Acoustic Metamaterials and Phononic Crystals.* Springer Series in Solid-State Sciences, no. 173, 2013

[Doyle 1997]   DOYLE, J. F.: *Wave Propagation in Structures.* Second Edition. New York : Springer-Verlag, 1997

[Duhamel et al 2005]   DUHAMEL, D. ; MACE, B. R. ; BRENNAN, M. J.: Finite element analysis of vibrations of waveguides and periodic structures. In: *Journal of Sound and Vibration vol. 294, pp. 205-220* (2005)

[Egashira et al 2016]   EGASHIRA, K. ; FUKAYA, K. ; MORI, K. ; TAKAHASHI, T.: Application of acoustic metamaterial with stop band to panel and cylinder. In: *Proceedings of Inter-Noise, Hamburg, pp. 7462-7468* (2016)

[Erturk and Inman 2011]   ERTURK, A ; INMAN, D. J.: *Appendix C: Modal Analysis of a Uniform Cantilever with a Tip Mass.* John Wiley & Sons, Ltd, 2011

[Fahy and Gardonio 2007]   FAHY, F. J. ; GARDONIO, P.: *Sound and Structural Vibration: Radiation, Transmission and Response.* Elsevier, 2007

[Farhat et al 2009]   FARHAT, m. ; GUENNEAU, S. ; ENOCH, S.: Ultrabroadband Elastic Cloaking in Thin Plates. In: *Physical Review Letters, vol. 103, no. 024301* (2009)

[Feurtado and Conlon 2016]   FEURTADO, P. A. ; CONLON, S. C.: Assesing Acoustic Black Hole performance via wavenumber transforms. In: *Proceedings of Inter-Noise, Hamburg, pp. 2381-2386* (2016)

[Feurtado and Conlon 2017]   FEURTADO, P. A. ; CONLON, S. C.: Transmission loss of plates with embedded acoustic black holes. In: *The Journal of the Acoustical Society of America, vol. 142, no. 1390* (2017)

[Floquet 1883]   FLOQUET, G.: Sur les équations différentielles linéaires à coeffcients pérodiques. In: *Annales scientifiques de l'É.N.S 2ᵉ série, vol. 2, pp. 47-88* (1883)

[Galerkin 1915]   GALERKIN, B. G.: Series solution of some problems in elastic equilibrium of rods and plates. In: *Vestnik Inzh. Tech., vol. 19, pp. 897-908* (1915)

[Gauß 1815]   GAUSS, C.F.: *Methodus nova integralium valores per approximationem inveniendi.* apvd Henricvm Dieterich, 1815

[Gündel 2008]   GÜNDEL, A.: *Numerical study on active and passive noise control for multiple propeller tones - Comparison and Optimization Strategies*, TU Dresden, Dissertation, 2008

[Golub et al 1996]   GOLUB, G.H. ; VAN LOAN, C.F. ; VAN LOAN, C.F. ; VAN LOAN, P.C.F.: *Matrix Computations.* Johns Hopkins University Press, 1996 (Johns Hopkins Studies in the Mathematical Sciences)

[Hahnkamm 1933]   HAHNKAMM, E.: Die Dämpfung von Fundamentalschwingungen bei veränderlicher Erregerfrequenz. In: *Ingenieur Archiv, vol. 4, pp. 192-201* (1933)

[Hambric et al 2016]   HAMBRIC, S. A. ; SUNG, S. H. ; NEFSKE, D. J.: *Engineering Vibroacoustic Analysis.* Wiley, 2016

[Hartog 1956]   HARTOG, J. P. D.: *Mechanical Vibrations.* 4. Auflage. New York : McGraw-Hill, 1956

[Huang et al 2016]   HUANG, W. ; JI, H. ; QIU, J. ; CHENG, L.: Flexural wave focalization in plates with imperfect two-dimensional acoustic black hole. In: *Proceedings of Inter-Noise, Hamburg, pp. 2392-2402* (2016)

[Huang et al 2018]   HUANG, Wei ; JI, Hongli ; QIU, Jinhao ; CHENG, Li: Analysis of ray trajectories of flexural waves propagating over generalized acoustic black hole indentations. In: *Journal of Sound and Vibration, vol. 417, pp. 216-226* (2018)

[Huanyang and Chan 2009]   HUANYANG, C. ; CHAN, C. T.: Acoustic cloaking in three dimensions using acoustic metamaterials. In: *New Journal of Physics, vol. 11* (2009)

[Hughes 2002]   HUGHES, T. J. R.: *The finite element method: linear staticand dy-namic finite element analysis.* Mineola : Dover, 2002

[Igusa and Xu 1993]   IGUSA, T. ; XU, K.: Vibration control using multiple tuned mass dampers. In: *Journal of Sound and Vibration, vol 175, no. 4, pp. 491-503* (1993)

[Inglis 1951]   INGLIS, C. E.: *Applied Mechanics for Engineers.* Cambridge University Press, 1951

[Jacobi 1826]   JACOBI, C. G. J.:   Ueber Gauß neue Methode, die Werthe der Integrale näherungsweise zu finden. In: *Journal für Reine und Angewandte Mathematik, vol. 1, pp. 301-308* (1826)

[Jeon 2016]   JEON, W.: Vibration damping using a spiral acoustic black hole. In: *Proceedings of Inter-Noise, Hamburg, pp. 2387-2391* (2016)

[Kadic et al 2012]   KADIC, M. ; BÜCKMANN, T. ; STENGER, N. ; THIEL, M. ; WEGENER, M.: On the practicability of pentamode mechanical metamaterials. In: *Applied Physical Letter, vol. 100, no. 191901* (2012)

[Kausel 2017]   KAUSEL, Eduardo: *Advanced Structural Dynamics.* Cambridge University Press, 2017

[Klausner 1991]   KLAUSNER, Y.: *Fundamentals of continuum mechanics of soils.* Berlin : Springer, 1991

[Krylov 1989]   KRYLOV, V. V.:   Conditions for validity of the geometrical acoustics approximation in application to waves in an acute-angle solid wedge. In: *Soviet Physics - Acoustics, vol. 35, pp. 176-180.* (1989)

[Krylov 1990]   KRYLOV, V. V.:   Geometrical-acoustics approach to the description of localized vibrational modes of an elastic solid wedge. In: *Soviet Physics - Theoretical and Mathematical Physics, vol. 35, pp. 137-140.* (1990)

[Krylov 2001]   KRYLOV, V. V.: Laminated plates of variable thickness as effective absorbers for flexural vibrations. In: *Proceedings of International Conference on Acoustics, Rome, pp. 270-271* (2001)

[Krylov 2004]   KRYLOV, V. V.:   New type of vibration dampers utilizing the effect of acoustic 'black holes'. In: *Acta Acoustic United With Acustica, vol. 90, no. 5, pp. 830-837* (2004)

[Krylov 2007]   KRYLOV, V. V.:   Propagation of plate bending in the vicinity of one- and two-dimensional acoustic 'black holes'. In: *Proceedings of the ECCOMAS International Conference on Computational Methods in Structural Dynamics and Earthquake Engineering (COMPDYN 2007)* (2007)

[Krylov and Tilman 2004]   KRYLOV, V. V. ; TILMAN, F. J. B. S.: Acoustic 'black holes' for flexural waves as effective vibration dampers. In: *Journal of Sound and Vibration, vol. 274, pp. 605-619* (2004)

[Krylov and Winward 2007]   KRYLOV, V. V. ; WINWARD, R. E. T. B.:   Experimental investigation of the acoustic black hole effect for flexural in tapered plates. In: *Journal of Sound and Vibration, vol. 300, pp. 43-49* (2007)

[Krylov 2019]   KRYLOV, Victor: Overview of localised flexural waves in wedges of power-law profile and comments on their relationship with the acoustic black hole effect. In: *Journal of Sound and Vibration, vol 468* (2019)

[Langley 1993]   LANGLEY, R.: A note on the force boundary conditions for two-dimensional periodic structures with corner freedoms. In: *Journal of Sound and Vibration, vol. 167, pp. 377-381* (1993)

[Li and Chan 2004]   LI, J. ; CHAN, C. T.: Double-negative acoustic metamaterial. In: *Physical Review E, vol. 70* (2004)

[Link 1984]   LINK, M.: *Finite Elemente in der Statik und Dynamik.* Teubner, 1984

[Liu et al 2000]   LIU, Z. ; ZHANG, X. ; MAO, Y. ; ZHU, Y. Y. ; YANG, Z. ; T., Chan C. ; SHENG, P.: Locally resonant sonic materials. In: *Science, vol. 289, no. 5485, pp. 1736-1738* (2000)

[Mace et al 2005]   MACE, B. R. ; DUHAMEL, D. ; BRENNAN, M. J. ; HINKE, L.: Finite element prediction of wave motion in structural waveguides. In: *Journal of the Acoustical Society of America vol. 117, no. 5, pp. 2835-2843* (2005)

[Mace and Manconi 2008]   MACE, B. R. ; MANCONI, E.: Modelling wave propagation in two-dimensional structures using finite element analysis. In: *Journal of Sound and Vibrationm, vol. 318, pp. 884-902* (2008)

[Mead 1973]   MEAD, D. J.: A general theory of harmonic wave propagation in linear periodic systems with multiple coupling. In: *Journal of Sound and Vibration, vol. 27, no. 2, pp. 235-260* (1973)

[Mead 1996]   MEAD, D. J.: Wave propagation in continous periodic structures: research contributions from Southhampton, 1964–1995. In: *Journal of Sound and Vibration, vol. 190, no. 3, pp. 495-524* (1996)

[Melo et al 2016]   MELO, N. F. ; CLAEYS, C. C. ; DECKERS, E. ; PLUYMERS, B. ; DESMET, W.: Dynamic metamaterials for structural stopband prediction. In: *SAE Int. Journal of Passenger Cars - Mechanical Systems, vol. 9, issue 3, pp. 1013-1019* (2016)

[Mencik 2014]   MENCIK, J. M.: New advances in the forced response computation of periodic structures using the wave finite element (WFE) method. In: *Computational Mechanics archive vol. 54, issue 3, pp 789-801* (2014)

[Miksch 2017]   MIKSCH, M.: *Modeling Aspects for Acoustic Metamaterials in Vibroacoustics*, Technische Universität München, Master's Thesis, 2017

[Miksch et al 2018a]   MIKSCH, M. ; AUMANN, Q. ; MÜLLER, G.: Reducing structure-borne noise in thin-walled structures by local thickness variations. In: *PAMM 2018, vol 18, no 1* (2018)

[Miksch and Müller 2019]   MIKSCH, M. ; MÜLLER, G.: Rückschlüsse aus Wellenlösungen von unendlich periodischen Strukturen auf die Systemantwort einer endlich periodischen Struktur. In: *DAGA 2019* Deutsche Gesellschaft für Akustik (Veranst.), 2019, p. 1274–1277

[Miksch et al 2018b]   MIKSCH, M. ; MÜLLER, U. C. ; PEIFFER, A. ; MÜLLER, G.: Einfluss von akustischen schwarzen Löchern auf die Energieverteilung von dünnwandigen Plattenstrukturen. In: *DAGA 2018* Deutsche Gesellschaft für Akustik (Veranst.), 2018, p. 1251–1254

[Miksch et al 2018c]   MIKSCH, M. ; MÜLLER, U. C. ; PEIFFER, A. ; MÜLLER, G.: Numerische Berechnung der Dispersion von flächig verteilten Schwingungstilgern und akustischen schwarzen Löchern mithilfe von Wave-Finite-Elements. In: *DAGA 2018* Deutsche Gesellschaft für Akustik (Veranst.), 2018, p. 56–59

[Miksch et al 2019]   MIKSCH, M ; PEREZ RAMIREZ, J D. ; MÜLLER, G: Numerical computation of the spatial decaying wave characteristics for the design of locally resonant acoustic metamaterials. In: *Journal of Physics: Conference Series, vol. 1264* (2019)

[Milton et al 2006]   MILTON, G. W. ; BRIANE, M. ; WILLIS, J. R.: On cloaking for elasticity and physical equations with a transformation invariant form. In: *New Journal of Physics, vol. 8* (2006)

[Milton and Cherkaev 1995]   MILTON, G. W. ; CHERKAEV, A.: Which Elasticity Tensors are Realizable? In: *Journal of Engineering Materials and Technology, vol 117, issue 4* (1995)

[Miranda and Dos Santos 2016]   MIRANDA, E. J. P. ; DOS SANTOS, J. M. C.: Flexural Wave Band Gaps in an Elastic Metamaterial Beam with Periodically Attached Spring-Mass Resonators. In: *Proceedings of ISMA and USD* (2016)

[Mironov 1988]   MIRONOV, M. A.: Propagation of a flexural wave in a plate whose thickness decreases smoothly to zero in a finite interval. In: *Soviet Physics Acoustics, vol. 34, pp. 318-319* (1988)

[Mironov and Gladilin 2016]   MIRONOV, W. ; GLADILIN, A.: Analytical solution of black hole equation and some consequences. In: *Proceedings of Inter-Noise, Hamburg, pp. 2356-2360* (2016)

[Müller 2019a]   MÜLLER, G..: *Integral Transform Methods*, Technische Universität München, Lecture notes, 2019

[Müller 2019b]   MÜLLER, G..: *Structural Dynamics*, Technische Universität München, Lecture notes, 2019

[Müller and Möser 2013]   MÜLLER, G. ; MÖSER, M.: *Handbook of Engineering Acoustics.* Berlin : Springer, 2013

[Müller and Faulhaber 2018]   MÜLLER, U. C. ; FAULHABER, P.: Druck von requqnezgenauen metallischen Tilgerarrays für akustische Metamaterialien aus Metall mit Additive Layer Manufacturing: Entwurfsprozess und erste Ergebnisse. In: *DAGA 2018* Deutsche Gesellschaft für Akustik (Veranst.), 2018, p. 64–67

[Mohtat and Dehghan-Niri 2011]   MOHTAT, A. ; DEHGHAN-NIRI, E.: Generalized framework for robust design of tunedmass damper systems. In: *Journal of Sound and Vibration, vol. 330, pp. 902-922* (2011)

[Mollo and J. 1989]   MOLLO, C. G. ; J., Bernhard R.: Generalized method of predicting optimal performance of active noise controllers. In: *AIAA Journal, vol. 27, no. 11, pp. 1473-1478* (1989)

[Möser and Kropp 2010]   MÖSER, Michael ; KROPP, Wolfgang: *Körperschall, Physikalische Grundlagen und technische Anwendungen.* Springer, 2010

[Nateghi et al 2019]   NATEGHI, A. ; SANGIULIANO, L. ; CLAEYS, C. ; DECKERS, E. ; PLUYMERS, B. ; DESMET, W.: Design and experimental validation of a metamaterial solution for improved noise and vibration behavior of pipes. In: *Journal of Sound and Vibration, vol. 455, pp. 96-117* (2019)

[Norris and Shuvalov 2011]   NORRIS, A. N. ; SHUVALOV, A. L.: Elastic Cloaking Theory. In: *Wavemotion, vol. 48, pp. 525-538* (2011)

[Oberst 1952]   OBERST, H.: Über die Dämpfung der Biegeschwingungen dünner Bleche durch fest haftende Beläge. In: *Acustica, vol. 2, pp. 181-194* (1952)

[O'Boy et al 2010]   O'BOY, D. J. ; BOWYER, E. P. ; KRYLOV, V. V.: Damping of flexural vibrations in thin plates using one and two dimensional acoustic black hole effect. In: *10th International Conference on Recent Advances in Structural Dynamics (RASD 2010), Southampton, UK* (2010)

[Ormondroyd and Den Hartog 1928]   ORMONDROYD, J. ; DEN HARTOG, J. P.: The theory of the dynamic vibration absorber. In: *Transactions of the American Society of Mechanical Engineers, vol. 50, pp. 9-22* (1928)

[Orris and Petyt 1974]   ORRIS, R. M. ; PETYT, M.: A finite element study of harmonic wabe propagation in periodic structures. In: *Journal of Sound and Vibration, vol. 33, no. 2, pp. 223-236* (1974)

[Pavic et al 2002]   PAVIC, A. ; WILLFORD, M. ; REYNOLDS, P. ; WRIGHT, J.: Key results of modal testing of the Millennium Bridge, London. In: *Footbridge* (2002)

[Pavic 1987]   PAVIC, G.: Structural surface intensity: An alternative approach in vibration analysis and diagnosis. In: *Journal of Sound and Vibration, vol. 115, pp. 405-422* (1987)

[Pendry et al 1999]   PENDRY, J. B. ; HOLDEN, A. J. ; ROBBINS, D. J. ; STEWART, W. J.: Magnetism from conductors and enhanced nonlinear phenomena. In: *IEEE Trans. Microwave Theory Tech, vol. 47, pp. 2075-2084* (1999)

[Perez Ramirez 2017]   PEREZ RAMIREZ, J. D.: *Investigation of Periodic Structures for the Design of Acoustic Metamaterials Using Unit-Cell Modeling*, Technische Universität München, Master's Thesis, 2017

[Petersen 1996]   PETERSEN, Christian: *Dynamik der Baukonstruktion.* 1. Auflage. Braunschweig / Wiesbaden : Friedr. Vieweg & Sohn Verlagsgesellschaft mbH, 1996

[Poon et al 2004]   POON, D. ; SHIEH, S. ; JOSEPH, L. ; CHANG, C.: Structural Design of Taipei 101, the World's Tallest Building. (2004)

[Popa et al 2011]   POPA, B. I. ; ZIGONEANU, L. ; CUMMER, S. A.: Experimental Acoustic Ground Cloak in Air. In: *Physical Review Letter, vol. 106* (2011)

[Prill et al 2016]   PRILL, O. ; ROOS, C. ; BUSCH, R.: Finite Element simulations of acoustic black holes as lightweight damping treatment for automotive body panels with apllication to full vehicle interior wind noise prediction. In: *Proceedings of Inter-Noise, Hamburg, pp. 2440-2451* (2016)

[Rade and Steffen 2000]   RADE, D. A. ; STEFFEN, V.: Optimisation of dynamic vibration absorbers over a frequency band. In: *Mechanical Systems and Signal Processing, vol. 14, issue 5, pp. 679-690* (2000)

[Ritz 1909]   RITZ, W.: Über eine Methode zur Lösung gewisser Variationsprobleme der mathematischen Physik. In: *Journal für reine und angewandte Mathematik, vol. 135, pp. 1-61* (1909)

[Ross et al 1960]   ROSS, D. ; UNGAR, E. E. ; KERWIN, E. M.: Damping of plate flexural vibrations by means of viscoelastic laminae. In: *Structural Damping, Oxford, pp. 49-87.* (1960)

[Ruzzene 2015]   RUZZENE, M.: Internally Resonating Metamaterials for Wave and Vibration Control. In: *Noise and Vibration - Emerging Technologies (NOVEM)* (2015)

[Ruzzene and Scarpa 2003]   RUZZENE, M. ; SCARPA, F.: Wave beaming effects in two-dimensional cellular structures. In: *Smart Materials and Structures, vol. 12, pp. 363-372* (2003)

[Schur 1909]   SCHUR, I.: On the Characteristic Roots of a Linear Substitution with an Application to the Theory of Integral Equations. In: *Mathematische Annalen, vol. 66, pp. 488-510* (1909)

[Sharma and Sun 2016]   SHARMA, B. ; SUN, C.T.: Local resonance and Bragg bandgaps in sandwich beams containing periodically inserted resonators. In: *Journal of Sound and Vibration, vol. 364, pp. 133-146* (2016)

[Shelby et al 2001]   SHELBY, R. A. ; SMITH, D. R. ; SCHULTZ, S.: Experimental verification of a negative index of refraction. In: *Science, vol. 292, pp. 77-79* (2001)

[Silva 2015]   SILVA, Priscilla: *Dynamic analysis of periodic structures via wave-based numerical approaches and substructuring techniques*, University of Campinas, Ph.D. thesis, 2015

[Spadoni et al 2009a]   SPADONI, A. ; RUZZENE, M. ; CUNEFARE, K.: Vibration and Wave Propagation Control of Plates with Periodic Arrays of Shunted Piezoelectric Patches. In: *Journal of Intelligent Material Systems and Structures, vol. 20, pp. 979-990* (2009)

[Spadoni et al 2009b]   SPADONI, A. ; RUZZENE, M. ; GONELLA, S. ; SCARPA, F.: Phononic properties of hexagonal chiral lattices. In: *Wave motion, vol. 46, pp. 435-450* (2009)

[Spadoni et al 2014]   SPADONI, R. ; COHEN-ADDAD, S. ; DORODNITSYN, V.: Closed-cell crystalline foams: Self-assembling, resonant metamaterials. In: *Journal of the Acoustical Society of America, vol 135, issue 4* (2014)

[Stanton and Mann 2010]   STANTON, Samuel C. ; MANN, Brian P.: On the dynamic response of beams with multiple geometric or material discontinuities. In: *Mechanical Systems and Signal Processing, Vol. 24, no. 5, pp. 1409.1419* (2010)

[Stenger et al 2012]   STENGER, N. ; WILHELM, M. ; WEGENER, M.: Experiments on Elastic Cloaking in Thin Plates. In: *Applied Physical Letter, vol. 100, no. 191901* (2012)

[Sun and Wu 2006]   SUN, J. H. ; WU, T. T.: Propagation of surface acoustic waves through sharply bent two-dimensional phononic crystal waveguides using a finite-difference time-domain method. In: *Physical Letter Review B, vol. 74, no. 174305* (2006)

[Tang et al 2016]   TANG, W. ; CHENG, L. ; JI, H. ; QIU, J.: Enhanced acoustic black hole effect using a modified theckness profile. In: *Proceedings of Inter-Noise, Hamburg, pp. 2361-2369* (2016)

[Timoshenko and Woinowsky-Krieger 1959]   TIMOSHENKO, S. ; WOINOWSKY-KRIEGER, S.: *Theory of plates and shells.* New York: McGraw-Hill, 1959

[Unruh et al 2016]   UNRUH, O. ; HAASE, T. ; MONNER, H.P. ; POHL, M.: *Aktives akustisches schwarzes Loch zur Schwingungs- und Lärmreduktion.* july 14 2016. – DE Patent App. DE201,510,100,442

[Van Belle et al 2019]   VAN BELLE, L. ; CLAEYS, C. ; DECKERS, E. ; DESMET, W.: The impact of damping on the sound transmission loss of locally resonant metamaterial plates. In: *Journal of Sound and Vibration, vol. 461* (2019)

[Veselago 1968]   VESELAGO, V. G.: The electrodynamics of substances with simultaneously negative values of μ and ϵ. In: *Soviet Physics, vol. 10, no. 4, pp. 509-514* (1968)

[Vitiello et al 1989]   VITIELLO, P. ; NELSON, P. A. ; PETYT, M.: Numerical stdiues of the Active Control of Sound Transmission Through Double Partitions. In: *ISVR Technical Report, no. 183, University of Southampton* (1989)

[Waki et al 2009]   WAKI, Y. ; MACE, B.R. ; BRENNAN, M.J.: Numerical issues concerning the wave and finite element method for free and forced vibrations of waveguides. In: *Journal of Sound and Vibration, vol. 327, no. 1, pp. 92-108* (2009)

[Wei et al 2014]   Wei, P. ; Liu, F. ; Liang, Z. ; Xu, Y. ; Chu, S. T. ; Li, J.: An acoustic beam shifter with enhanced transmission using perforated metamaterials. In: *EPL, vol. 109* (2014)

[Willis 1981]   Willis, J. R.: Variational principles for dynamic problems for inhomogeneous elastic media. In: *Wave Motion, vol. 3, pp. 1-11* (1981)

[Xiao et al 2012]   Xiao, Y. ; Wen, J. ; Wen, X.: Broadband locally resonant beams containing multiple periodic arrays of attached resonators. In: *Physics Letters A, vol. 376, no. 16, pp. 1384-1390* (2012)

[Xiao et al 2013]   Xiao, Y. ; Wen, J. ; Yu, D. ; Wen, X.: Flexural wave propagation in beams with periodically attached vibration absorbers: Band-gap behavior and band formation mechanisms. In: *Journal of Sound and Vibrations, vol. 332, pp. 867-893* (2013)

[Zhang 2010]   Zhang, Shu: *Acoustic Metamaterials Design and Applications*, University of Illinois at Urbana-Champaign, Dissertation, 2010

[Zhao et al 2014]   Zhao, L. ; Colon, S. C. ; Semperlotti, F.: Broadband energy harvesting using acoustic black hole structural tailoring. In: *Smart Materials and Structures, vol. 23, no. 065021* (2014)

[Zhao et al 2015]   Zhao, L. ; Conlon, S. C. ; Semperlotti, F.: An experimental study of vibration based energy harvesting in dynamically tailored structures with embedded acoustic black holes. In: *Smart Materials and Structures, vol. 24, no. 065039* (2015)

[Zhong and Williams 1995]   Zhong, W. X. ; Williams, F. W.: On the direct solution of wave propagation for repetitive structures. In: *Journal of Sound and Vibration, vol 181, pp. 485-501* (1995)

[Zhou 2014]   Zhou, Changwei: *Wave and modal approach for multi-scale analysis of periodic structures*, Ecole Centrale de Lyon, Ph.D. thesis, 2014

[Zienkiewicz and Taylor 2005]   Zienkiewicz, O. C. ; Taylor, R. L.: *The Finite Element Method For Solid and Structural Mechanics.* Elsevier, 2005

[Zienkiewicz et al 2005]   Zienkiewicz, o. C. ; Taylor, R. L. ; Zhu, J. Z.: *The Finite Element Method: Its Basis and Fundamentals.* Elsevier, 2005

[Zigoneanu et al 2014]   Zigoneanu, L. ; Popa, B.-I. ; Cummer, S. A.: Three-dimensional broadband omnidirectional acoustic ground cloak. In: *Nature Materials, vol. 13, pp. 352–355* (2014)